UNIVERSITÉ PARIS-SACLAY

Ecole Doctorale de Chimie

Sciences Chimiques: Molécules, Matériaux, Instrumentation et Biosystèmes

Laboratoire de Chimie-Physique (LCP)

THESE

PRESENTEE POUR OBTENIR LE GRADE DE

DOCTEUR EN SCIENCES DE L'UNIVERSITE PARIS-SACLAY

Spécialité Chimie-Physique

Surface Modified Semiconductors with Metal Nanoparticles: Photocatalysts with High Activity Under Solar Light

Par: *María Guadalupe Méndez Medrano*

Soutenue le 10/05/2016

Commission d'examen:

Dr. José Luis Rodríguez López, *Directeur de thèse, Instituto Potosino de Investigación Científica y Tecnológica A.C.*

Dr. Hynd Remita (DR), *Co-directrice de thèse, CNRS-Univ. Paris-Sud, Univ. Paris-Saclay*

Dr. Nancy Brodie-Linder (MC), *Rapporteur, Université de Cergy-Pontoise*

Dr. Alma Gabriela Palestino Escobedo, *Rapporteur, Univ. Autónoma de San Luis Potosí*

Prof. Isabelle Lampre, *Examinatrice (PR), Univ. Paris-Sud, Univ. Paris-Saclay*

Dr. María Guadalupe Cárdenas Galindo, *Examinatrice, Univ. Autónoma de San Luis Potosí*

INSTITUTO POTOSINO DE INVESTIGACIÓN CIENTÍFICA Y TECNOLÓGICA, A.C.

Doctorado en Nanociencias y Materiales

Surface Modified Semiconductors with Metal Nanoparticles: Photocatalysts with High Activity Under Solar Light

Tesis que presenta

María Guadalupe Méndez Medrano

Para obtener el grado de

Doctorado en Nanociencias y Materiales

Director de tesis:
Pr. José Luis Rodríguez López

Co-director de tesis:
Pr. Hynd Remita
San Luis Potosí, SLP, 10 de Mayo de 2016

IPICYT

Constancia de Aprobación de la Tesis

La tesis "**Surface Modified Semiconductors with Metal Nanoparticles: Photocatalysts with High Activity under Solar Ligh**" presentada para obtener el Grado de Doctor(a) en Nanociencias y Materiales fue elaborada por **María Guadalupe Méndez Medrano** y aprobada el **10 de Mayo del 2016** por los suscritos, designados por el Colegio de Profesores de la División de Materiales Avanzados del Instituto Potosino de Investigación Científica y Tecnológica, A.C.

Dr. José Luis Rodríguez López Director de la tesis	Dr. Hynd Remita Co-director de la tesis
Dr. María Guadalupe Cárdenas Galindo (Miembro del Comité Tutoral)	Dr. Nancy Brodie-Linder, (Miembro del Comité Tutoral)
Dr. Alma Gabriela Palestino Escobedo (Miembro del Comité Tutoral)	Prof. Isabelle Lampre (Miembro del Comité Tutoral)

Créditos Institucionales

Esta tesis fue elaborada en la División de Materiales Avanzados del Instituto Potosino de Investigación Científica y Tecnológica, A.C., y en el Laboratoire de Chimie Physique de la Université de Paris-Sud, bajo la dirección y co-dirección de los Drs. Prof. José Luis Rodríguez López y la Prof. Hynd Remita.

Durante la realización del trabajo la autora recibió una beca académica del Consejo Nacional de Ciencia y Tecnología (356872).

La autora recibió una beca mixta en la modalidad de co-tutela del Consejo Nacional de Ciencia y Tecnología (290752) y apoyos diversos en modalidad de beca por parte del Instituto Potosino de Investigación Científica y Tecnológica, A. C. y Université Paris–Sud.

La autora recibió también una beca Ecos-Nord México-Francia, bajo el proyecto M11-P02 (2012) para la realización de experimentos en una estancia de investigación en el Laboratoire de Chimie Phisique de la Université Paris–Sud.

La autora recibió una beca de Excelencia Eiffel del gobierno francés (812714K) Campus France.

Página en Blanco que se va a utilizar para colocar la copia del acta de examen.

Dedicatorias

Dedico esta tesis a mi familia mi Madre, Padre y Hermanos que han estado a mi lado apoyándome todo este tiempo siendo mi motor en todo lo que hago. A mis Amigos y a todos los que me brindaron su apoyo,

A todos ellos dedico esta tesis con cariño y un muy grande agradecimiento

Acknowledgments

I would like to thank both of my supervisors, for giving me the opportunity of being part of this project of investigation in the modality of joining PhD (Co-tutelle) and for giving me all the necessary conditions to finish my PhD thesis in a satisfactory way.

I express my thanks to my supervisor, José Luis Rodríguez López, at Instituto Potosino de Investigación Científica y Tecnológica, A.C. (IPICYT, A.C.) for the support offered for the accomplishment of this thesis and throughout my PhD, by the knowledge that he gives me, its suggestions, and advices.

I want to express my sincere gratefulness and recognition to my co-supervisor Prof Hynd Remita. I thank her for letting me participate in her group of research at the Laboratoire de Chimie Physique (LCP) of the University of Paris-Saclay, Orsay. I thank her for all the knowledge and experience that she gives me. I really appreciate her delivery to research and dedication to my work. I also wish to thank her for amiability and hospitality when I was in France.

I would like to express a special gratefulness to my committee Dr. Guadalupe Cárdenas, Dr. Nancy Brodie-Linder, Dr. Alma Gabriela Palestino, Dr. José Luis Llamazares, Dr. Armando Encinas and Prof. Isabelle Lambre, for having taken time in reading my thesis and for giving me their comments and suggestions.

I would also like to thank Prof. Christophe Colbeau-Justin for all his support, advices and his help in analysis of Time Resolved Microwave Conductivity (TRMC) results. I also express to Dr. Ewa Kowalska (Hokkaido University), a very special gratitude, for taking time to analyze my work and for her very useful comments.

I would like also to thank Prof. Ohtani Bunsho (Hokkaido University) and Prof. Sven Rau (University of Ulm) for providing me all the necessary tools for working in their laboratories. The stays in their laboratories gave to my work new perspectives and were very enriching for my PhD thesis.

I thank Dr. Daniel Bahena, Dr. Anaïs Lehoux, and Dr. Alexandre Herissan for their help and support in the characterization techniques.

I would also like to thank Dr. Vladimir Escobar for all his support, advices and his financial help.

I want to be thankful to the graduate program and administrative team at IPICYT and the LCP, to Ivonne Cuevas, Edith Rodríguez, Karla Gómez, Laura Sánchez, Marie-Françoise Lecanu, Anne Morel, Séverine Bourguignon and Delphine Lelièvre, for all their support, and for being always helpful.

I thank Mireille Benoît for all her technical support in the chemistry laboratory of the LCP. I also thank the technicians of LINAN-IPICYT for their time and help in the characterization techniques: Dr. Gladis Labrada, M.Sc. Beatriz Rivera, Dr. Nicolas Cayetano, Dr. Héctor Silva, Dr. Mariela Bravo.

I would like to express a special gratefulness to all the people that I met in this stage of my life, companions that shared with me their experiences and knowledge, as well as their friendship. To Marcelo Lozano, thanks for his unconditional support, to Anel Perales, Hugo Ibarra, Jackeline Iturbe, Alan Sustaita, thanks to offer me their friendship and support, to students from the UASLP Juan Manuel Arce, Israel Sustaita and Ilse Ávila, to students from the Hokkaido University, Shugo Tekeuchi, Haruna Hori, Maya Endo, and to students from the University of Ulm, Michael Pfeffer and Philipp Lang, thanks for help me and to offer me their support.

Special thanks to my friends and colleagues of the LCP. First I would like to thank Alexandre Herissan for all his help, but mainly for arriving in my life and being a part of her. I thank Iyad Sarhid, Dita Floresyona, Marie Clement, Zibin Hai, Jonathan Verrett, Cecilia Coletta, Anaïs Lehoux, Priyanka Ray, Srabanti Ghosh, Natalie Kouame, Daniela Salado and Ana Laura Luna for their help and for making very pleasant my stay at the LCP.Thanks to all for your amiability, good humor and great atmosphere of work.

Guadalupe Méndez

Index

Tables and Figures

Tables

Figures

Appendices

Abbreviations

AOPs:	Advanced Oxidation Processes
AOT:	Advanced Oxidation Technologies
SC:	Semiconductor
NPs:	Nanoparticles
MNPs:	Metal nanoparticles
CB:	Conduction Band
VB:	Valence Band
UV:	Ultraviolet
NHE:	Normal Hydrogen Electrode
LSPR:	Localized Surface plasmon resonance
THPC:	Tetrakis Hydroxymethyl Phosphonium Chloride
P25:	A mixture of anatase (80%) and rutile (20%)
IMP:	Impregnation method
DRS:	Diffuse Reflectance Spectroscopy
XRD:	X-ray Diffraction
BE:	Binding Energy
EDS	Energy-Dispersive Spectroscopy
HAADF:	High Angle Annular Dark Field
HRTEM:	High Resolution Electron Microscopy
SEM:	Scanning Electron Microscopy
TEM:	Scanning Transmission Electron Microscopy
TRMC:	Time Resolved Microwave Conductivity
AS:	Action Spectra

XPS:	X-ray Photoelectron Spectroscopy
XAS:	X-ray Absorption Spectroscopy
ROS:	Reactive Oxygen Species
IEQ:	Indoor Enviromental Quality
PWS	Photocatalytic Water Splitting

Motivation

TiO_2 is a very abundant, cheap, stable and non-toxic material, which is used in several products and goods of normal use and every day consumption such as creams for solar protection, cosmetics, papers, paints, food industry, etc.

It is well known that TiO_2 has the peculiar property that when it is irradiated with light at sufficient energy (higher than its band-gap), reactive species are formed on its surface. These species are capable to carry out redox reactions. This phenomenon is known as “photo-activation”, and these kind of materials are known as photocatalysts.

This material can be used for self-cleaning surface modification due to the superhydrophilicity property of TiO_2 induced by UV irradiation. The photocatalytic activity and the hydrophilicity property of TiO_2 are exploited to obtain self-cleaning surfaces: TiO_2 is added to several surfaces such as glass, plastic, ceramic, cement, etc.[1]

TiO_2 is a semiconductor with band gap around 3.2 eV. When it is excited with UV light, electrons and holes are formed. These electrons and holes can recombine. When they escape recombination, they can migrate to the surface of the photocatalyst, and thus react with electrons and acceptor donors to carry out redox reactions. Thus, TiO_2 can be used to solve global environmental problems for depollution of air and water. Indeed, it can work as air purifier, cleaning the air that we breath, and it is also used in reactors for air purification. Another social and technological application is wastewater treatment (mineralization of pollutants in water), destruction of bacteria and fungi and it can also be used to split the water molecule to produce hydrogen as a new source of energy.

Besides all the above mentioned advantages, one and the most important limitation of TiO_2 is that it can be only activated by UV irradiation (only about 5% of UV irradiation is within the solar spectra),[2] which basically means high energy costs for technological applications. Many studies focus on modification of TiO_2 to extend its activity toward the visible range and thus obtain a photocatalytic material very active under the solar light, a free and inexhaustible source of energy.

Our research group is interested in modification of TiO_2 and in development of materials for photocatalytic application under visible light. In this thesis work, we are focused on the development of new active photocatalysts based on TiO_2 working under visible light. With this in mind, we proposed the surface modification of titania with metals such as gold (Au), or silver (Ag), *i.e.,* metals known as "noble and transition metals" since these metal modifications can activate the material under visible light. But why these metals? Why they are so special? It turns out that nanoparticles made of these metals, present constructive resonant oscillations among the surface electrons of the metal nanoparticles (MNPs) and the electric field of the incident light, and therefore present strong absorption in the visible range, a phenomenon known as "*surface plasmon resonance*" (SPR). The photocatalytic semiconductors modified with plasmonic metal nanoparticles are known as ***plasmonic photocatalysts***.[2] When visible light interacts with the plasmonic photocatalysts, there is strong evidence in the literature, that SPR play an important role in enhancing the rate of photocatalytic reactions on nearby semiconductors, as obtained in the measurements with rate enhancements induced by plasmonic metals as a function of the excitation wavelengths.

Another modification that enhances the photo-activity of TiO_2 under visible light, is to join it (physically) to another semiconductor with a narrow band gap, this last one being able to be activated under the visible range, such as CuO. The semiconductor CuO is active under visible light, and the junction with TiO_2 can lead to active photocatalysts under visible light.

Environmental pollution is today a very important issue that must be considered seriously to prevent further problems in the future, for example the large amounts of wastes dumped in various water effluents, such as rivers, lakes and seas can be very harmful to fish, animals and humans. The emission of greenhouse gases and other pollutants are threatening the biodiversity and our future. On another hand, the energy demand is increasing, and it is urgent to develop new clean energy sources such as solar fuels.

Solar energy is the only feasible long-term way of meeting the world's ever increasing needs for energy, and its storage technology will be the key enabling factors to make sunlight practical as a dominant source of energy. The development of nanostructured materials has opened new paths in different scientific fields and is providing new opportunities in environmental science. The field of heterogeneous photocatalysis has attracted considerable attention in recent years due to its potential use in many applications in environmental technology, ranging from purification of water and air to photo-electrocatalytic production of hydrogen. There is still much research and engineering work to do, but we can say that the plasmonic photocatalysts and the modification of titania with another semiconductor are interesting alternatives to overcome the limitations of TiO_2 and to develop very active photocatalytic materials under solar light.

Hypothesis

The modification of photoactive semiconductor titania with size and structure control of metal nanoparticles (Au, Ag, CuO and Ag@CuO) enhance the quantum yield of titania under UV irradiation retarding the recombination process and can also activate the titania under visible irradiation with the electron transfer from the metal NPs to the conduction band of titania semiconductor. This modification can induce an enhancement in the photocatalytic activity.

Objectives

The general objective in this thesis work, is the development of new or improved photocatalytic titania, controlling the size, loading and structure of metal-based nanoparticles. A particular attention was paid to surface modification with one and two metal-based nanoparticles, synthesized by radiolysis or by a chemical method.

The objectives of the PhD thesis were to:

- Understand the effect of surface modification of titania with metal nanoparticles on the charge carrier dynamics and on the photocatalytic activity. We carried out studies with time resolved microwave conductivity (TRMC) technique coupled to a tunable laser (from UV to infrared irradiations: from 220 nm to 2000 nm) and we measured the action spectra of the photocatalysts.

- Understand the effect of surface modification of TiO_2 with Au, Ag, CuO and CuO@Ag nanoparticles on the photocatalytic processes, *i.e.*; (a) the role of metal nanoparticles as electron traps and the effect on the electron-hole recombination processes (UV region), and (b) also electron transfer from the metal nanoparticles to the conduction band of the TiO_2.

- Study their photocatalytic activity for different oxidation reactions and for hydrogen generation.

- Study the antifungal properties of TiO_2 modified with Ag, CuO and CuO@Ag nanoparticles.

General Abstract

Surface Modified Semiconductors with Metal Nanoparticles: Photocatalysts with High Activity Under Solar Light

The modification of TiO_2-P25 with one or two metal-based nanoparticles have attracted considerable attention in recent years as a new class of highly active catalysts and photocatalysts under both UV and visible light irradiation. One or two-metal-based structures, such as Au, Ag, Ag@CuO and CuO deposited on TiO_2-P25 have the ability to absorb visible light in a wide spectral range. Surface modified TiO_2 with metal nanoparticles (such as Cu, Au, Ag) absorb visible light due to the localized surface plasmon resonance (LSPR). In the case of semiconductor heterojunctions, they absorb visible light due to the narrow band gap of the second semiconductor, lower than TiO_2-P25. The modification with one or two metal-based nanoparticles induces a higher activity under visible light compared to pure TiO_2-P25, due to the transfer of electrons to the conduction band of TiO_2-P25. On the other hand, under UV irradiation, the speed of trapping photoexcited electrons can be improved, to inhibit the recombination process and have the capability to store photoexcited electrons.

This thesis presents recent advances in the preparation and environmental application of the surface modification of TiO_2-P25 with one or two-metal-based nanoparticles: The Au-NPs were synthesized by chemical method using tetrakis(hydroxymethyl) phosphonium chloride (THPC), and the nanoparticles of Ag, Ag@CuO and CuO-NPs were synthesized by gamma irradiation. Moreover, the effects of various parameters (such as particle size, shape of the nanoparticles and amount of metals) on the photocatalytic activity (phenol, 2-propanol and acetic acid oxidation, as well as hydrogen generation) were also studied. The charge carrier dynamics was studied by time resolve microwave conductivity (TRMC).

Résumé Général

Semiconducteurs Modifiés en Surface par des Nanoparticles Metalliques: Photocatalyseurs avec une Grande Activité sous Lumière Solaire

La modification du TiO_2 P25 par un ou deux métaux a connu un intérêt considérable ces dernières années, car ils constituent des catalyseurs et photocatalyseurs très actifs à la fois sous lumière UV et visible. Des nanostructures à un ou deux métaux, comme Au, Ag, Ag@CuO et CuO déposés sur le TiO_2 P25 ont la capacité d'absorber la lumière visible sur un large domaine de longueurs d'onde. Le TiO_2 modifié par des nanoparticules métalliques (comme, Cu, Au ou Ag) absorbe la lumière visible grâce à la résonance de plasmon de surface localisée (LSPR) des métaux. Dans le cas d'une hétérojonction de semi-conducteurs, la lumière visible est absorbée grâce à l'énergie du gap plus faible du second semi-conducteur (par rapport à celle du TiO_2 P25). La modification par une ou deux nanoparticules métallique induit une plus grande activité photocaralytique sous lumière visible par rapport au TiO_2 P25 pur, par transfert d'électrons vers la bande de conduction du P25. De plus sous lumière UV, la vitesse de capture d'électrons photo-excités peut être améliorée, ce qui inhibe les processus de recombinaison et permet de stocker ces électrons photo-excités.

Cette thèse présente une synthèse des récentes avancées dans la préparation de TiO_2 modifié en surface par un ou deux métaux et ses applications environnementales. Des nanoparticules d'or ont été synthétisées par une méthode chimique à partir de chlorure de tetrakis(hydroxymethyl) phosphonium (THPC), des nanoparticules de Ag, Ag@CuO et CuO ont été synthétisées sur TiO_2 par radiolyse. L'effet de nombreux paramètres (comme la taille et la forme des particules ou la quantité de métal déposé) sur l'activité photocatalytique (oxydation du phénol, du 2-propanol et de l'acide acétique et génération d'hydrogène) a été étudié. La dynamique de porteurs de charge a été étudiée par conductivité microonde résolue en temps (TRMC).

Resumen General

Modificación de Semiconductores por Nanopartículas Metálicas: Fotocatalizadores con Alta Actividad Bajo la Luz Solar

La modificación del TiO_2-P25, con uno o dos-metales, han atraído una considerable atención en los últimos años, como una clase de catalizadores y photocatalizadores altamente activos bajo la radiación UV y la luz visible. Estructuras de uno o dos metales, tales como Au, Ag, Ag@CuO y CuO depositados sobre TiO_2-P25, tienen la capacidad de absorber la luz visible en una amplia gama de longitudes de onda. La modificación superficial del TiO_2 con nanopartículas metálicas (como, Cu Au, Ag) absorben la luz visible debido a su propiedad de la resonancia localizada del plasmón de superficie (RLPS). En el caso de la unión de dos semiconductores, el sistema es foto-activo bajo la luz visible debido al valor de la banda de energía prohibida del segundo semiconductor, (procurando que esta sea menor que la del TiO_2-P25), por lo tanto, la modificación con uno o dos metales, induce una mayor actividad bajo la región del visible comparado con el TiO_2 puro. Por otro lado, bajo la radiación UV, pueden mejorar la velocidad de captura de electrones foto-excitados e inhibir el proceso de recombinación debido a su capacidad de almacenamiento de electrones foto-excitados.

En esta tesis presentamos la preparación y aplicación ambiental de la modificación del TiO_2-P25 con uno o dos metales, las nanopartículas de Au, fueron sintetizadas por método químico usando *tetrakis(hydroxymethyl) phosphonium chloride* (THPC), y las nanopartículas de Ag, Ag@CuO y CuO-NPs fueron sintetizadas por irradiación gamma. Además, estudiamos y discutimos los efectos de diversos parámetros (tales como el tamaño y forma de las partículas, y la cantidad de metales) en la actividad fotocatalítica (oxidación de fenol, 2-propanol y ácido acético y generación de hidrogeno) fue también estudiado. La dinámica de portadores de carga fue estudiada mediante la conductividad de microondas resuelta en el tiempo (TRMC).

Preface

The photocatalytic process requires a semiconductor (SC) material to absorb photons from an incident irradiation, to generate electrons and holes capable to achieve reduction and/or oxidation (redox) reactions of chemicals products, making these materials useful for a wide range of applications such as air purification, CO_2 reduction, effective degradation of organic pollutants in water or air, and hydrogen (H_2) production by the water splitting process.[3,4,5] However, the main drawbacks of the currently used photocatalysts such as TiO_2 are the high rate of recombinations between electron and holes, resulting in a low quantum yield,[6,7] and the ineffective (or limited) response under solar light, which is considered as a green energy source due to its natural availability, low cost and abundance. One way to enhance the efficiency of the photocatalysts and activate them under visible light is based on the recently developed plasmonic photocatalysts systems, which consist on the surface modification of semiconductors (such as titanium dioxide, which is actually the most used semiconductor for photocatalytic processes) with plasmonic metal nanoparticles (MNPs). In this context, TiO_2 has been modified with gold, silver and copper oxide NPs for several applications such as oxidation of organic molecules, selective oxidation of aromatic alcohols to carbonyl compounds in wastewater treatment,[8] hydrogen formation from alcohols,[9] antibacterial properties and selective reduction of organic compounds.[10] Since they provide a promising and environmentally friendly way to perform these processes at low-cost using visible light, or in the best of cases, take advantage of the sunlight.

This PhD thesis document contains five chapters:

In Chapter 1, we will describe the theoretical background that involves the plasmonic photocatalysts. We will highlight the critical environmental problems present in the world of water and air pollution, with focus in the specific cases of Mexico and France. The choice of these countries is clear since the thesis is result of the bilateral collaboration between Mexico and France. This chapter will present the description of advanced oxidation processes for waste water treatment, and it will focus on the photocatalytic process due to the versatility of its applications not only in water treatment but also as a new process to obtain H_2 from water splitting. We will present the drawbacks of TiO_2 used as a photocatalysts and we will summarize the ways to improve the photocatalysts photoactivity especially under visible irradiation. In this chapter we will explain the principle of plasmonic photocatalysis, and the influence of the localized surface plasmon resonance (LSPR) and the Schottky barrier on the photocatalytic processes. Different methods of plasmonic photocatalysts synthesis will also be presented, principally the chemical method using a reducing agent and the radiolysis method. And finally, we will introduce possible applications of these plasmonic photocatalytic materials.

In Chapter 2 we will describe the experimental setups, materials, experimental conditions, synthesis protocols, characterization techniques and the photoreactors used to measure the photoactivity.

In Chapter 3, gold nanoparticles (Au-NPs) were used to modify the surface of titanium dioxide as visible-light absorbers and as thermal redox active centers. Au-NPs were synthesized on commercial TiO_2-P25 by reduction of Au salt with tetrakis (hydroxymethyl) phosphonim chloride. The Au/P25 composites were characterized with different techniques, such as X-ray diffraction (XRD), high resolution transmission electron microscopy (HRTEM), diffuse reflectance spectroscopy (DRS), X-ray photoelectron spectroscopy (XPS) and time resolved microwave conductivity (TRMC). The photocatalytic activity of Au/P25 was evaluated for the degradation of phenol, 2 propanol and acetic acid (used as models of pollutants) and for H_2 production by the photocatalytic water splitting (PWS) process. Charge carrier dynamics were studied by TRMC and action spectra (AS) were measured to correlate the photoactivity of the modified titania with its absorbance.

In Chapter 4, small CuO nanoclusters were synthesized on TiO_2-P25 surface by radiolysis with different loadings. Surface modification of TiO_2 by CuO clusters induces a photocatalytic activity under visible light irradiation in a wide range of wavelengths. The photocatalysts were characterized by different techniques including X-ray absorption spectroscopy (XAS), DRS and TRMC. The photocatalytic properties of bare and modified TiO_2-P25 were studied for phenol, 2-

propanol degradation and acetic acid oxidation in aqueous suspensions under UV and visible irradiation as well as hydrogen production, and antibacterial properties under visible irradiation.

In Chapter 5, the modification with Ag, CuO and Ag@CuO NPs synthesized on the surface of commercial TiO_2-P25 by radiolytic reduction were characterized by DRS, TEM, High Angle Annular Dark Field Scanning Transmission Electron Microscopy (HAADF-STEM), Energy-Dispersive X-ray Spectroscopy (EDS), XPS and XAS. The modification with the two metal-based silver and copper, present a core-shell structure Ag@CuO nanoparticles. The photocatalytic properties of bare and modified TiO_2-P25 were studied for phenol and 2-propanol photodegradation, acetic acid oxidation under UV and visible irradiation as well as the production of hydrogen by PWS process. The mechanisms involved in photocatalysis were studied by TRMC and AS.

Chapter I

State of the Art

Chapter 1. State of the Art

1.1. Global Environmental Pollution

One of the greatest problems that the world is facing today is the environmental pollution. An increased scale of human activity has brought with environmental pollution, defined as an undesirable change in the physical, chemical, or biological characteristics of the air, soil, and water that may be harmful to affect human life or that of any other species, or will waste or deteriorate our raw material resources.[11] Every passing year, the environmental pollution causes serious and irreparable damage to Earth and Life.

Nowadays there are several environmental problems. It is well known that there are many global research efforts in this direction, to find possible solutions or to control damage or to avoid future problems due to water and air pollution, and the greenhouse effect. On another hand, the energy demand is increasing and the development of green energy and alternative not polluting fuels is a main challenge. In this thesis work, we were interested in water treatment and hydrogen generation.

1.1.1. Water Depollution and the Renewable Water Resources

What are the preoccupations regarding water pollution? First of all, it is the amount of water that is accessible for consumption. On Earth, oceans represent 1,335 million km^3 (96.7% of total); trapped water in ice: 28 million km^3 (2.2%); groundwater 15 million km^3 (1.2%), and only a little percentage from surface water and the atmosphere: about 400 000 km^3, by the role of the water cycle. But, which of these resources are actually available and for what purpose? The humanity is confined to freshwater resources that ultimately represent only about 35 million km^3, of which only 16 million are accessible. However, the demand necessarily tends to increase with the continued growth in the number of population as shown in the **Figure I-1**, and their raising standard of living.[12] In the case of Mexico, the population growth is more than the world average but had the tendency to decrease in the years 2013-2014. On the other hand, France is always bellow than the population growth world average.

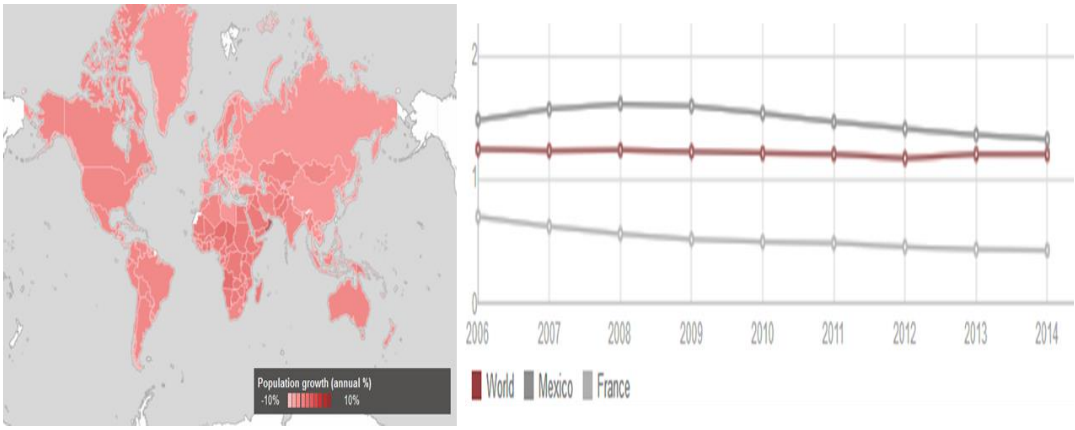

Figure I-1. *Population growth in the world and in the special cases of Mexico and France.*[12]

However, the differences in water consumption are striking between an Australian, who consumes 23,346 m^3/inhabitant/year, a Mexican 4,212 and a French 3,401 m^3/inhabitant/year and a South African, whose consumption is around 1,007 m^3/inhabitant/year. **Figure I-2** shows the total renewable water resources in the world. However, it is still necessary to add the heavy use of water and social and economic inequalities, according to some nations and regions.[13]

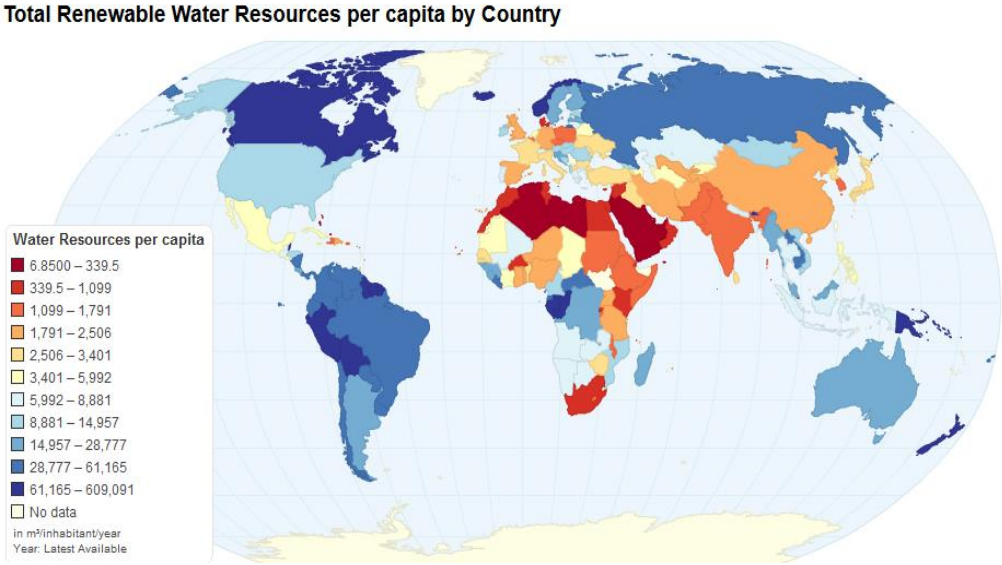

Figure I-2. *Total renewable water resources year 2008.*[13]

Everyone wants a drinking tap water free of pollutants. Unfortunately, the presence in aquatic ecosystems of micro-pollutants covering a wide range of chemical families such as metals, solvents, pesticides and some other pollutants called "emerging" because of lack in the knowledge of their behavior and impact to the environment, health and life ecosystems and citizens over the long term, is found and documented.[14] Although scientific studies have provided evidence to track some of these substances or to quantify the risks, questions to the research are numerous and are the subjects of international collaborations on this shared challenge. The European Water Framework Directive (DCE, from *Directive-cadre sur l'eau*) provides the list of priority substances, which is reviewed regularly and in the last fifty years, the number of chemical substances found in water has steadily increased (**Figure I-3**).

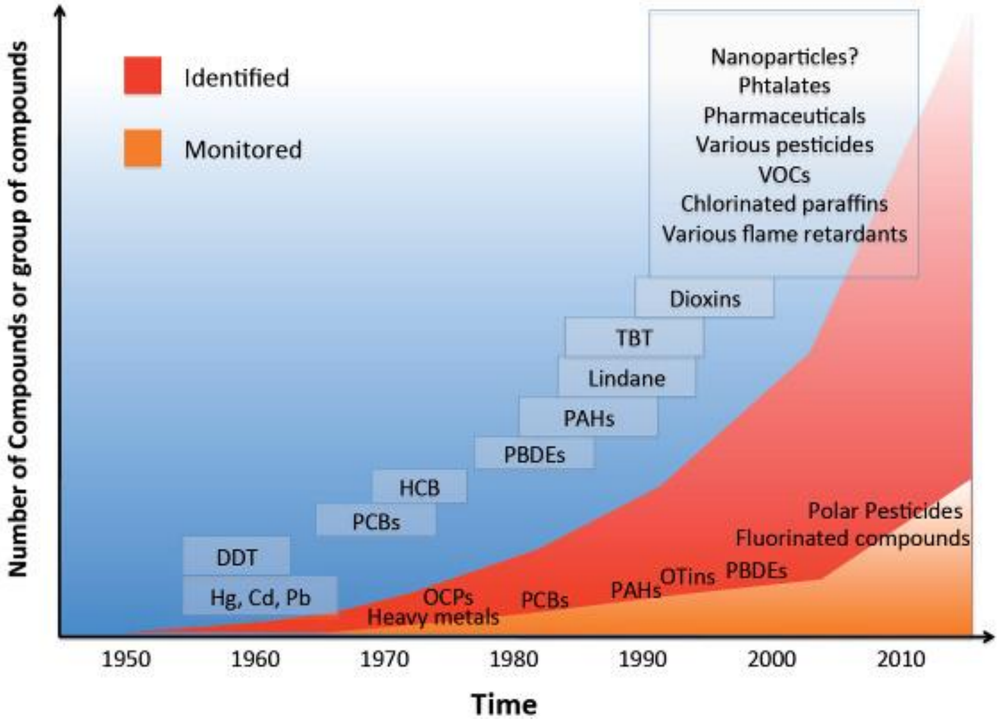

Figure I-3. *Increased number of chemical substances, identified and tracked, in aquatic ecosystems.*[14]

This pollution worries the population, so the authorities have launched a number of actions or plans to monitor and control the pollution in order to avoid possible infections, and to bring the access of drinking water to rural communities.[15]

Therefore, the removal or degradation of hazardous materials and contaminants from wastewater, ground and surface water is a significant global challenge. Several methods for achieving this goal have been reported, among which the oxidation processes (biological, chemical or physical) have received great attention.[16]

Nanomaterials offer the possibility of an efficient removal of pollutants and germs, showing potential for the improvement of water treatment technologies. In recent years, catalysis and photocatalysis processes have received great attention due to their effectiveness in degrading and mineralizing organic compounds.[17]

1.1.2. The Air Pollution, and Hydrogen as a New Energy Source

Carbon dioxide (CO_2) makes up the largest share of the greenhouse gases contributing to global warming and climate change. Converting all other greenhouse gases (methane (CH_4), nitrous oxide (N_2O), hydro-fluorocarbons (HFCs), per-fluorocarbons (PFCs), sulphur hexafluoride (SF6)) to CO_2 equivalents makes it possible to compare them and to determine their individual and total contributions to the global warming. The Kyoto Protocol, an environmental agreement adopted in 1997 by many of the parties to the United Nations Framework Convention on Climate Change (UNFCCC) and the United Nations conference (COP21) are working towards curbing CO_2 emissions globally.[18]

CO_2 is a naturally occurring gas fixed by photosynthesis into organic matter. However, it is the principal anthropogenic greenhouse gas that affects the Earth's radiative balance. It is the reference gas against which other greenhouse gases are measured, thus being a Global Warming Potential number one, due to burning of carbon-based fuels since the industrial revolution (oil, coal and gas for energy use, wood and waste materials, and from industrial processes such as cement production). The concentrations of atmospheric carbon dioxide has rapidly increased, consequently increasing the rate of global warming and causing anthropogenic climate change.[18]

The CO_2 emissions of a country are an indicator of only one greenhouse gas, but it is representative of how a country influences the climate change (see **Figure I-4**). In the case of Mexico, its emission is below the world average but started to increase, while France, which had higher CO_2 emission in 2006, in 5 years started to decrease. This decrease is in large part due to the actions that the French government took to boost the use of green energy sources and to encourage the citizens to use insulation in houses, less polluting cars (including electric cars, etc). However, in 2011 the French CO_2 emissions was still higher than the world average.

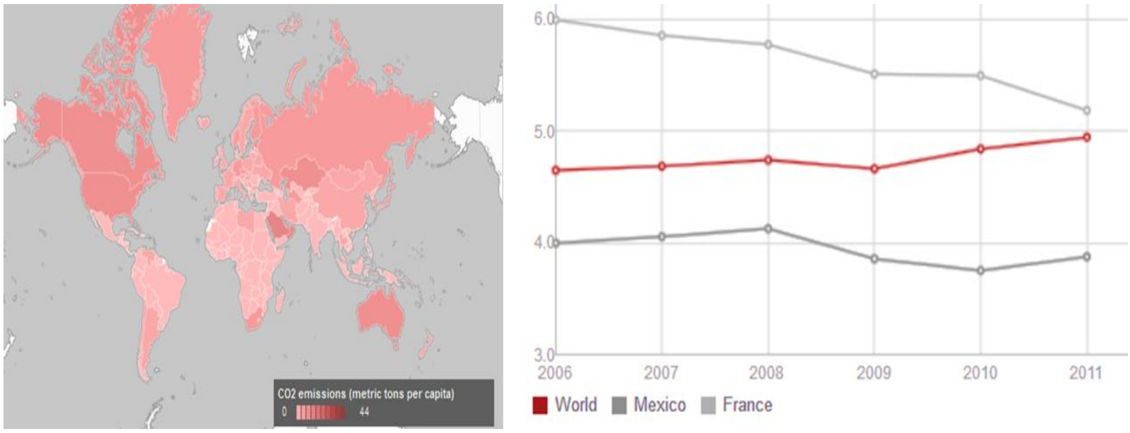

Figure I-4. *CO_2 emissions in metric tons per capita in the world and in the specific cases of Mexico and France.*[18]

Hydrogen (H_2) can be considered as a clean energy carrier similar to electricity, with a number of advantages for the future. For example, a large volume of hydrogen can be easily stored in several ways. It is also considered as a highly efficient, low polluting fuel that can be used for transportation (for example, NASA uses hydrogen fuel to launch the space shuttles),[19] heating, and power generation in places where it is difficult to use electricity.

Hydrogen can be produced from various domestic resources such as water, renewable energy and nuclear energy. For example, hydrogen is produced from separation of hydrocarbons through the application of heat, a process known as steam reforming. Currently, most hydrogen is made this way from natural gas. However, by steam reforming generates carbon dioxide (CO_2). An electrical current can also be used to separate water into its components of oxygen and hydrogen. This process is known as electrolysis.[20] Water offers enormous potential benefits for the energy sector, environment and chemical industries. There are many methods for producing hydrogen from water and these include solar, thermal,[21] combined photo-voltaic/electrolysis,[22] artificial photosynthesis[23] and photocatalysis.[24] Economic feasibility studies[25] indicate that at 5% solar photon conversion, the price of hydrogen produced photocatalytically from water would be competitive with conventional non-renewable processes (e.g., methane steam reforming). Photocatalytic water splitting has the simplicity of using a powder in solution and sunlight to produce H_2 and O_2 from water and can provide a clean, renewable energy, without producing greenhouse gases or having many adverse effects on the atmosphere. In the long-term, hydrogen will simultaneously reduce the dependence on fossil fuels and the emission of greenhouse gases and other pollutants, such as the well-known CO_2.

1.2. Photocatalysis

Photocatalysis is the conceptual name for the “photocatalytic reactions” and it can be defined as a chemical reaction induced by absorption of photons by a solid material, or ‘‘photocatalyst’’, which remains unchanged during the reaction.[26] Photocatalysis is one of the Advanced Oxidation Processes (AOPs), which are technologies with a significant importance in environmental application for wastewater treatment. The AOPs concept was established by Glaze et al.,[27] who defined AOPs as processes involving the generation of highly reactive oxidizing species able to attack and degrade organic substances until their mineralization to carbon dioxide, water and inorganics or, at least, to their transformation into harmless products. These species, mainly hydroxyl radicals ($HO^•$) [$E^0(HO^•/H_2O = + 2.8\ V_{NHE})$] and ($O_2^{•-}$) [$E^0(O_2^{•-}/O_2 = + 2.3\ V_{NHE})$][28] are of particular interest because their high oxidation capability.[29] Among the different approaches for pollutants removal from water, ozonation and ozone related processes (O_3/H_2O_2, UV/O_3), heterogeneous photocatalysis (TiO_2/UV), homogeneous photocatalysis with iron oxides (Fenton and Fenton-like processes) and electrochemical oxidation are considered as the most efficient for the degradation of organic products in water.[29,30] Heterogeneous photocatalysis is a discipline which includes a large variety of reactions: mild or total oxidations, dehydrogenation, hydrogen transfer, O_2^{18}–O_2^{16} and deuterium-alkane isotopic exchange, metal deposition, water detoxification, gas pollutant removal, etc. In line with the two latter points, it can be considered as one of the new AOPs for air and water purification treatments.[31]

Heterogeneous photocatalysis is based on semiconductors which absorb photons generating active electrons and holes, which can then be used to initiate reduction and/or oxidation reactions.[32] Heterogeneous photocatalysis can be carried out in several media: gas phase, pure organic liquid phases or aqueous solutions. It is found to be useful for a wide range of applications such as air purification, wastewater treatment, water splitting, CO_2 reduction, oxidation of water, disinfection and self-cleaning surfaces.[31,33,34,35,36]

When a semiconductor (SC) catalyst of the chalcogenide type, e.g., oxides (TiO_2, ZnO, ZrO_2, CeO_2, ...), or sulfides (CdS, ZnS, ...) is illuminated with photons whose energy is equal to or larger than their band-gap energy E_g ($h\nu \geq E_g$), there is absorption of these photons and formation within the bulk of electron-hole pairs, which dissociate into free photo-electrons in the conduction band and photo-holes in the valence band. Simultaneously, in the presence of a fluid phase (gas or liquid), a spontaneous adsorption occurs and according to the redox potential of each adsorbate, each ion formed, subsequently, reacts to form the intermediates and final products.

$$hv + (SC) \rightarrow e^- + h^+ \quad \textbf{(1. 1)}$$

$$A_{ads} + e^- \rightarrow A_{ads}^- \quad \textbf{(1. 2)}$$

$$D_{ads} + h^+ \rightarrow D_{ads}^+ \quad \textbf{(1. 3)}$$

1.2.1. Semiconductor Materials Used as Photocatalysts

Scientific studies on photocatalysis started about two and a half decades ago, and since then, researchers have used SC materials to absorb photons and so induce active electrons and holes. Nowadays, metal oxide semiconductors are promising materials for photocatalytic applications, but large scale applications in the environmental and energy industries are still rare.[4] Among these types of materials, titanium dioxide or titania (TiO_2), which is one of the most basic materials in our daily life, has emerged as an excellent photocatalyst material for environmental purification.[37] TiO_2 is used in photocatalysis due to its chemical and thermal stability, production at large scale, non-toxicity, higher photoactivity under UV irradiation.[8,32,38,39] The meaning of ‘‘non-toxicity’’ of titania originates from its chemical properties, but not from its physical structure, and as such, nanoparticles of titania (and all other nanomaterials) are considered as potentially toxic, due to their ability to go through the biological barriers causing damage to various organs.[40]

TiO_2 crystallizes in three polymorphic forms: anatase, rutile and brookite. Anatase and brookite are metastable, while rutile is thermodynamically stable. Brookite has been seldom studied, due to more complicated synthetic methods for its preparation, which often needs application of highly concentrated acids or high temperature and pressure.[41] Anatase and rutile are mainly used as photocatalysts, anatase even more than rutile. Their band-gaps are of 3.2 eV and 3.1 eV, respectively (see **Figure I-5**). Anatase is a metastable form that transforms into rutile at high temperature.[42] It is well known that the anatase phase presents higher photoactivity compared to rutile phase.

Colbeau-Justin *et al*. studied the dynamics of photogenerated charge-carriers by time resolved microwave conductivity (TRMC) technique. [42] In normalized signals shown in **Figure I-5**, it can be clearly seen that rutile shows faster decay of the signal than anatase, indicating more electron-hole recombinations in rutile.[42] The lifetime of charge carriers in anatase powder is extended, this behavior was previously observed by Schindler *et a*l.,[43] and interpreted in the following way: the short free electron lifetime in rutile is due to a high recombination rate whereas in anatase, the recombination process is slower than rutile due to a possible competition between a fast recombination process and a fast trapping part of charge-carriers not participating in the TRMC signal (*i.e.*, the free holes). This trapping process reduces the number of holes available for recombination processes and thus increases the lifetime of charge-carriers that are contributing to the TRMC signal (the electrons). This technique will be described with more details in the next chapter.

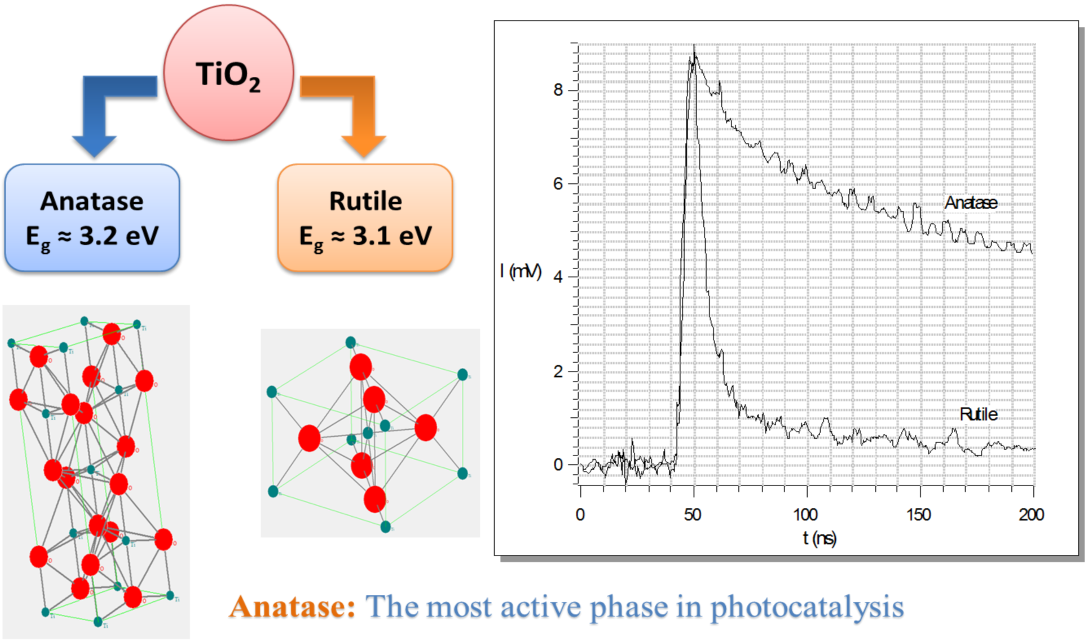

Anatase: The most active phase in photocatalysis

Figure I-5. a) *Schematic representation of crystalline structures anatase and rutile of* TiO_2; ***b)*** *Differences between rutile and anatase on charge-carriers dynamics under UV irradiation.*[42]

TiO_2 is the most widely used SC in photocatalytic processes, due to its suitable properties such as (a) high photochemical and (b) biological stability, and (c) low cost. However, it is known that its use has significant drawbacks such as the high rate of recombination between electrons and holes, as it is shown in **Figure I-5** and **Figure I-6a**, resulting into a *low quantum yield*, and most important: TiO_2 can only be excited under UV irradiation with wavelengths shorter than 400 nm, thus resulting in a low photo-conversion efficiency (see **Figure I-6b**).

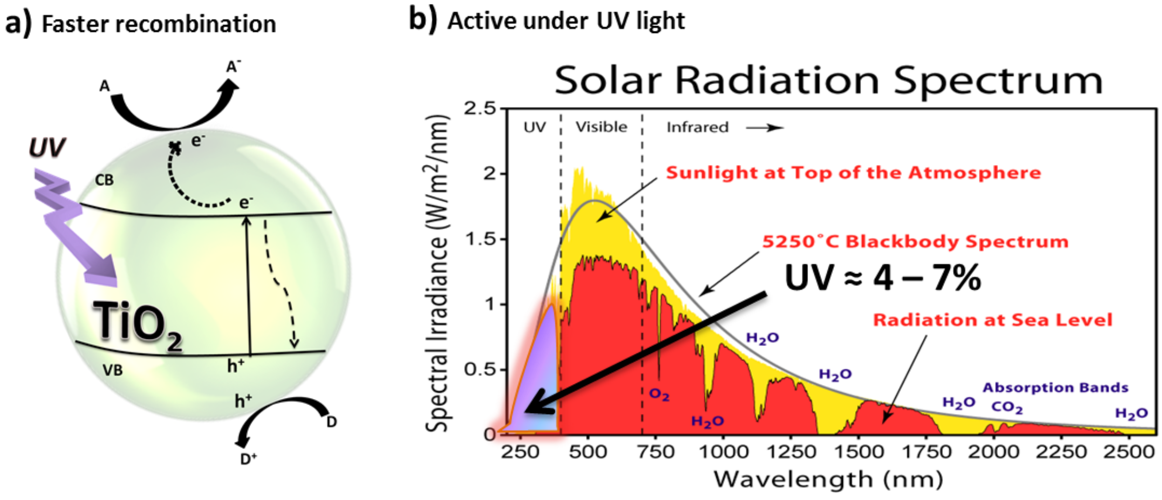

Figure I-6. a) *Typical diagram for the recombination process of the electron-hole pair.* ***b)*** *Solar spectrum that shows the UV region within the solar radiation spectrum, available or used for normal (no modified) TiO_2 photocatalysts.*

1.3. Basic Principles of the Photocatalysis Process

1.3.1. The Importance of Charge-Carriers Dynamics in TiO_2-based Photocatalysts

When TiO_2 is exposed to an irradiation source with energy higher than its band-gap, a photochemical process takes place, *i.e.*, an electron is excited from the valence band to the conduction band forming the so-called charge-carriers or electron-hole pairs.

$$TiO_2 \xrightarrow{h\nu \geq E_G} TiO_2 + e^{-}_{CB} + h^{+}_{VB} \qquad \textbf{\textit{(1. 4)}}$$

Once the electron-hole pairs are formed, different phenomena can occur as illustrated in **Figure I-7**. Among diverse processes, there is recombination of these charge-carriers, some electrons and holes can escape from recombination and migrate to the surface of the SC, where they can (A) recombine with each other, or (B) the recombination takes place in the core of the SC. Besides these processes, though they seem similar, there is also a recombination that occurs on the surface between the electrons and holes that are generated *in-situ*, on the surface. But once the system presents electrons and holes on the surface, (C) they can either react with electron acceptors, or (D) electron donors, respectively. These two paths are examples of direct reactions between the SC and the adsorbate (being either an electron donor or an acceptor). Meanwhile, the recombination in (A) and (B) results in luminescence.[5]

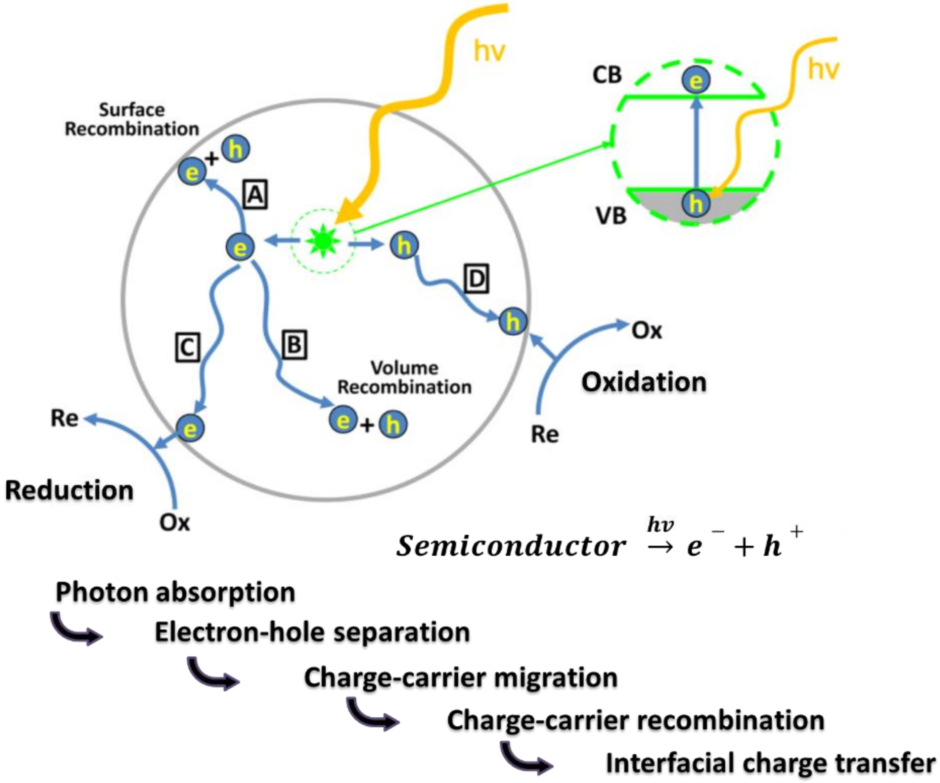

Figure I-7. *Schematic photo-excitation in a solid followed by de-excitation events. Quantum efficiency (QE).*[5]

1.3.2. Quantum Efficiency (QE) of the Photocatalytic Processes

The efficiency of the photoreaction process is expressed by a quantum yield (Φ), which is:

$$\Phi = \frac{\text{rate of reactant consumption or product formation}}{rate\ of\ photons\ absorption} \qquad \textbf{\textit{(1. 5)}}$$

The rate of reactant consumption or product formation is proportional to the rate of charge (electron/hole) transfer (k_{CT}) from the semiconductor to the reactant molecules, and the rate of photon absorption is proportional to the sum of the rates of the charge transfer (k_{CT}) and electron−hole recombination (k_R). In other words, Φ can be expressed as:[44]

$$\Phi = \frac{k_{CT}}{(k_{CT} + k_R)} \qquad \textbf{\textit{(1. 6)}}$$

It is very difficult to measure the real absorbed light in heterogeneous systems because of the scattering of light by the semiconductor surface. Generally, it is assumed that all the light is absorbed and the efficiency is quoted as an apparent quantum yield (QE). Sometimes the QE is measured as the yield of a particular product in spite of several products produced in the photocatalytic reactions.

1.4. Ways to Enhance the Photocatalytic Activity

There exist several ways to enhance the photoactivity of the semiconductor materials, among which are the following:

- **Quantum Size Effects (QSE)**

The size of the semiconductor has an effect on the band–gap position, which is called QSE. The anomalies arise when the SC nanoparticle size gets smaller and smaller (in the order of 10-100 Å in size) that it becomes comparable to the *de Broglie* wavelength of the charge-carriers in the semiconductor, in a manner that could have an effect in increasing the band-gap of the SC. For instance, in **Figure I-8**, it is shown that the band-gap decreases when the size of the CdSe increases:[45] CdSe NPs with a size of 2.8 nm have an energy band gap equal to 2.51 eV, while the CdSe NPs of 4.2 nm have a band-gap of 2.19 eV.

The quantum confinement (generated as the particle size is reduced) produces a quantization of electronic states and thus increases the effective band-gap of the semiconductor. The more positive valence band implies an increased oxidizing capability of the holes. Likewise, the more negative conduction band induces an enhancement of the reducing capability of the generated electrons.

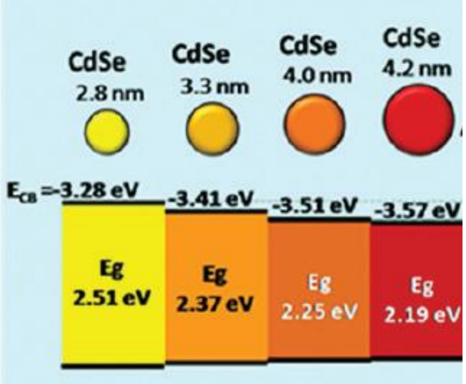

Figure I-8. *Decrease of the quantum size effects of CdSe.*[45]

- **Composite Semiconductors**

The modification with coupled semiconductor photocatalysts is another way to enhance the photo absorption in a wide range toward visible light or to decrease the recombination process. Band gaps and band positions of different semiconductors are shown in **Figure I-9**. Serpone *et al.* reported for the first time the coupling between the CdS and TiO_2 semiconductors, and this modification showed an enhancement in the efficiency of the photocatalytic process.[46] In this case, the photoexcitation path for a CdS-TiO_2 composite has been reported (see **Figure I-11a**), and it has been shown that the photogenerated electrons can be injected from the valence band (VB) of CdS into the conduction band (CB) of TiO_2. The difference in the energy levels between these two semiconductors plays a significant role in achieving such a charge-carriers separation. The basic principle for a photocatalyst composite in direct contact will be explained for a system containing two different components, that depending on the band positions of those two semiconductors, the formed heterojunction can be classified into three different types depicted in **Figure I-10**. In a *Type I* heterojunction (**Figure I-10a**), the VB of semiconductor B is lower than of semiconductor A, and the CB of semiconductor B is higher than the CB of semiconductor A. Since electrons and holes gain energy by moving down and up respectively, photoexcited electrons can transfer from CB(B) to CB(A), resulting for this case that all the charge carriers are accumulated on the semiconductor A, and this will not decrease the charge carrier separation, and thus photocatalytic activity will not be improved. A *Type II* heterojunction

(**Figure I-10b**) provides the optimum band positions for efficient charge carrier separation leading to improved photocatalytic activity. Photoexcited electrons are transferred from CB(B) to CB(A). Whether this occurs directly via electron transfer between the semiconductors due to the favorable energetics of the relative positions of the CBs, reducing significantly the electron-hole recombination probability and increasing electron lifetimes.

Finally, in *Type III* heterojunctions (**Figure I-10c**), the charge carrier transfer is the same as in *Type II* semiconductors, only that the band positions CB and VB of the second semiconductor are above of the CB of the first semiconductor. Such arrangements of band positions are also called broken-gap situations.[47]

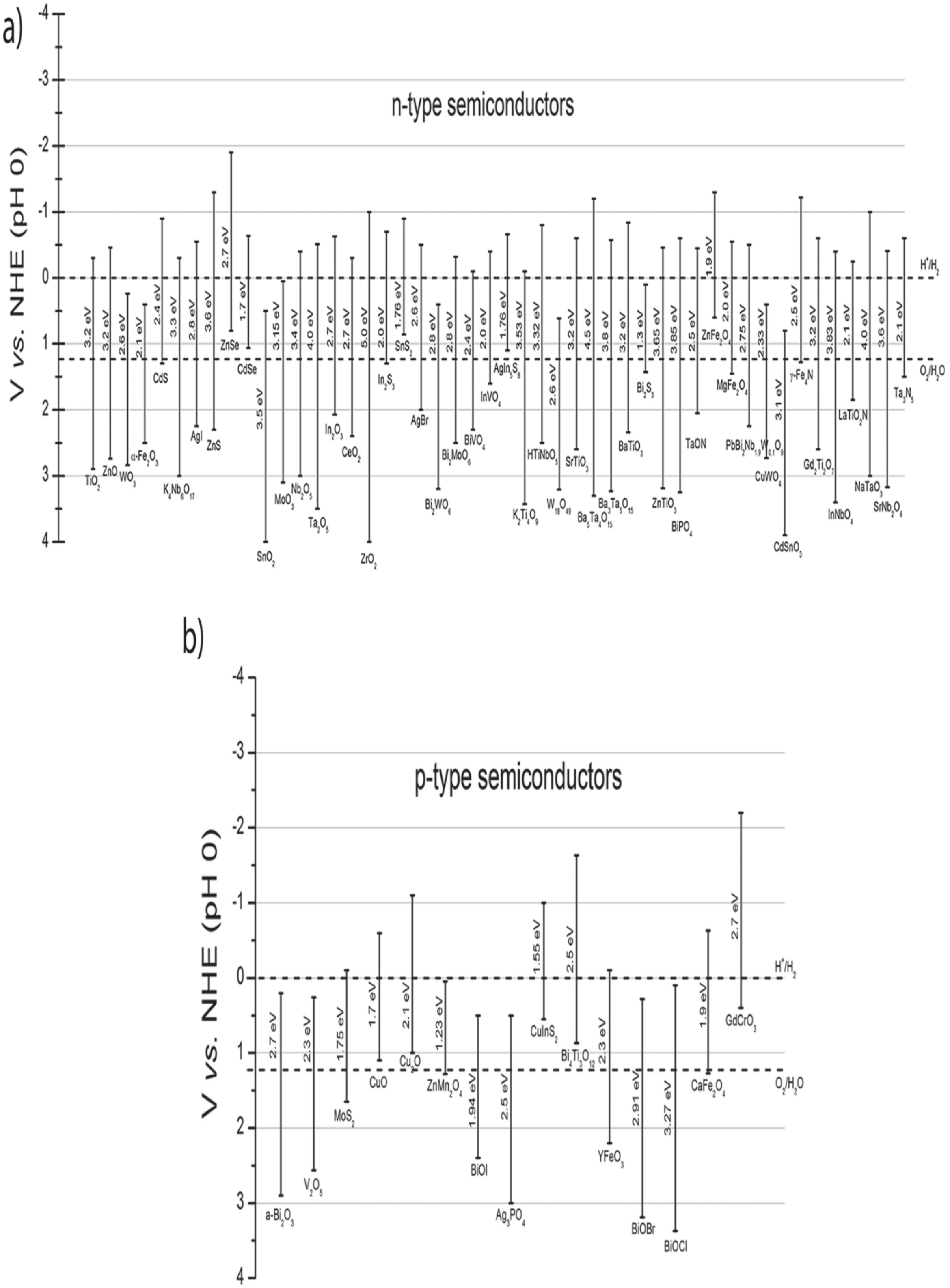

Figure I-9. *Band gaps and band positions in* ***a)*** *n-type semiconductors and* ***b)*** *p-type semiconductors used for composite photocatalysts heterojunctions, and different types of semiconductor heterojunctions.*[47]

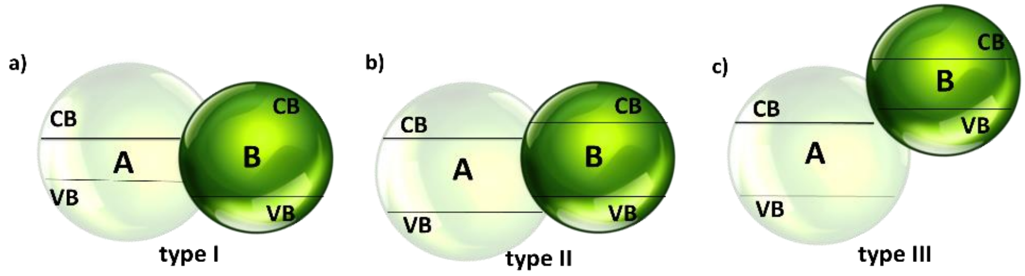

Figure I-10. *Different types of semiconductor heterojuntions.*

- **Metal and Non-Metal Doping**

Another way to decrease the band-gap of TiO_2, is by modifying the crystalline lattice of TiO_2. The metal-doped TiO_2 (using transition metals such as: Cu, Co, Ni, Cr, Mn, Mo, Nb, V, Fe, Ru, Au, Ag, Pt, Rh)[48,49] can be explained by new energy levels produced in the band-gap of TiO_2 through the insertion of metal ions in the TiO_2 matrix. As shown in **Figure I-11b**, the electrons can be excited from the defect state to the TiO_2 conduction band by photons with an energy (*hv)* higher than the band gap. An additional benefit of transition metal doping (very small amount) is the improved trapping of electrons to inhibit electron-hole recombination during irradiation. The decrease of charge-carriers recombination results also in enhanced photoactivity.

Among the most common non-metal doping of TiO_2 that can be mentioned is doping with N, S, C, B, P, I, F.[48] There are in this regard three different explanations. One explanation is that doping will result in a band–gap narrowing as reported by Asashi *et al*.,[50] who concluded that the visible light sensitivity of nitrogen-doped TiO_2 was due to the narrowing of the band gap by mixing the N 2p and O 2p states. The second one is the introduction of additional energy levels due to N impurity reported by Irie *et al*.,[51] who stated that oxygen sites in TiO_2 are substituted by nitrogen atoms forming isolated impurity energy levels above the valence band. Under UV irradiation, electrons in both, the VB of TiO_2 and the additional energy levels are excited, but under visible light irradiation only the electrons in the impurity energy levels are excited. And the last explanation regarding oxygen vacancies is reported by Ihara *et al*.[52] They concluded that oxygen-deficient sites formed in the grain boundaries are important to obtain a visible activity, and that the introduced nitrogen atoms in place of oxygen-deficient sites are important to block re-oxidation.

- **Photo-Sensitization**

Photo-sensitization could be explained with surface sensitization by chemisorbing or physisorbing photosensitive dyes. **Figure I-11c** shows this modification that can also expand the absorption spectral range of the semiconductor to higher wavelengths. The dye (S) is excited with visible light to the electronically excited state S*. If this state lies energetically above the conduction band edge of the semiconductor, electron injection to the semiconductor can occur in a fast time scale (fs). These ultrafast electron injection kinetics are contrasted with the charge recombination reaction, which occurs on the microsecond-millisecond time scales.[53] The photo-sensitization is the base of the Grätzel cell. In a typical Grätzel cell, I^-/I^{3-} ions in organic solvents serve as charge-carriers.

Many photosensitizers have been already reported such as: Fe, Re, Rh or Os complexes, rhodamine 6G, blackberries pigments etc.[54]

- **Metal Surface Modification**

The addition of the metal can lead to enhancement of the photocatalytic yield under UV irradiation. Sato and White reported the first enhancement observed in water splitting into H_2 and O_2 using Pt/TiO_2.[55] The authors found that after excitation of the modified titania, the electrons migrate to the metal retarding the recombination process (see **Figure I-11d**). In another hand, the noble metal nanoparticles such as Au, Ag have absorbed visible light due to their surface plasmon resonance (SPR). Therefore, a new class of photocatalysts formed by semiconductors modified with plasmonic metal nanoparticles is emerging, termed *plasmonic photocatalysts*. Next section will explain in detail plasmonic photocatalysis.

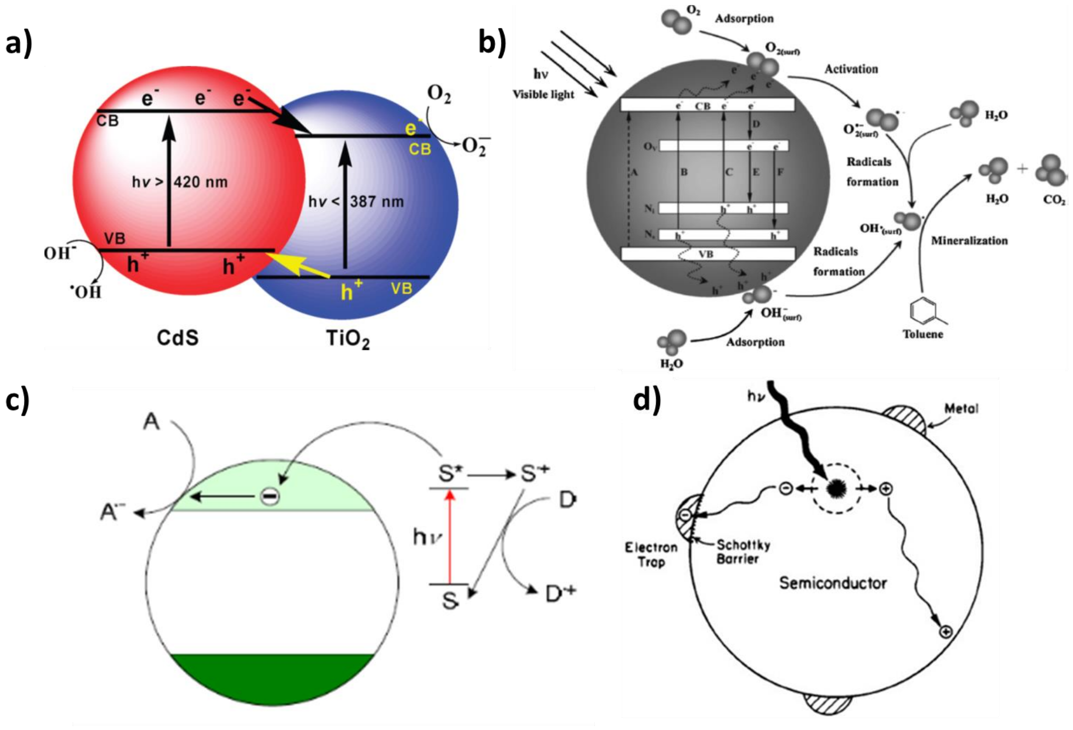

Figure I-11. *Schematic representations for different ways of TiO$_2$ modification.* ***a)*** *shows the formation of composite semiconductors,*[46] ***b)*** *doping with metal and non-metal atoms,*[50] ***c)*** *photosensitization with organics and inorganics chromophores,*[54] *and* ***d)*** *metal surface modification.*[5]

1.5. Plasmonic Photocatalysts

Plasmonic photocatalysis is a term coined by Awazu *et al.* in 2008,[56] and it has recently come into focus as a very promising technology for high-performance photocatalysis.[56,57,58] In order to enhance the electron–hole recombination and then raise the photocatalytic efficiency of TiO$_2$, modifications of crystalline TiO$_2$ are proposed. In particular, to enhance their photocatalytic activity under both, UV and visible light, TiO$_2$ can be modified with MNPs to form metal/TiO$_2$ heterostructures. Compared with the common semiconductor photocatalysts, plasmonic photocatalysts possess two distinct features: a Schottky junction and localized surface plasmon resonance (LSPR); where each phenomenon benefits the photocatalysis differently.

The concept of “plasmonic” refers mainly to the LSPR and the induced effect. Although the Schottky junction is not a plasmonic effect, it is a natural result of the metal-semiconductor contact and it can be regarded as an intrinsic feature of the plasmonic photocatalysts. Accordingly, the development of plasmonic photocatalysts is an interesting option to overcome the limitations presented by TiO_2 and other semiconductors. These type of photocatalysts consist in the addition of NPs of noble metals (mostly Au and Ag, in size of ten to hundreds of nanometers), since they may enhance the transfer of photo-generated electrons prolonging the charge-carrier lifetime. Indeed, metal NPs act as electron traps as it can be seen in the scheme shown in **Figure I-12a**, where the irradiation source activates the semiconductor, and the electrons are transferred to the metal. The recombination process is then decreased. Moreover, gold or silver, due to the LSPR may also activate TiO_2 and other wide band-gap semiconductors towards visible light as shown in **Figure I-12b**. In this case, the MNPs adsorb visible light photons and electrons can be injected from the MNPs to the conduction band of the semiconductor.

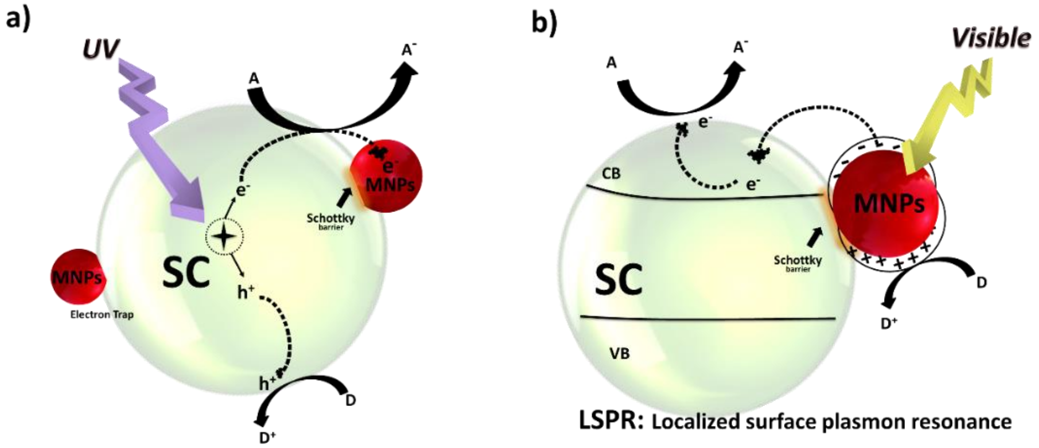

Figure I-12. *Proposed photocatalytic mechanisms under **a)** UV, and **b)** visible light excitation for semiconductors modified with metal NPs.*

1.5.1. The Schottky Barrier

The band bending concept was first developed by Schottky and Mott to explain the rectifying effect of metal semiconductors. **Figure I-13** shows the ideal energy band of two kind of semiconductors of *n*-type and *p*-type. When the semiconductor photocatalyst is of *n*-type, its Fermi level E_f is close to the conduction-band energy E_{CB}, and the valence band energy E_{VB} is far below. For the *p*-type semiconductor photocatalyst, the E_f is close to the E_{VB}. TiO_2 is an *n*-type semiconductor. In the next section, we will describe only the interaction between metal NPs and *n*-type semiconductors.

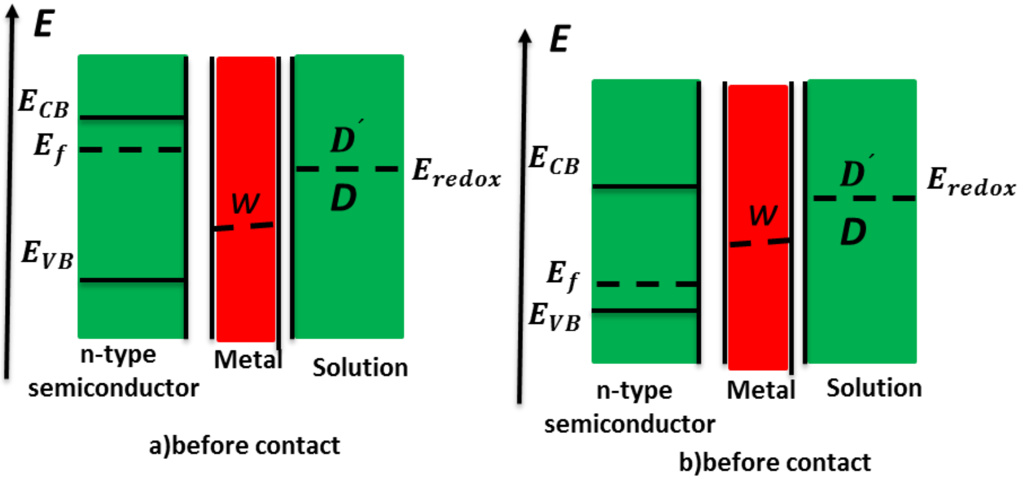

Figure I-13. *Energy diagrams of the plasmonic photocatalytic materials in different states.* ***a)*** *Before contact, n-type semiconductor photocatalyst;* ***b)*** *before contact, p-type semiconductor photocatalyst.*[4]

Figure I-14 shows the ideal energy band diagrams of metal and *n*-type semiconductor contacts. Free electrons can be transferred between the metal and the semiconductor, due to the work function difference. If the metal work function (φ_m) is higher than that of the semiconductor (φ_s) (which means $\varphi_m > \varphi_s$) as it is shown in **Figure I-14** (left), the electrons will flow from the semiconductor to the metal and the transfer of electrons will continue until the Fermi levels of the metal ($E_{F,m}$) and the semiconductor ($E_{F,S}$) reach the same value. When equilibrium is established, the metal will be negatively charged and the semiconductor will be positively charged at the metal/semiconductor interface due to the electrostatic induction. This region is called the space charge region, also when $\varphi_m > \varphi_s$, the electrons are depleted in the *space charge region*, and this region is therefore called the *depletion layer* and is characterized by excess positive charge.[33] And If the metal work function (φ_m) is lower than that of the semiconductor (φ_s) which means $\varphi_m < \varphi_s$ as is shown on the left side of **Figure I-14**, the electrons are accumulated in the space charge region due to the electron transfer from the metal to the semiconductor, and this region is called the *accumulation layer*.[33] In general, when the Fermi level of the metal is below that of the semiconductor, charge will flow to the metal causing the semiconductor Fermi level to decrease, and *vice versa*.

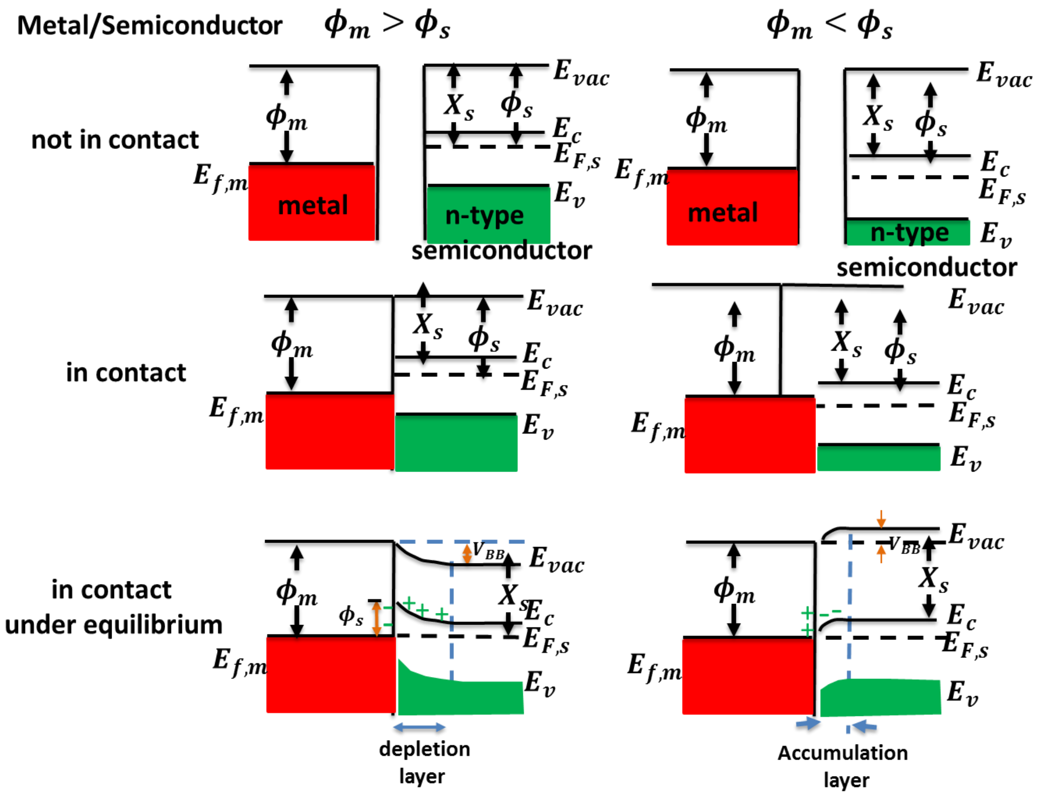

Figure I-14. *Energy band diagrams of metal and n-type semiconductor contacts.* E_{vac}*, vacuum energy;* E_c*, energy of conduction band minimum;* E_v*, energy of valence band maximum;* ϕ_m*, metal work function;* ϕ_s*, semiconductor work function;* χ_s*, electron affinity of the semiconductor.*[33]

The Schottky junction results from the contact of the noble metal and the semiconductor. It builds up an internal electric field in a region (the space-charge region) inside the photocatalyst particle but close to the metal/semiconductor interface. This would force the electrons and holes to move in different directions once they are created inside or near the Schottky junction.[58] In addition, the metal part provides a fast lane for charge transfer[59] and its surface acts as a charge-trap center to host more active sites for photoreactions. The Schottky junction and the fast-lane charge transfer work together to suppress the electron–hole recombination.

1.5.2. Localized Surface Plasmon Resonance

The more prominent feature of plasmonic photocatalysts is the LSPR, which represents the strong oscillation of the metal's free electrons being in phase with the varying electric field of the incident light, **Figure I-15.**[60]

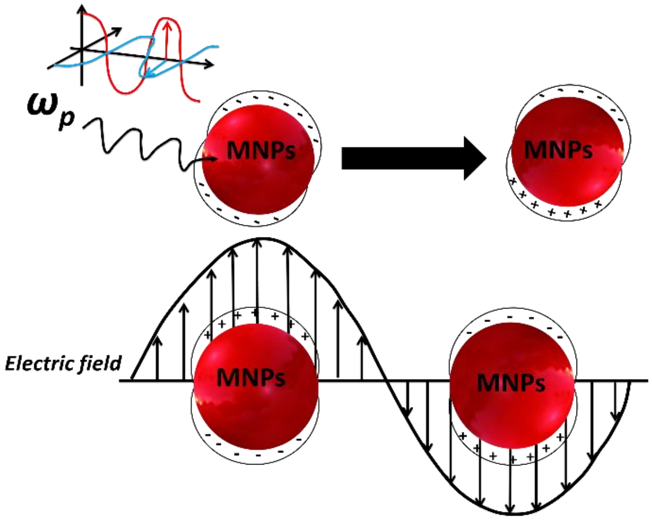

Figure I-15. *Scheme of the optical response of a spherical particle, the localized surface plasmon resonance (LSPR) of noble metal nanoparticles.*[61]

This brings several significant benefits to photocatalysis:

- The resonance wavelength for metal nanoparticles, such as Ag or Au, can be tailored to fall in the visible range or the near-UV range, depending on the size, the shape and the surrounding environment.[62] If in the visible range, it renders a visible light response to the large band-gap photocatalysts *e.g.*, TiO_2.
- The LSPR can drastically enhance the visible-light absorption of the low-band-gap photocatalysts (e.g., Fe_2O_3)[63] and the UV absorption of the large-band-gap materials,[56] which is very useful for weakly absorbing materials.

- The strong absorption causes most of the incident light to be absorbed in a thin layer (~10 nm) under the surface, and thus there is only a short distance between the photoexcited electrons and/or holes and the surface, making it comparable to the minority carrier diffusion length (~10 nm).[63,64] This is beneficial to materials presenting poor electron transport.
- The LSPR creates an intensive local electric field, which favors the photocatalytic reactions in several ways. For instance, it powers the excitation of more electrons and holes,[65,66] heats up the surrounding environment to increase the redox reaction rate and the mass transfer,[67,68] and polarizes the nonpolar molecules for better adsorption.[68]

In addition to these beneficial effects of the plasmonic photocatalysis (described above), MNPs themself often present a catalytic effect for specific reactions (*e.g.* Pt on hydrogen production or Au for CO oxidation).

1.6 Influence of the Plasmonic Effect on Photocatalysis

1.6.1. Interaction of Light with Metal Nanoparticles

The optical response of the noble metal nanoparticles is related to the effect of the LSPR and has been well described in many books and review articles with formulations, principles and some applications.[4,60,69].The optical response is measured principally for a spherical shape because the nanosphere has the simplest shape and most importantly, it produces strict analytical solutions in response to an electromagnetic field. Fundamentally, under conditions of the quasi-static approximation ($r<<\lambda$) valid up to about 100 nm, the description of the electrodynamic response of a single spherical particle is given by Mie theory,[70] and the interaction of the NPs with the light can be described by the Maxwell's equations. Under these conditions only plane-wave crosses the particle, and thus the spatial distribution of the electric field is simply the response of the particle under an electrostatic field (see **Figure I-16a**).

In this consideration of a homogeneous spherical nanoparticle under the irradiation of a plane-wave light, the electric field of incident light is written as:

$$\vec{E} = E_0 e^{-\omega t}\,\hat{x}$$

(1. 7)

Where E_0 is a constant, $\hat{x}$ the unit vector of the x direction and t the time interval. The wavelength dependent complex dielectric constant $\varepsilon(\omega)$,and ω is the angular frequency, and the sphere is surrounded by material with dielectric constant ε_m. Conceptually, the conduction electrons in the nanosphere are displaced by the external electric field to create a negative charge center on one end and a positive change center on the other end, forming a dipole (**Figure I-16b**). If ω is not very high, the dipole can oscillate fast enough to follow the phase of $\vec{E}$ It is easy to imagine that to the first order, the dipole moment $\vec{p}$ is linearly proportional to $\vec{E}$, as given by

$$\vec{p} = \varepsilon_m \alpha \vec{E}$$

(1. 8)

Where α is the static polarizability of the sphere. Outside of the sphere, the dipole generates an electric field and superimposes on the incoming electric field $\vec{E}$. The polarizability is related to other parameters such as the permittivity of vacuum.

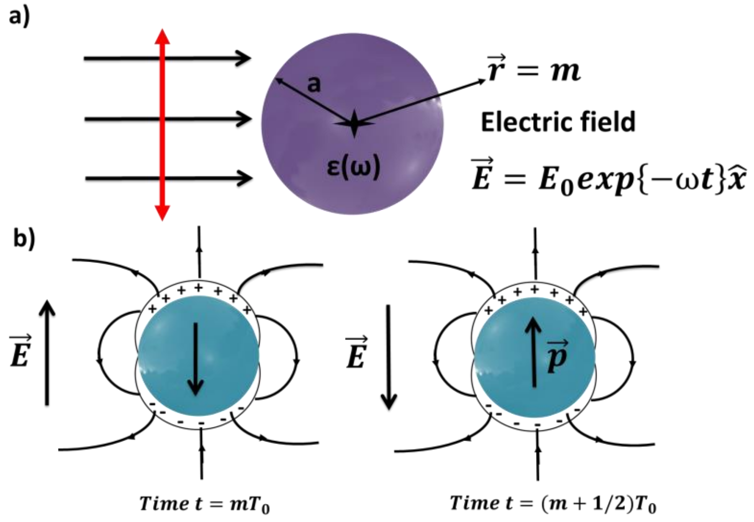

Figure I-16. a) *Diagram of a homogeneous nanosphere irradiated by a plane incident light;* ***b)*** *Conduction electrons oscillating in phase with the external electric field and generating an oscillating dipole, which in turn enhances the local electric field and radiates energy. The radiation in far field is regarded as scattering.*[4]

1.6.2. Influence of Metal Nanoparticle Environment and Shape

As discussed above the spherical shape is the simplest structure, but metal NPs in plasmonic photocatalysis can also have different shapes such as: triangles, ellipsoids, nanoshells, or other anisotropic shapes, such as nanorods. There are many studies related to synthesis of nanoparticles of controlled shapes for different applications. For example, gold nanorods of different aspect ratios have attracted a lot of attention because of their optical properties: they present two plasmon peaks in the transverse and longitudinal directions under visible light and near IR. Nanorods of high aspect ratios can be used for photothermal therapy and cancer cell imaging under near-infrared region.[71] Au nanorods are also interesting in the field of plasmonic photocatalysis, because the MNPs absorb a broad spectral range from visible to near infrared, and can then utilize different light sources (sunlight, xenon lamps, LEDs, see **Figure I-17a**). On the other hand, it is reported that different shapes of metal NPs have an influence on the scattering spectra, like in the case of Ag NPs (see **Figure I-17b**).[72,73]

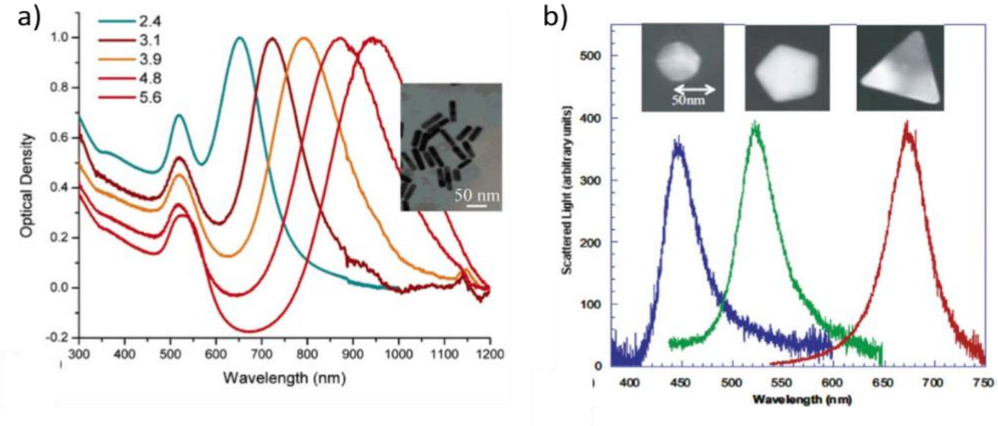

***Figure I-17**. **a)** Absorption spectra of gold nanorods of different aspect ratios[71] **b)** Scattering spectra of single silver nanoparticles of different shapes.[73]*

The LSPR is strongly affected by the local environment. In plasmonic photocatalysis, the MNPs could have different contact states with the photocatalysts, *e.g.*, in TiO_2 they could be in contact only through the surface, or the MNPs could be fully or partially enclosed by the photocatalysts: Metal form (no semiconductor, only metal nanoparticles, see **Figure I-18a**); embedment form (the metal nanoparticle is partially embedded into the semiconductor (SC) and is still partially exposed to the surrounding environment, see **Figure I-18b**); encapsulation form (the metal nanoparticle is fully covered by the SC and is thus not exposed to the surrounding. However, the metal has a direct electrical contact with the SC, see **Figure I-18c**), and isolation form (the metal nanoparticle is isolated from the semiconductor by a non-conducting layer so that there is no direct electric contact between them, and the metal nanoparticle is not exposed to the surroundings, see **Figure I-18d**). As an example, **Figure I-18e** illustrates the shift of the resonant wavelength when a silver nanosphere (radius 10 nm) is gradually embedded into a mica shell (10 nm thick). The resonant wavelength is red-shifted from 350 to 430 nm with the increment of the contact area.[62]

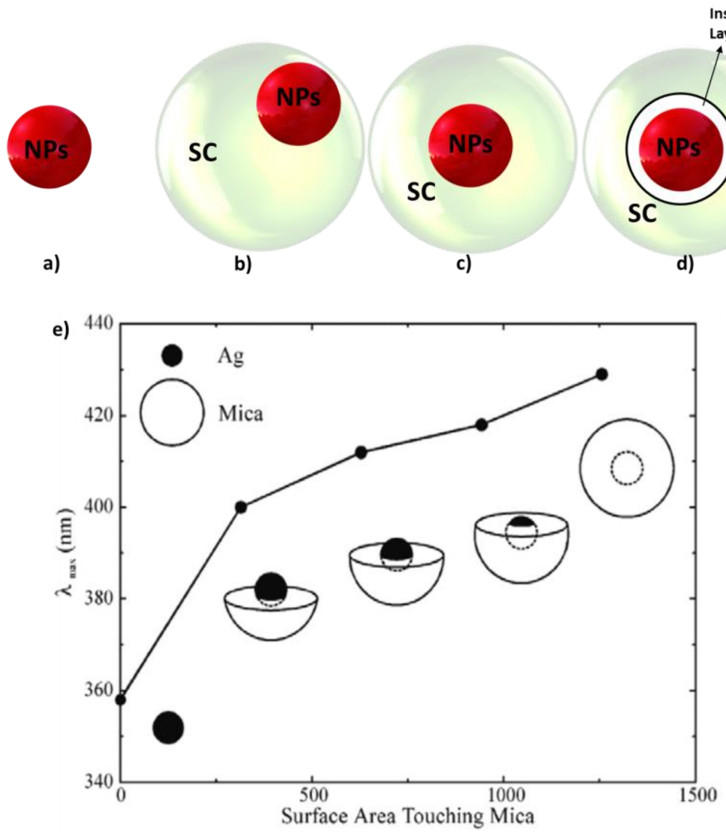

__Figure I-18.__ Classification of the plasmonic photocatalytic systems based on the contact form. __a)__ Naked metal nanoparticles. __b)__ Embedment form, __c)__ Encapsulation form, __d)__ Isolation form, __e)__ Shift of the resonant wavelength with the change of embedment of the silver nanosphere (radius 10 nm) into the mica shell.[62]

1.6.3. TiO_2 Modification with Monometallic or Bimetallic Nanoparticles

The synergy of noble metals and semiconductor photocatalysts brings in significant changes to many aspects of photocatalysis. Under UV irradiation, noble metal nanoparticles deposited on TiO_2 enhance transfer of photogenerated electrons prolonging the lifetime of the charge-carriers, see **Figure I-19a**. Metals (such as Pt, Au, and Ag) and the semiconductor (TiO_2) have different Fermi level. Electron migration from TiO_2 to the metallic nanoparticles occurs until two Fermi levels are aligned, since the metal has a work function (φ_m) larger than that of TiO_2 (φ_m). The electrical contact resulted in a space charge layer, the Schottky barrier, which trapped electrons and suppressed electron-hole recombination.[5,44] Surface of metal acquires an excess of negative charge, while TiO_2 exhibits an excess of positive charges as a result of electron migration from the barrier region. An increase of activity under visible light after modification of titania with plasmonic nanoparticles such as gold, silver, platinum, and palladium results from additional metal impact on the mechanism of electron transfer. The charge oscillations of noble metals at the surface take place at optical frequencies, as shown in **Figure I-19b**, the electron is transferred from noble metal (Ag, Au) by the excitation of their plasmon to the conduction band of titania.[61]

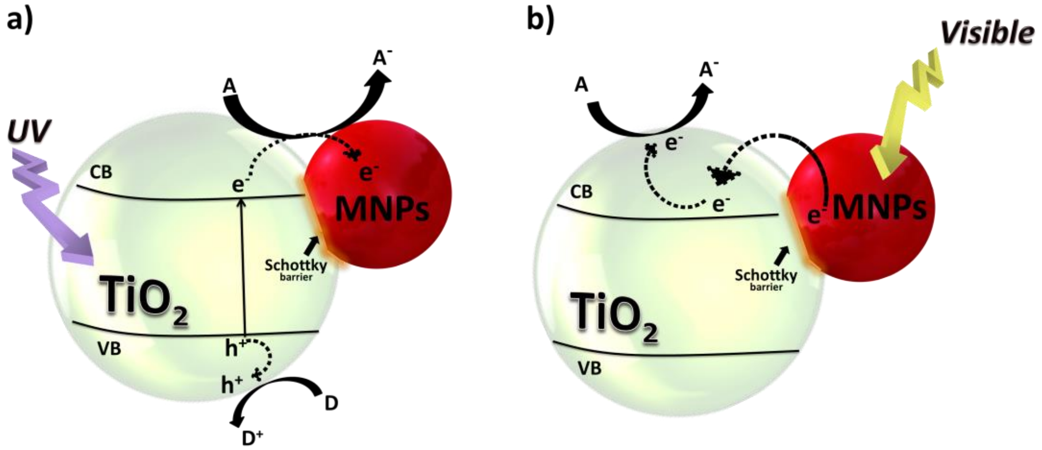

Figure I-19. *Schematic illustration of TiO_2 modified monometallic NPs mechanism of organic pollutants* ***a)*** *degradation under Vis and* ***b)*** *UV light irradiation.*

It has been widely reported that surface modification of TiO_2 with metal NPs can improve its photocatalytic activity, especially with noble metals such as Pt, Pd, Cu, Ag and Au.[6,8,74,75,76,77] However, there are only few works focused on modification of TiO_2 with bimetallic nanoparticles, such as: Ag-Au, Ag-Pt, Ag-Cu, Pt-Cu, Pt-Pd (good catalysts for oxidation reactions) or Au-Pt, Au-Pd, Au-Rh, Au-Ni, Au-Co, and Pt-Ru and Au-Cu (good catalysts for reduction reactions). The mechanism of photocatalyst excitation depends on the bimetallic nanoparticles structure.[61]

Bimetallic nanoparticles of the same size, shape, and composition show significant differences in activity when configured into different structures. Their structure depends on distribution modes of the two elements, which can be oriented, see **Figure I-20**: (a) alloy or intermetallic structure, which represents homogenous mixture of two metals, (b) heterostructure, which results from independent nucleation and growth of two different metal crystals, (c) core-shell, (d) multishell structure, and depends on the processing parameters, miscibility, and reduction kinetics of metal ions.[78]

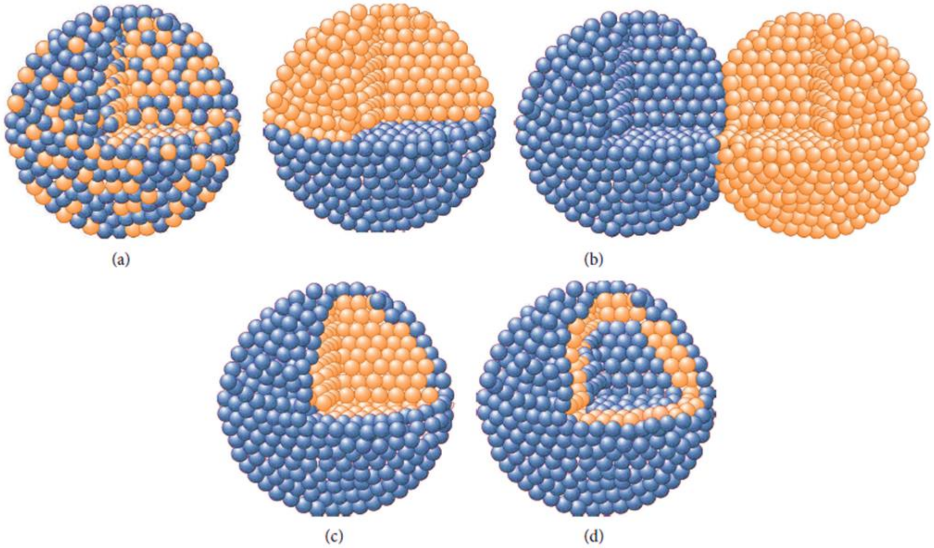

Figure I-20. *Schematic illustration NPs with different structure* ***a)*** *alloy,* ***b)*** *herostructure,* ***c)*** *core-shell, and* ***d)*** *multishell structure.*[61]

For an alloy structure the mechanism is similar to the excitation mechanism of monometallic NPs deposited on TiO_2 as shown in **Figure I-21a**. It is well known that the work function of a metal decreases by alloying with another metal having a lower work function. This suggests that alloying of another metal with Pt would decrease the work function of Pt-alloy based nanoparticles. This may decrease the energy value of the CB and promote efficient electron$^-$ transfer from the metal nanoparticles to the semiconductor.[79]

The promoting effect of bimetallic nanoparticles is attributed to either the improved spatial charge separation in TiO_2 semiconductor or charge carrier transfer from metal NPs to the conduction band of TiO_2. Based on catalytic, optical, and photocatalytic properties the synergy between two metals in bimetallic systems is also related to the electronic and geometric effects. A bimetallic structure formed by metals with lower electronegativity and other metals with higher electronegativity seems to lead to better activity in photocatalytic oxidation reactions.[80] The second metal is more subjected to oxidation than the other, which is enriched on the surface and may form metal oxide patches or shells on the first metal surface. The less electronegative metal can participate directly in oxidation reactions by providing reactive oxygen.

Segregation between two metals may occur upon treatment in an oxidizing atmosphere, or in either reaction preparing process, and sometimes the shell of the structure is oxidized. Kowalska *et al.* reported for example the formation Ag-Au core-shell structure NPs on TiO_2 obtained by the photodeposition method: Silver nanoparticles were oxidized and formed a shell on gold-rich core.[81] Larger ability of charge generation at the interface of a bimetallic structure does not mean better photoactivity, since in the Au_{core}-Ag_{shell} plasmonic structure, the electrons, instead of being transferred from silver to CB of titania may sink in nearby gold NP and vice versa, as is shown in the scheme from **Figure I-21b**.[81]

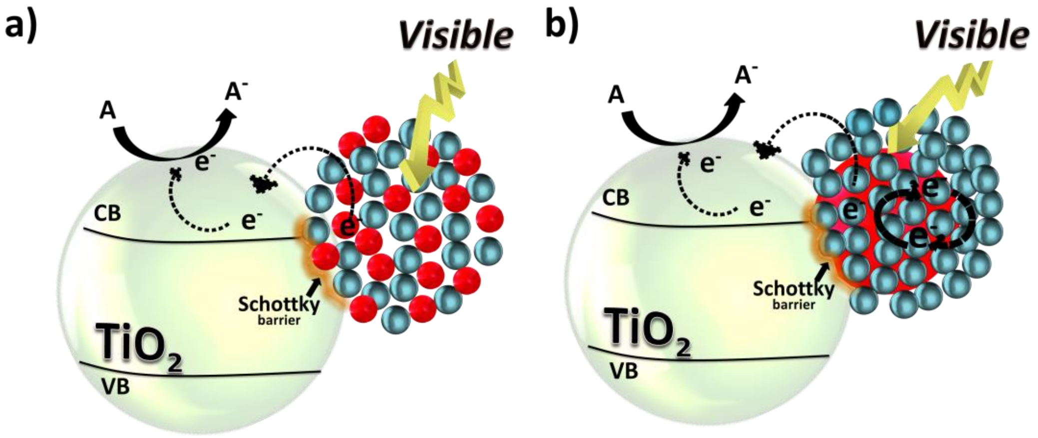

Figure I-21. *Schematic illustration of TiO$_2$ modified bimetallic NPs with **a)** allow and **b)** core-shell structure.*

1.7. Deposition Methods of Metal Nanoparticles

Surface modification of photocatalysts material with metal nanoparticles was investigated and the mainly used methods are: photodeposition, deposition-precipitation (DP), and colloidal deposition. Each precursor, conditions and methods used can present different responses in the photoactivity of the modified material that depends of different factors such as the distribution, loading, localization of the metal nanoparticles on the semiconductor and metal nanoparticle size. The characteristics of each method is presented in the following paragraphs.

1.7.1. Photodeposition

Photodeposition has been widely used to prepare titania supported metal NPs. The method of photo-deposition is valid when the support is a semiconductor such as titania. Electrons and holes are able to be generated when the semiconductor is irradiated with light of sufficient energy. The photo-generated electrons are so reductive that they can reduce metal ions into metal NPs that will be simultaneously deposited on the semiconductor surface. Generally, a hole scavenger such as an alcohol is added to scavenge the oxidative radicals. Parameters such as metal precursors, preparation pH, light intensity and deposition time, have a significant influence on the nanoparticles size and on the final properties of metal deposits.[82]

1.7.2. Deposition-Precipitation (DP)

The DP method is very simple and convenient and leads to homogeneous samples with reproducible properties and very small metal nanoparticle size (less than 5 nm). For many catalytic reactions, supported gold catalysts are more active when metal gold particles are smaller than 5 nm.[83] In the DP method, the metal precursors are mixed with the supports forming an aqueous suspension, subsequently precipitated as a hydroxide by increasing the pH value. The key point of the DP method is the prevention of precipitation away from the surface of the supports. The most widely used method for preparing Au-TiO_2 catalysts is deposition-precipitation method.[84]

1.7.3. Colloid Deposition

Colloid deposition consists in preparation of colloidal solutions in water or other solvents followed by adsorption of the MNPs on the substrate surface. For instance, the most popular methods are reduction of $AuCl_4^-$ with citrate in aqueous phase (the Türkevich method)[85] or the two-phase protocol consisting of reduction of $AuCl_4^-$ by $NaBH_4$ in water and extraction into toluene of the Au-NPs by means of a phase transfer agent (the Brust method).[86] Gold NPs of 5 nm with narrow size distribution can be obtained with these methods. Besides, an alternative method is the reduction of Au^{III} complexes by tetrakis (hydroxymethyl) phosphonium chloride (THPC), giving a hydrosol of gold NPs with average diameter 1~2 nm.[87] THPC acts simultaneously as a reducing and a stabilizing agent. These prepared metal colloids can be put in contact with a support and adsorb on it. However, it has been often observed that in the adsorption stage, the prepared metal colloidal particles undergo coalescence and agglomeration forming metal islands of particle size above 50 nm. This would result in inactivation of the photocatalyst due to the weak interaction with the substrate or the small surface/volume ratio of metal NPs.[88] Moreover, radiolytic reduction can be used to synthesize metal colloidal suspensions in the presence of surfactants, polymer or supports as stabilizing agents.[89,90] Strong reducing species such as aqueous electrons, hydrogen radicals generated by water radiolysis are able to reduce metal ions to lower valences and finally to metal atoms. The radiolytic synthesis will be discussed in details in the following section.

1.7.4. The Radiolysis Method

Several chemical and physical routes have been used to prepare composites of MNPs supported on TiO_2. In aqueous solution, the preparation methods involve in general the reduction of the metal precursors by adding a reducing agent such as sodium borohydride, ascorbic acid, formaldehyde and hydrazine, THPC, etc. The metal reduction can also be achieved by microwaves, sonochemistry or by radiation chemistry using UV irradiation and ionizing radiations (such as γ-rays, X-rays or electron (or ion) beams). The radiolytic method (high energy radiations) in solution presents the advantage of using simple physico-chemical conditions such as, atmospheric pressure and room temperature, absence of additional chemical reducing agents (as the reducing species are induced by solvent radiolysis) and absence of contaminants. The method results in homogeneous reduction and nucleation leading to metal nanoparticles of controlled size and shape.[91] When aqueous solutions are irradiated by high energy radiation (γ-rays, electron beams, X-rays), excitation and ionization of water takes place as following:[92]

$$\mathrm{H_2O} \xrightarrow{\gamma - ray} e_s^-, \mathrm{H_3O^+}, H^\cdot, HO^\cdot, H_2, H_2O_2 \qquad \textbf{\textit{(1. 9)}}$$

Indeed, high energy radiation (γ-rays, X-rays, electrons or ions beams) of water leads to the formation of free radicals such as solvated electrons (e^-_s) (which are strong reducing species (E^0 (H_2O/ e^-_s = -2.87V_{NHE})) and $H^\bullet$ (E^0 ($H^+/H^\bullet$) = -2.3 V_{NHE}) and $HO^\bullet$ radicals (E^0 ($HO^\bullet/H_2O$)= +2.8 V_{NHE}).[93] The radiolytic yields (quantity of radicals formed per Joule of deposited energy) of the radicals are: G (e_s^-) = 0.26, G ($H^\bullet$) = 0.06 µmol J^{-1}.[94,95]

These radicals can reduce dissolved metal complexes to the zero valence state. In the case of monovalent metal ions M^+, the reduction process can be written as follows:

$$M^+ + e_s^- \to \mathrm{M}^0 \qquad \textbf{(1. 10)}$$

$$M^+ + H^\bullet \to \mathrm{M}^0 + H^+ \qquad \textbf{(1. 11)}$$

In the case of multi-valent metal ions, they are firstly reduced to lower valences and finally to the zero valence like in the case of $\mathrm{Au^{III}}$. The reactions of $\mathrm{Au^{III}}$ with the reducing species generated from water radiolysis lead first to the formation of $\mathrm{Au^{I}}$, then to $\mathrm{Au^0}$ clusters, and then of Au-NPs, as has been established by the pioneering research of Belloni *et al.*,[96,97] Henglein,[98] and Meisel *et al.*[99] **Figure I-22**.

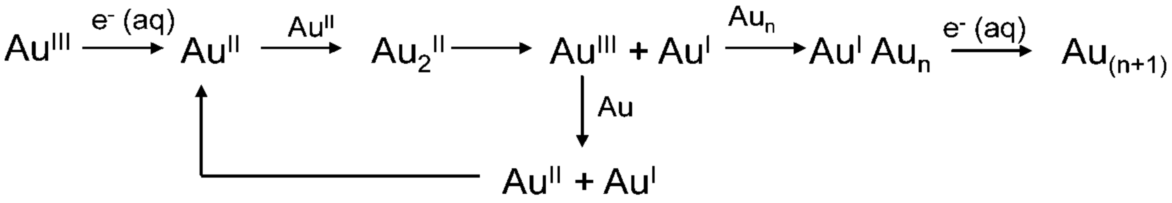

Figure I-22. *Schematic illustration of radiolytic route for the reduction of aqueous* $\mathrm{Au^{III}}$.

In the reaction strong oxidative hydroxyl radicals $\mathrm{HO^\bullet}$ [E^0 ($\mathrm{HO^\bullet/H_2O}$) = + 1.9 $\mathrm{V_{NHE}}$ at pH 7, G($\mathrm{HO^\bullet}$) = 0.27µmol $\mathrm{J^{-1}}$] are also generated during the irradiation of deoxygenated water.[94] In this case, primary and secondary alcohols (such as 2-propanol) are used in solution to remove the oxidative species working as hydroxyl radical scavengers, which also react with hydrogen atoms to form alcohol reducing radicals:[92,100]

$$CH_3CHOHCH_3 + OH^\bullet \to \; CH_3C^\bullet OHCH_3 + H_2\mathrm{O} \quad k_1 = 1.9\mathrm{x}10^9\ \mathrm{L}mol^{-1}s^{-1} \qquad \textbf{(1. 12)}$$

$$CH_3CHOHCH_3 + H^\bullet \to CH_3C^\bullet OHCH_3 + H_2 \qquad k_3 = 7.4\mathrm{x}10^7\ \mathrm{L}mol^{-1}s^{-1} \qquad \textbf{(1. 13)}$$

$$HCOO^- + HO^\bullet or\ H^\bullet \to \; \mathrm{CO}O^{\bullet -} + H_2\mathrm{O\ or}\ H_2 \qquad \textbf{(1. 14)}$$

The redox potentials of the generated radicals are: E^0 ($(CH_3)_2CO/(CH_3)_2C^{\bullet}OH$) = –1.8 V_{NHE} at pH 7, and $E^0(CO_2/COO^{\bullet-})$ = -1.9 V_{NHE}. The radicals formed by reactions (1.12) and (1.13) are almost as powerful reducing agents as $H^{\bullet}$ atoms (E^0 ($H^+/H^{\bullet}$) = -2.3 V_{NHE}). Therefore, these secondary radicals are able to directly reduce mono and multi-valence metal ions into a zero valence. The mechanisms of the reactions in the case of monovalent cations are the following:[93]

$$M^+ + CH_3C^{\bullet}OHCH_3 \rightarrow \mathrm{M}^0 + CH_3COHCH_3 + H^+ \qquad \textbf{(1. 15)}$$

$$M^+ + \mathrm{CO}O^{\bullet-} \rightarrow M^0 + CO_2 \qquad \textbf{(1. 16)}$$

Owing to these reductive species, the metals ions are homogeneously reduced leading to a homogeneous nucleation through the solution. Considering that the binding energy between two metal atoms is stronger than the atom-solvent or atom-ligand bond energy, the atoms dimerize when they encounter. Then, by a cascade of coalescence processes, M_2 progressively coalesce to growing clusters:

$$M^0 + M^0 \rightarrow M_2 \qquad \textbf{\textit{(1. 17)}}$$

$$M_m + M_p \rightarrow M_n \qquad \textbf{\textit{(1. 18)}}$$

The bonding between atoms or clusters with unreduced ions is also strong and these association processes are fast:

$$M^0 + M^+ \rightarrow M_2^+ \qquad \textbf{\textit{(1. 19)}}$$

$$M_2^+ + M_2^+ \rightarrow M_4^{2+} \quad \text{coalescence processes} \qquad \textbf{\textit{(1. 20)}}$$

$$M_m + M^+ \rightarrow M_{m+1}^+ \qquad \textbf{\textit{(1. 21)}}$$

$$M_{m+x}^{x+} + M_{p+y}^{y+} \rightarrow M_{n+z}^{z+} \quad \text{coalescence processes} \qquad \textbf{\textit{(1. 22)}}$$

Followed by steps of coalescence of atoms separately created. In contrast, in the continuous irradiation regime the association of M^+ ions with atoms, as in the charged dimer M_2^+ and clusters M_{n+1}^+, and the coalescence processes are faster than the production rate of the reducing radicals. Therefore, the reduction of M^+

ions occurs mostly *in situ* on clusters already formed M_{n+1}^{+}, where m, n and p represent the cluster nuclearities (number of reduced atoms), and x, y and z refer to the number of associated ions.[92]

$$M_{n+1}^{+} + e_s^{-}, CH_3C^{\bullet}OHCH_3 \text{ or } \mathrm{CO}O^{\bullet -} \rightarrow M_{n+1} + CH_3COHCH_3 + CO_2 + H^{+} \qquad \textbf{\textit{(1. 23)}}$$

In the case of bimetallic nanoparticles, the final structure depends mainly on the metal precursors and on the reduction kinetics fixed by the dose rate. The two metal precursors M^+ or M'^+ have generally equal probabilities to be reduced by the radiolytic radicals.

In the case of core-shell clusters, an electron transfer from the less noble metal (nascent M'^0 formed by radiolytic reduction) to the ions of the more noble metal M^+ (Eq. 1.24), favors first the reduction into M^0. Therefore, core-shell structures are obtained with the more noble metal in the core surrounded by the less noble metal

$$M'^0 + M^+ \rightarrow (MM') \rightarrow M^0 + M'^+ \qquad \textbf{\textit{(1. 24)}}$$

$$(M_m M'_n)^{x+} + M^+ \rightarrow (M_{m+1} M'_n)^{(x+1)+} \rightarrow (M_{m+1} M'_{n-1})^{x+} + M'^+ \qquad \textbf{\textit{(1. 25)}}$$

If the ionic metal precursors are multivalent, an electron transfer is possible as well between the intermediate low valencies of both metals, so increasing the probability of segregation. The less noble metal ions act as an electron relay towards the noble ions. Thus, monometallic clusters M_n are formed first. Then, when almost all the M^+ ions are reduced, M'^+ ions will be reduced at the surface of M_n. The final result is a core-shell cluster where the more noble metal *M* is coated by the less noble metal *M'*.[92]

In the case of alloyed clusters, the initial reduction reaction is followed by mixed coalescence:

$$\mathrm{M}' + \mathrm{M} \rightarrow (MM') \qquad \textbf{\textit{(1. 26)}}$$

$$(MM') + \mathrm{M} \rightarrow (M_2 M') \qquad \textbf{\textit{(1. 27)}}$$

$$(M_m M'_n)^{x+} + M^+ \rightarrow (M_{m+1} M'_n)^{(x+1)+} \qquad \textbf{\textit{(1. 28)}}$$

$$(M_{m+1}M'_n)^{(x+1)+} + e_s^- (\text{or R}) \rightarrow (M_{m+1}M'_{n-1})^{x+} (\text{or R}^+) \qquad \textit{(1. 29)}$$

To limit the growth and to obtain small nanoparticles, ligands, polymers, surfactants or supports are added to the irradiated solution.[94,100]

Figure I-23 shows a scheme of metal ions reduction in solution by ionizing radiation in the presence of alcohol (added to scavenge $HO^{\bullet}$ radicals induced by radiolysis). These nanoparticles can be synthesized directly on a support such as TiO_2.

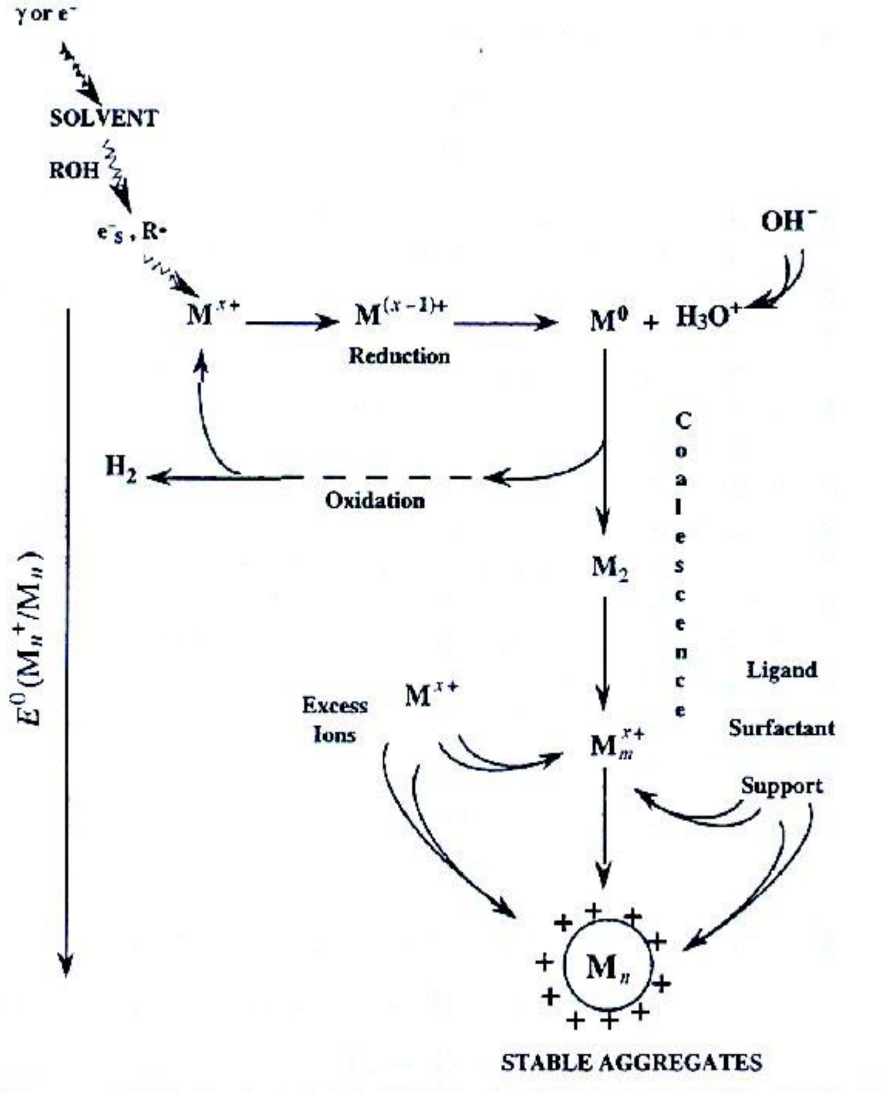

__Figure I-23.__ Scheme of metal ion reduction in solution by ionization radiation in the presence of alcohol for scavenging oxidizing $HO^{\bullet}$.[100]

- **Effect of the Dose Rate**

The reducing agents are homogeneously induced in the solution leading to a homogeneous reduction (of the metal ions) and nucleation. The binding energy between two metal atoms is stronger than the atom-solvent or atom-ligand bond energy, and the metals started to coalescence as cascade and M_2 progressively coalesce into growing clusters. In the case of monometallic nanoparticles in **Figure I-24**, the growth of the clusters depends on the dose rate, which fixes the reduction kinetics. At high dose rate, the reduction is very fast and followed by the steps of coalescence of atoms separately created (**Figure I-24a**). At low dose rate, the reduction is slower and association of M^+ ions with atoms are faster than the production rate of reducing radicals (**Figure I-24b)**. Therefore, the reduction of M^+ ions occurs mostly *in situ* on clusters already formed $M_{n+1}{}^+$.

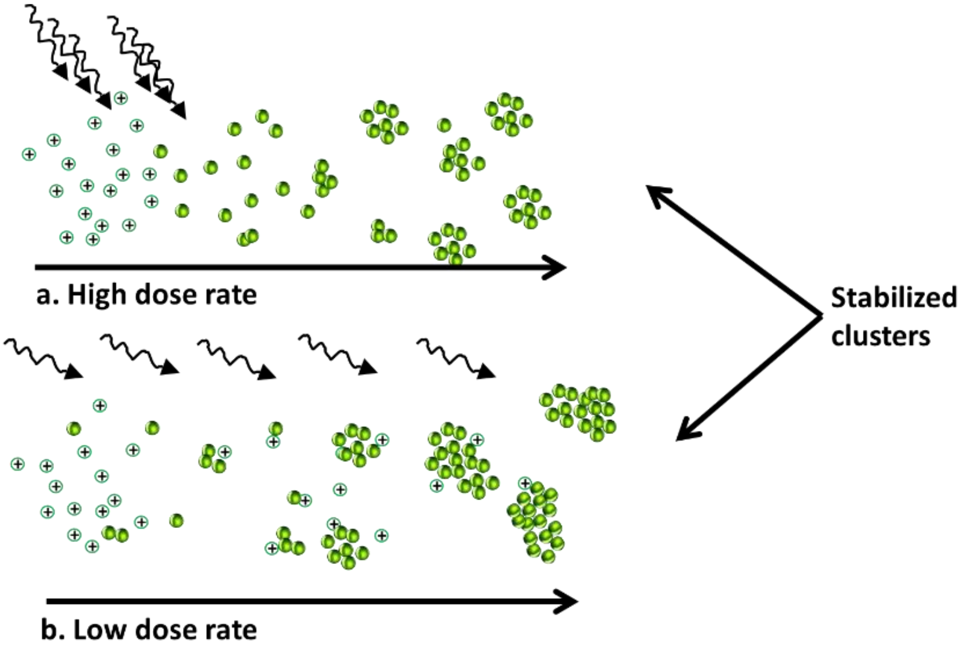

Figure I-24. *Nucleation and growth of clusters generated by radiolytic radicals at* ***a)*** *high and* ***b) low*** *dose rates.*

If ions of two metals are present in the solution, (**Figure I-25**) the irradiation induces reduction of both metal salts, and the competition reactions depend on the metals precursors and on the dose rate. At low dose rate, the electron transfer occurs from the atoms of the less noble metal to the ions of the more noble metal.

This results in bimetallic nanoparticles with a core shell structure (the more noble metal being in the core). A high dose rate prevents the electron transfer from one metal to the other (because of the fast reduction), therefore with fast and total reduction alloyed clusters are obtained.[93,94]

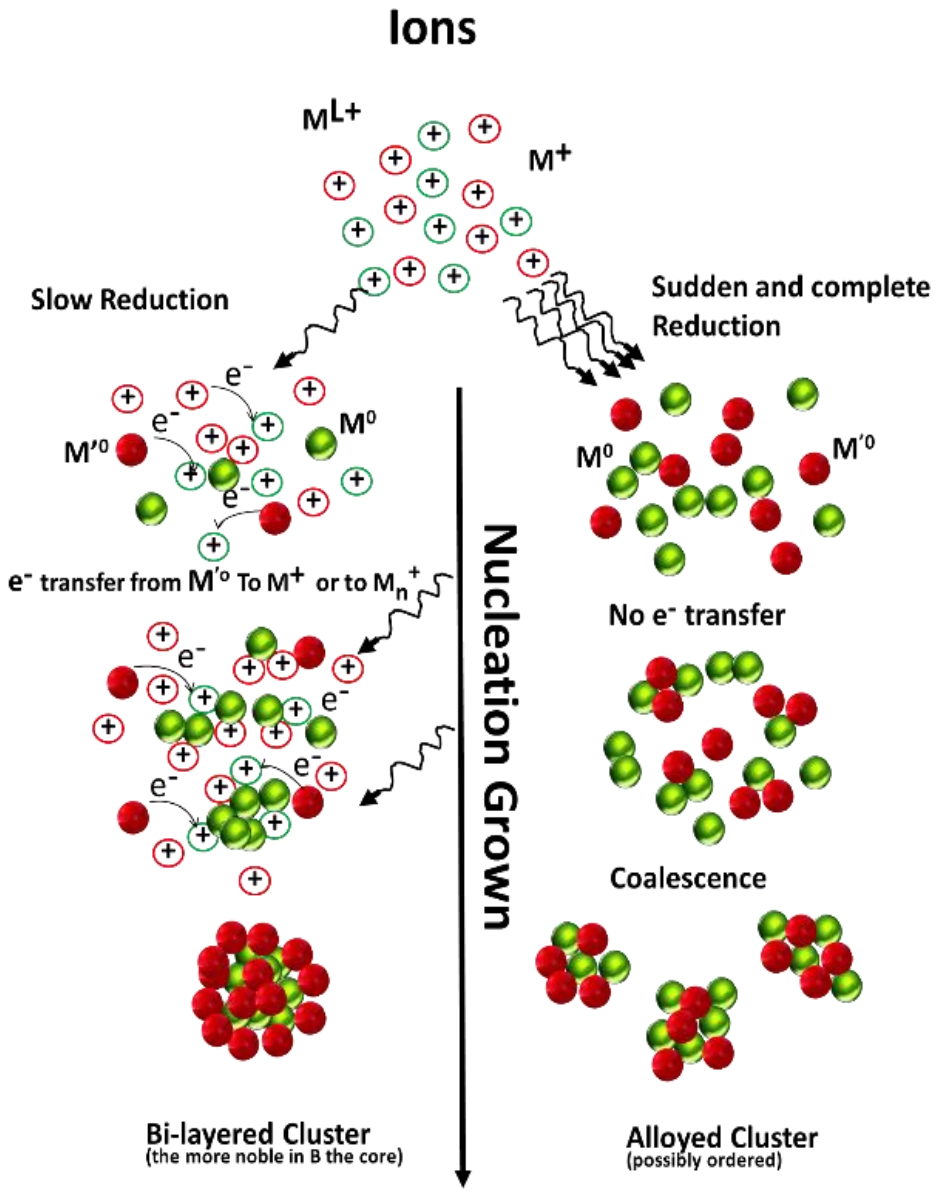

Figure I-25. *Scheme of the influence of the dose rate on the competition between the inter-metal electron transfer and the coalescence processes during the radiolytic reduction, of mixed metal ion solutions. High dose rates favor alloying, whereas low dose rates favor core-shell segregation of the metals in the nanoparticles.*[70]

Some examples of two metals systems are presented in **Table 1**.

Table 1. *Different structures obtained at different dose rates*

Multimetallic clusters		
Gamma Irradiation Conditions		**Particle Structure (Ref)**
Mixed salts	**Dose rate (kGyh^{-1})**	
Ag_n, $Au(CN)_2^-$	0.9	Ag/Au, core-shell[101]
Ag+, $AuCl_4^-$	3.8	Ag/Au, core-shell[102]
Ag+, $AuCl_4^-$	35 EB	Ag/Au, alloy[102]
Ag_n, Cu^{2+}	0.87	Ag/Cu, core-shell[103]

*EB: Electron beams

The dose rate is generally determined with a Fricke dosimeter (see **Appendix II)**.

1.8. Catalyst and photocatalysts

Catalysis is, by general definition an acceleration of a reaction that proceeds spontaneously from the viewpoint of thermodynamics by reducing the activation energy. Photocatalysts are catalysts which are activated by light. Like catalysts, they are not consumed, but they are regenerated after photocatalytic cycles.

1.9. Application of photocatalytic materials

Many factors affect the photoreactions and their efficiencies, such as nanoparticle material types, nanoparticle size and morphology, metal loading, pH value, temperature, etc. However, one of the dominant factors is the energy band positions of the materials. For example, the energy band positions of the photocatalysts determine its cut-off absorption wavelength, while those of the redox group relative to those of the photocatalysts determines whether a specific reduction or oxidation reaction is possible or efficient.

The band edge positions of some semiconductors are presented in **Figure I-26** in three categories, the left side shows the commonly used semiconductor photocatalysts such as TiO_2, ZnO, Bi_2O_3, CdSe, WO_3 and CdS. Silver halides (AgCl, AgBr and AgI) are included as well, they have been used extensively as the redox balance materials for Ag nanoparticles. In the lower part of **Figure I-26**, the decompositions to metallic Ag atoms and the corresponding potentials are also listed for easy reference. The second group displays work functions of common noble metals, including Ag, Au, Pd and Pt. On the right side, the third group presents the potential levels of common redox groups, including $O_2/O_2^{\bullet-}$, H_2/H^+, O_2/OH^-, O_2/H_2O_2, Ag/Ag^+, O_2/H_2O and Au^+/Au.[4]

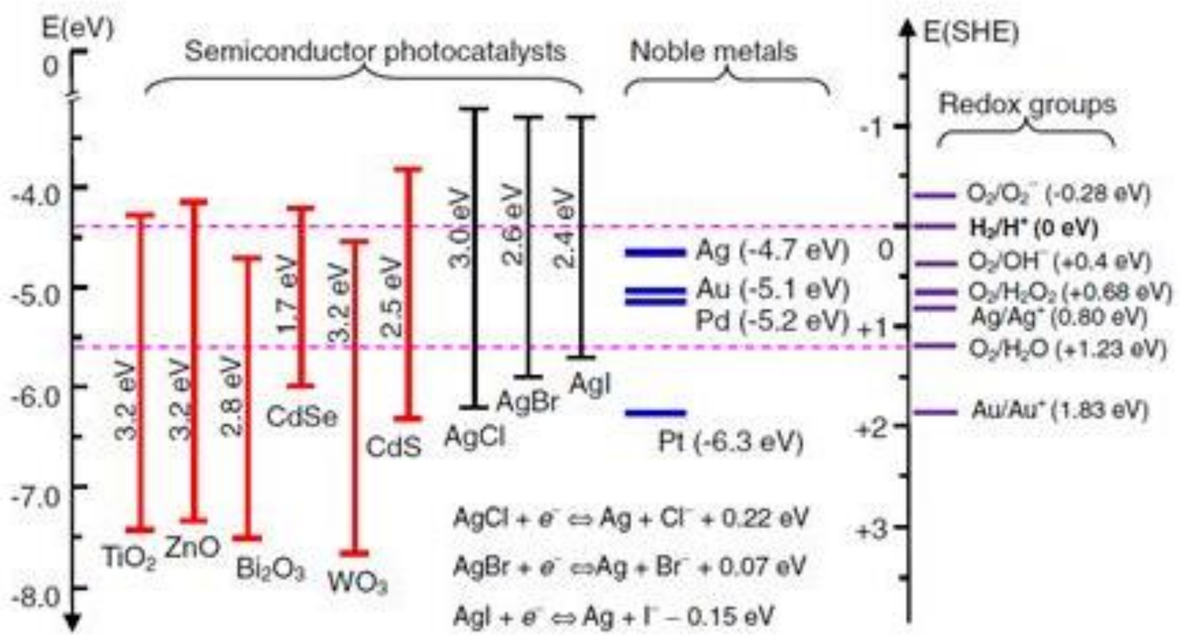

Figure I-26. *Energy band positions of common materials in plasmonic photocatalysis, including the conduction and valence bands of the SC, the work functions of the noble metals, and the electrochemical potentials of redox groups.*[4]

Plasmonic materials can be obtained with modification of a semiconductor with MNPs and these materials can be excited by light. The photoexcited charge carriers can be used to perform redox reactions.

The top of the conduction band of TiO_2, (see **Figure I-27**), must be more positive than the reduction potential of H_2/H^+ to achieve overall water splitting. TiO_2 is inefficient for H_2 generation attributed to high hydrogen over-potential linked to fast electron-hole recombination.[101] However, plasmonic materials increase the quantum yield in hydrogen generation, due to *(i)* the decrease of the recombination process under UV, *(ii)* the injection of electrons to the semiconductor under visible irradiation, and also *(iii)* to metal NPs that can act as catalyst sites for atomic hydrogen ($H^\bullet$) formation leading to H_2. Electrons injected in the conduction band can reduce H^+ to H_2, while the holes on the surface of the semiconductor are scavenged by adding electron donors (sacrificial reagent or hole scavengers), to react with the photo-generated holes, and thus enhancing the photocatalytic reaction. Organic compounds (hydrocarbons) are widely used as electron donors, such as: EDTA, methanol, ethanol, CN^-, lactic acid and formaldehyde.[102] Also, with the addition of alcohols, they can be decomposed into CO, CO_2 and HCO_2H (see **Figure I-27**).

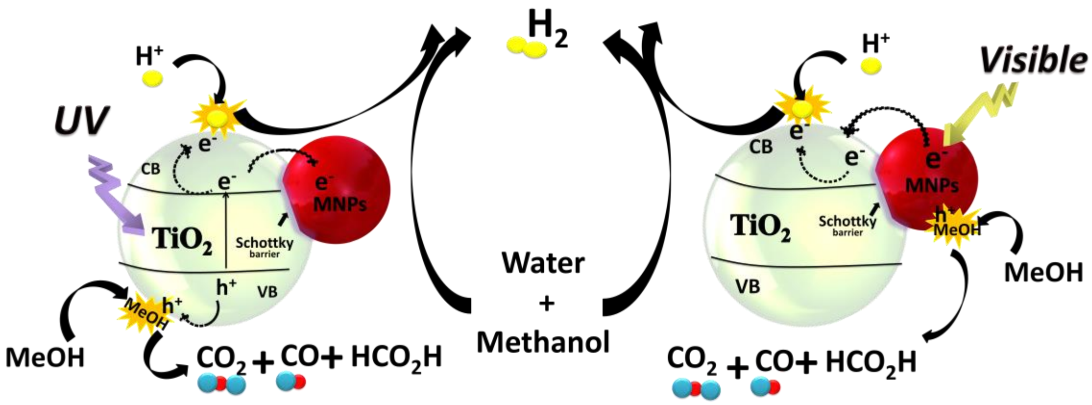

Figure I-27. *Schematic of degradation of generation of hydrogen, with a plasmonic photocatalyst.*

The bottom of the valence band of TiO_2 must be much more negative than the redox potential of O_2/H_2O (at pH 7), that can oxidize organic compounds. With these characteristics, in recent years, interest in plasmonic photocatalysis has focused on development of efficient semiconductor based materials as photocatalysts under UV and visible irradiation for the removal of organic and inorganic pollutants from aqueous solutions in environmental clean-up, drinking water treatment. **Figure I-28** illustrates the mechanism of plasmonic photocatalysts in the degradation of organic pollutants. These mechanisms will be discussed in more details later.

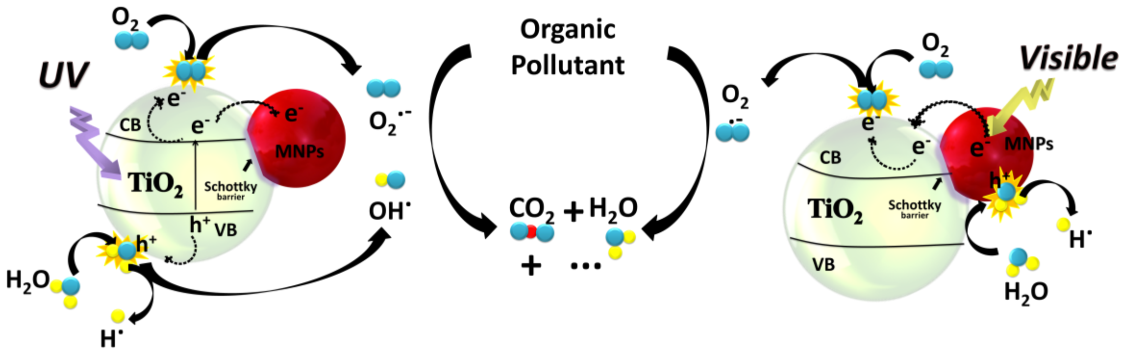

Figure I-28. *Schematic of degradation of organic compounds using plasmonic photocatalysts under UV and visible light irradiation.*

Chapter II

Experimental Procedure

Chapter 2. Experimental Procedures

2.1. Materials

Commercial titanium(IV) oxide P25 (TiO_2-P25, Evonik, surface area of ca. 50 m^2 g^{-1}), composed of a mixture of the crystalline phases: anatase (73-85%), rutile (14-17%) and amorphous titania (0-13%),[103] was used as support material. Silver sulfate (Ag_2SO_4, Fulka, purity ≥ 99.4%), cupric sulfate ($CuSO_4$, Sigma, purity ≈ 99%) and chloroauric acid ($HAuCl_4 \cdot 3H_2O$, Aldrich, ≥99.8%), were used as metal precursors. Tetrakis (hydroxymethyl) phosphonim chloride (THPC) in an 80% aqueous solution was purchased from Sigma Aldrich and used as reducing agent. Sodium hydroxide (NaOH, Prolabo, 97%). The other chemicals used were methanol (CH_3OH, ACS reagent, ≥ 99.8%), phenol (C_6H_5OH, Fulka), 2-propanol ($CH_3CH(OH)CH_3$) purchased from Sigma-Aldrich, 99.5%), and acetic acid (CH_3COOH, 99.7%) from Wako). We used deionized water (Milli-Q with 18.6 MΩ).

2.2. Photocatalyst Preparation

2.2.1. Surface Modification of TiO_2-P25 by Chemical Reduction Using THPC Method

The Au/TiO_2 photocatalysts, with different Au-NPs loadings (0.5, 1.0, and 2.0 wt%), were prepared according the Duff and Baiker method.[8,104] This preparation is based on a gold salt solution and THPC as a reducing and stabilizing agent. In a beaker containing 45 mL of deionized water, 1.5 mL of a NaOH solution 0.2 M, freshly prepared, was added under vigorous stirring. After 5 minutes, 1 mL of a THPC solution 0.05 M was added to the mixture, followed by 5 mL of $HAuCl_4$ (10^{-2} M) for the sample with a gold content 1 wt%. The color of the solution instantaneously changed from transparent to brown, indicating the reduction from Au^{III} to Au^0. Afterwards, 1 g of TiO_2-P25 was added as support to the mixed solution, which was maintained under vigorous stirring at room temperature during

2 h. The powder was separated by centrifugation (3 times at 4500 rpm for 15 min), and washed thoroughly with deionized water. The supernatants were completely transparent after deposition and centrifugation, indicating that all the Au-NPs were deposited on TiO_2-P25.

The samples were then dried at 60 °C for 48 h. After drying, the reduced samples were thermally treated under hydrogen in a volumetric apparatus adapted with vacuum pump and a proper oven for thermal treatment. First, as a previous treatment, the sample was heated under vacuum with a heating rate of 5 °C/min, to remove any remaining THPC residues. When the temperature reached 500 °C, it was maintained for 2 h, afterwards, vacuum of at least 10^{-4} torr was produced. Then, a pressure of 100 torr of H_2 was introduced into the sample cell. The samples were exposed to H_2 during 30 min for further reduction of the metal nanoparticles. Afterward, H_2 was removed by using the vacuum pump and then a second dose of H_2 was added and maintained again for 30 min. Finally, the samples were cooled down to room temperature, see **Figure II-1**.

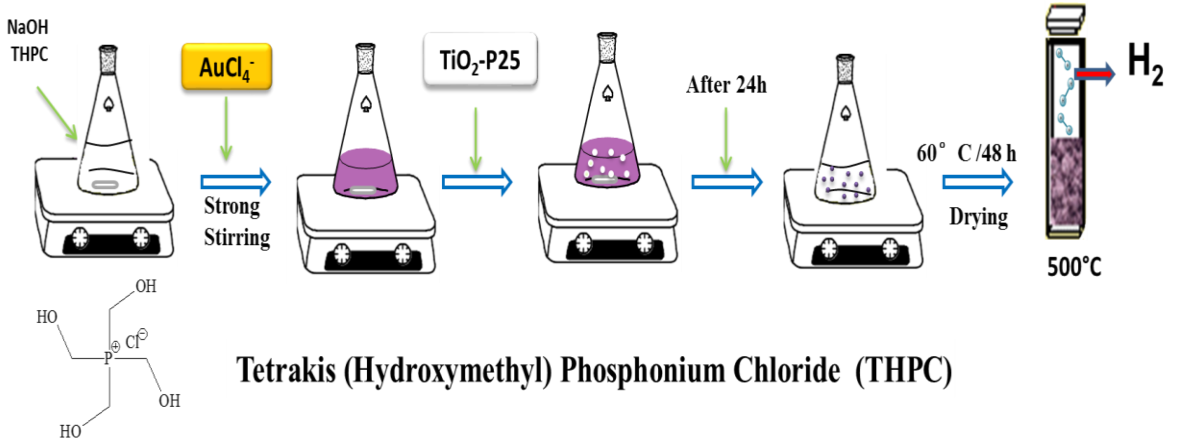

Figure II-1. *Scheme synthesis of Au/TiO_2 by THPC method.*

2.2.2. Photocatalyst Preparation: Modification of TiO_2-P25 by Radiolysis

We used a panoramic ^{60}Co gamma source located at the LCP, Orsay, more information about the ^{60}Co gamma source is in **Appendix I.** To measure the dose rate on the gamma source, a Fricke dosimetry (based on radiation-induced Fe^{2+} oxidation, see below **Appendix II**) was done for different positions of the samples.

In our case the highest dose rate is: 4.1 kGy/h. More details about the calculation are presented in **Appendix II.**

- **Calculation of Gamma Dose Rate.**

The reaction involved in the Fricke dosimeter, is the radiation-induced oxidation of ferrous ion to ferric ion ($Fe^{2+} \rightarrow Fe^{3+}$) at low pH, and in the presence of oxygen. The standard dosimeter solution contains 10^{-3} M ferrous sulfate or ferrous ammonium sulfate, 10^{-3} M NaCl in 0.4 M of H_2SO_4 (pH 0.46) and is saturated with air. The experimental conditions are presented in **Table 2**.

250 mL of this Fe^{2+} solution was prepared and was irradiated in specific positions in beaker of 25 mL at different times. The spectra of the solutions were measured each 2 min of irradiation until 16 min, to obtain the saturation of the solution due to Fe^{3+} absorption at 304 nm.

Table 2. *Experimental conditions for the Fricke dosimeter.*

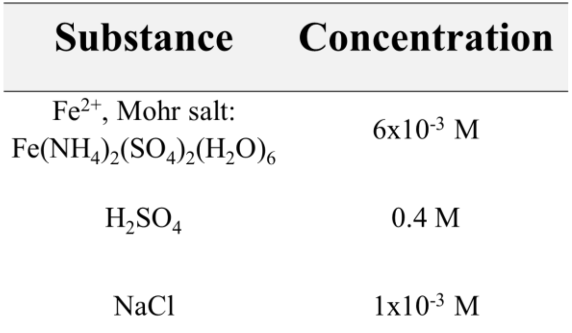

Substance	Concentration
Fe^{2+}, Mohr salt: $Fe(NH_4)_2(SO_4)_2(H_2O)_6$	$6x10^{-3}$ M
H_2SO_4	0.4 M
NaCl	$1x10^{-3}$ M

In position 8, we obtained the maximum dose rate. The radiolytic dose rate is deduced from the slope of the graph (absorption at 304 nm versus time, ε=2204 L mol^{-1} cm^{-1}) shown in **Figure II-2**: In this position the dose rate is 4.1 kGy/h.

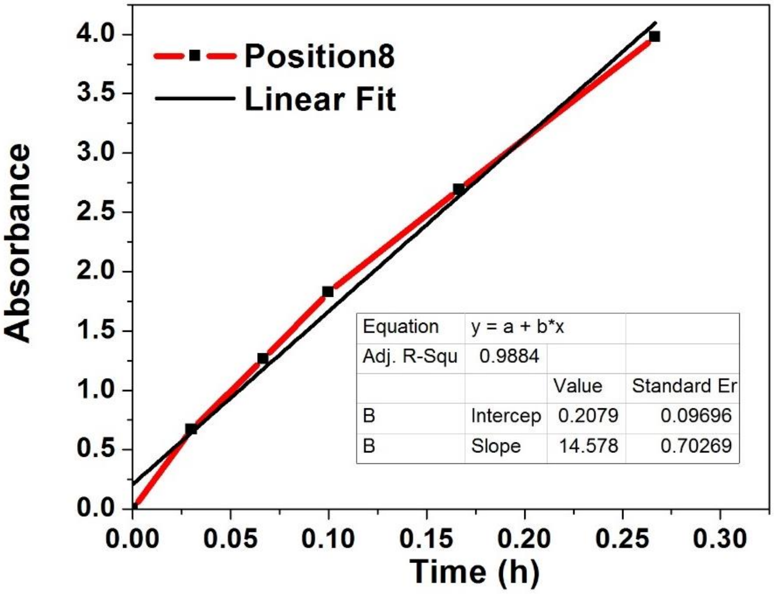

Equation	y = a + b*x		
Adj. R-Squ	0.9884		
		Value	Standard Er
B	Intercep	0.2079	0.09696
B	Slope	14.578	0.70269

Figure II-2. *Calculation of the dose rate at the position 8 in the gamma source.*

Metal ions were reduced on TiO_2-P25 surface by solvated electrons and reducing $(CH_3)_2C^{\bullet}OH$ radicals induced by radiolysis as it is shown in the scheme **Figure I-23**. Indeed, it is well known that high energy radiation (γ-rays, X-rays, electrons or ions beams) of water leads to the formation of free radicals such as solvated electrons (e^-_s) (which are strong reducing species ($E^0(H_2O/\ e^-_s = -2.87V_{NHE})$), $H^{\bullet}(E^0\ (H^+/H^{\bullet}) = -2{,}3\ V_{NHE}$ and $OH^{\bullet}$ radicals ($E^0(HO^{\bullet}/H_2O) = +2{,}8\ V_{NHE}$).[93] Generated hydroxyl radicals $OH^{\bullet}$ (strong oxidant species) are scavenged by addition of 2-propanol (0.1 M), which yields after reactions with $OH^{\bullet}$ and $H^{\bullet}$ to a secondary reducing radical $(CH_3)_2C^{\bullet}OH$ ($E^0((CH_3)_2CO/\ (CH_3)_2C^{\bullet}OH)) = -1.8V_{NHE}$).[93]

Alcohol radicals and e^-_s are powerful reducing agents, which are able to reduce metal ions to lower valences and finally to metal atoms. The energy deposition throughout the suspension ensures an homogeneous distribution of the radiolytic radicals and therefore a homogeneous reduction and nucleation leading to formation of nanoparticles homogeneous in size.[93,100]

Surface modification of TiO_2 with Cu and Ag: Ag^+, and/or Cu^{2+} ions and complexes were reduced by radiolysis on TiO_2-P25 surface, see **Figure II-3**. Aqueous solutions (0.1M 2-propanol, used as scavenger of $HO^{\bullet}$ radicals generated by water radiolysis)[93] containing one or two metal salts Ag_2SO_4 and $CuSO_4$ (the total concentration in salt being $1x10^{-3}$ M) were put in contact with TiO_2 P25. The surface modification of TiO_2-P25 with monometallic nanoparticles was performed with three different metals: copper (Cu), and silver (Ag). Different weight percentages were used for each case, *i.e.*, for silver, samples with 0.5 wt% in metal were prepared, however for copper NPs, the catalysts were prepared with 0.5, 1 and 2 wt% in metal. Ag NPs were synthesized only for comparative purposes (The sample was labeled Ag/P25). The loading of Cu was 0.5 wt%, 1w% and 2 w%. The samples were labeled as P25, Ag/P25, CuO_x/P25 where x is the loading in Cu.

The suspensions were first sonicated for 3 minutes, deaerated with nitrogen (under stirring) for 20 min, then irradiated with the ^{60}Co panoramic gamma source (dose rate = 2.3 kGy h^{-1}). The metal ions were reduced by the solvated electrons and the alcohol radicals induced by solvent radiolysis. The applied doses (deduced from calculations) were sufficient to reduce all the metal ions into their zero valency. The modified TiO_2-P25 photocatalysts were separated by centrifugation and dried at 60°C for 18 h. The supernatant was completely transparent after centrifugation, indicating that all the metal NPs were deposited on TiO_2-P25.[93,100]

- Ag@CuO nanoparticles.

For the suspensions containing a mixture of Ag^+ and Cu^{2+}, different molar ratios of Ag:Cu were used, *i.e.* 1:1, 1:3, and 3:1. Keeping the total nominal metal content at 1 wt%. The resulting modified catalysts were respectively labeled as Ag@CuO1:1/P25, Ag@CuO1:3/P25, and Ag@CuO3:1/P25. The suspensions were first sonicated for 3 minutes, deaerated with nitrogen (under stirring) for 20 min and then irradiated with a ^{60}Co panoramic gamma source (dose rate = 2.3 kGy h^{-1}) for 3.5 h. The modified TiO_2-P25 photocatalysts were separated by centrifugation and dried at 60°C for 18 h. The supernatant was completely transparent after centrifugation, indicating that all the Ag and CuO-NPs were deposited on TiO_2-P25.[93,100]

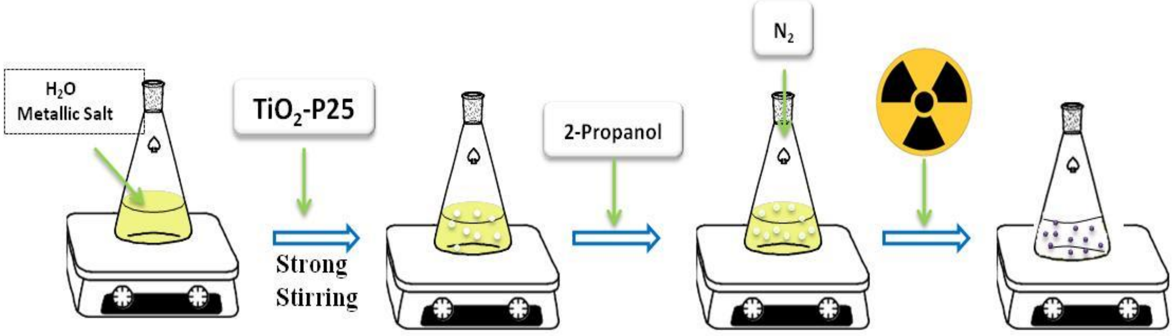

Figure II-3. *Scheme synthesis by radiolysis method.*

2.3. Characterization Techniques

X-ray diffraction (XRD) was used to identify the atomic and molecular structure of the modified TiO_2. The photocatalysts were characterized with a DX8 Bruker Advance diffractometer using Cu-Kα radiation (λ=1.5406 Å) over the 2θ range of 10-80° in a step mode, with steps of 0.02° and 2 s per step.

Diffuse Reflectance Spectroscopy (DRS) was used to measure the UV-visible spectra of the modified samples, and was recorded with a UV-Vis-NIR spectrophotometer, model Cary 5000 Series from Agilent Technologies, equipped with an integrating sphere for diffuse and total reflection measurements and using a KBr reference sample.

High Resolution Transmission Electron Microscopy (HRTEM) was used to study the particle size and distribution of the metal nanoparticles supported on TiO_2, and to study the different arrangements of the crystallographic planes of the support and the nanoparticles. For this characterization technique, we used a FEI Tecnai F30 microscope equipped with a tungsten field emission gun operated at 300 keV. The samples were dispersed in 2-propanol under sonication, and then, few drops of the suspension were deposited on a holey carbon copper grid (Quantifoil Micro Tools GmbH, Germany). The particle size and the interplanar distances were measured using Digital Micrograph software.

High Angle Annular Dark Field-Scanning Transmission Electron Microscopy. (HAADF-STEM). The HAADF-STEM images were recorded using Cs corrected

JEOL-ARM-200F electron transmission microscope at 200 kV. The HAADF-STEM images were acquired with a camera length of 8 cm and the collection angles of 70-280 mrads were also employed to characterize the morphology of modified TiO_2. The samples were dispersed in 2-propanol in an ultrasonic bath for few minutes and then, one drop of the suspension was deposited on a gold coated holey carbon grids (SPI method).

Energy-Dispersive X-ray Spectroscopy (EDS) measurements for line scan profiles and mapping were obtained with a solid state detector from Oxford with an 80 mm^2 window. EDS was used to analyze the structure and composition of the deposited Ag and Cu-based NPs.

X-ray Photoelectron Spectroscopy (XPS) characterization was conducted on a JEOL JPS-9010MC with a hemispherical electron energy analyzer, using Mg Kα radiation. The samples were mounted on carbon films, each carbon film was fully covered with the sample in order to avoid powder release. After overnight degassing in the preparation chamber, the samples were inserted in the analysis chamber with a pressure lower than 10^{-7} torr. High resolution scans were taken for five elements, and the number of scans differed depending on each element content in the sample, *i.e*., 50 scans were taken for Ti and O, 100 scans for C and 300-500 scans for Ag and Cu. This technique was used to analyze the chemical composition of the modified TiO_2-P25 and to identify the chemical state of Cu and Ag elements in the samples.

X-ray absorption near edge structure (XANES), Cu K edge XANES measurements were carried out at the SAMBA beamline (SOLEIL synchrotron, Saint-Aubin) using a Si (220) fixed-exit double crystal monochromator. Harmonic rejection was done by two Pd coated mirrors at 5.5 mrad grazing incidence. Measurements were done on pellets of samples at room temperature in fluorescence mode using a Ge 35 pixel-array detector. This technique was used in order to corroborate the oxidation states of Cu.

Time Resolved Microwave Conductivity (TRMC), this technique was used to study the dynamics of photogenerated charge-carriers under UV and visible irradiation. TRMC technique uses a pulsed laser source with an optical parametric oscillator (OPO) EKSPLA, NT342B, tunable in the range between 220–2000 nm. The full width at half-maximum (FWHM) of one pulse was 8 ns with repetition frequency of the pulses at 10 Hz, and microwaves generated by a Gunn diode (30 GHz).

More details for the characterization techniques are presented in **Appendix VI.**

2.4 Photocatalytic Tests

2.4.1. Photodegradation of Phenol

The photocatalytic activity of the modified photocatalysts was tested for photooxidation of phenol (C_6H_5OH) (used as model pollutant in water (50 ppm)), under UV and visible illumination. The photodegradation was carried out in a 10-mm light path quartz cell reactor containing 3.5 mL of phenol solution and 1 g L^{-1} of a photocatalyst. Before irradiation, the photocatalyst was dispersed in the solution by sonication for 30 s, and then by magnetic stirring for 10 minutes in the dark to reach the equilibrium between adsorption and desorption. Then, the solution was irradiated using a xenon lamp (Oriel 300W, see **Figure A3**) with or without cut-off filter (AM-32603-1, LOT-Oriel) for experiments carried out under visible light ($\lambda >$ 450 nm) or UV irradiation, respectively. The photocatalytic tests were conducted under oxygen bubbling at a fixed rate flow.

Aliquots of 0.5 mL were sampled from the reactor at different time intervals. The powder was separated by centrifugation and then the resultant transparent solution was analyzed by High Performance Liquid Chromatography (HPLC, Agilent 1260 infinity quaternary LC) equipped with a UV-detector set at 260 nm for phenol analysis. The column was an adsorbosphere C18 in reverse phase (5 µm, l = 150 mm, ID = 4.6 mm, Alltech) combined with an All-Guard cartridge system TM (7.5x4.6 mm, Alltech) for elution at 1 mL min^{-1} flow rate. An isocratic mobile phase consisted of 80% H_2O and 20% acetonitrile (ACN). Star software was applied for data analysis. The mechanism of phenol degradation was presented in the **Appendix III: Figure A3**

2.4.2. 2- Propanol Degradation

The photocatalytic decomposition of 2-propanol was carried out with 50 mg of a photocatalyst suspended in 5 mL of an aqueous solution of 2-propanol (5 v%). The photocatalyst was irradiated using a xenon lamp and a cut-off filter (Y48, Asahi Techno Glass) with wavelengths above 450 nm (λ ≥ 450 nm) and under vigorous magnetic stirring (1000 rpm), see **Figure A5**. The vials with aerated liquid suspensions were covered with a septum to avoid any vaporization of acetone. The reactor was immersed into water bath to maintain the reaction temperature at 25 °C. Samples were taken at different irradiation times until 3 h of experiments: Every hour, a volume of the liquid phase was taken and was filtrated using (Whatman Mini-UniPrep, PVDF). Then, 0.2 mL of the filtrated solutions were analyzed using a Shimadzu GC-14B gas chromatograph equipped with a flame ionization detector for follow the acetone generated according to the reaction.[74]

$$2(\mathrm{CH_3})_2\mathrm{CHOH} + \mathrm{O_2} \rightarrow 2(\mathrm{CH_3})_2\mathrm{O_2} + 2\mathrm{H_2O} \qquad \textbf{\textit{(2.1)}}$$

2.4.3. Hydrogen Production by Methanol Deshydrogenation

The H_2 production through the PWS process was performed in a closed Pyrex glass reactor with an argon atmosphere and vigorous stirring. For this, 2 mg of each photocatalyst were suspended in 2 mL of a degassed aqueous solution with 25 v% of methanol, used as a sacrificial agent. As mentioned by Ortega *et al.,*[9] methanol is interesting because it does not contain carbon-carbon links, thus reduces the risk of the formation of more carbon-based sub-products (the main intermediates generated in the reaction for H_2 from methanol are formaldehyde, formic acid, and CO_2), and with this the fouling of the photocatalyst.[9,102] intermediates. The photocatalyst was dispersed in the solution by sonication. LEDs (Innotas Elektronik) with wavelengths of 400 and 470 nm were used as irradiation sources, see **Figure A6**. The amount of hydrogen produced was determined by gas chromatography (GC) on a Bruker Scion GC/MS, with a thermal conductivity detector (column: Mol. Sieve 5 A 75 m x 0.53 mm I.D., oven temp. 70 °C, flow rate 22.5 mL min^{-1}, detector temperature of 200 °C with argon as carrier gas).

2.4.4. Action Spectra for Acetic Acid Degradation

Action spectra express the relative effectiveness of the photocatalytic response, that depends strongly of the wavelength radiation (most effective at longer wavelength, while at lower wavelength the chemical response is ineffective). Thereby for each particular wavelength we have a particular response, which depends on the photocatalyst. More details about Action Spectra are given in **Appendix IV.**

The photocatalytic degradation of acetic acid was carried out for 30 mg of photocatalyst suspended in 3 mL of an aqueous solution of acetic acid (5 v%), inside quartz cells with a volume of ca. 12 mL. The cells were sealed with a septum to avoid the leakage of generated CO_2. The suspensions were stirred in the dark for 10 min (to attain the adsorption equilibrium). The illumination with a 300-W xenon lamp (Hamamatsu Photonics C2578-02) equipped with a diffraction grating type illuminator (Jasco CRM-FD) allowed the selection of the irradiation wavelength in the range between 350–680 nm, with an interval of 30 nm, see **Figure A7**. The samples were irradiated with a monochromatic light with a full-width at half-maximum (FWHM) of 15 nm irrespective of the selected wavelength, and the intensity of irradiation (1.24–3.9x10-8 Einstein s-1), measured by a Hioki 3664 optical power meter was maintained at ca. 3.5 mW.

The samples were irradiated for 90 min under stirring. Every 30 min, a 0.2 mL of gas sample was taken with a syringe from the quartz cell and the CO_2 generated was analyzed with a gas chromatograph (Shimadzu GC-14B) equipped with a flame ionization detector (FID). The sensitivity of a FID detector was enhanced by converting carbon dioxide into methane in an in-line methanizer (Shimadzu MTN-1). The reaction of acetic acid degradation is the following:[74]

$$\mathrm{CH_3COOH + 2O_2 \rightarrow 2CO_2 + 2H_2O} \qquad \textbf{\textit{(2.2)}}$$

Through the reaction rate and the intensity of the light, it is possible to calculate the apparently quantum efficiency (Φ_{app}) and obtain the action spectrum:

$$\phi_{\text{app}} = \frac{\text{reaction rate of CO}_2 \text{ generation (mol/s)}}{\text{light Flux (mol/s)}} \times 100 \qquad \textit{(2.3)}$$

The apparent quantum efficiency was calculated as the rate of CO_2 evolution from the decomposition of acetic acid versus the flux of incident photons, assuming that four photons were required for the reaction.

2.4.5. Antifungal Properties of Modified Samples with Ag, CuO and Ag@CuO.

We studied the fungi growth or the inhibition of the growth of the different fungi Aspergillus Melleus and Penicillium Chrysogenum in the presence of the photocatalysts. This study was carried out by the agar plate method supplemented with a dispersion of 20 g dm^{-3} of the photocatalysts in 48 g dm^{-3} of Malt Extract Agar (MEA). The dispersion was first sterilized in an autoclave at 121°C for 15 min. The solution was then deposited in Petri plates and the media will form a gelly. Ten-day old fungal cultures on MEA slants at 25 °C were used for preparation of spore suspensions. 5 µL of sterile spores of fungi suspensions were dispersed in 8.5 g/L of NaCl solution contained in a slant. The slant was then vigorously shaken by a vortex for 3 min. Three drops were inoculated on the Petri plates and incubated at room temperature under natural indoor light (intensity of ca. 120 Wm^{-2}) and in the dark. The incubation was carried out for 8 days at 25 °C. The colony diameters were measured after 2, 4, 6, and 8 days of incubation. The daily growth rates (mm/day) were calculated from the linear regression equation:

$$r = at + b \qquad \textbf{(2.4)}$$

Where ‘‘r’’ is colony radius (mm); ‘‘t’’ is incubation time (day), ‘‘a’’ is daily growth rate, and ‘‘b’’ is growth retardation time (lag phase; λ). This activity where analyzed as well as the appearance (color, the droplets) of fungus colonies.

2.4.6. Study of Stability of the Photocatalyst Under Visible Light

The stability of the material was studied after cycling. The photocatalytic activity of the as-prepared $Au_{0.5\%}$/P25 and $CuO_{0.5\%}$/P25 samples were studied for the photodecomposition of phenol, used as model pollutant in water (50 ppm) in a suspension (1 mg/1 mL). The photodegradation was carried out in Pyrex tube reactor containing 15 mL of the phenol solution and 15 mg of a photocatalyst. Before irradiation, the photocatalyst was dispersed in the solution by sonication for 30 s, and then the suspension was stirred (magnetic stirring) for 30 min in dark to ensure the equilibrium between adsorption and desorption. Then the solution was irradiated using a xenon lamp (Oriel 300 W) with a cut-off filter (AM-32603-1, LOT-Oriel) for experiments carried out under visible light ($\lambda > 450$ nm). The photocatalytic tests were conducted under oxygen bubbling at a fixed rate flow. Aliquots of 1 mL were sampled from the reactor at the point of absorption and after 8 h of irradiation. The powder was separated by centrifugation and dried at 60 °C, over night the collected sample was weighted and reused at the same ratio 1 mg/1 mL, then the resultant transparent supernatant (obtained after centrifugation) in each case was analyzed by HPLC.

Chapter III

Surface Modification of TiO_2-P25 with Au Nanoparticles

Chapter 3. Surface Modification of TiO_2-P25 with Au Nanoparticles

3.1. Introduction

Gold nanoparticles (Au-NPs) have attracted much attention due to their Localized Surface Plasmon Resonance (LSPR) in the visible (and near infrared for anisotropic nanoparticles), that is, the oscillation of metal free electrons in constructive interference with the electric field of the incident light. These plasmonic properties can be used to induce a photocatalytic activity of the semiconductor material under visible light.[4]

Extensive research has been performed with the Au/TiO_2 system, because the addition of Au-NPs on the surface of TiO_2 brings several benefits to the photocatalyst. First, Au-NPs can enhance the visible light absorption of the TiO_2 and this effect has been attributed to the interaction of the LSPR of the Au-NPs and the optical band of the semiconductor. Second, an electric field is created by the LSPR. This electric field may power the generation of more electrons and holes, and heat up the surrounding environment, inducing an increase of the redox reaction rates and the mass transfer, and also a polarization of the nonpolar molecules for better adsorption. Another interesting property is the Schottky junction due to the contact between the Au-NPs and the semiconductor TiO_2. This barrier creates an internal electric field close to the metal-semiconductor interface and force the transfer of the electrons-holes in different directions, and so the metal provides a fast lane for charge transfer, retarding the recombination process.[2]

The LSPR and Schottky junction properties are characteristic of the plasmonic photocatalysts and metal nanoparticles, and are, in fact, the main properties responsible of the enhancement of the photoactivity of the Au/TiO2 system.[3,4] Therefore, TiO_2 has been modified with Au-NPs for several applications such as oxidation of organic molecules, selective oxidation of aromatic alcohols to carbonyl compounds, hydrogen formation from alcohols, and selective reduction of organic compounds.[10] In recent years, the applications of plasmonic photocatalysts have focused on the generation of hydrogen[9] and in wastewater treatment[8] since they provide a promising and environmentally friendly way to perform these processes at low-cost using visible light, or in the best of the cases, leveraging the sunlight.

Gold in bulk is chemically inert and has been regarded to be poorly active as a catalyst until the pioneer work of Haruta *et al*. who have shown that small gold nanoparticles (diameters bellow 5 nm) were very active for CO oxidation.[105] This discovery has opened the door to the field of catalysis by gold.[106,107,108]

The presence of Au is essential, but the support also plays an important effect in the case of TiO_2, which presents two principal crystalline forms, *i.e.*, anatase and rutile. And these two forms play an important role: 1. Electron-hole recombination for anatase and rutile particles has been studied and this recombination process, has been found to be higher for rutile than anatase phase.[42,43,103,109] 2. The higher Fermi level of anatase can result in stronger electronic interaction with Au-NPs, which can inhibit the growth and agglomeration of metal nanoparticle.[110] 3. The difference in energy band gap of anatase (3.2 eV) and rutile (3.0 eV)[111] that could result in activation of TiO_2 at longer wavelengths for rutile.[112] 4. The dielectric constant of the support could shift the LSPR of metal nanoparticles toward the red spectral region.[2,113] For example, it was shown that crystalline composition and surface properties of Au-TiO_2 photocatalysts, prepared by photodeposition of gold on fifteen commercial titania, influenced significantly resultant photocatalytic activities in a different manner under UV and visible light irradiation.[74] Under UV irradiation, the presence of gold results in high enhancement of photocatalytic decomposition of acetic acid for all modified samples. On the other hand, under visible light irradiation, mainly Au-TiO_2 samples possessing large crystallites of rutile exhibited the highest level of photocatalytic activity.[74] It was proposed that polydispersity of gold deposits, *i.e.*, various sizes and shapes (nanoparticles, nanorods) results in broad LSPR and therefore in higher overall photocatalytic activity than that of Au-TiO_2 of fine gold NPs with narrow LSPR.

In this chapter, we report an active Au/TiO_2 system prepared according the Duff and Baiker method[104] with three different loadings of Au-NPs: 0.5, 1, and 2 wt%, using commercial P25 as TiO_2 material. The photocatalytic activity of these plasmonic photocatalysts has been studied for different processes: water treatment with the photo-oxidation reactions (phenol, 2-propanol and acetic acid oxidations) and the photoreduction for hydrogen generation by PWS process.

3.2 Materials Characterization

TEM observations show small gold nanoparticles homogeneously dispersed on TiO_2-P25 surface for all the modified titania samples. In all the cases, the Au-NPs are smaller than 5 nm of diameter, with a mean size of around 2-3 nm, and with the increase of Au loading, a slightly larger particle size is observed (see **Figure III-1** and **Table 3**).

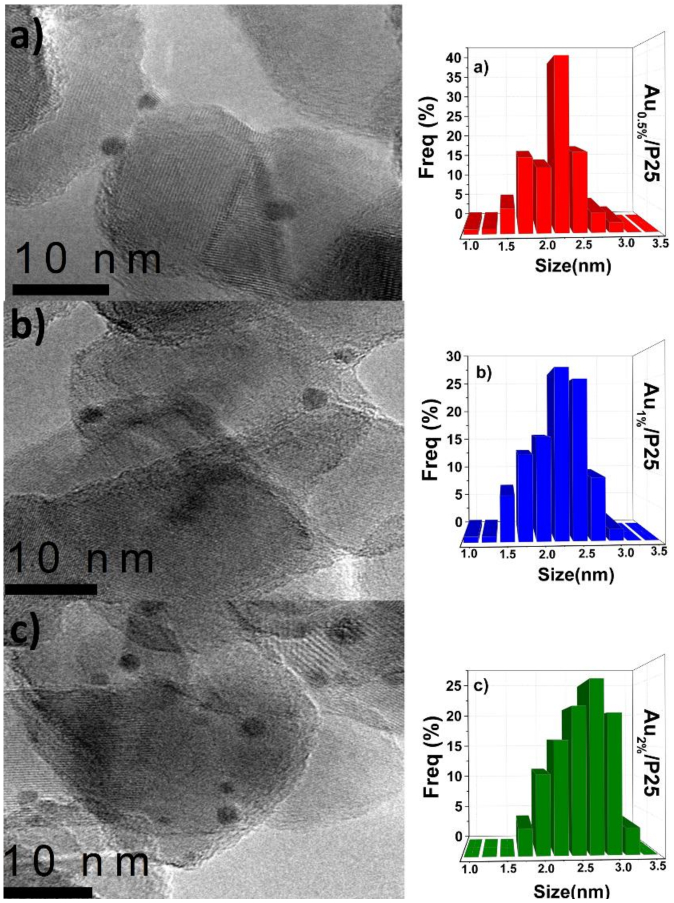

Figure III-1. *TEM images of* ***a)*** *$Au_{0.5\%}$/P25;* ***b)*** *$Au_{1\%}$/P25;* ***c)*** *$Au_{2\%}$/P25, with the corresponding histograms of size distribution of Au-NPs.*

Table 3. *Characteristics of the photocatalysts Au/P25 prepared by a chemical method with THPC.*

Photocatalyst	Theoretical Weight w%	Color of sample	TEM Average Size (nm)*
$Au_{0.5\%}$/P25	0.5%	Light-purple	2.0
$Au_{1\%}$/P25	1%	Purple	2.0
$Au_{2\%}$/P25	2%	Dark-purple	2.0

*TEM size was measured manually with the *Digital Micrograph* software.

In the HRTEM images (**Figure III-2**), the anatase and rutile phases of TiO_2-P25 were identified based on the interplanar distances determined using the *Digital Micrograph* software. HRTEM images show that the Au-NPs tend to be located on the anatase phase after thermal treatment of 500 °C. This result is in agreement with literature results. Tuskamoto *et al.* and Wen *et al*. reported that gold nanoparticles have different localization on P25 (anatase or rutile) depending on the temperature treatment.[114,115] The increase of the calcination temperature have an effect in the location and particle size of Au-NPs, showing bigger sizes and interphase preference location. The interplanar spacing (*d*) deduced by the fast Fourier Transform (FFT) technique (see **Figure III-2d**) was found to be equal to *d* = 0.20 nm, which corresponds to the interplanar distance for (111) planes of Au, according to PDF No. 01-1174.

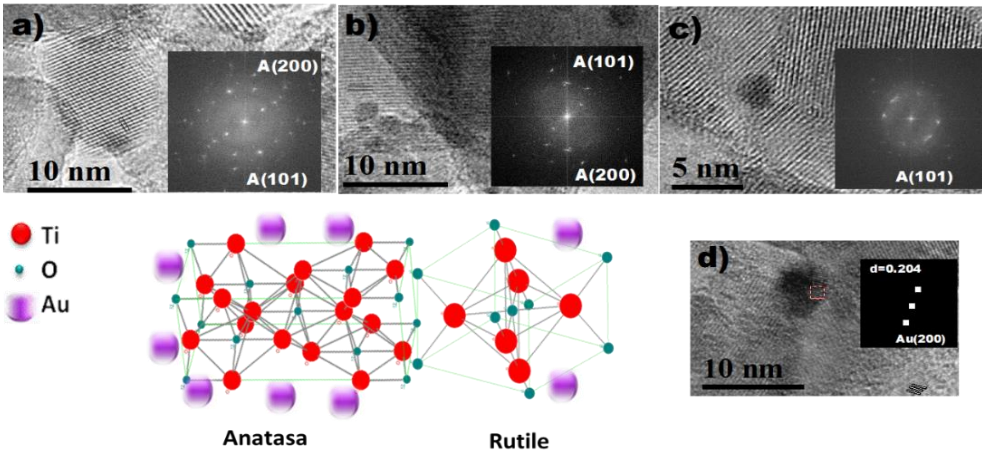

Figure III-2. *HRTEM images of* ***a)*** *$Au_{0.5\%}$ /P25;* ***b)*** *$Au_{1\%}$/P25;* ***c)*** *$Au_{2\%}$/P25, localization of Au-NPs on the surface of the TiO_2-P25 and* ***d)*** *HRTEM image of Au-NPs with FFT (fast Fourier transform) images for the plane of Au.*

Figure III-3 shows the XRD patterns of the as-prepared Au/P25 samples: The characteristic diffraction peaks of anatase and rutile phases of TiO_2-P25, according the data JCPDS files No 21-1272 and No. 21-1276, respectively, are observed for all the samples.[116] For the Au/P25 samples, the patterns show also peaks attributed to the Au-diffraction planes (111), (200) and (220), according the JCPDS No.01-1174. As expected, the intensity of the observed peaks for Au planes is increasing with the amount of gold.

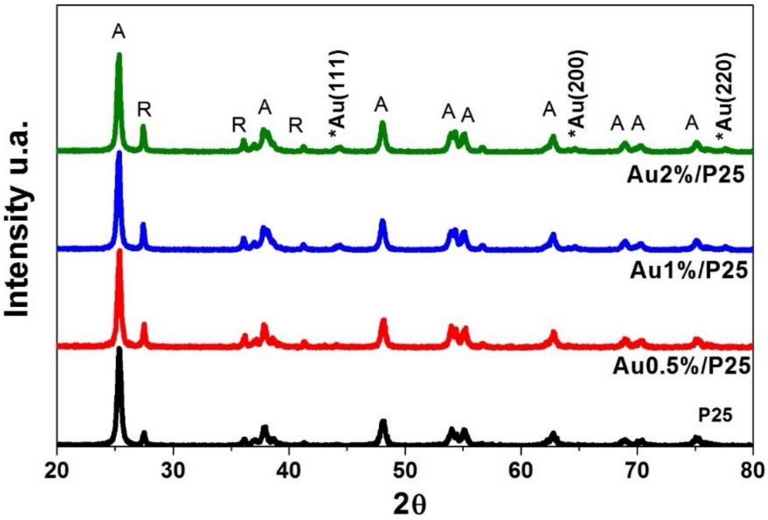

Figure III-3. *XRD patterns of P25 and of the as-synthesized Au/P25 samples.*

The dependences of Au particle sizes on the support have been attributed to the differences in metal/support interaction[117] as it has been reported by Murdoch *et al*. Au-NPs supported on anatase are smaller than Au-NPs supported on rutile.[110] The higher Fermi level of anatase can result in stronger electronic interactions with Au-NPs, which can inhibit Au agglomeration, leading also to smaller Au-NPs.[110]

In order to analyze the chemical composition of the modified TiO_2-P25 and to identify the chemical state of Au-NPs, we have performed XPS analyses. The Ti *2p* peaks are characteristic of Ti^{4+} in TiO_2 with two main components at 458.4 and 464.5 eV associated with Ti $2p_{3/2}$ and Ti $2p_{1/2}$ orbitals and the O *1s* peaks at 529.6 eV attributed to oxygen of TiO_2. XPS spectra attested the metallic nature of Au-NPs, as shown in **Figure III-4**. The Au $4f_{7/2}$ core levels present their binding energy (BE) in the Au (84 eV), the same value of the metallic state of Au^0 (84 eV). Other contributions appear at 84.6 and 83.4 eV and correspond to Au^{3+} and Au^{0} species, respectively.[118] Au signal presents a specific low BE position, which has already been reported in literature.[8,75,119]

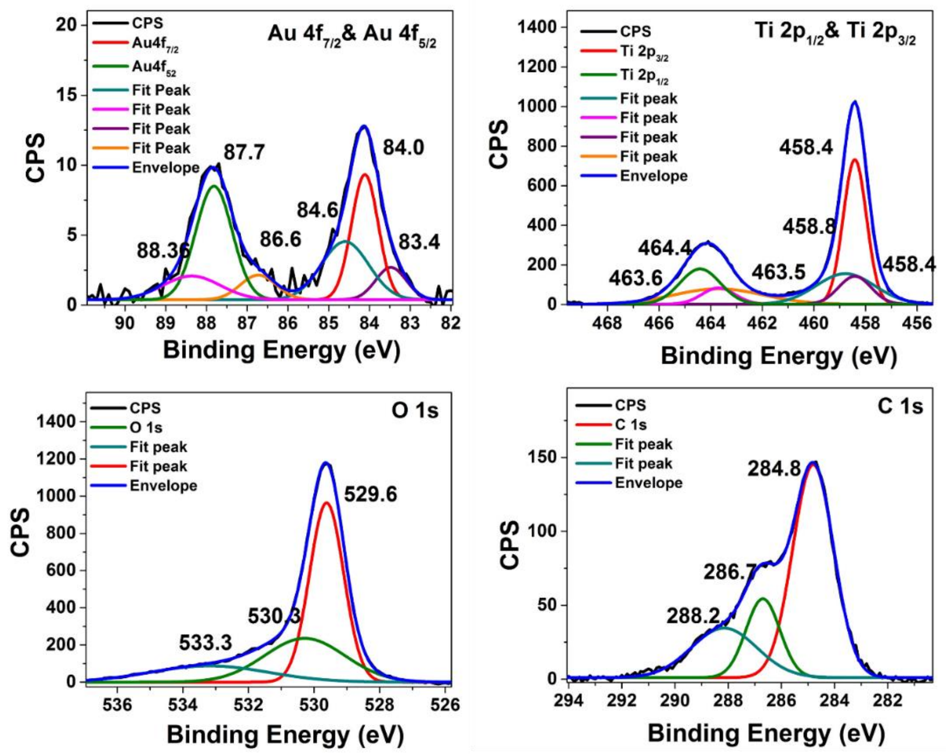

Figure III-4. *XPS spectra of Au$_{0.5\%}$/P25, binding energy of Au 4f peaks, Ti 2p peaks, O 1s peak and the C 1s peak.*

The optical properties of the modified surface of TiO$_2$-P25 were studied by DRS. In **Figure III-5**, the spectrum of TiO$_2$-P25 shows an absorption edge at around 400 nm due to the presence of rutile.[112] The photoabsorption properties of Au/P25 materials are higher than that of pure TiO$_2$-P25, since the Au-NPs induce a shift of the absorbance toward the visible light attributed to the interaction between the metal and the semiconductor, *i.e.*, the so-called Schottky barrier[120] and because of the plasmon of gold. The position of the LSPR peak of the Au-NPs at 520 nm for 13-nm gold NP, in aqueous solution is sensitive to the dielectric constant of the surrounding medium.[2,113] This shift in the plasmon is due to the interaction between the Au-NPs and the semiconductor TiO$_2$-P25. Indeed, this plasmon band is sensitive to the size, and environment, and can be shifted depending on the stabilizer or the substrate. Because of the coupling between the metal nanoparticles and TiO_2 support having a high reflective index, the plasmon band in case of modified titania is usually red-shifted, as already reported for Au/TiO_2 (Au NPs < 2 nm size absorb at 410 nm,[121] 560-610 nm[74,115,122]), Ag/TiO_2[6,123,124] and Au-Cu/TiO_2.[8,75] A weak LSPR band from 500 to 650 nm with maximum values at 548, 554 and 560 nm for Au0.5%, Au1% and Au 2% respectively, are observed in **Figure III-5**, due to the plasmon of small nanoclusters.[114,115] These absorptions result in a pink-purple color of the modified TiO_2-P25 samples. It has to be noted that the LSPR maximum absorption peaks are located at different values, which is consistent with the fact that the size of the Au-NPs present a slightly increase for the different loadings, as it was previously observed by TEM images.

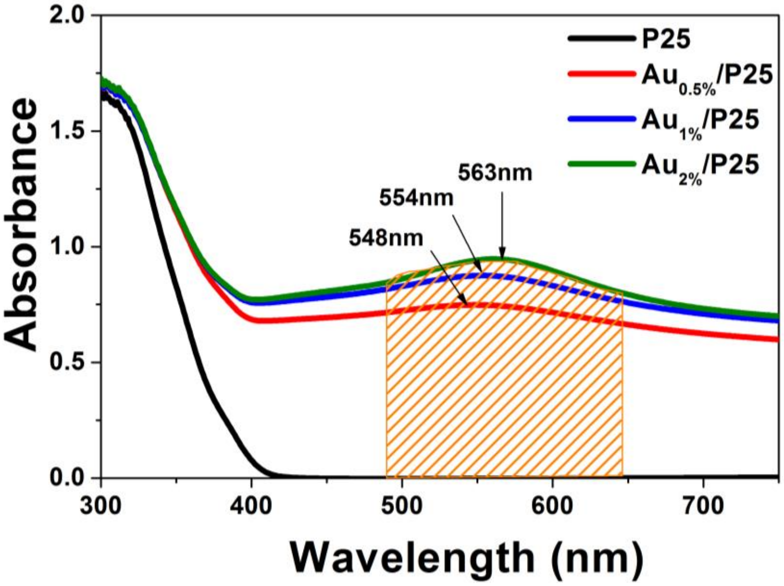

Figure III-5. *DRS spectra of Au/P25 samples, where the LSPR of the Au-NPs is observed between marked lines.*

The electronic properties of the samples were studied by the TRMC technique at different excitation wavelengths considering both the UV and visible regions. The samples were excited at different wavelengths of 365, 400, 450, 470, 500, 550, and 560 nm. The corresponding laser energies were 1.4, 0.7, 6.1, 5.7, 5.3 and 3.7 mJ.cm^{-2} respectively, to study the charge carrier dynamics under UV and visible light irradiation, with a particular attention paid to excitation energy close to the plasmon of gold. The corresponding TRMC signals are shown in **Figure III-6**. The surface modification with Au-NPs shows a strong influence on the charge-carriers dynamics in TiO_2-P25.

At 365 nm, the intensity of the signal I_{max} for the modified TiO_2-P25 is lower than for pure TiO_2-P25, especially for the case with lower loadings in gold, *i.e.*, 0.5% and 1%. These results indicate that a lower amount of free electrons is generated (lower I_{max} value) in the conduction band of the modified semiconductor, and that the life time of photogenerated electrons in the samples is shortened, or the recombination is retarded (the decrease of the signal is less pronounced), than for pure TiO_2-P25. On the normalized signals (**Figure III-6a** inset), one can see that the decay of the signal is faster in case of modified TiO_2-P25, which means that the electrons are trapped by the Au-NPs. Metal NPs deposited on TiO_2 act as electron scavengers, decreasing the recombination process.[6,8,75] At excitation wavelength of 400 nm (the limit between the UV and the visible regions), for all the photocatalysts, the I_{max} values are lower than those obtained under excitation at 365 nm as expected. Indeed, since the irradiation energy is lower that the band-gap of anatase, only the rutile phase, which is in minority, is activated. However, the samples containing gold reach a lower I_{max} values, which represent a lower amount of free electrons in the conduction band of TiO_2-P25. Au-NPs deposited in TiO_2-P25 work as electron scavengers at this wavelength.

At 450 nm excitation wavelength, the TRMC signals for bare and modified TiO_2-P25 are very similar, indicating that the electron dynamics with and without Au-NPs are quite similar. But, when the samples were irradiated at 470 nm, 500 nm and 550 nm close to the plasmon of gold, a small TRMC signal is observed for the Au-P25 samples, while for bare-P25 no signal is obtained attesting the generation of free electrons in the conduction band of the Au-modified TiO_2-P25. This suggests that excess electrons are injected in the conduction band of TiO_2-P25 after excitation of the Au nanoparticles at a wavelength very close (or equal) to their LSPR. So that, under visible light, the electrons of the metal NPs are excited, and are then driven towards the conduction band of the TiO_2-P25.

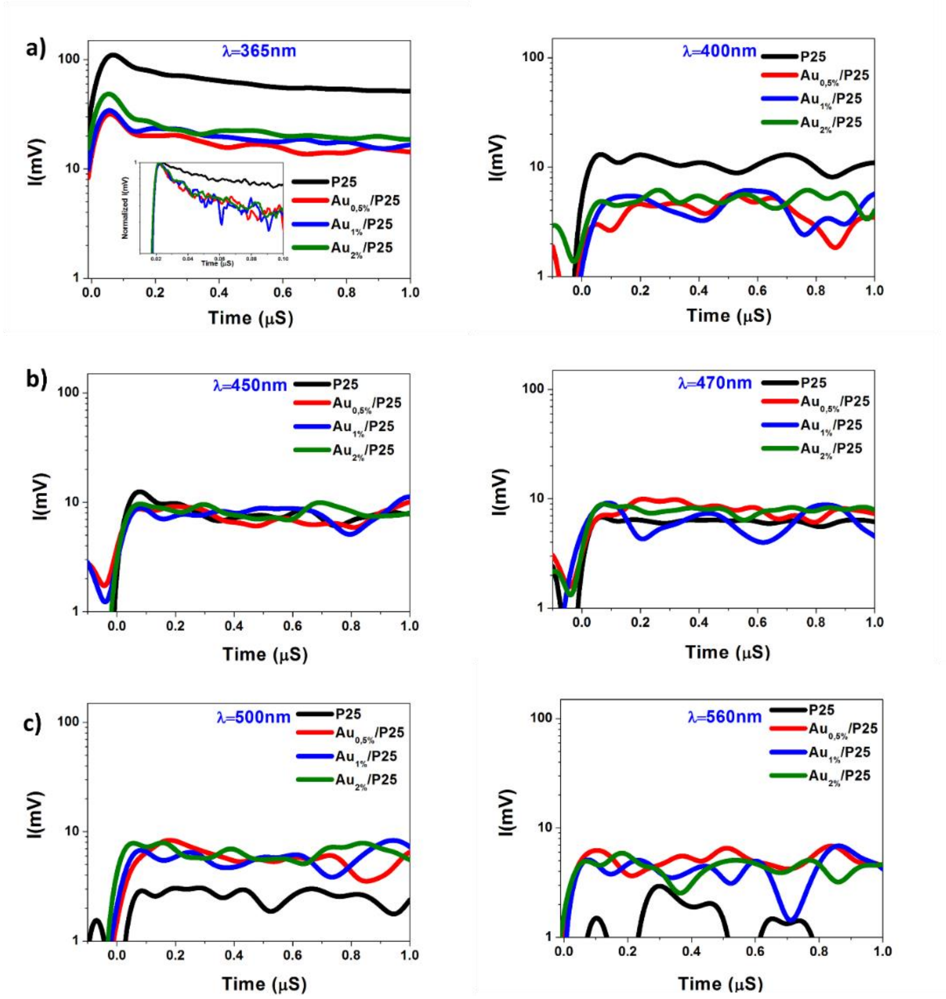

Figure III-6. *TRMC signals of pristine and modified TiO*$_2$*-P25 at different excitation wavelengths:* ***a)*** *365 nm and 400 nm UV irradiation,* ***b)*** *450 nm and 470 nm visible irradiation and* ***c)*** *500 nm and 560 nm (Plasmon excitation).*

3.3 Photocatalysic Tests

3.3.1. Phenol Degradation Under UV and Visible Light

The photoactivity of the modified TiO$_2$-P25 samples was evaluated for the degradation of phenol under UV and visible light.

The bare and the modified TiO$_2$-P25 with Au-NPs present quite similar activity in the degradation of phenol under UV light (see **Figure III-7a**), only the sample with the lower amount of Au presents a slightly higher activity.

Under visible light, the presence of gold induced an increase in the photocatalytic activity as shown in **Figure III-7b**: TiO_2-P25 achieves a degradation of phenol of 7% after 4 h of exposure to visible light irradiation, while the $Au_{0.5\%}$/P25 sample reaches a degradation of 19% after the same irradiation time. However, the photoactivity of Au-P25 is reduced when the gold loading is increased (see **Figure III-7**), and the highest degradation rate is obtained with the $Au_{0.5\%}$/P25 sample (see Table 4).

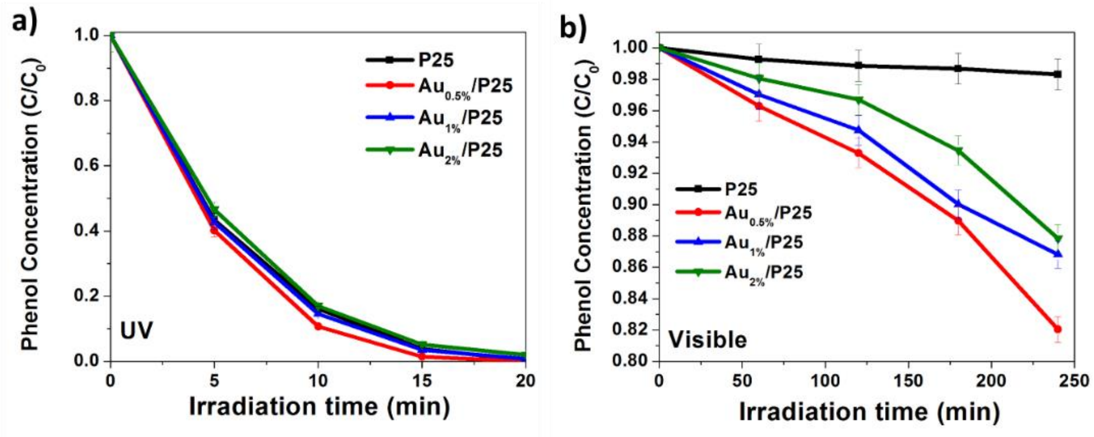

Figure III-7. *Degradation curves of phenol (50 ppm) under* ***a)*** *UV and* ***b)*** *visible light (λ≥450nm) for bare TiO_2-P25 and TiO_2-P25 modified with Au-NPs with different Au loadings, in the ratio $1gL^{-1}$.*

It is clear that at low loading of gold, very small Au-NPs (< 5 nm) are obtained on the anatase phase of TiO_2-P25 inducing an enhancement of the photocatalytic activity of TiO_2-P25 for phenol degradation in water. The corresponding kinetics data for the degradation of phenol under UV and visible light are shown in **Table 4**. Under UV light phenol decay seems to be exponential and the fit using the calculation in the **Appendix V** is well-matched with the kinetics of pseudo-first order. Under Visible light decay it seems to be more linear, following the calculation in **Appendix V** we suggest a pseudo-zero order of reaction. Because this fits better the curves. It has to be noted that the $Au_{0.5\%}$/P25 sample shows a rate constant three times higher than bare TiO_2-P25. Surface modification of TiO_2-P25 with very small Au nanoparticles < 5 nm and with a low metal loading induced an enhancement of the pseudo first-order rate constant, as is reported by Orlov *et* *al*.[106,125] Sonawane and Dongare *et al.* have also shown that TiO_2-P25 modification with Au (1%-2% wt) improved the activity by 2.3 times compared with bare TiO_2-P25.[126] Tsukamoto *et al*. also obtained the highest photocatalytic activity for the aerobic oxidation reactions with the small sizes of Au-NPs (d_{Au} < 5nm) and lower loading of Au (2 wt %); the preference location of Au-NPs in this case was at the interface of anatase and rutile.[114]

Table 4. *Photocatalytic rates constant for phenol degradation using different Au loading under UV irradiation (pseudo first order reaction) and visible light (zero order reaction).*

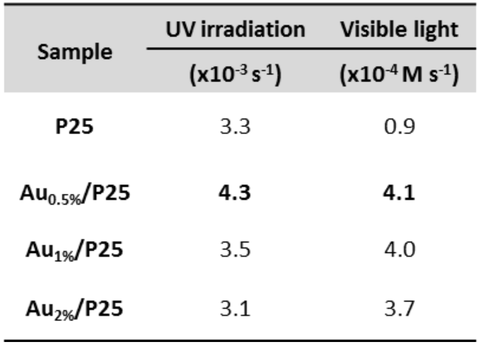

Sample	UV irradiation	Visible light
	($x10^{-3}$ s^{-1})	($x10^{-4}$ M s^{-1})
P25	3.3	0.9
$Au_{0.5\%}$/P25	**4.3**	**4.1**
$Au_{1\%}$/P25	3.5	4.0
$Au_{2\%}$/P25	3.1	3.7

3.3.2. 2-Propanol Degradation Under Visible Irradiation

These modified TiO_2-P25 samples show also a high photocatalytic activity for oxidation of 2-propanol under visible light (λ ≥ 450 nm). In this reaction, only acetone is detected as product,[127] following the reaction shown in **Eq. 2.1.** This means that the small Au-NPs with a preferential localization on anatase phase present activity under visible light. The sample $Au_{0.5\%}$/P25 presents again the highest activity, and this activity decreases with the Au loading as is shown in **Figure III-8**. It is well known that a high amount of metal loading strongly affects the activity of plasmonic photocatalysts.

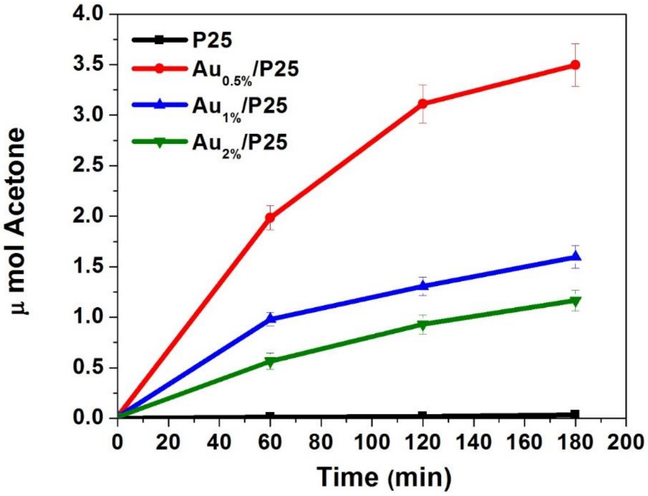

Figure III-8. *2-propanol oxidation (5 v%) under visible irradiation (λ ≥ 450nm) on TiO_2-P25 and modified TiO_2-P25 in a ratio 10 gL^{-1}.*

3.3.3. Acetic Acid Degradation — Action Spectrum

The photocatalytic activity of $Au_{0.5\%}$/P25 was evaluated for the decomposition of acetic acid under monochromatic irradiations in order to obtain the action spectrum or the quantum yield per unit of incident photons as a function of the wavelength. The decomposition is carried out in the aerated aqueous solution according to the following reaction:

$$CH_3COOH + 2O_2 \rightarrow 2CO_2 + 2H_2O \qquad \textbf{2.2}$$

We followed the photocatalytic evolution of CO_2, which is the result of the decomposition of acetic acid. Exemplary data for different irradiation wavelengths, *i.e.*, UV at λ = 350 nm, and visible light at λ = 470, 530, 590, and 650 nm are shown in **Figure III-9a**. **Figure III-9b** shows the action spectrum of TiO_2-P25 and modified TiO_2-P25 for the oxidation of acetic acid.

The Au-modified TiO_2-P25 samples present higher generation of CO_2 at 350 nm and in the visible range as shown in **Figure III-9a**. It is possible to correlate these results with TRMC signals at 365 nm, where the presence of Au-NPs induces a decrease of the signal of electrons in the conduction band of the semiconductor retarding the recombination process and increasing the photoactivity as shown for the phenol degradation. Under visible light irradiation, surface modified TiO_2-P25 with Au-NPs are also more active in the production of CO_2 compared to bare TiO_2-P25. These results confirm that surface modification with the plasmonic Au metal nanoparticles improves significantly the activity of the semiconductor TiO_2-P25 in the visible range, confirming the previous findings with Au/TiO_2, Ag/TiO_2 and Ag-Au/TiO_2 obtained with larger size metal nanoparticles.[81] This photocatalytic activity can be related to the TRMC signals obtained for visible light excitation and indicates that electrons are generated in the conduction band of Au-modified TiO_2-P25 due to the excitation of the LSPR.

The photodecomposition of acetic acid decreased rapidly with increasing the wavelength of the incident light. These results suggest that the apparent quantum efficiency (calculated with **Eq. 2.3**, as it is shown in **Figure III-9b**.) for decomposition of acetic acid is lower under visible light than under UV. In the visible range, the samples modified with Au-NPs show higher apparent quantum efficiency in the range between 450–650 nm, which is related to the LSPR.

$$\phi_{\text{app}} = \frac{\text{reaction rate of } \mathrm{CO_2} \text{ generation (mol/s)}}{\text{light Flux (mol/s)}} \times 100 \qquad (2.3)$$

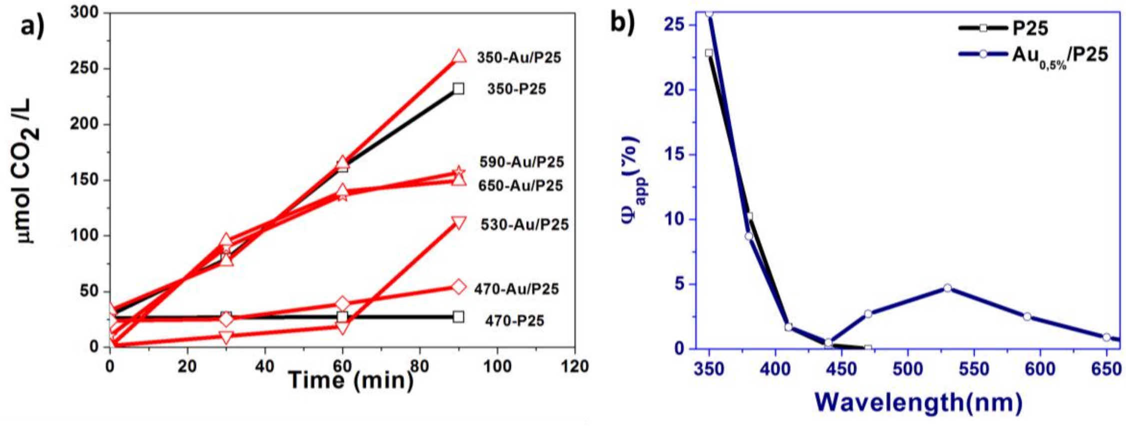

Figure III-9. a) *Photocatalytic evolution of CO_2 resulting from the decomposition of acetic acid (5 v%) using TiO_2-P25 and modified TiO_2-P25 with Au0.5wt%, in a ratio 10 gL^{-1}* ***b)*** *Action spectrum for the decomposition of acetic acid with $Au_{0.5\%}$/P25 and pure TiO_2-P25 samples.*

A comparison between the action spectra and the absorption spectrum obtained by DRS is shown in **Figure III-10**. The action spectrum presents a shift toward the blue and this is related to the conditions of the sample (one is measured in powder and the other is measured in water dispersion).

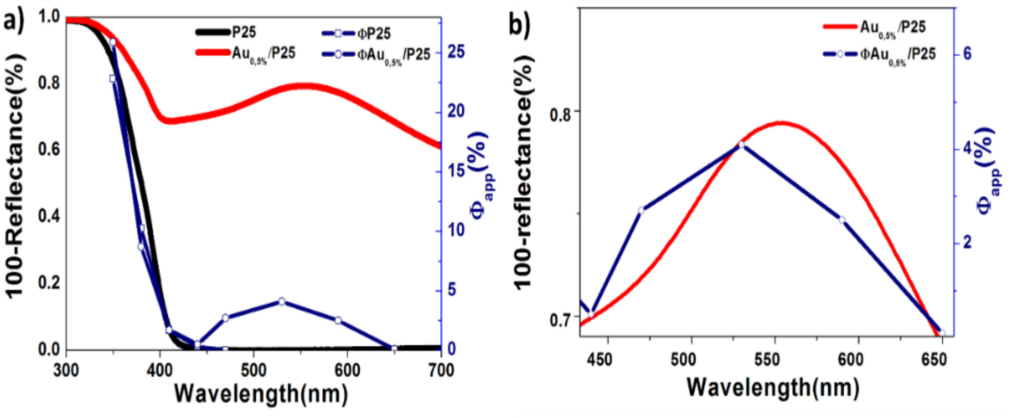

Figure III-10. *Comparison between DRS spectra and the action spectrum of* ***a)*** *TiO_2-P25 and modified TiO_2-P25 with Au0.5wt% and* ***b)*** *LSPR correlation, of visible absorption with the Φ_{app} of $Au_{0.5\%}$/P25.*

The action spectrum is compared with the DRS spectra[74,114,128] for pure TiO_2-P25 and modified TiO_2-P25 with Au0.5wt%, and an appreciable response is obtained under UV and visible light and confirmed that the LSPR band of Au is very well correlated with the apparent quantum efficiency (Φ_{app}). This correlation indicates that the photoreaction is carried out by a photocatalytic mechanism under UV and visible light.

3.3.4. Photocatalytic Production of Hydrogen (H_2)

In the case of PWS process by photocatalysis, electrons in the conduction band reduce hydrogen ions to H_2, and holes in the valence band can oxidize oxygen ions to O_2: The main drawback of the PWS process by photocatalysis is the low H_2 production due to the fast recombination of the charge-carriers.[9,129,130] For H_2 production tests under λ = 400 nm and 470 nm, the addition of Au-NPs activate TiO_2-P25 as shown in graphs of **Figure III-11**, where a considerable higher amount of H_2 is produced with Au/P25 samples, compared to the amount produced with bare TiO_2-P25. For the tests performed at 400 nm (See **Figure III-11a**), the activity for H_2 production decreases with the Au-loading and the highest photocatalytic activity is obtained with $Au_{0.5\%}$/P25 (17.5 µmol g^{-1} s^{-1} or 1.05 mM g^{-1} h^{-1}). Here, as we discussed before, excess of Au-NPs on TiO_2-P25 could act as recombination centers of photo-generated charges reducing the photocatalytic activity in H_2 production. Under visible irradiation, at 470 nm [**Figure III-11b**], only a small amount of H_2 is obtained (0.23 µmol g^{-1} s^{-1}) with the Au/P25 samples. Similar results have been reported by Joo *et al.* in the range of 300-600 nm using methanol as a hole scavenger (~4 µmol g^{-1} s^{-1} using Au/P25 and around 0.2 µmol g^{-1} s^{-1} using Au@SiO_2 (Thin)/P25).[130] Furthermore, this activity does not depend on the Au loading (**Figure III-11b**).

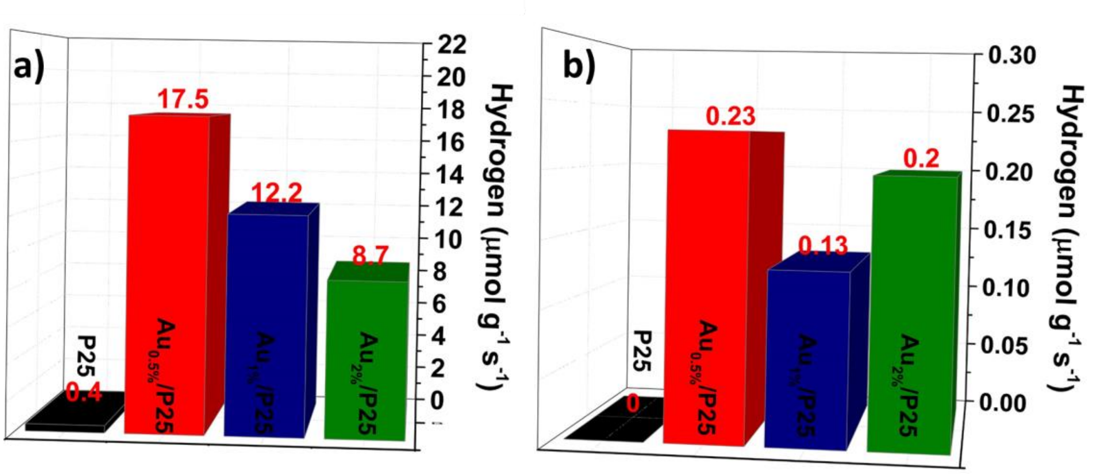

Figure III-11. *Production of H_2 by methanol dehydrogenation (25 v%) under* ***a)*** *visible light (λ = 400 nm) and* ***b)*** *visible light (λ = 470 nm) for pure TiO_2-P25 and TiO_2-P25 modified with Au-NPs at different loading, in a ratio of 1 gL^{-1}.*

The maximum of H_2 production by methanol dehydrogenation was obtained with 0.5 wt% of Au under 400 nm and 470 nm. Small gold nanoparticles can induce a much higher change of the Fermi level compared to larger particles, and this change is an indication of a larger charge separation and improved reduction potential for the photocatalysts and metal/TiO_2 interface. Metals with higher work function than that of TiO_2 increase the Schottky barrier effect, which help to lower the electron–hole recombination. The work function of Au is 5.1 eV, which is higher than that of TiO_2 (4.2 eV).[9,131] It has to be noted that the work function of Au NPs slightly decreases with the particle size and is also sensitive to the support, but the charge state of the NPs have higher influence on the work function.[131]

As discussed above, TRMC signals show that the presence of Au-NPs induces under UV irradiation a lower amount of electrons in the conduction band, but present also a faster decay. These results can be interpreted as electron scavenging by the Au-NPs. In the case of visible irradiation, TRMC signals suggest that electrons are injected in the conduction band of TiO_2-P25 due to LSPR of the Au nanoparticles. But TRMC signal also shows faster recombination of electrons in the conduction band. Indeed, Au-NPs can also act as recombination center, and this effect is probably enhanced with Au loading. This effect can explain why the enhancement of the photocatalytic activity is only observed at lower metal loading for the same size of metal NPs.

3.3.5. Mechanism Proposed for TiO_2-P25 Modified with Au-NPs Under UV and Visible Light

Figure III-12a and **Figure III-12b** show the photoinduced mechanisms proposed for TiO_2-P25 modified with Au-NPs, under UV and visible light irradiation respectively. Under UV light excitation, gold nanoparticles on anatase phase work as electron pools retarding the recombination process as supported by the TRMC results. The rate of electron-hole recombination for anatase and rutile particles has been determined and was found to be higher in the case of rutile.[42,43,109] This scavenging phenomenon helps to increase the photoactivity due to the formation of the Schottky junction (due to contact of the metal NPs with the semiconductor TiO_2). At 400 nm, a small TRMC signal is generated due to the activation of the rutile phase. This signal decreases with the modified samples: The Au-NPs are still working as electrons traps, but the Au-NPs can also catalyze the reaction leading to a better activity of the modified samples for the hydrogen production.

Joo *et al.*[130] reported a different mechanism of charge carriers with metal nanoparticles, under UV irradiation for hydrogen generation (reduction reaction) and showed that Au-NPs catalyze the recombination reaction of H radicals producing hydrogen. This mechanism may be also possible with our photocatalysts for hydrogen production, where the enhancement of the photoactivity with the modified samples is appreciable. But, in the other side, in the case of oxidation of organic compounds under UV light, the photoactivity of the modified materials it is a little bit higher or equal than the pure TiO_2-P25. In brief, the Au-NPs could catalyze the reduction reaction, but not the oxidation of organic reactions. In the case of oxidation Au-NPs only play the role of electron traps, retarding the recombination process.

As it was reported by Kowalska *et al*,[74] the mechanisms involved in TiO_2 modified with noble metal NPs under visible irradiation are not really elucidated. Here, the action spectra show that the photocatalytic activity under visible light is directly correlated to the LSPR and TRMC signals show that Au-NPs inject electrons in the conduction band of the semiconductor due to their surface plasmon resonance inducing an activity in the visible. It has to be noted that Carretti *et al*. and Priebe *et al*. have recently detected by EPR, excess electrons in the CB of titania by excitation of plasmonic Au/TiO_2 under visible light. Direct proof for electron transfer has recently been reported by Caretti *et al*. by EPR experiments under UV and visible excitation of Au/TiO_2 photocatalyst.[132] The existence of both trapped electrons (Ti^{+3}) and holes (O^-) were observed under UV excitation, but only trapped electrons under visible excitation were observed confirming that electron transfer was the main mechanism of plasmonic titania activation. Similar EPR results were obtained by Priebe *et al*., *i.e.*, transfer of electrons from Au NPs and their trapping by Ti^{+4} lattice or surface oxygen vacancies.[133]

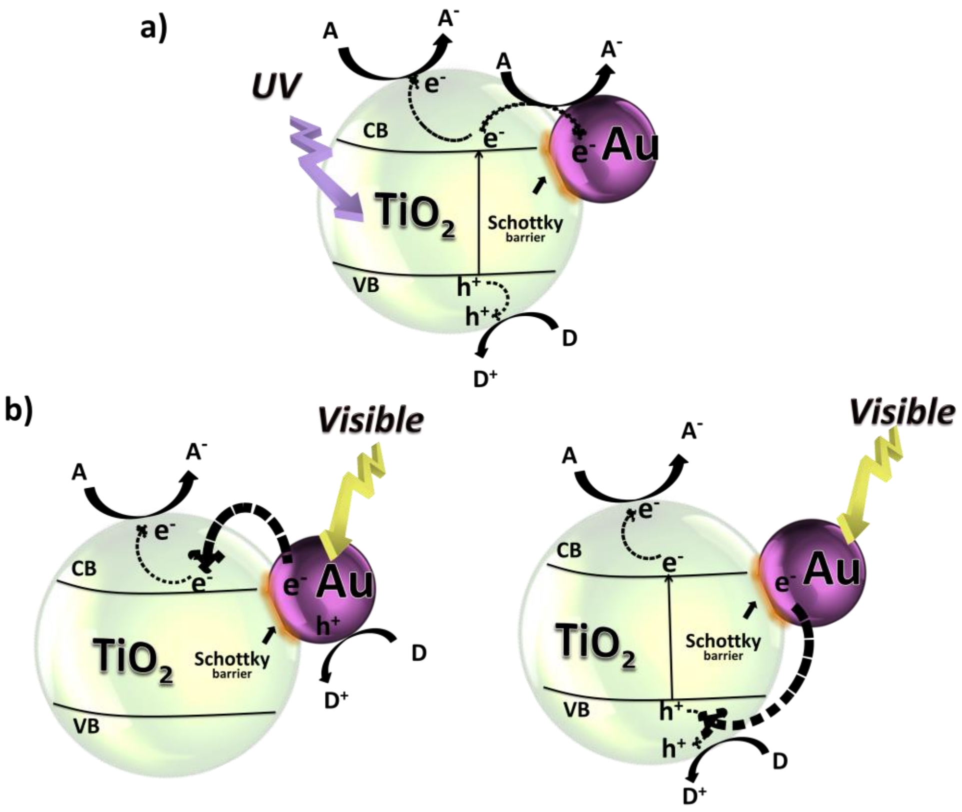

Figure III-12. *Proposed mechanism for modified TiO_2 with Au-NPs* ***a)*** *UV and* ***b)*** *visible irradiation by electron and energy transfer.*

The electrons are probably injected from the metal NPs to the CB of TiO_2 by electrons transfer or by energy transfer simultaneously, due to excitation of the LSPR of Au-NPs and this corresponds to a higher photocatalytic activity.

3.3.6. Stability Study of $Au_{0.5\%}$/P25 Synthesized by THPC Method

For applications, it is really important to obtain stable photocatalysts. Therefore, we have tested the stability of our modified titania with cycling. The activity of the sample $Au_{0.5\%}$/P25 for the phenol degradation with cycling is presented in **Figure III-13**. The photoactivity decrease no so fast after several cycles. These results show that the composite $Au_{0.5\%}$/P25 (with small Au-NPs localized on anatase phase) is stable and can be efficiently reused after repeated cycles. In dark, no phenol degradation was detected, and this attests that the Au/TiO_2 materials are not catalytically active at least for the first step of oxidation reaction. However, this test cannot exclude that Au-NPs are not acting as catalysts in the other oxidation steps. (see **Figure III-13**).

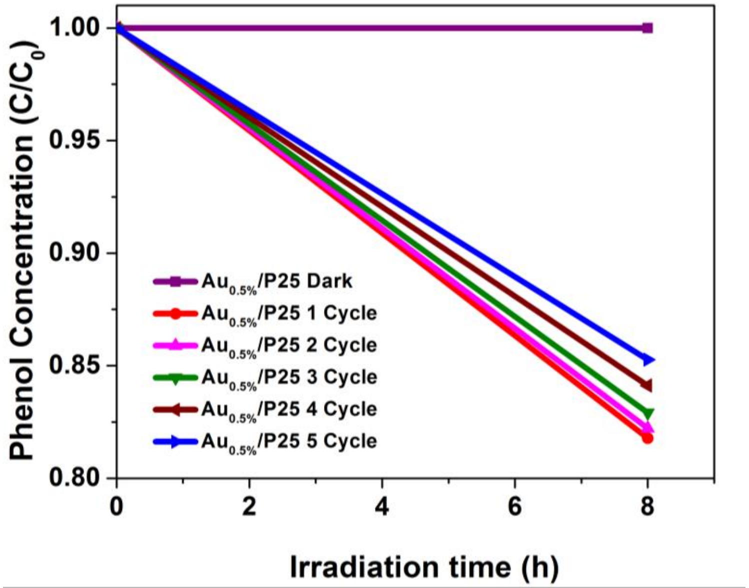

Figure III-13. *Recycling of Au$_{0.5\%}$/P25, photocatalytic phenol degradation (50 ppm) after five cycles under visible light irradiation during 8h irradiation.*

No differences have been found in the metallic state of Au-NPs after repeating cycling. The XPS analysis (**Figure III-14a**) show the same binding energy for Au $4f_{7/2}$ core levels (84 eV). The position range is in agreement with the Au(0) chemical state. TEM observations show that the size of the Au-NPs increases after repeating cycling as it is shown in the histogram in **Figure III-14b**. It has to be noted that this increment in size of Au-NPs with cycling is known in the field of catalysis.[134] The size is principally in the range of 3-5 nm. The Au-NPs are still on the anatase phase (see **Figure III-14c**). HRTEM and STEM-BF images of Au$_{0.5\%}$/P25 before and after cycling (**Figure III-14d** and **e**) show that after cycling larger Au NPs are obtained.

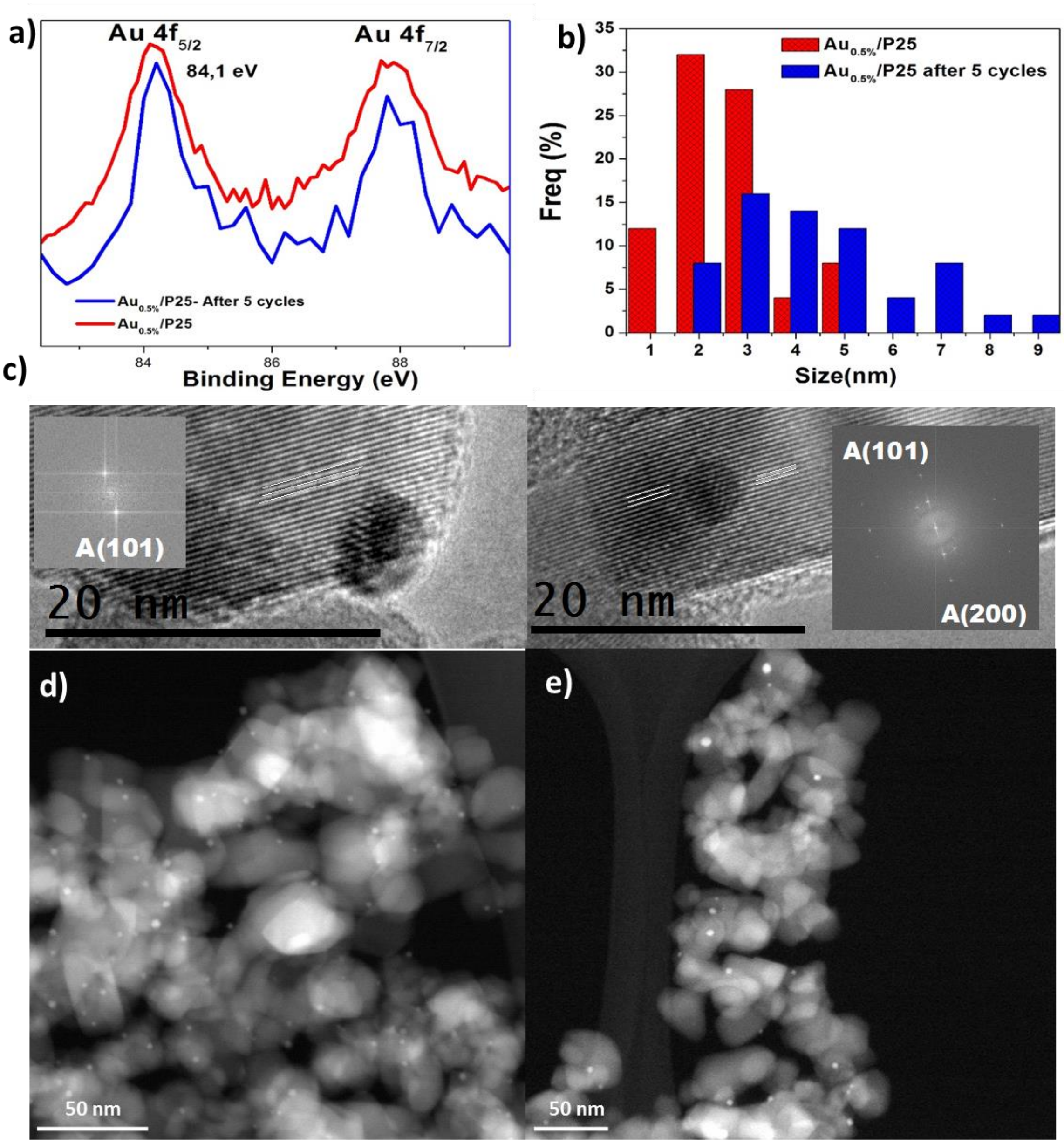

Figure III-14. a) *Binding energy of Au 4f peaks, of Au$_{0.5\%}$/P25, and Au$_{0.5\%}$/P25 after 5 cycles of phenol degradation,* ***b)*** *Histogram of Au-NPs after 5 photocatalytic cycles,* ***c)*** *HRTEM images showing the localization of the Au-NPs on the surface of TiO$_2$-P25 after cycling,* ***d)*** *STEM-BF images of Au$_{0.5\%}$/P25 particles before and after catalytic cycles; and* ***e)*** *STEM-BF image of Au$_{0.5\%}$/P25 particles after 5 cycles.*

These results attest that the Au/P25 systems are stable photocatalysts, which can be reused several times without appreciable change in structure, activity or composition.

3.4. Conclusions

The Au-NPs synthesized on titania by THPC method are small (around 2 nm) and they are principally located on the anatase phase, the more active phase of TiO_2-P25. The as-prepared photocatalysts show a high activity under UV and visible light for oxidation of organic pollutants (phenol, 2-propanol and acetic acid oxidation) and for reduction in the process of hydrogen production. The TRMC results show that under UV irradiation, the Au-NPs work as electron pools retarding the recombination process, and that under visible excitation electrons are injected in the conduction band of TiO_2-P25. In correlation with the action spectra, the modified samples present higher quantum yield, in the UV and visible range, as it is shown for CO_2 production from acetic acid degradation.

Under visible irradiation, the modified photocatalysts absorb incident photons due to the LSPR of Au as it is shown with action spectra and TRMC signals, which demonstrate that under visible light irradiation the modified samples present electrons in the CB of TiO_2 after excitation of the Au nanoparticles at a wavelength very close (or equal) to their LSPR. The highest photoactivity is obtained with lower Au loading ($Au_{0.5\%}$/P25). The action spectra prove that the photoactivity is related to the LSPR of Au-NPs, due to the correlation of the quantum efficiency with the absorption spectra. This result proves that the decomposition of acetic acid is driven by a photocatalytic reaction, and that surface modification with Au results in an enhancement of quantum yield under visible light irradiation in the range of the LSPR. THPC method leads to stable plasmonic photocatalysts, which can be reused several times without appreciable loss of activity.

Chapter IV

Surface Modification of TiO_2-P25 with CuO Nanoclusters

Chapter 4. Surface Modification of TiO_2-P25 with CuO Nanoclusters

4.1. Introduction

TiO_2 is the most commonly used photocatalyst and to enhance its photocatalytic activity under UV and visible light, it is often doped (with N, C, S…) or modified with metal nanoparticles (such as, Au, Ag, Cu…) and other semiconductor (SC) (such as ZrO, ZnS, CdS, WO_3). The junction with semiconductors with a narrow band gap (NBG-SC) resulted in the so called "*multiphase heterojuntion materials*", that have resulted in some advantages, such as: *i)* photoactivity under visible irradiation, *ii)* better charge carrier separation,[135] *iii)* lower cost than the metal modification, *iv)* possibility of co-catalysis of the redox-reactions.[136]

The coupling of TiO_2 (*n*-type semiconductor, band gap of 3.0 eV — 3 .2 eV) with copper oxide (*p*-type semiconductor, with a narrow band gap of 1.7 eV)[47] results in a heterojuntion *Type II* (optimum band position for efficient charge-carrier separation, from **Ch. 1**) That could overcome its limitations in terms of visible light absorption and charge carriers recombination, enhancing the photoactivity under UV irradiation but principally under visible irradiation.[137,138] The first described heterojuntion *Type II* and most investigated photocatalyst multicomponent heretojuntion is the CdS/TiO_2 system, reported in 1984 by Serpone *et al*.[46]

However, there are few works focused on the modification of TiO_2 with Cu-based NPs.[8,75,79,] For example, Qiu *et al*., reported that Cu(II) clusters grafted on the surface of semiconductor with narrow band-gap [$(Sr_{1-y}Na_y)$ $(Ti_{1-x}Mo_x)O_3$], act as a co-catalyst to efficiently reduce oxygen molecules (multi-electron reduction).[139]

Xu and Sun reported significant photoactivity for H_2 generation from water/methanol with TiO_2 modified with CuO nanoparticles, and this photocatalytic activity is higher even than that of TiO_2/Pt, being CuO nanoparticles working as electron scavengers and as co-catalysts in the hydrogen production.[136] CuO/TiO_2

are also efficient photocatalysts for wastewater treatment, in the degradation of organic pollutants under visible light.[135] Furthermore, the use of Cu presents some advantages because of its low cost and excellent catalytic and antifungal properties, although nanoparticles of Cu are not stable at nanoscale.[140]

Several chemical and physical routes have been used to prepare composites with TiO_2 as support. In aqueous solution, the methods of preparation involve the impregnation method,[136] the sol-gel technique, hydrothermal methods, and ionizing radiations (γ-rays, X-rays or electron or ion beams). The radiolytic method presents the advantage of using simple physicochemical conditions such as, atmospheric pressure and room temperature, and the absence of contaminants. The method results in homogeneous reduction and nucleation of metal nanoparticles.[91]

In this chapter, we report radiolytic synthesis of CuO nanoclusters (with different loading of Cu: 0.5—2 w%) on TiO_2. The photocatalysts were characterized by different techniques and the photocatalytic activity was evaluated for different reactions: oxidation reactions (degradation) of several organic pollutants and for hydrogen production in a water/methanol mixture.

4.2. Materials Characterization

TEM observations show small Cu-based nanoclusters (around 1-3 nm) homogenously dispersed on the surface of the TiO_2-P25, as it is shown in **Figure IV-1**.

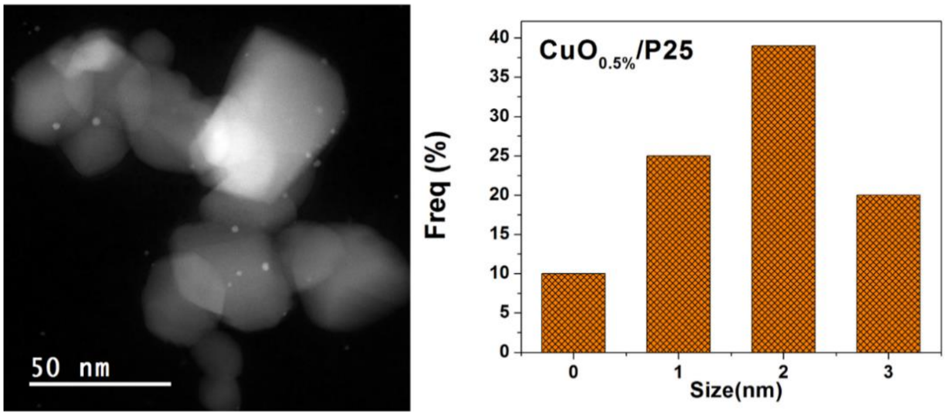

Figure IV-1. *TEM images of* ***a)*** *$CuO_{0.5\%}$/P25 with* ***b)*** *the corresponding histogram of the size distribution of CuO nanoclusters.*

The HAADF-STEM images for CuO nanoclusters show arrangements of crystallographic planes, corresponding to CuO. The measurement of the interplanar spacing (*d*) was found equal to 0.2 nm, which corresponds to the interplanar distance for (11-1) planes of CuO according to JCPDS file no. 48-1548.[141] These crystallographic planes and the FFT (fast Fourier transformation) can be observed in **Figure IV-2**.

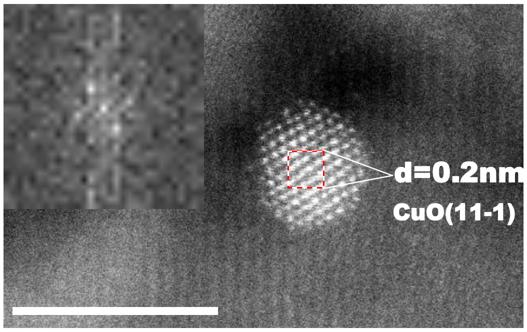

Figure IV-2. *HAADF-STEM of BF-STEM images of, CuO$_{0.5\%}$/P25 with FFT (fast Fourier transform) images for the planes of CuO.*

The composition of the CuO-nanoclusters was determined by EDS. Different clusters were analyzed: the profile spectra across the different individual nanoclusters show the presence of Cu (L and K edges) and Au (L and M edges, from gold coated holey carbon grids) (**Figure IV-3**).

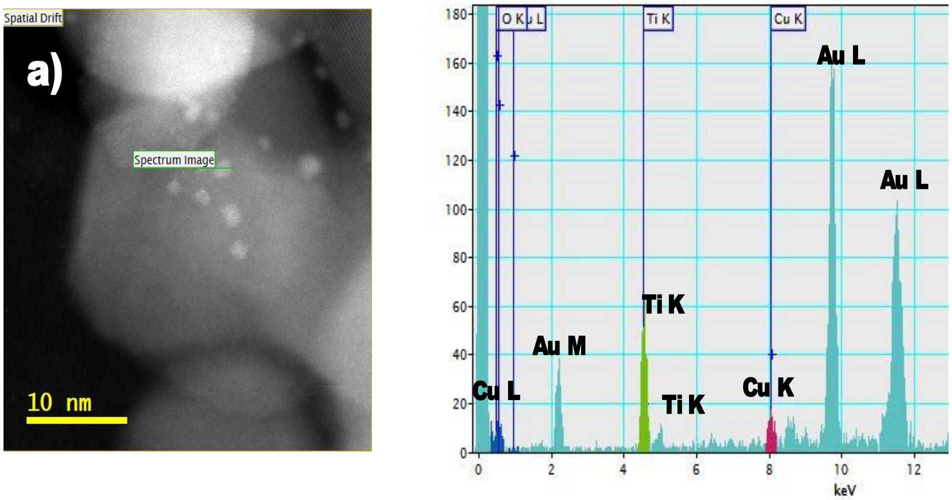

Figure IV-3. a) *STEM images for the samples and* ***b)*** *Energy dispersive X-ray spectroscopy line scan across external and corresponding STEM images for the samples of CuO$_{0.5\%}$/P25 (CuO signal is in red and blue).*

The analysis of the chemical composition of the modified TiO_2-P25 was also carried out by XPS. The core level signals of Cu, Ti, O and C were observed. The results are presented in **Figure IV-4** and in **Table 5**. The characterization by XPS demonstrates the presence of the Ti *2p* peaks characteristic of Ti^{4+} in TiO_2 with two main components at 458.7 and 464.6 eV related to Ti $2p_{3/2}$ and Ti $2p_{1/2}$ orbitals, respectively. Other peaks at 529.9 eV are attributed to O *1s* of TiO_2, and an additional peak at 284.8 eV is attributed to C *1s* peak (signal obtained from the carbon films, or contamination of CO_2 and carbonates). Two components Cu $2p_{3/2}$ and Cu $2p_{1/2}$ are observed for the Cu core peaks.[142] Concerning Cu $2p_{3/2}$ core levels, the E_B positions are in the range of 932.4 eV. The copper position range is in agreement with Cu^{2+} chemical state,[143] but also characteristic of Cu^0. However the characteristic *shake-up* or *satellite peak* of Cu^{II} ions is naught or very weak. Therefore, from XPS analysis, it is hard to conclude about the oxidation state of Cu^{II}. Chusue *et al*. reported that the XPS *shake-up* is sensitive to the CuO particle size, and that this satellite decreases with the reduction of Cu^{II} (into Cu^I and Cu^0) but also with the decrease of the particle size.[144]

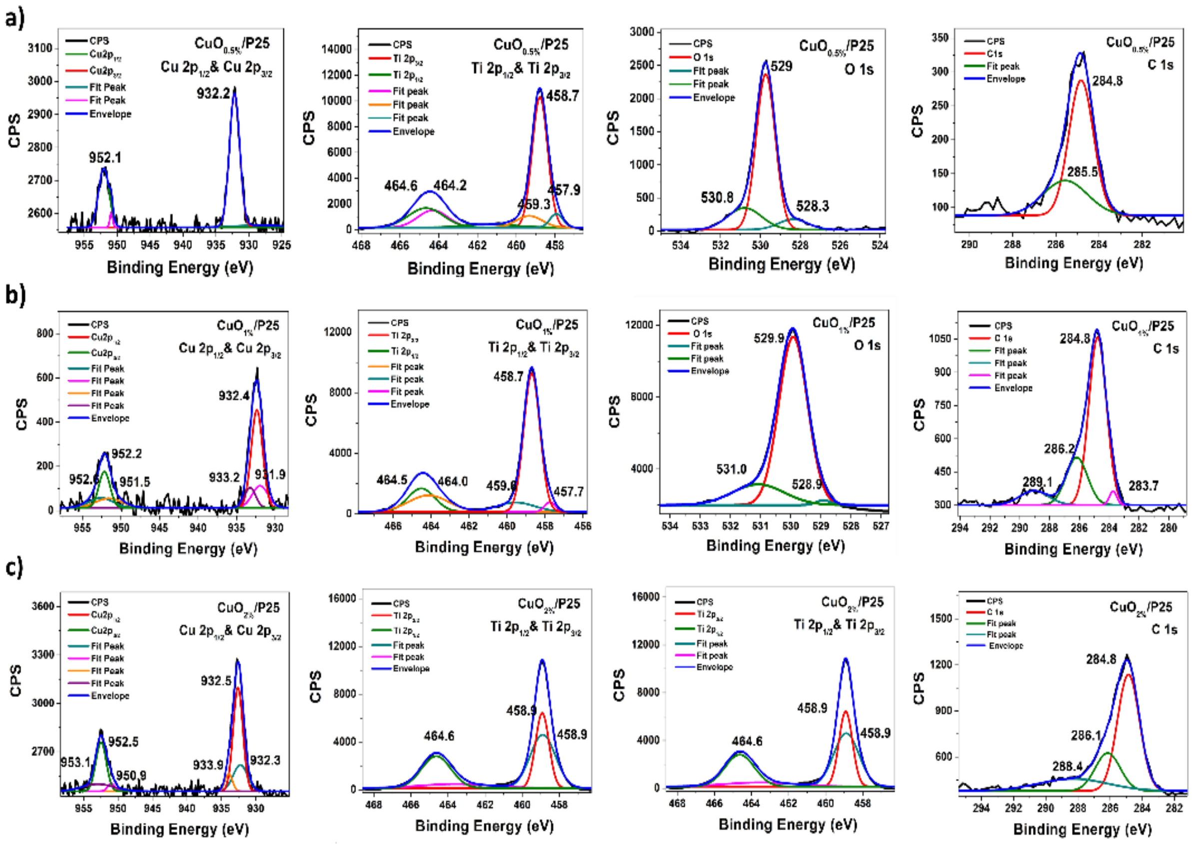

Figure IV-4. *XPS spectra for Cu2p, Ti 2p, O 1s and C 1s of the modified sample.*

Table 5. *Binding energies of the composite $CuO_{0.5\%}/TiO_2$ determined by XPS*

Samples	Cu		Ti		O	C
	2p$_{1/2}$	2p$_{3/2}$	2p$_{1/2}$	2p$_{3/2}$	1s	1s
	[eV]					
$CuO_{0.5\%}$/P25	952.1	932.2	464.6	458.7	529	284.8
$CuO_{1\%}$/P25	952.2	932.4	464.5	458.7	529.9	284.8
$CuO_{1\%}$/P25	952.5	932.5	464.6	458.9	530	284.8

Therefore, Cu K-edge XANES spectra were measured in order to corroborate the oxidation states of Cu deduced from XPS. It has been found, that the energy position of the rising edge of the spectra and shape of white line for all the TiO_2-P25 modified with copper (Cu alone) are characteristic of Cu^{II} species,[145] as is shown in **Figure IV-5**.

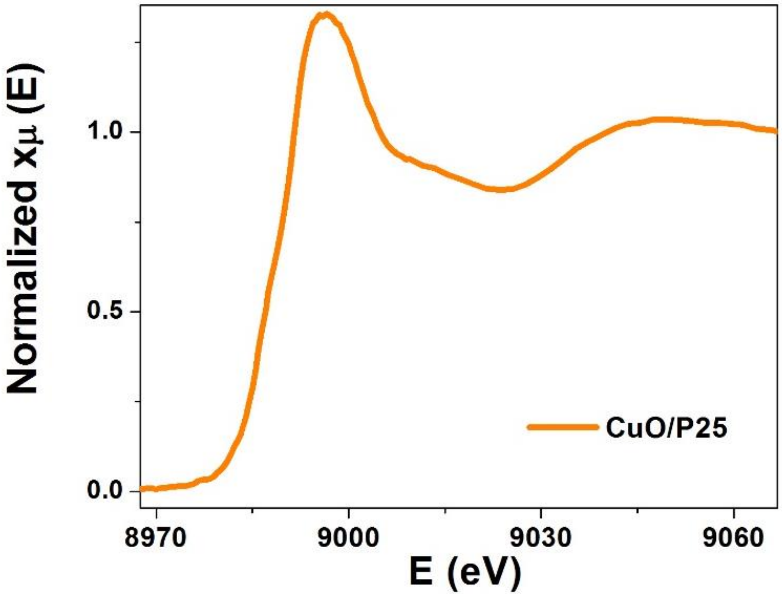

Figure IV-5. *Cu K-edge XAS spectra for $CuO_{0.5\%}$/P25.*

Solvated electrons induced by radiolysis are very strong reducing species able to reduce non noble metals, which are difficult to reduce by chemical methods.[100,146,147] However, copper clusters are sensitive to oxygen and are most probably very fast oxidized in air.

The optical properties of the modified TiO_2-P25 were studied by DRS. **Figure IV-6** shows the spectra of bare and modified TiO_2-P25. The spectrum of TiO_2-P25 shows an absorption edge at around 400 nm due to the presence of rutile.[112] The DRS of the modified samples exhibit a slight shift in the absorption toward visible light, attributed to the stabilization of the conduction band of TiO_2-P25 by the interaction with the CuO-nanoclusters. The modified samples absorb in the visible and near infra-red (IR) region, while bare TiO_2-P25 does not. The addition of CuO-nanoclusters have a large absorption band with a maximum at 800 nm, and these absorptions result in light green color, CuO-nanoclusters are known to exhibit an absorption band in the IR attributed to $2E_g \rightarrow 2T_{2g}$ inter-band transitions in the Cu^{II} clusters, which are deposited on TiO_2.[148]

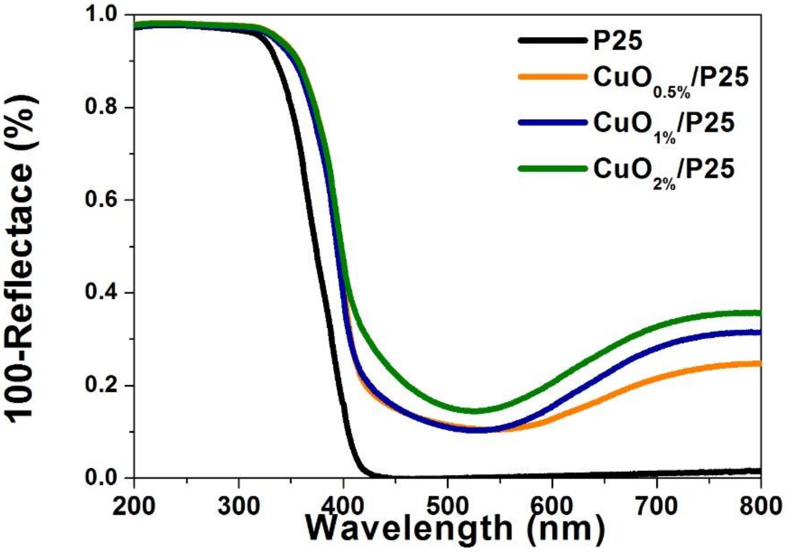

Figure IV-6. *UV-Vis diffused reflectance spectra of TiO_2-P25 and modified TiO_2-P25 with different loadings of CuO-nanoclusters.*

The electronic properties of the samples were studied by TRMC technique at different wavelengths considering both UV and visible regions. The excitation wavelengths were 365, 450, 480, 550, 600 and 950 nm, and the corresponding laser energies were 1.4, 6.1, 5.8, 4.5, 2.5, and 2.7 $mJ.cm^{-2}$, respectively. The TRMC signals are shown in **Figure IV-7**. The surface modification of TiO_2 with CuO-nanoclusters results in a strong influence on the charge-carriers dynamics in TiO_2-P25.

TRMC signals show that under UV excitation at 365 nm (**Figure IV-7a**), all the photocatalysts are activated, *i.e.,* free electrons are injected in the CB of TiO_2-P25, as is shown by the sharp increase of TRMC signal reaching I_{max} values. However, the decay of the signals is faster for the modified samples. In case of titania, the TRMC signals are mainly related to the electron mobility. The decrease of the TRMC signals is probably caused by efficient electron scavenging by the CuO-nanoclusters deposited on TiO_2-P25, thus diminishing the number of mobile electrons. The photogenerated electrons can be trapped by Cu^{II} (due to the unfilled 3d shell, $t_{2g}^6 e_g^3$ configuration),[149] It implies a decrease of the charge-carriers recombination that is beneficial for the photoactivity. It has to be noted that the acceleration of the decay is faster for TiO_2-P25 modified with CuO-nanoclusters possessing larger amount of CuO.

The CuO-nanoclusters on TiO_2-P25 generated a TRMC signal under visible light **Figure IV7 b-f**. The samples modified with CuO exhibit higher I_{max} values compared to pure TiO_2-P25 excited with wavelengths within the visible range (450 nm, 480 nm, 550 nm and 600 nm), besides the I_{max} value increases the CuO loading. At 450 nm, all the CuO containing samples show similar signals I_{max} values. However, the samples show different signal decays. The decay is slower with decreasing the amount of CuO, indicating that the recombination of photogenerated charge-carriers is slower. At 480 nm, the samples still present signals with similar I_{max} values and signal decay. However, at 550 nm and 600 nm different signals are obtained and the increase in CuO loading results in a higher I_{max} value. These results indicate that with increasing the CuO loading more electrons are injected in the CB of TiO_2. And at the excitation wavelength of 900 nm, the samples showed no signal.

These results indicate that, under visible light excitation, electrons are promoted from CuO-nanoclusters to the CB of TiO_2-P25. Also, it is worth noting that copper is able to activate the TiO_2 photocatalysts in a wider range of wavelengths under visible light irradiation.

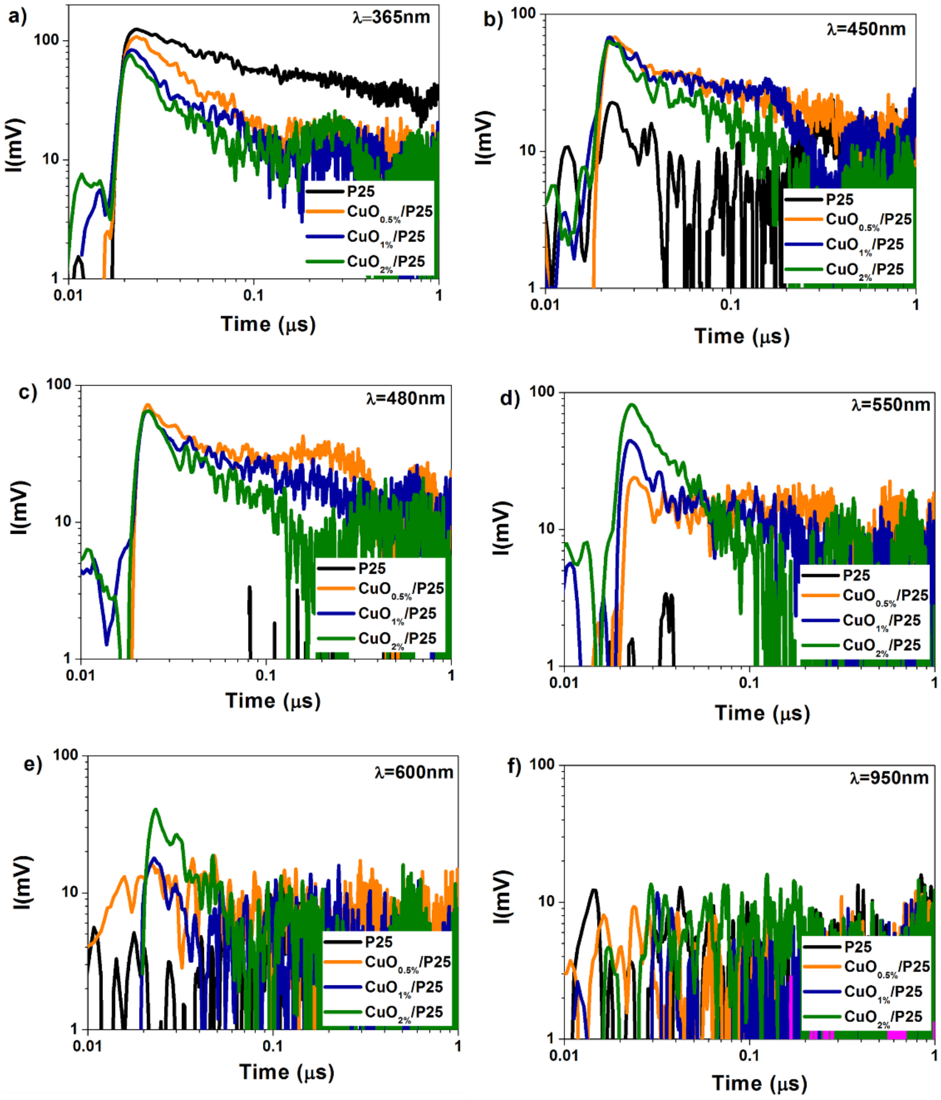

Figure IV-7. *TRMC signals at **a)** 365, **b)** 450, **c)** 480, **d)** 550, **e)** 600 and **f)** 900 nm of TiO_2-P25 and modified TiO_2-P25 with CuO-nanoclusters.*

4.3. Photocatalytic Tests

The photocatalytic activity of the modified TiO_2-P25 samples was evaluated for the degradation of phenol, acetic acid under UV and visible light, 2-propanol degradation, hydrogen production, and antibacterial properties under visible light.

4.3.1. Phenol Degradation Under UV and Visible Light

The curves of phenol degradation are shown in **Figure IV-8**. Surface modification of TiO_2-P25 with CuO does not influence markedly the photocatalytic activity of TiO_2-P25 under UV light. A slight enhancement of activity was observed for samples modified with 0.5% and 1% of CuO-nanoclusters. This increase in the photocatalytic activity can be due to less recombination of charge-carriers because of the reduction of Cu^{II} into Cu^{I}.[149] Foster *et al.* found that the oxidation of Cu^{I} into Cu^{II} by O_2, decreased the electron-hole recombination.[150] Indeed, TRMC data at λ_{ex} = 365 nm indicates a better separation of the charge-carriers probably due to electron sinking by CuO (lower I_{max} and faster decay, **Figure IV-8a**). The electrons and holes recombination rates decrease with CuO loading because of higher number of CuO clusters on the surface of titania acting as recombination centers.[151]

Under visible light, the photoactivity of pure TiO_2-P25 is usually very low because the illumination energy is lower than its band-gap energy. Modification of titania results in visible photocatalytic activity, as is shown in **Figure IV-8b** for phenol degradation. The modification with the smaller amount of CuO (0.5% in Cu) leads to a slightly higher enhancement in the photocatalytic activity compared to the modification with 0.1% and 2% of CuO-nanoclusters. Surface modification with copper oxide induces a modification of the absorption properties of the TiO_2-P25 and particularly an enhancement of the absorption in the visible range creating an activity under visible light.

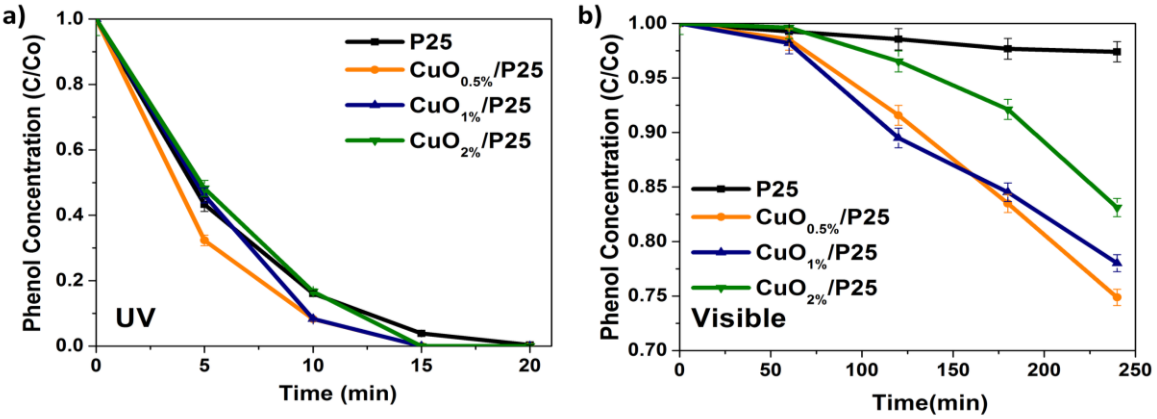

Figure IV-8. *Degradation curves of phenol (50 ppm) under* ***a)*** *UV and* ***b)*** *visible light λ > 450 nm for pure and modified TiO_2-P25 with different loadings of CuO-nanoclusters, in a ratio $1gL^{-1}$.*

This photocatalytic activity can be related to the TRMC signals previously discussed: The CuO/P25 samples showed the highest I_{max} value (compared to that obtained with bare titania) in a wide range of excitation wavelengths within the visible range, which represents more electrons in the conduction band of the TiO_2-P25 semiconductor.

4.3.2. 2-Propanol degradation under visible irradiation

The CuO modified TiO_2-P25 samples show a high photocatalytic activity for the oxidation of 2-propanol under visible light (λ ≥ 450 nm) (see **Figure IV-9**). The sample $CuO_{0.5\%}$/P25 presents a slightly higher activity than the other samples with higher CuO loading. In this reaction, only acetone is detected as intermediate.[152]

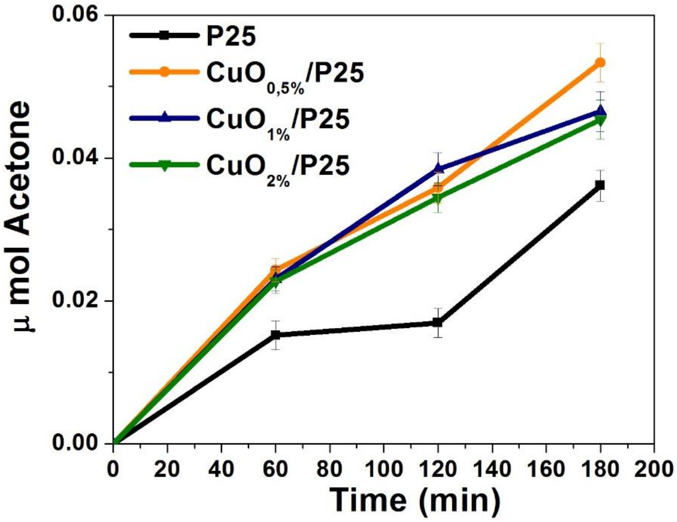

Figure IV-9. *2-propanol (5 v%) degradation under visible irradiation (λ ≥ 450nm) of TiO_2-P25 and TiO_2-P25 modified with different loadings of CuO-nanoclusters, in a ratio 10 gL^{-1}.*

4.3.3. Acetic Acid Degradation — Action Spectrum

The $CuO_{0.5\%}$/P25 sample, was evaluated in the decomposition of acetic acid. The decomposition of acetic acid under the light irradiation results in the formation of CO_2. **Figure IV-10a**, presents the photoactivity under UV at λ = 350 nm, and visible light at λ = 470 nm. The CuO-modified samples are more active in the production of CO_2 compared to bare TiO_2-P25. These results confirm that surface modification with the CuO-nanoclusters improves significantly the activity of the semiconductor TiO_2-P25 under UV and visible range. In **Figure IV-10b**, the action spectrum shows for the photodecomposition of acetic acid, an appreciable UV and visible response and a photoactivity of the modified samples. However, this activity decreases rapidly with increasing the excitation wavelength. These results show that the apparent quantum efficiency is much lower under visible light than under UV. Nevertheless, it is noteworthy that from 400 to 470 nm excitation wavelength, the CuO/P25 samples once again produces more CO_2 than pure TiO_2-P25. This implies that the incident visible light activates the CuO-NPs, thus inducing injection of the electrons in the conduction band of TiO_2-P25, as it was also suggested by the TRMC results.

Figure IV-10c and **d** show the action spectra compared to the absorption spectra obtained by DRS. The action spectra indicates that the photoreaction is carried out by a photocatalytic mechanism.[153] The action spectra correlates well with absorption spectrum for bare titania, (**Figure IV-10c**) reaching a quantum yield of 22.8, 10.2 and 1.7% for irradiation at 350, 380 and 410 nm, respectively. However, for the modified samples with CuO-nanoclusters **Figure IV-10d** only a part of the absorption spectra matches with the AS (below 500 nm). We can infer that the absorption at wavelengths longer than 500 nm does not drive a photocatalytic activity, and that the small TRMC signals observed at $\lambda > 500$ nm for $Cu_{0.5\%}$/P25 are probably due to the mobile, but inactive generated electrons with lower energy that cannot drive degradation of organic compounds, or these electrons are reactive but with lower quantum yield. It is possible that electron excitation with lower energy results in their injection from CuO nanoclusters to deep traps (localized in band-gap of TiO_2) of energy much lower than the CB of titania, and thus reduction of oxygen molecules is not possible.

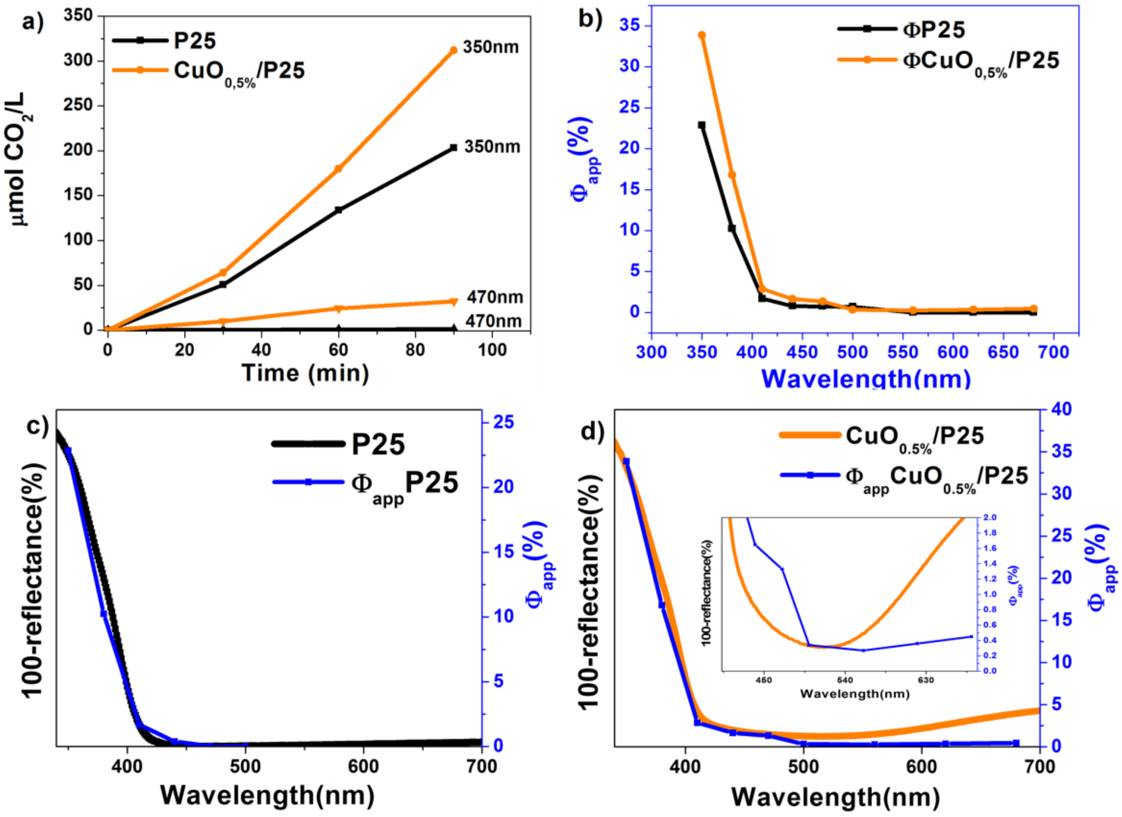

*Figure IV-10. **a)** Photocatalytic evolution of CO_2 resulting from the decomposition of acetic acid (5 v%), at 350 nm, and 470 nm of P25 and $CuO_{0.5\%}$/P25, in a ratio 10 gL^{-1} and **b)** Action Spectra for the acetic acid decomposition using bare titania and $CuO_{0.5\%}$/P25, comparison between the action spectrum and the DRS spectrum for the used samples: **c)** pure TiO_2-P25; **d)** $CuO_{0.5\%}$/P25.*

4.3.4. Photocatalytic Production of Hydrogen (H_2)

For PWS process, namely the H_2-production tests under visible light (λ=470 nm), the addition of CuO-nanoclusters activates the TiO_2-P25 as is shown in **Figure IV-11**.

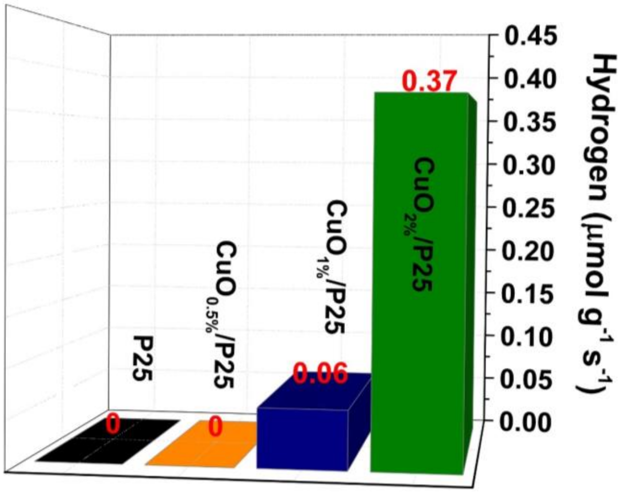

Figure IV-11. *Photochemical H_2 generated by methanol dehydrogenation (25 v%) with bare and CuO-modified TiO_2-P25 in a ratio of 1 gL^{-1}.*

Despite only a small amount of H_2 is produced by CuO_x/P25 samples, this is higher than the amount produced by pure TiO_2-P25. The hydrogen generation increases with CuO-loading. In case of $CuO_{0.5\%}$/P25, the activity drastically decreases.

4.3.5. Mechanism Proposed of Charge-Carriers Dynamics Under UV and Visible Light

These TRMC and AS results shed light on the photocatalytic mechanisms, for TiO_2-P25 modified with CuO- nanoclusters under UV and visible light irradiation, and the schemes for these mechanisms are shown in **Figure IV-12a** and **Figure IV-12b**, respectively.

Under UV light, CuO-NPs works as electron pools retarding the recombination process as supported by TRMC results. The number of charge-carriers decreases because of the relaxation of photogenerated electrons from the CB of TiO_2-P25 to the valence band (VB) of CuO, acting in this system as electron traps. The photogenerated holes are only generated in the VB of CuO and accumulate there due to the higher VB position of CuO with respect to that of TiO_2. It is known that coupling of TiO_2 with other semiconductors of different redox energy levels can lead to more efficient charge-carrier separation process, *i.e.*, an increase in the charge-carriers lifetime and an enhancement of the interfacial charge-transfer efficiency to adsorbed substrate.[52,72]

Under visible light excitation, TRMC signals and action spectra show that the photogenerated electrons of CuO-nanoclusters [due to the narrow band-gap of CuO (about 1.7 eV)[47]] are transferred in the CB of the semiconductor TiO_2, thus due to slightly separation of the CBs of CuO and TiO_2 , reducing then the recombination process, and inducing an activity in the visible region. This corresponds to a higher photocatalytic activity under visible light of P25 modified with CuO-NPs. It has to be noted that this energy band-gap value increases with the size of CuO, and Ge *et al*. had reported that for CuO nanoclusters, the band-gap decreases from 2.6 eV to 1.4 eV when the size increases from 1.1 nm to 2 nm.[154] Under visible irradiation (**Figure IV-12b**), due to the position and the value of the energy band-gap of CuO, visible light photo-generates electrons from CuO, and these electrons are injected into the CB of TiO_2-P25.

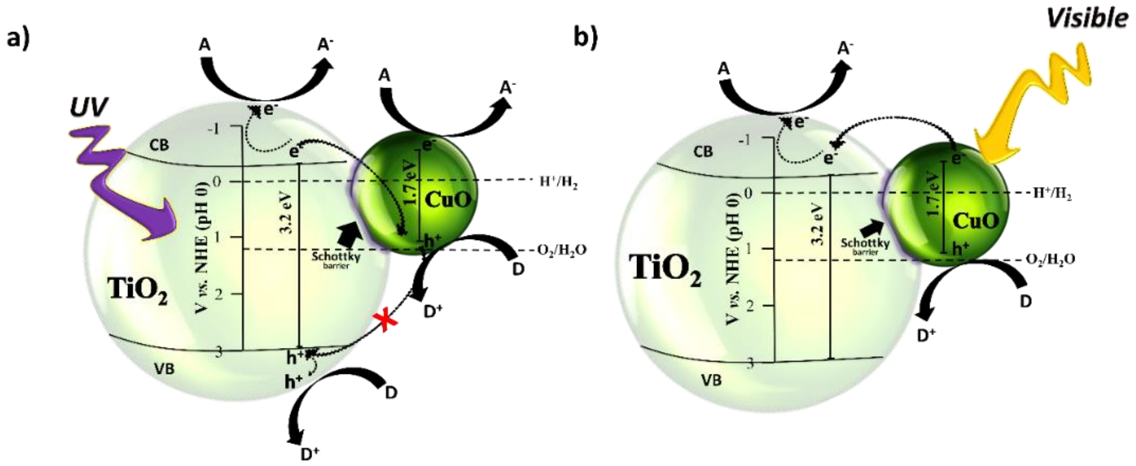

Figure IV-12. *Mechanisms proposed for TiO_2-P25 modified with CuO-nanoclusters under* ***a)*** *UV and* ***b)*** *visible light.*

4.3.6. Stability Study for $Cu_{0.5\%}$/P25 Synthesized by Radiolysis

The stability after cycling of the sample $CuO_{0.5\%}$/P25 under visible light (λ ≥ 450 nm) was studied for phenol degradation, see **Figure IV-13a**. Its photoactivity decreases after three cycles, signifying that the composite $CuO_{0.5\%}$/P25 (with small CuO nanoclusters) is less stable than the system $Au_{0.5\%}$/P25.

The samples were characterized after three cycles, and the XPS analysis shows that the peaks corresponding to the binding energy of Cu*2p* core levels disappeared after recycling (**Figure IV-13b**), and the STEM images (**Figure IV-13c, d, e**) show that after cycling (3 cycles) some aggregations of CuO nanoparticles are present and that TiO_2 is free of CuO **Figure IV-13e**). This CuO leaching explains the loss of the Cu *2p* XPS signal and the decrease in the photocatalytic activity.

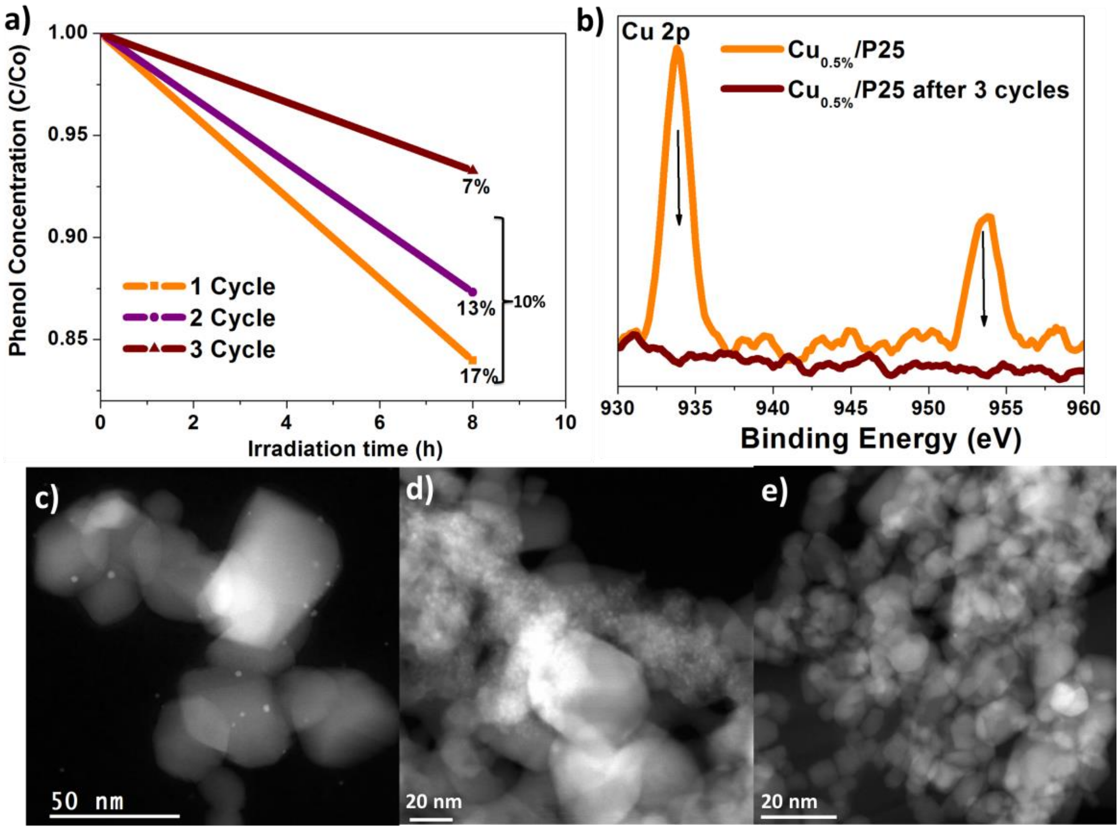

Figure IV-13. a) *Recycling of CuO$_{0.5\%}$/P25, photocatalytic phenol degradation (50ppm) after three cycles under visible light irradiation during 8h,* ***b)*** *Binding energy of Cu 2p peaks, of CuO$_{0.5\%}$/TiO$_2$, and CuO$_{0.5\%}$/TiO$_2$ after 3 cycles of degradation of phenol,* ***c)*** *STEM images of CuO$_{0.5\%}$/P25 and* ***d)*** *and* ***e)*** *STEM image after 3 cycles.*

4.3.7. Anti-Fungi Properties

The antifungal properties were investigated with the daily growth of fungi mycelium (*Aspergillus Melleus* and *Penecillium Chrysogenum*) in the dark and under visible light, in the media (blank), pure TiO_2-P25 and modified with $CuO_{0.5\%}$/P25 NPs.

Figure IV-14 shows the fungal daily growth for *Aspergillus Melleus* in a control media (no titania), the same growth is observed under dark and visible light. TiO_2-P25 presents an activity only when it is irradiated with visible light, as is explained above. It is suggested that the rutile phase of TiO_2-P25 is mainly responsible for titania activity under visible irradiation. The addition of CuO decreases the fungal growth due to the activation of its narrow band gap, thus it can be active under visible light. However, CuO/P25 presents lower activity than pure TiO_2-P25 under dark and under visible irradiation.

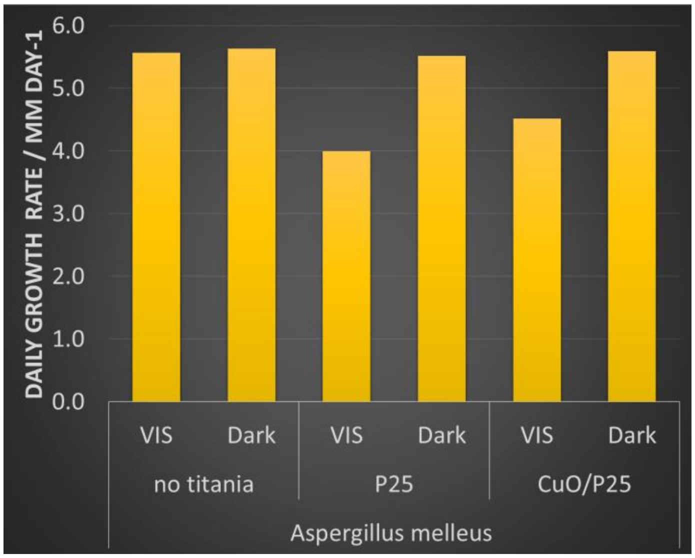

Figure IV-14. *Antibacterial daily radius growth under visible (vis) and dark for the fungi Aspergillus Melleus.*

The decrease of the fungus diameters and the change of the color of the media is shown in the **Figure IV-15**. It is clear to observe the decrease of the diameter of the spores, the reduction of the spores amount with CuO/P25 is lower that for pure TiO_2-P25. mycotoxin generation (small sphere in pink color) were observed.

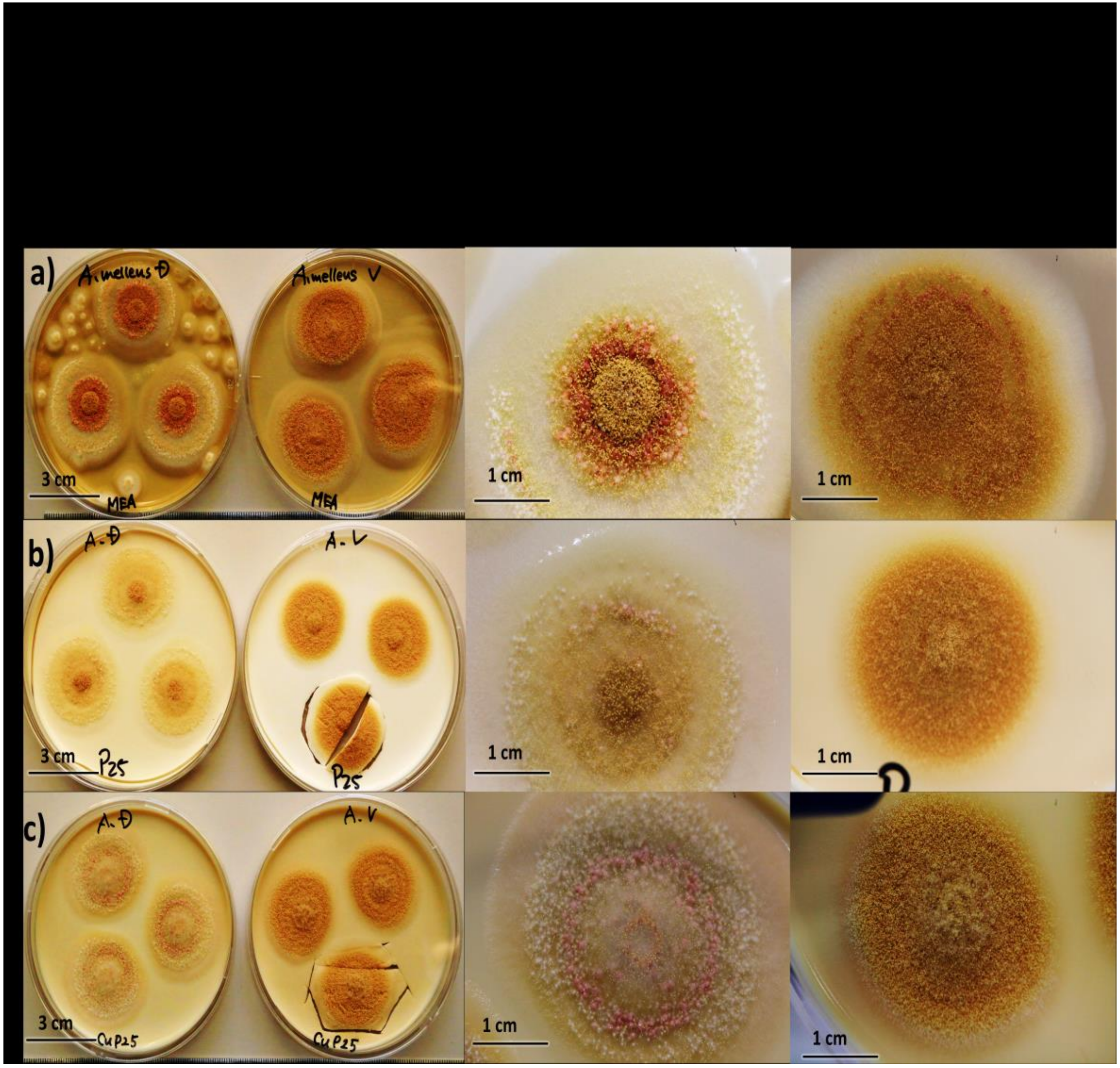

Figure IV-15. *Photograph of mycelium growth of Aspergillus Melleus fungi after 8 days incubation of a) blank (no titania), b) P25, c) $CuO_{0.5\%}$/P25 under visible light and in dark. In the left a picture: at scale of the fungi growth, in the right picture: the extension of a mycelium.*

The sporulation and the mycotoxin generation were observed for all the samples in dark, as shown in **Figure IV-16**. It was observed that under dark conditions, TiO_2-P25 presents less sporulation than $CuO_{0.5\%}$/P25. Under visible exposition the decrease the mycotoxins formation for TiO_2-P25 and $CuO_{0.5\%}$/P25 is observed, however, the sporulation decreases slightly with TiO_2-P25.

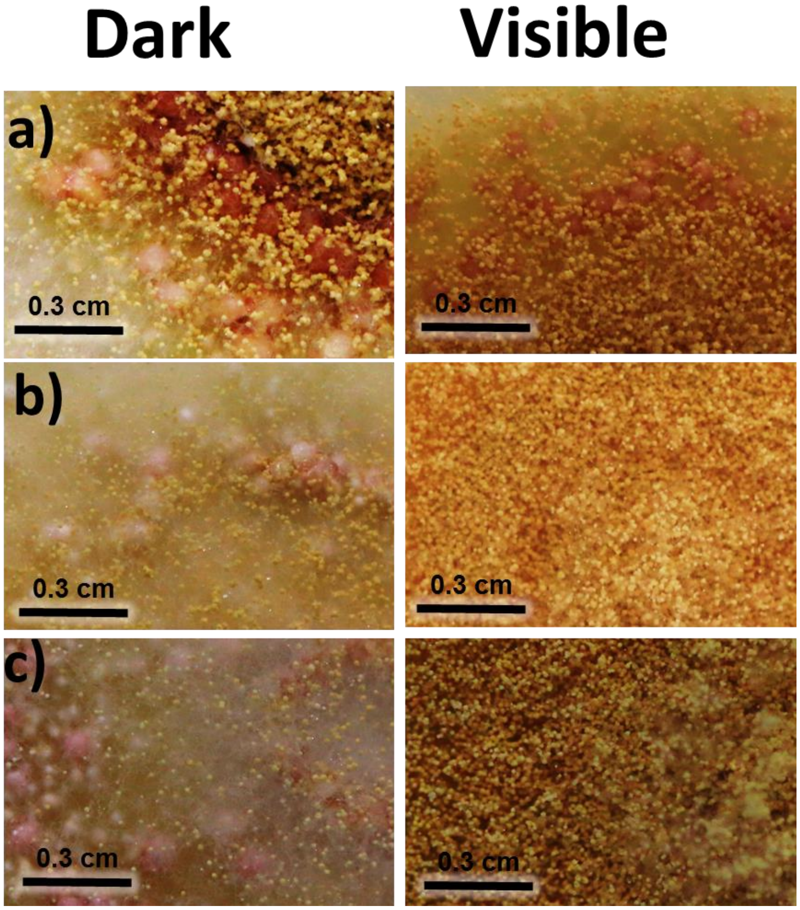

Figure IV-16. *Photograph of 8-day growth of Aspergillus Melleus in dark and under irradiation.* ***a)*** *Under media* ***b)*** *TiO_2-P25 and* ***c)*** *$CuO_{0.5\%}$/P25.*

In the **Figure IV-17** is showing the fungal daily growth of *Penicillium Chrysogenum*, in the control media (without titania) the growth is higher in the dark than under visible light, with the pure TiO_2 and the modified sample accelerates the growth of the fungi under visible irradiation. It was reported by Markowska-Szczupak *et al*., that anatase stimulated fungal growth due its superhydrophilic properties (fungi needs water for growth), a fact that could influence water accessibility by fungi.[155] In dark, $CuO_{0.5\%}$/P25 stimulated fungal growth, and in the other side, TiO_2-P25 shows a slight inhibition in the growth.

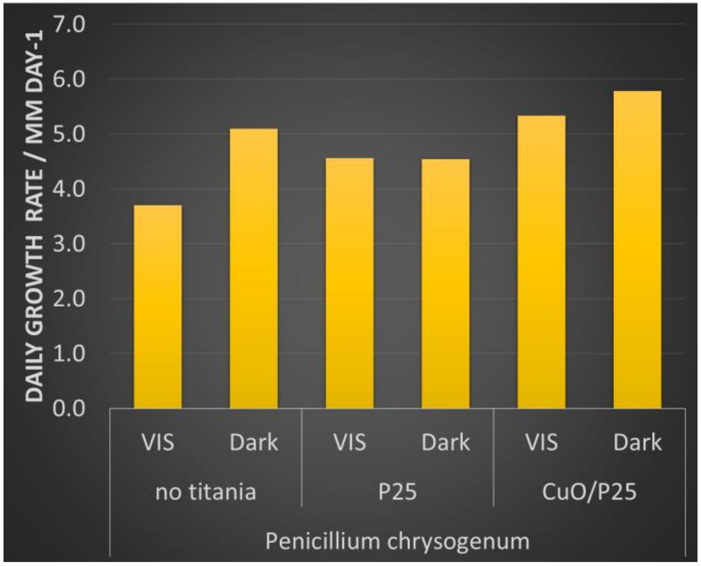

Figure IV-17. *Antibacterial daily radius growth under visible (vis) and dark for the fungi Penicillium Chrysogenum.*

The picture in **Figure IV-18** shows the fungus diameter and the change of the media color, under dark and under visible exposition. The inhibition of fungal growth by non-irradiated TiO_2-P25, can be explained by its absorption on fungal surface, which could result in inhibition of sporulation, according to Calvo *et al*.[156]

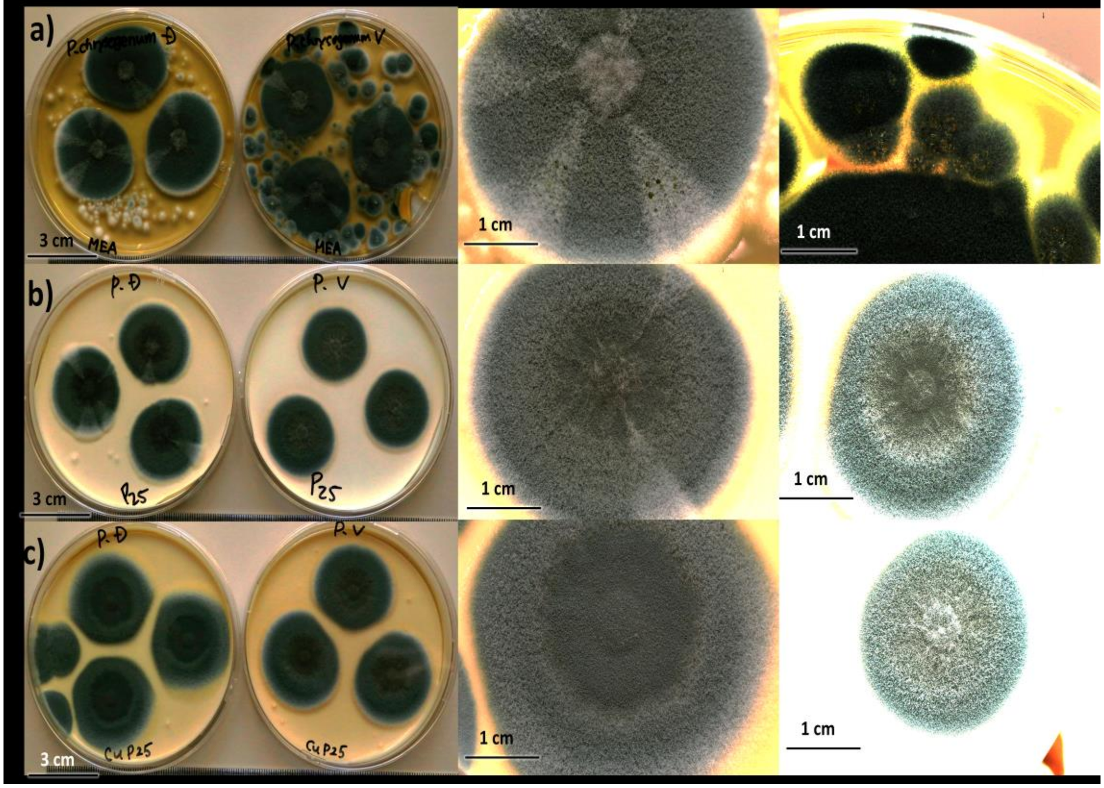

Figure IV-18. *Photograph of mycelium growth of Penicillium Chrysogenum fungi after 8 days incubation of a) blank (no titania) b) P25 c) $CuO_{0.5\%}$/P25 under visible light and dark. In the left: a picture at scale of the fungi growth, in the right, the extension of a mycelium.*

In **Figure IV-19**, it is possible to see that the mycotoxin is present in the media (without titania) and $CuO_{0.5\%}$/P25, the addition of TiO_2-P25 inhibits the formation of droplets of mycotoxin, after 8 days of exposition.

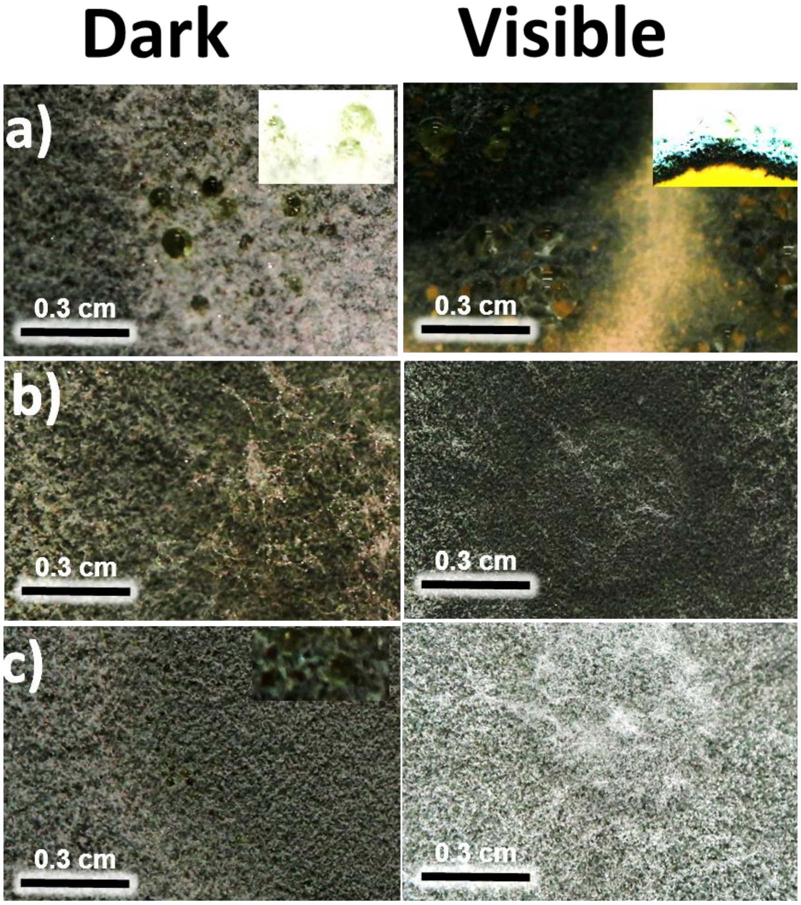

Figure IV-19. *Pictures of 8-day growth of Penicillium Chrysogenum in dark and under irradiation.* ***a)*** *Under media,* ***b)*** *TiO_2-P25, and* ***c)*** *$CuO_{0.5\%}$/P25.*

4.4. Conclusions

In conclusion, small CuO nanoclusters (1-3 nm) were synthesized by radiolysis on the surface of TiO_2-P25. This surface modification leads to an enhancement in the photocatalytic activity of TiO_2-P25, under both UV and visible light. TRMC signals and action spectra show that under UV light excitation, CuO clusters act as electron traps decreasing the recombination process, and thus increasing the apparent quantum yield, while under visible excitation, they absorb incident photons due to the narrow band gap of CuO. Under visible light excitation, electrons are injected from CuO into the conduction band of TiO_2. The action spectra clearly prove that decomposition of acetic acid is driven by photocatalytic reaction. The modification with CuO nanoclusters results in a high enhancement of the quantum yield under UV and visible light irradiations. However, only a short part of visible absorption (< 500 nm) is responsible for photocatalytic activity. The CuO loading affects the electron transfer decreasing the photoactivity for oxidation processes, but in the case of a reduction process, the photoactivity increases with CuO loading. These nanomaterials can also find applications in CO_2 reduction.

The heterojunction with CuO and titania does not enhances the antifungal properties of titania, the sample CuO/P25 always presents lower activity than pure TiO2-P25 under dark and under visible irradiation, which means higher sporulation and it does not avoid the mycotoxin formation for both Aspergillus Melleus and Penicillium Chrysogenum fungus.

Chapter V

Surface Modification of TiO_2-P25 with Ag Nanoparticles and CuO Nanoclusters

Chapter 5. Surface Modification of TiO_2-P25 with Ag Nanoparticles and CuO Nanoclusters

5.1 Introduction

In this chapter, we will present the results of surface co-modification of TiO_2-P25 with copper and silver on the photocatalytic activity.

Silver NPs are extremely attractive because of their high catalytic activity, widespread optical properties (size- and shape-dependent), antimicrobial properties, and potential applications in biological and chemical sensing based on phenomena of Surface-Enhanced Raman Scattering (SERS), LSPR, and Metal-Enhanced Fluorescence (MEF).[6] In addition, modification of TiO_2 with silver NPs results in enhanced photocatalytic activity under both UV and visible irradiation and improved anti-bacterial properties.[6,119,157]

However, the use of Cu, in agreement with Irie *et al.*,[140] is more desirable due to its low cost and excellent catalytic and antifungal properties. It has recently been reported that surface modification of TiO_2 with bimetallic Ag-Cu nanoparticles leads to enhancement of the photocatalytic activity of TiO_2 for CO_2 reduction compared to its modification with monometallic NPs.[158]

Cu and Ag nanoparticles are known for their antibacterial and antifungal properties.[157,159]In 1985, Matsunaga *et al*. reported the photocatalytic activity of TiO_2 for destruction of *Lactobacillus acidophilus, Escherichia coli* and *Saccharomyces cerevisiae* with possible applications in water and air disinfection.[160] Most of the studies on the antimicrobial activity of titanium dioxide were performed with simple microorganisms, such as bacteria and viruses.[155,161,162,] TiO_2–based photocatalysts could be used for treatment of common contaminants found in office and home environments: The microorganisms represent approximately 70% of the dust, and the main group of organisms present in bioareosol are filamentous fungi. They might be a direct threat to health (*e.g*. causing allergic reactions and upper respiratory track infections). Therefore, if the fungal contamination is not controlled, the problems connected with indoor environment quality (IEQ) can arise. Thus, TiO_2-based photocatalysts (bare TiO_2 or modified with NPs such as Cu and Ag, for example) can be used to improve the environmental quality. Irradiation of the photocatalyst under UV (bare TiO_2) and/or under visible light (modified TiO_2) can generate reactive oxygen species (ROS) which are responsible for the decontamination.[155]

In this chapter, we present synthesis of Ag nanoparticles and/or CuO nanoclusters by radiolysis on commercial TiO_2-P25. The photocatalytic activity of these plasmonic photocatalysts has been investigated for photooxidation reactions of phenol, 2-propanol, acetic acid, and hydrogen production by PWS process. The antibacterial and antifungal properties of TiO_2 modified with CuO and/or Ag were studied for the inhibition of two fungis *Aspergillus melleus* and *Penicillium chrysogenum*. TRMC has been used to study charge-carriers dynamics. The aim of this study was to correlate the photocatalytic activity of modified TiO_2-P25 with Ag nanoparticles and CuO nanoclusters with AS and TRMC signals obtained at different excitation wavelengths, in order to understand the mechanisms involved in the photocatalytic process under UV and visible light.

5.2 Materials Characterization

Ag^+ and Cu^{2+} ions were reduced on TiO_2-P25 by solvated electrons and reducing $(CH_3)_2C^{\bullet}OH$ radicals induced by radiolysis. The modified TiO_2-P25 with Ag and/or Cu presented different colors (see **Table 6**).

Table 6. *Characteristics of the modified photocatalysts CuO, Ag and Ag@CuO samples*

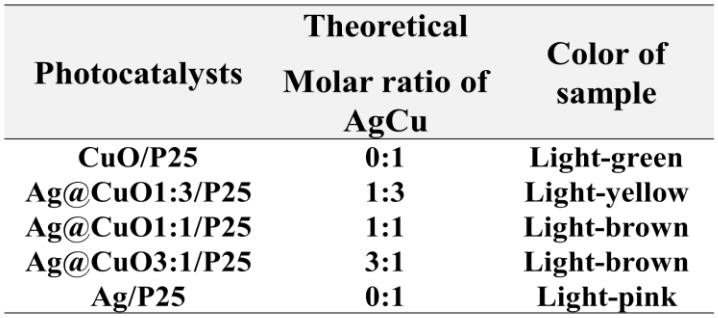

Photocatalysts	Theoretical Molar ratio of AgCu	Color of sample
CuO/P25	0:1	Light-green
Ag@CuO1:3/P25	1:3	Light-yellow
Ag@CuO1:1/P25	1:1	Light-brown
Ag@CuO3:1/P25	3:1	Light-brown
Ag/P25	0:1	Light-pink

For all the modified titania samples, TEM observations show metal nanoparticles homogeneously dispersed on TiO_2-P25 surface (see **Figure V-1-1**). For CuO/P25 and Ag/P25 samples, small nanoparticles of around 1-2 nm were observed on the surface of TiO_2-P25 (**Figure V-1-2a** and **Figure V-1-2e**). For the titania co-modified with both elements, larger nanoparticles (5-12 nm) were formed on the TiO_2-P25 surface (see **Figure V-1-2b-d**).

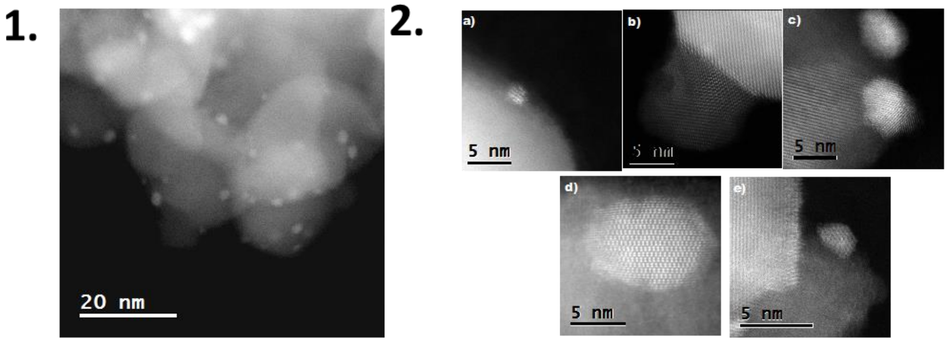

Figure V-1. 1. *A Low magnification of Ag@CuO1:1 nanoparticles deposited on TiO_2-P25.* ***2.*** *HRTEM images of modified TiO_2-P25 with metal nanoparticles* ***a)*** *CuO/P25,* ***b)*** *Ag@CuO1:3/P25,* ***c)*** *Ag@CuO1:1/P25,* ***d)*** *Ag@CuO3:1/P25, and* ***e)*** *Ag/P25.*

For the titania modified with both Cu and/or Ag, the HAADF-STEM images (**Figure V-2**) show metal nanoparticles located on the TiO_2-P25 surface. Since the brightness is approximately proportional to Z^2 (Z being the atomic number), any difference in brightness would reflect the presence of two different elements. Therefore, due to the atomic number difference between Ag (47) and Cu (29), the areas with higher brightness within the NPs are attributed to columns of atoms richer in silver, and the areas with lower brightness are attributed to columns richer in copper. As the brightness is not regular, there is segregation between Ag and Cu. The HAADF-STEM images for Ag@CuO1:3/P25 sample (**Figure V-2c**) show that Ag-Cu-based NPs have a core-shell structure, where Ag is the core, and the Cu is the shell part. A similar core-shell structure is obtained for the other Ag:Cu molar ratios, *i.e*, Ag@CuO1:1 and Ag@CuO3:1, as it can be seen in the **Figure V-2b** and **2c**, respectively. In the Ag@CuO3:1/P25 sample, the core composed of Ag covers a larger area of the total particle, compared to that observed in the Ag@CuO1:3/P25 sample. Additionally, an image with the bright field (BF) observation mode in the STEM technique is shown in the right part of **Figure V-2a-**

e, where it is possible to observe different arrangements of the crystallographic planes.

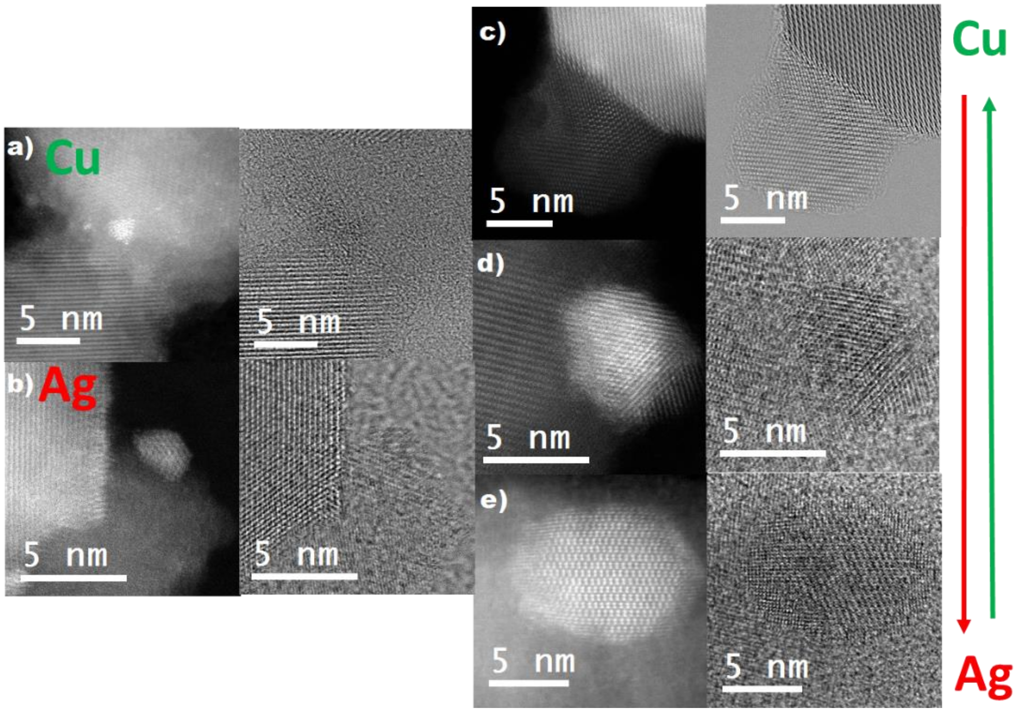

Figure V-2. *HAADF-STEM (left) and BF-STEM (right) of* ***a)*** *Cu/P25,* ***b)*** *Ag/P25, and Ag@CuO systems;* ***c)*** *Ag@CuO1:3/P25,* ***d)*** *Ag@CuO1:1/P25, and* ***e)*** *Ag@CuO3:1/P25.*

The composition of the Ag and Cu-based NPs was investigated by EDS. Different nanoparticles were analyzed, and the profile spectra across the various individual NPs were taken. **Figure V-3a**. **Figure V-3b** shows chemical mappings for Ag and Cu-based nanoparticles. Ag (L) and Cu (L) maps clearly revealed the formation of the core (Ag)-shell (Cu) (or shell (CuO)) (composite image). Ag nanoparticles seem to be decorated on their surface by small clusters of Cu (Cu^0 or Cu oxides).

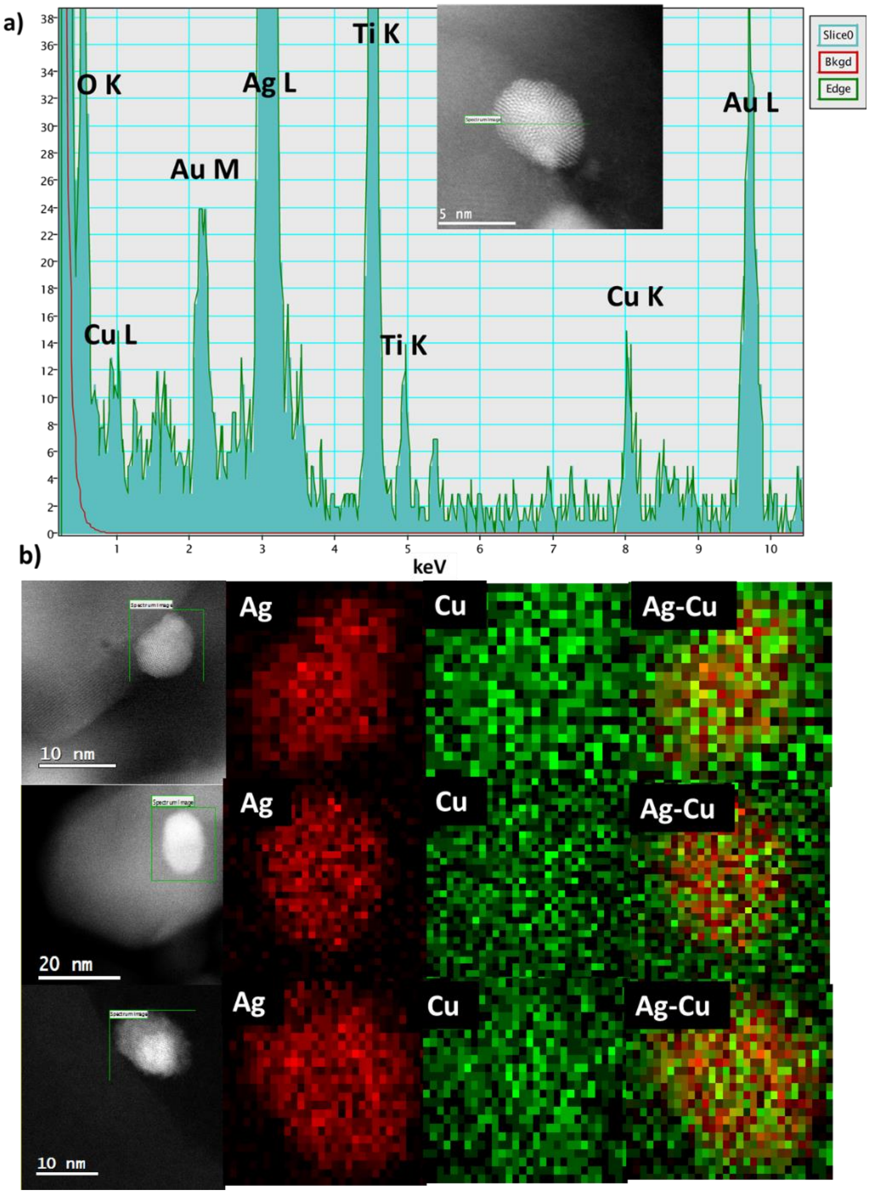

***Figure V-3**. **a)** EDS analysis and **b)** Elemental mapping (EDS analysis) performed on a nanoparticle of Au@CuO1:1/P25 (Cu signal in green and Ag signal in red).*

EDS line scan signals of Ag and Cu are shown in **Figure V-4**. Different intensities along the different regions of the NPs are clearly observed. The HAADF-STEM images of Ag@CuO1:1/P25 show nanoparticles adsorbed on TiO_2-P25 (**Figure V-4**f, left). Both of the Ag-L and Cu-L peaks demonstrate non-homogeneous dispersion of Ag and Cu atoms where the core is richer in Ag. Therefore, the EDS line scans evidenced the core-shell structure of co-modified samples (**Figure V-4f**, right). The information obtained from high resolution TEM images; HAADF-STEM and EDS analyses confirm the formation of core-shell Ag@Cu (or Ag@CuO) NPs on TiO_2-P25. The Cu–Ag system has a strong tendency to phase separation, due to the large difference in the atom size (r_{Ag}/r_{Cu} = 1.13, where r_M is the atomic radius of metal M), and the difference in the cohesive energies between the two metals E^{coh}_{Ag} - E^{coh}_{Cu} = 0.55 eV (the biggest atom (Ag) being the less cohesive).[163] This phase segregation has already been reported for the system Ag-Cu.[158,164,165,166] This surface segregation of silver and copper was also studied by Monte Carlo simulations.[164,166] Previous studies have shown that a system at thermodynamic equilibrium possesses silver as shell around copper core.[167] Our system is out of equilibrium and it is suggested that silver is reduced before copper leading to Ag_{core}-Cu_{shell} NPs. It has also been reported that when Cu is oxidized it segregates to the surface of the system.[168]

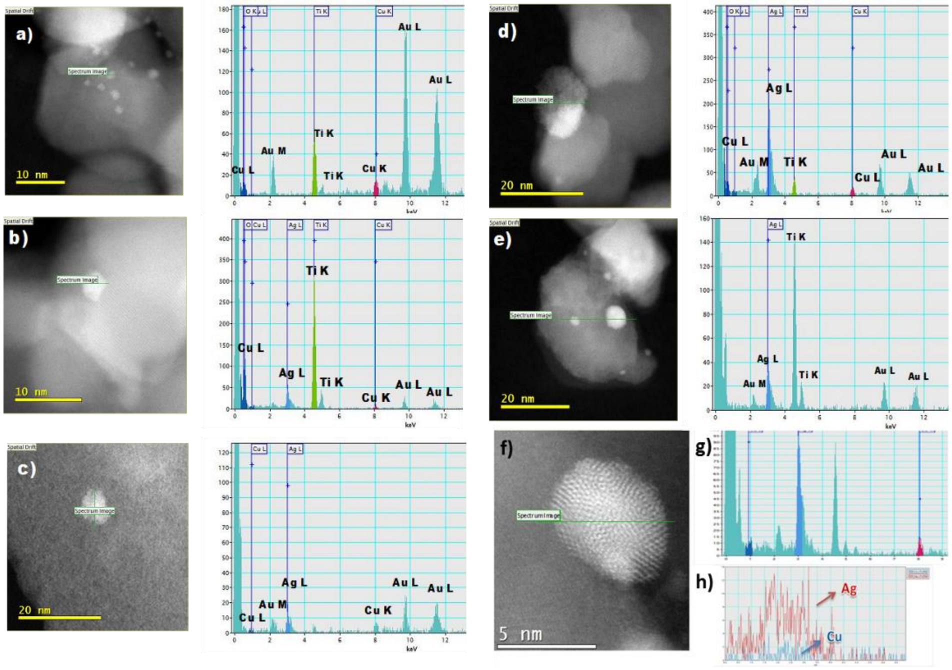

Figure V-4. *Energy dispersive X-ray spectroscopy line scan across external and corresponding STEM images for the samples* ***a)*** *CuO/P25****,*** ***b)*** *Ag@CuO1:3/P25,* ***c)*** *Ag@CuO1:1/P25,* ***d)*** *Ag@CuO3:1/P25 and* ***e)*** *Ag/P25.* ***f)*** *(left) EDS line scan across a nanoparticle of Ag@CuO1:1/P25,* ***g)*** *EDS analysis* ***h)*** *The profile was taken along the green line, (right) the blue graph corresponds to Cu-L and the red one to Ag-L signal.*

In order to analyze the chemical composition of the modified TiO_2-P25 and to identify the chemical state of Cu and Ag elements in the samples, XPS measurements were performed. It was found that samples were homogeneous because the XPS signals from different regions of the sample were very reproducible in both chemical composition and energy distribution as shown in **Figure V-5** and **Table 7**.

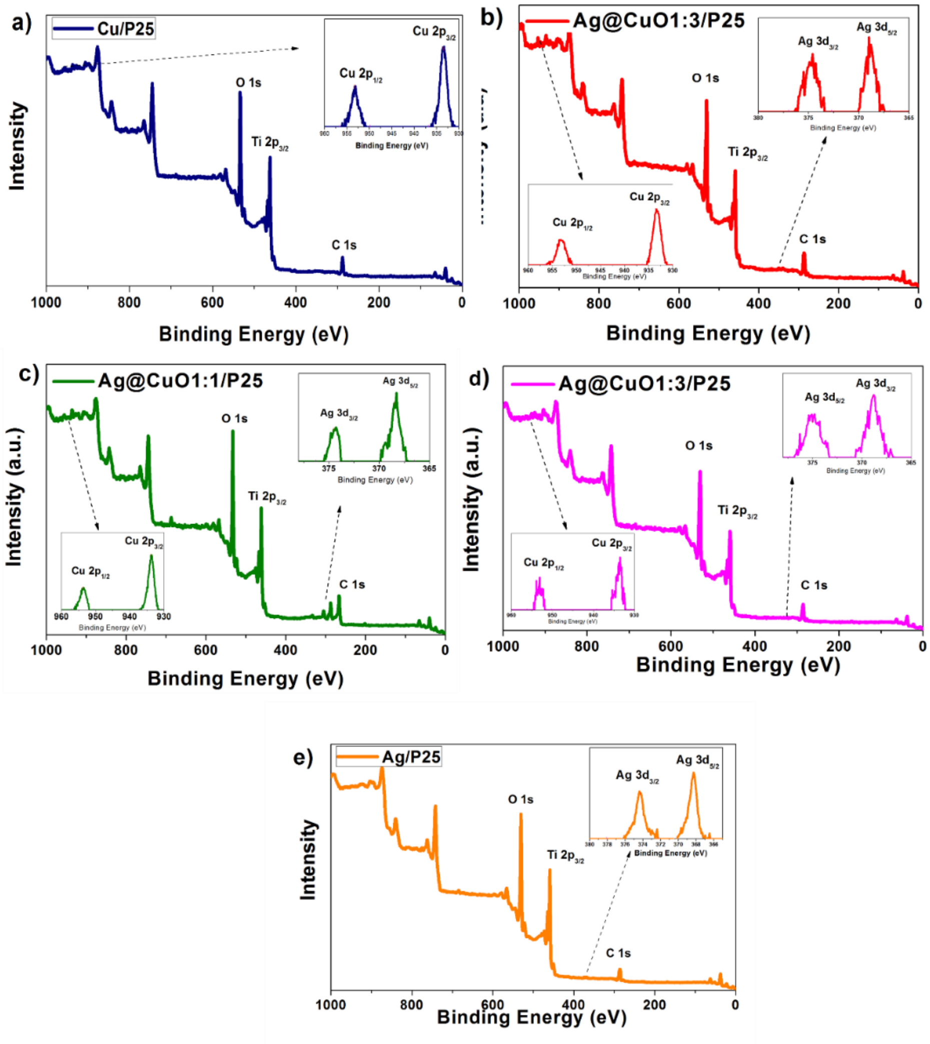

__Figure V-5.__ XPS spectra of TiO_2-P25 modified with Ag, Ag@CuO ratios and CuO.

The Ti *2p* peaks are characteristic of Ti^{4+} in TiO_2 with two main components at 459.5 and 465.5 eV related to Ti $2p_{3/2}$ and Ti $2p_{1/2}$ orbitals and the O *1s* peaks at 530.5 eV attributed to oxygen of TiO_2. The Ag *3d* core peaks are splitted into two components, Ag $3d_{5/2}$ and Ag $3d_{3/2}$, due to spin-orbit coupling (ΔBE(Ag $3d_{5/2-3/2}$) = 6eV), and the binding of the Ag $3d_{5/2}$ core peaks is characteristic of metallic silver.[6,169,170] In **Figure V-6a**, the Ag-modified TiO_2-P25 exhibits, at the Ag *3d* level, two reproducible peaks (at around 368.3 and 374.5 eV), which are typical of the $3d_{5/2}/3d_{3/2}$ spin–orbit splitting of Ag. The Ag $3d_{5/2}$ binding energy at peak maximum at 368.3 eV corresponds to the value reported for metallic Ag.[6,170,171,172] However, the broadening of the peak width is noticed when compared to that of pure metal for the same recording conditions. This feature is due to additional contributions associated to other chemical Ag environment. The small additional peaks at higher binding energy localized at 368.6 eV and 374.6 eV cannot be related to silver oxides (which are known to present a positive shift in the binding energy),[6,171,172,173] and then they may correspond to the interaction of Ag NPs with the TiO_2 substrate as it has been previously reported.[6]

In the same way, two components Cu $2p_{3/2}$ and Cu $2p_{1/2}$ are observed for the Cu core peaks.[142,174] In **Figure V-6b**, the BE positions of Cu $2p_{3/2}$ core levels are in the range of 933.4 – 933.5 eV. These positions are closer to the positions of CuO (Cu^{II}),[142,148] rather than Cu^0 , however the satellite peak characteristic of CuO (or Cu^{II}) is not observed or is very weak, and this behavior is presented in all the samples containing Cu (Fig.3b-d and S4-1). As it was explained in **Ch. 4**, the positions of the XPS peaks are sensitive to the cluster size, and especially for very small clusters (size < 3 nm).[144,175]

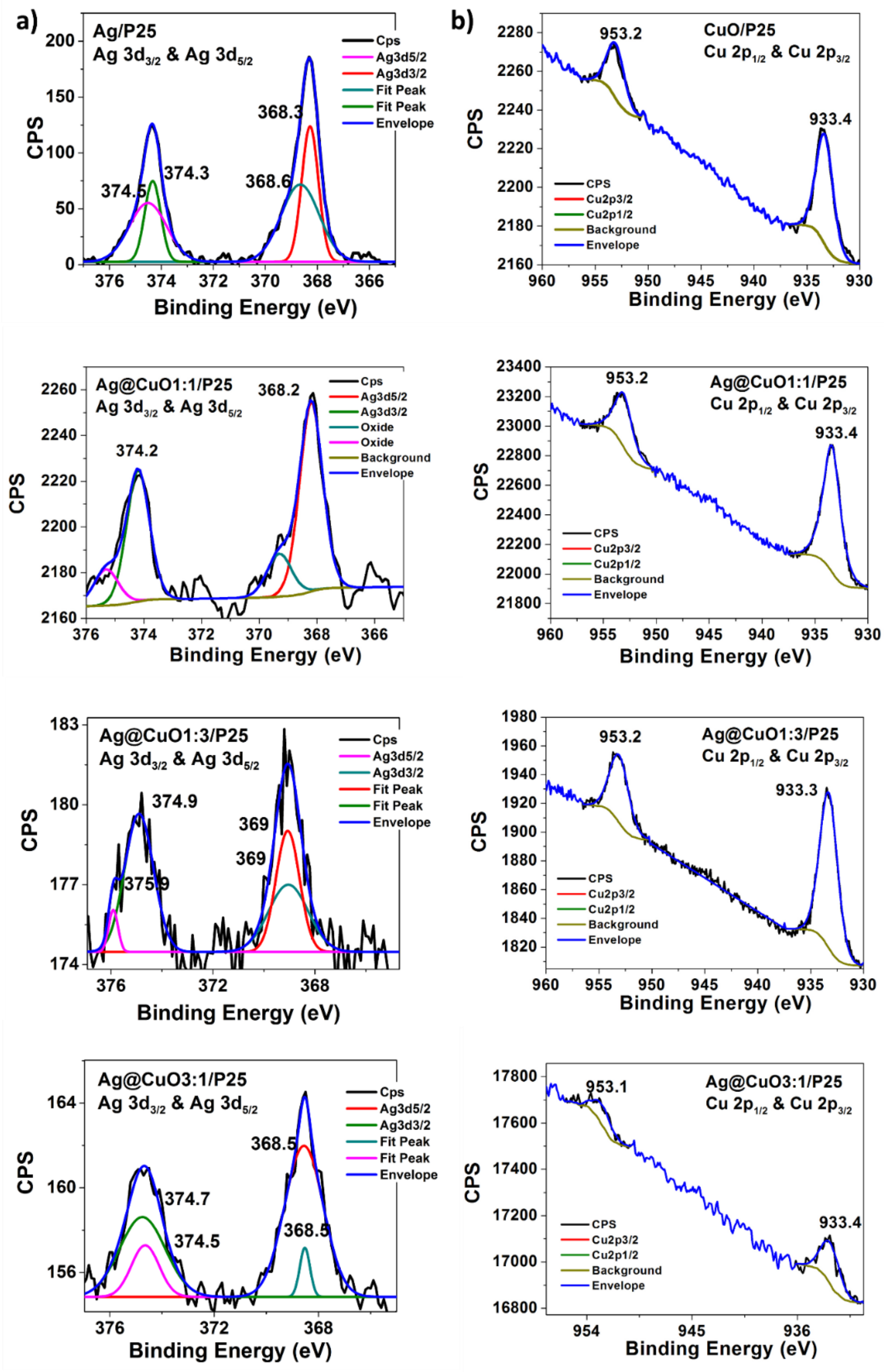

Figure V-6. *XPS spectra for* ***a)*** *Ag 3d and* ***b)*** *Cu 2p of the modified with Ag/P25, Ag@CuO/P25, CuO/P25 samples.*

Table 7. *Binding energies of CuO/P25, Ag/P25 and Ag@CuO/P25 samples determined by XPS showing the binding energies of Ag-3d, Cu-2p, Ti-2p, O-1s.*

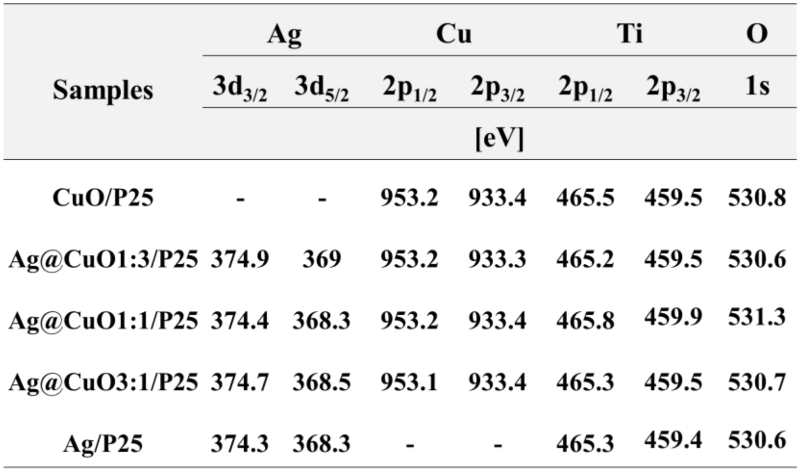

Samples	Ag		Cu		Ti		O
	$3d_{3/2}$	$3d_{5/2}$	$2p_{1/2}$	$2p_{3/2}$	$2p_{1/2}$	$2p_{3/2}$	1s
				[eV]			
CuO/P25	-	-	953.2	933.4	465.5	459.5	530.8
Ag@CuO1:3/P25	374.9	369	953.2	933.3	465.2	459.5	530.6
Ag@CuO1:1/P25	374.4	368.3	953.2	933.4	465.8	459.9	531.3
Ag@CuO3:1/P25	374.7	368.5	953.1	933.4	465.3	459.5	530.7
Ag/P25	374.3	368.3	-	-	465.3	459.4	530.6

Therefore, Cu K-edge XANES spectra were measured in order to corroborate the oxidation states of Cu deduced from XPS. It has been found that the energy position of the rising edge of the spectra and shape of white line for all the TiO_2-P25 modified with copper (Cu alone or associated with Ag) are characteristic of Cu^{II} species,[145] as shown in **Figure V-7**.

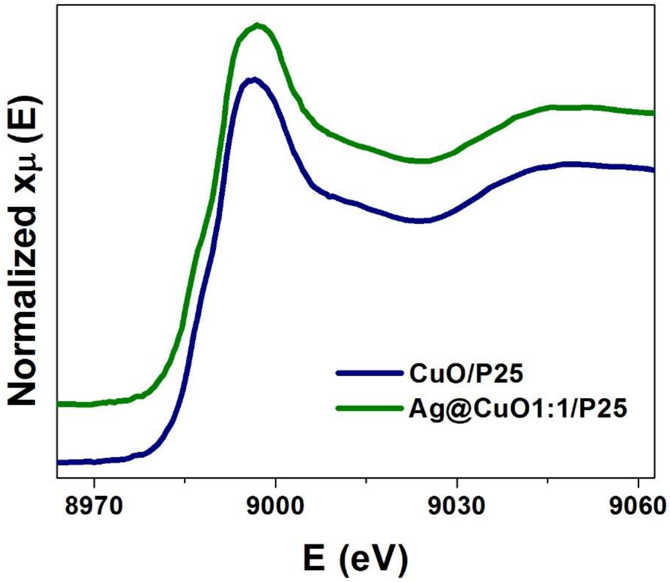

Figure V-7. *CuK-edge XAS spectra for CuO/P25 and the co-modification of Ag@CuO1:1/P25.*

Solvated electrons induced by radiolysis are very strong reducing species able to reduce non-noble metals, which are difficult to reduce by chemical methods.[100,146,147] Silver and copper ions are reduced on TiO_2-P25 by solvated electrons and alcohol radicals.[6,146] However, copper clusters are sensitive to oxygen and are most probably very fast oxidized in air. Thus, the Ag_{core}-Cu_{shell} nanoparticles turn into Ag@CuO in air. **Figure V-8a** shows an aberration corrected HAADF-STEM image of Ag@CuO(1:1)/P25 sample allowing to distinguish two different elements, *i.e.*, Ag and Cu, based on the brightness of the image. Accordingly, as well as results from XPS and XAS results, a representative scheme of this core-shell structure on the TiO_2-P25 surface is depicted in **Figure V-8b**.

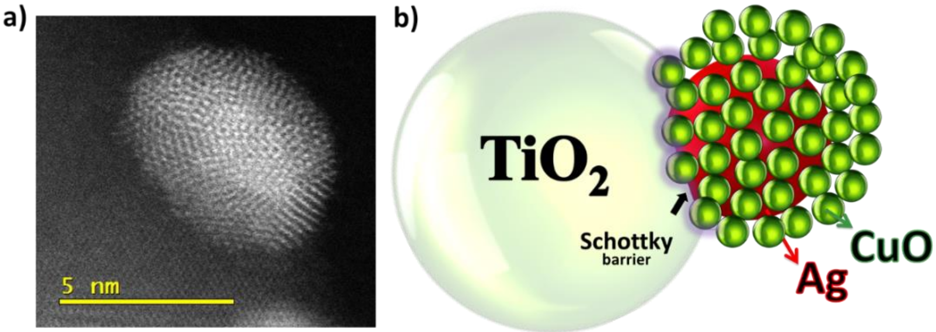

Figure V-8. a) *Representative aberration corrected STEM-HAADF image for an Ag@CuO1:1 particle supported on TiO_2-P25, showing Ag-NPs covered with an ensemble of CuO clusters, and* ***b)*** *A schematic morphology of the modified TiO_2–P25 with Ag-CuO nanoparticles.*

The optical properties of the modified TiO_2-P25 were studied by DRS. **Figure V-9** shows the spectra of bare and modified TiO_2-P25. The spectrum of TiO_2-P25 shows an absorption edge at around 400 nm due to the presence of rutile.[112] The DRS spectra of the modified samples exhibit a slight shift in absorption to longer wavelengths for all surface-modified photocatalysts. This effect has already been reported for TiO_2-based materials modified with Pt-, Pd-, Ag-, and Au-Cu,[6,8,77,176] and could be attributed to stabilization of the CB of TiO_2-P25 by the interaction with the Ag NPs and CuO nanoclusters. The modified samples absorb in the visible and near infra-red (IR) region, while bare TiO_2-P25 does not. Note that absorption with a maximum at 510 nm was obtained with Ag/P25 while a large absorption band with a maximum at 800 nm was observed for CuO/P25.

These absorptions result in pink and yellow colors of the modified TiO_2-P25 samples. TiO_2-P25 co-modified with Ag and CuO absorbs in the visible and near IR. The maximum absorption in the visible region is respectively at 480 nm for

Ag@CuO1:3/P25, and 470 nm for Ag@CuO1:1/P25 and Ag@CuO3:1/P25 (see **Figure V-9**). The absorption in the IR is very broad with a maximum at ca. 800 nm for the two samples rich in CuO (Ag@CuO1:3/P25 and Ag@CuO1:1/P25), while the sample Ag@CuO3:1/P25 shows no maximum absorption in this region. Ag NPs are known to exhibit a LSPR with a maximum around 410 nm in water. It is well known that the position of LSPR depends on the environment and the support.[177] Therefore, red-shift of LSPR is usually observed as a result of coupling between the metal nanoparticles and TiO_2 support having a high reflective index (the absorption coefficient and refractive index for anatase at a wavelength of 380 nm are 90 cm^{-1} and 2.19, respectively), as already reported for Au/TiO_2, Ag/TiO_2 and Au-Cu/TiO_2. [2,6,8,113] The addition of CuO to TiO_2-P25 extends clearly the absorption to visible light. The absorption band in the near IR is observed in the case of Cu loading, and this is attributed to $2E_g \rightarrow 2T_{2g}$ inter-band transitions in the Cu^{II} clusters deposited on different phases and sites of TiO_2 and with strong interaction with the support.[148]

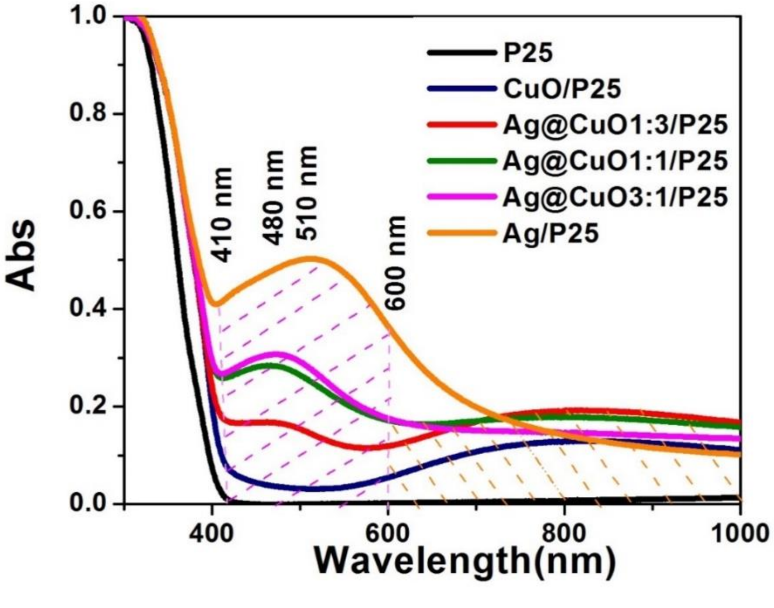

Figure V-9. *UV-Vis diffuse reflectance spectra of pure TiO_2-P25 and modified TiO_2-P25 with Ag, CuO and Ag@CuO at different molar ratios showing the regions of the plasmon band of Ag and the absorption band of CuO.*

The electronic properties of the samples were studied by the TRMC technique at different wavelengths considering both UV and visible regions. The excitation wavelengths were 355, 400, 450, 470, 480, 550, 600 and 650 nm and the corresponding laser energy were 1.7, 0.9, 6.7, 6.2, 5.8, 4.5, 2.5, and 1.7 mJ respectively. The graphs are shown in **Figure V-10**. The surface modification with Ag and/or CuO-NPs shows a strong influence on the charge-carriers dynamics in TiO_2-P25**.**

TRMC signals show that under UV excitation at 355 nm (**Figure V-10a**), all the photocatalysts are activated, *i.e.*, free electrons are induced in the CB of TiO_2-P25, as shown by the sharp increase of TRMC signal, reaching I_{max} values. However, the decay of the signals is faster for the modified samples. The TRMC signals are mainly related to the electron having higher mobility than holes. The decrease of the TRMC signals after modification is probably caused by efficient electron scavenging by Ag nanoparticles deposited on TiO_2-P25, resulting in decrease in the recombination of charge-carriers (e^-/h^+). Silver nanoparticles scavenge electrons, but these electrons can react with oxygen leading to $O_2^{\bullet -}$ radicals. It has to be noted that oxygen presents the trend to adsorb on silver, and this will help the formation of superoxide radicals. At the same time, and because of better separation of charge-carriers, more holes and $HO^{\bullet}$ radicals are generated. It should be pointed out that faster decay is observed for TiO_2-P25 co-modified with Ag NPs and CuO clusters, and this acceleration increases with the amount of CuO (**Figure V-10a**). The photogenerated electrons can be trapped by Cu^{II} (due to the unfilled 3d shell, $t_{2g}^{6}e_{g}^{3}$ configuration), on the surface of TiO_2-P25, decreasing the recombination process.[149] The TRMC measurements show that Ag@CuO nanoparticles [Ag@CuO(1:3) and Ag@CuO(1:1)] are very efficient in electron scavenging (see **Figure V-10a**) due to the synergic effect between Ag and CuO.

This acceleration of the signal decay, with metal exhibiting capacitive properties, has also been observed for the modification of TiO_2-P25 with Ag clusters and NPs, Au-NPs and Au-Cu-NPs.[6,8,157] This observation is different from previous results in the group with Pt and Pd modified TiO_2, where a slowdown of the overall decay was observed.[4,77,178] Indeed, with metals such as Pt and Pd, the experimental data agree with the model of a simple Schottky-type barrier between TiO_2 and metal. An increase in the lifetime of the electrons is observed, due, as expected, to a better separation of charge carriers caused by the barrier.[178]

Nonetheless, an important change is observed in the TRMC signals when the samples were irradiated at 400 nm (**Figure V-10b**), *i.e.*, at the transition between the UV and the visible regions. For TiO_2-P25, Ag/P25 and Ag@CuO3:1/P25, the I_{max} values are lower than those obtained under 355 nm as expected since the irradiation energy is lower than the band-gap of anatase, and thus only the rutile phase, being in the minority, can be activated. However, the samples containing copper reach a higher I_{max} value, which represents a higher amount of free electrons in the CB of TiO_2-P25. This is consistent with the shift of the band-gap toward the visible region observed by DRS for these samples compared to bare TiO_2-P25.

Under excitation in the visible region, there is no light absorption by pure TiO_2-P25 because of its large band-gap. Under excitation with wavelengths of 450, 470, 480 and 550 nm, TRMC signals are obtained with the samples modified with CuO due to its narrow band-gap, attesting the generation of free electrons in the conduction bands of TiO_2-P25 (**Figure V-10c**-**h**). The highest I_{max}, for all irradiation ranges, is obtained for TiO_2-P25 modified with CuO (sample CuO/P25). This suggests that a large amount of excess electrons are injected in the CB of TiO_2-P25 after excitation of the metal oxide clusters. Thus, under visible light, copper oxide is excited, and then electrons from its CB are transferred to the CB of the TiO_2-P25. This excitation of CuO induces also the same large amount of holes located on these clusters. However, the decay of the TRMC signals is very fast in the case of CuO/TiO_2 (**Figure 7b**-**c**). This fast decay is probably due to fast recombination of the electrons injected from CuO in the conduction band of TiO_2 with excess holes located on the numerous CuO clusters. However, for Ag@CuO co-modified samples, it should be reminded that silver-based NPs are still working as electron traps decreasing the signal with the Ag loading. In this case, the electron coming from excited CuO are not injected in the conduction band of TiO_2, but they are trapped by Ag NPs. These electrons probably recombine very fast with the holes located on CuO because of the large concentration of CuO on Ag NPs. It must be pointed out that electron transfer from silver NPs could not be excluded since TRMC operates at longer times (μs) than plasmonic excitation, *e.g.*, 240 fs was reported for electron transfer from 10-nm size gold to titania.[179.] At longer wavelengths (600 and 650 nm) (see **Figure V-10g** and **h**) only small signals for the samples with larger amount of copper, *i.e.*, Ag@CuO1:3/P25 and CuO/P25 were detected.

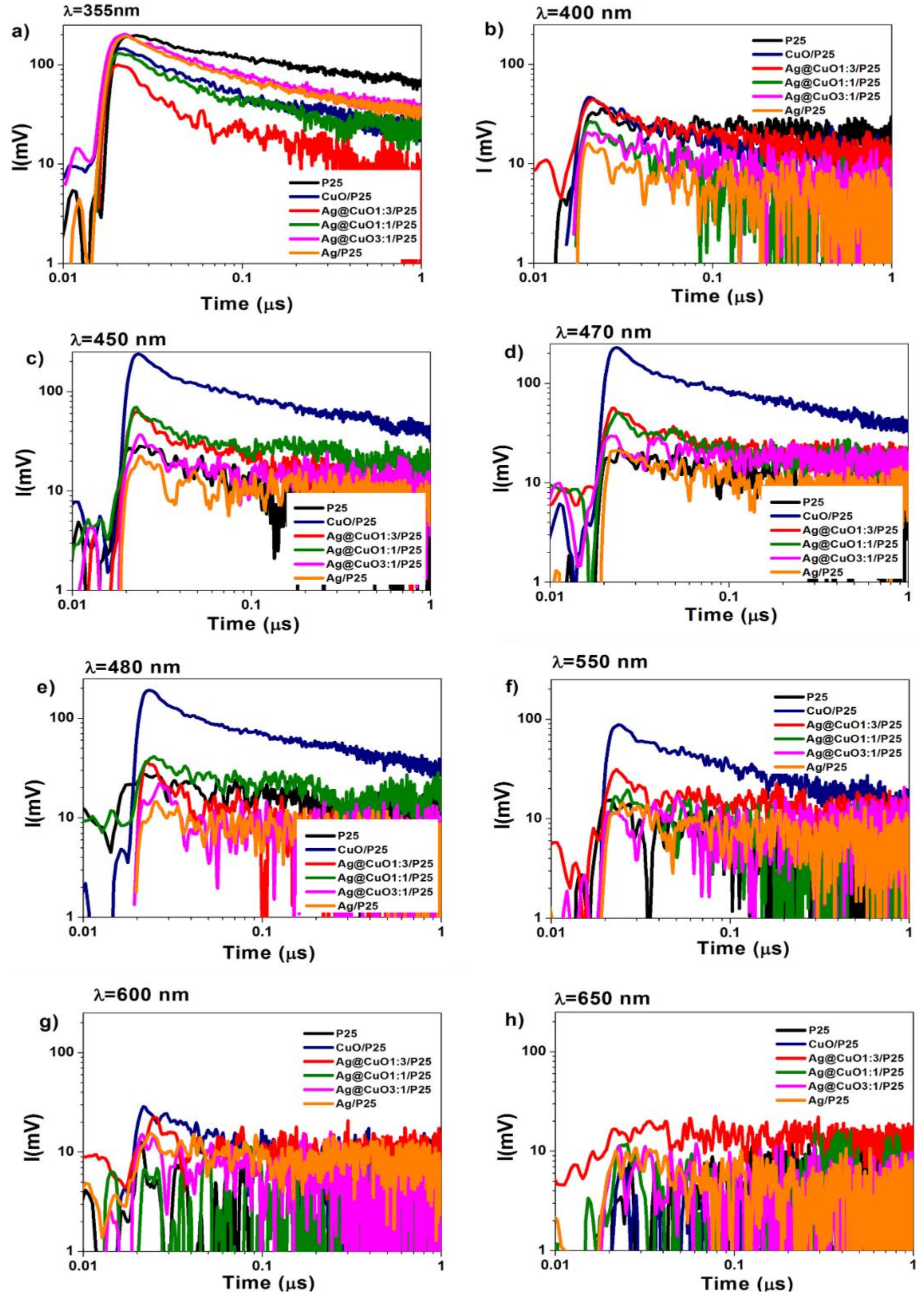

Figure V-10. *TRMC signals obtained after excitation at 355, 400, 450, 470, 480, 550, 600 and 650 nm of* TiO_2*-P25 bare and modified systems with, Ag, Ag@CuO and CuO.*

These results show that under visible light excitation, electrons are promoted from CuO-NPs to the CB of TiO_2-P25. Also, it is worth noting that copper oxide clusters are able to activate the TiO_2-P25 photocatalysts in a wider range of wavelengths under visible light irradiation, compared to the activation with the presence of silver.

5.3 Photocatalytic Tests

5.3.1. Photocatalytic Degradation of Phenol

The photocatalytic activity of the modified TiO_2-P25 samples was evaluated for the degradation of phenol under UV-and visible light.

The curves for phenol degradation are shown in **Figure V-11**. Surface modification of TiO_2-P25 with Ag NPs and CuO clusters does not influence markedly the photocatalytic activity of TiO_2-P25 under UV light. However, an enhancement of the photocatalytic activity is observed for samples modified with Ag@CuO clusters.

Under UV irradiation, (**Figure V-11a**) the Ag-CuO modified titania and Ag@CuO1:1/P25, Ag@CuO3:1/P25, Ag@CuO1:3/P25 achieve complete degradation of phenol after 15 minutes. The kinetic data can be fitted with a pseudo first-order reaction and the estimated reaction rates are shown in **Table 8**. Under UV excitation, the oxidation is due to $HO^•$ and $O_2^{•-}$ radicals, but under visible light the oxidation is mainly due to $O_2^{•-}$ radicals. We considered zero order for visible light and pseudo first order for UV light excitation which fits better the curves following the calculation in **Appendix V**, but it does not have a physical meaning as the mechanism is much more complex.

The higher photocatalytic activity is obtained with the sample Ag@CuO1:1/P25 with a reaction rate of around 5.0×10^{-3} s^{-1}, which is approximately 2 times higher than that of bare TiO_2-P25 (2.5×10^{-3} s^{-1}). This increase in the photocatalytic activity is attributable to the reduction of the recombination process of the charge-carriers due to the electron scavenging by Ag NPs and to the reduction of Cu^{II} into Cu^{I}.[149]

Foster *et al.* found that the oxidation of Cu^{I} into Cu^{II} by O_2 decreased the electron-hole recombination.[150]

These photocatalytic results can be related to the TRMC signals: TRMC data (λ_{ex} = 355 nm) indicate electron sinking by co-modification with Ag and CuO clusters (lower I_{max} and faster decay, **Figure V-10a**) beneficial for the photocatalytic activity.

However, surface modification with Ag and/or CuO-NPs, significantly increases the photoactivity of TiO_2-P25 under visible irradiation.

Under visible light, the photoactivity of the pure TiO_2-P25 is usually very low because the illumination energy is lower than the band-gap energy. Modification of titania results in visible photocatalytic activity, as shown in **Figure V-11b** for phenol degradation. The modification with CuO leads to a slightly higher enhancement in the photocatalytic properties compared to the modification with Ag or Ag@CuO. 25% and 17% phenol degradation are reached after 4-hour irradiation of CuO/P25 and Ag/P25, respectively. Surface modification with silver and copper oxide nanoparticles changes the absorption properties of the photocatalysts, particularly as an enhancement of the absorption in the visible range creating an activity under visible light.

The CuO/P25 sample exhibits the highest photocatalytic activity for phenol degradation under visible light. This photocatalytic activity can be related to the TRMC signal as previously discussed: The CuO/P25 sample showed the highest I_{max} value in a wide range of excitation wavelengths within the visible range (**Figure V-10b-f**), which represents more electrons in the CB of the semiconductor TiO_2-P25. The corresponding kinetics data following a zero order for the degradation of phenol under visible light are shown in **Table 8**. The highest values of the reaction rates are obtained with Ag/P25 and CuO/P25. It has to be noted that the CuO/P25 sample shows a reaction rate seven times higher than bare TiO_2-P25, thus demonstrating the enhancement of the photoactivity of TiO_2-P25 with its surface modification with CuO.

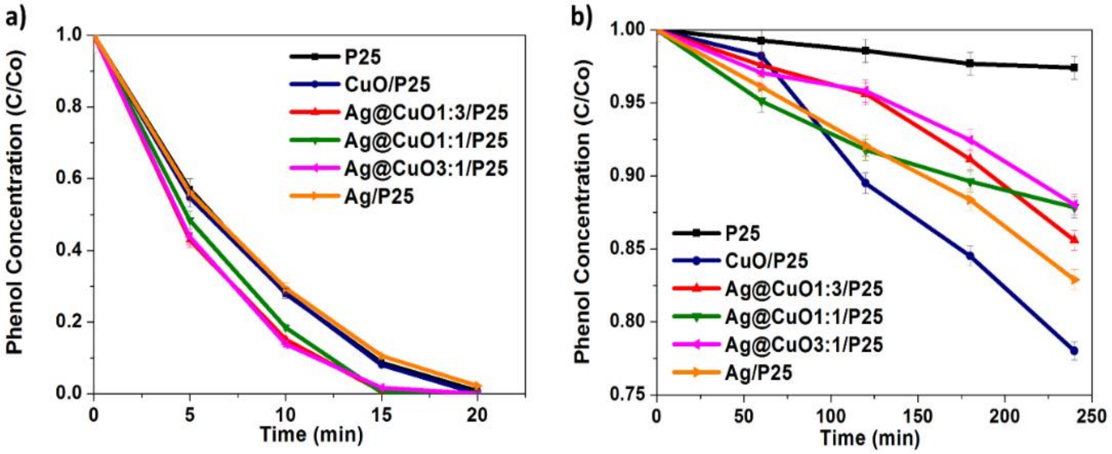

Figure V-11. *Degradation curves of phenol (50 ppm) under **a)** UV and **b)** visible light (λ > 450 nm), for bare and modified (with, Ag, Ag@CuO and CuO) TiO_2-P25, in the ratio $1gL^{-1}$.*

Table 8. *Photocatalytic rates constants for phenol degradation with Ag/P25, Ag@CuO and CuO-NPs under UV irradiation (pseudo first order reaction) and visible light (zero order reaction).*

Sample	**UV light**	**Visible light**
	($x10^{-3}$ s^{-1})	**($x10^{-4}$ M s^{-1})**
P25	**2.5**	**0.9**
CuO/P25	**2.6**	**7.5**
Ag@CuO1:3/P25	**4.1**	**4.7**
Ag@CuO1:1/P25	**3.4**	**3.6**
Ag@CuO3:1/P25	**4.7**	**3.6**
Ag/P25	**2.3**	**5.3**

5.3.2. Acetic Acid Degradation and Action Spectra

The modified TiO_2-P25 samples were also evaluated for the photocatalytic evolution of CO_2 as a result of the decomposition of acetic acid under monochromatic irradiation. Exemplary data for two different irradiation regions, *i.e*., UV at λ = 350 nm, and visible light at λ = 470 nm, are shown in **Figure V-12**.

Figure V-12 shows that the modified TiO_2 samples, are in general more active in the generation of CO_2 compared to bare TiO_2-P25, especially under visible light.

Under UV irradiation at 350 nm (**Figure V-12a**), the modified titania are more active than bare TiO$_2$-P25, TRMC signals at 355 nm show that CuO-based nanoparticles on TiO$_2$-P25 are efficient in electron scavenging (**Figure V-10a**). This higher photocatalytic activity (higher generation of CO$_2$) at 350 nm for TiO$_2$-P25 modified with CuO-based nanoparticles (Ag, Ag@CuO1:3, Ag@CuO1:1 and CuO) can be caused by better charge-carrier separation, with exception of Ag@CuO3:1/P25 sample.

Under visible light at 470 nm irradiation (**Figure V-12b**), surface modified TiO$_2$-P25 with Ag, CuO clusters are more active in the production of CO$_2$ compared to bare TiO$_2$-P25. Surface modification with CuO nanoclusters induces a higher increase in the photocatalytic activity under visible light compared to the modification with plasmonic Ag and Ag@CuO NPs. The highest production of CO$_2$ is again obtained with CuO/P25. Indeed, it has to be noted that CuO/P25 presents a higher TRMC signal at 470 nm compared to Ag@CuO1:3/P25, Ag@CuO1:1/P25 and Ag@CuO3:1/P25, and this indicates that more electrons are generated in the CB of CuO modified TiO$_2$-P25.

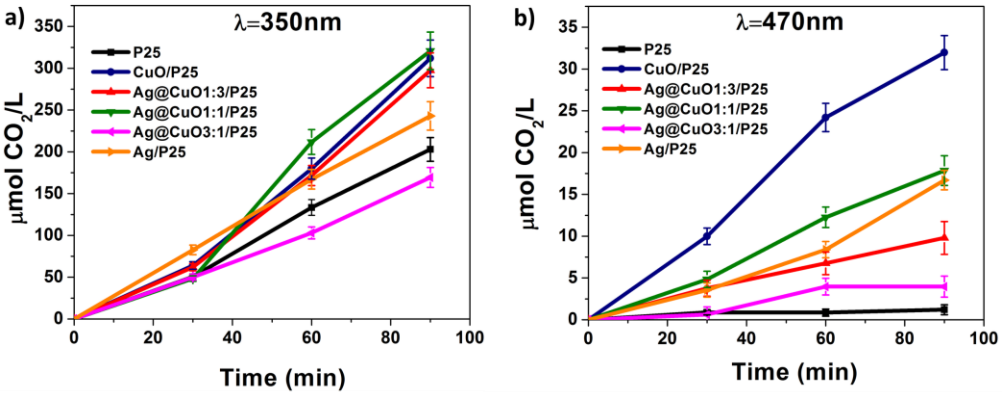

***Figure V-12**. Photocatalytic evolution of CO$_2$ resulting from the decomposition of acetic acid (5 v%) under irradiation with **a)** 350 nm, and **b)** 470 nm of pure system TiO$_2$-P25 and modified systems with, Ag, Ag@CuO and CuO, in a ratio 10 gL^{-1}.*

Based on acetic acid decomposition at various monochromatic irradiations, the AS of the synthesized samples were obtained, and the results are shown in **Figure V-13**. The samples containing mainly CuO/P25 exhibit higher activity than bare TiO$_2$-P25 under UV irradiation. In the visible range, the modified TiO$_2$-P25 with Ag and CuO show higher apparent quantum efficiency in the range between 410–500 nm, which can be related to the LSPR of silver or/and to the injection of electrons from CuO in the CB of TiO_2-P25.

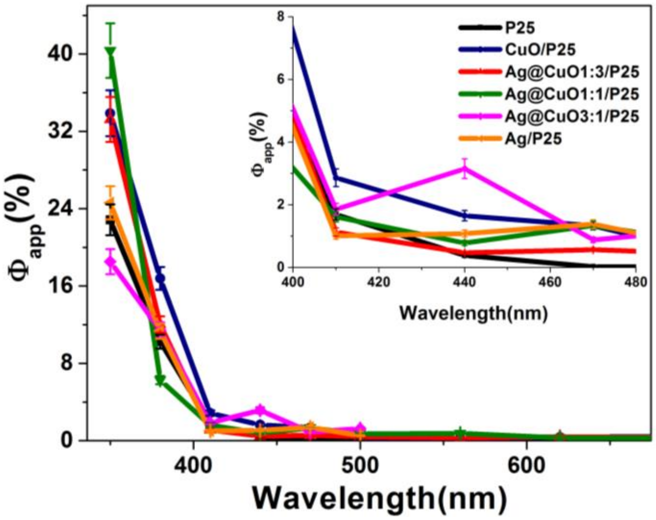

Figure V-13. *Action spectra for the acetic acid decomposition on bare and modified TiO_2-P25 (with Ag, Ag@CuO different ratios and CuO).*

It has to be noted that, under visible light, for both phenol degradation and CO_2 generation, the modification with CuO induces the higher photocatalytic activity.

These results are shown in **Figure V-11b** and **Figure V-12b**. In the case of CuO/P25, CuO is in direct contact with TiO_2-P25, and a high amount of electrons are directly injected from CuO into the CB of TiO_2-P25 as is shown by the TRMC signals under excitation with the visible light. However, in the case of TiO_2-P25 modified with Ag@CuO, the CuO shell is deposited on Ag nanoparticles. Under visible light excitation, the electrons cannot be directly injected from CuO into the CB of TiO_2-P25, due to the interaction of the $Ag_{core}@CuO_{shell}$ structure. This is consistent with the TRMC signals under visible excitation, which are lower for Ag@CuO/P25 than for CuO/P25 (**Figure V-10b-h**), affecting the photoactivity as is shown in most of the tested reactions, where the activity of Ag@CuO/P25 samples is lower than that of Ag/P25 and CuO/P25.

The AS was compared to the absorption spectra obtained by DRS (**Figure V-14**) and they indicate that the photoreaction is carried out by a photocatalytic mechanism.[153]

Action spectrum correlates well with absorption spectrum for bare titania, reaching quantum yield of 22.8%, 10.2% and 1.7% for irradiation with 350, 380 and 410 nm, respectively. However, for the modified samples only part of the absorption spectra (below 480 nm) correlates with their photocatalytic activity, reaching a maximum at 470 nm, which confirms that LSPR of Ag NPs and the narrow band gap of CuO are responsible for the photocatalytic activity under visible light irradiation.

CuO/P25 and Ag@CuO/P25 exhibit no photocatalytic activity at λ > 500 nm (negligible quantum efficiency) but present small TRMC signals: We hypothesized that these generated electrons with lower energy are mobile but inactive for degradation of organic compounds or these electrons are reactive but with lower quantum yield.

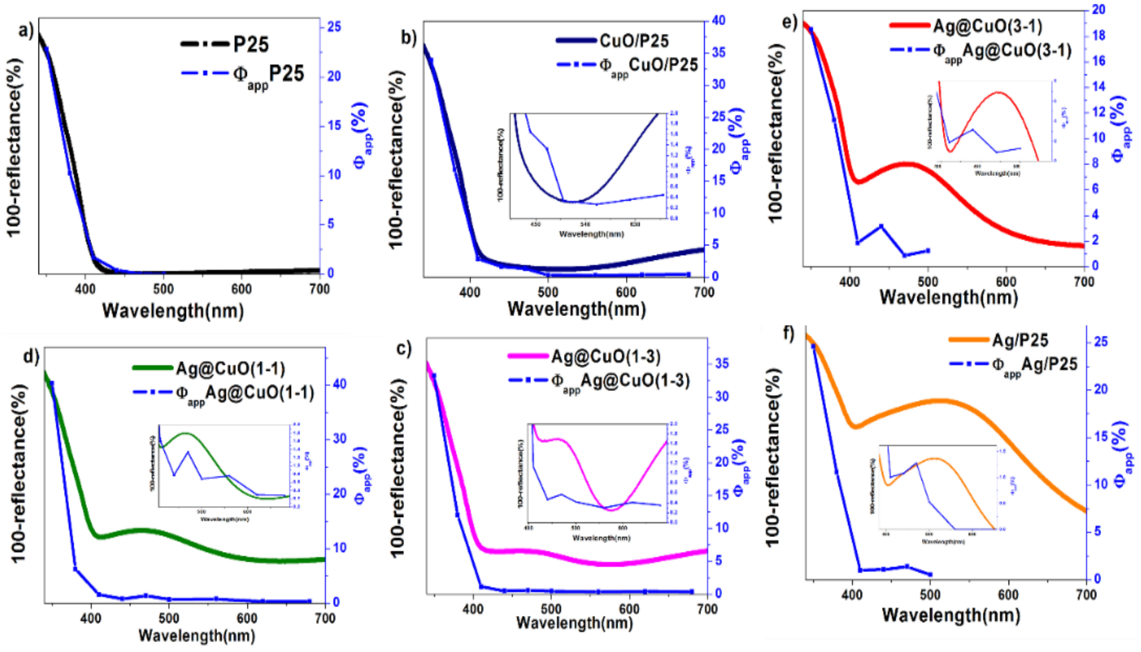

Figure V-14. *Comparison between the action spectrum and the DRS spectrum for the used samples:* ***a)*** *pure TiO2-P25;* ***b)*** *CuO/P25,* ***c)*** *Ag@CuO1:3/P25,* ***d)*** *Ag@CuO1:1/P25,* ***e)*** *Ag@CuO3:1/P25, and* ***f)*** *Ag/P25.*

It is important to mention that the DRS of dried Ag-modified samples differ from suspended ones,[12,157] showing a red-shift, due to enhanced scattering, which is highly dependent on the particle size and shape[72] contrasting with Au/TiO_2 systems, that shows almost the same DRS.[74]

These combined results by TRMC and AS sheds light on the photocatalytic mechanism: Under UV light, the Ag nanoparticles and CuO clusters work as electron pools, retarding the recombination process as it is supported by TRMC results. This scavenging phenomenon helps to increase the photoreactions due to the formation of the Schottky junction when Ag and CuO are in contact with the semiconductor TiO_2-P25. It is known that coupling of TiO_2 with other semiconductors of different redox energy levels can lead to a more efficient charge-carrier separation process, *i.e;* an increase in the lifetime of the charge-carriers and an enhancement of the interfacial charge-transfer efficiency to adsorbed substrate.[47,52] It is proposed that electrons trapped by CuO would react with adsorbed oxygen or air retarding (or inhibiting) the electron-hole recombination.[149] TRMC signals show that Ag@CuO nanoparticles are more efficient in electron scavenging compared to the Ag NPs and CuO clusters, and this leads to higher photocatalytic activity under UV light.

Under visible light excitation, TRMC signals and AS show that Ag NPs, due to their surface plasmon resonance and CuO due to its narrow band gap (1.7eV)[47] induce an activity in the visible. It has to be noted that this energy band-gap value increases with the size of CuO, *e.g*., Ge *et al*. had reported that for CuO nanoclusters, the band-gap decreases from 2.6 eV to 1.4 eV when the size increases from 1.1 nm to 2 nm.[154] The CuO clusters are excited under visible light injecting electrons in the CB of TiO_2-P25. In case of CuO/P25, more electrons are injected compared to the other modified samples and this corresponds to higher photocatalytic activity under visible light. However, the photocatalytic activity under visible light of TiO_2-P25 co-modified Ag@CuO clusters is lower than that of CuO/P25 and Ag/P25. This behavior is probably due to the electron scavenging by Ag, instead of transferring the electrons to the CB of titania.

5.3.3. 2-Propanol Degradation Under Visible Irradiation

The samples, were analyzed in the degradation of 2-propanol under visible light with λ ≥ 450 nm. The results are shown in **Figure V-15**, where it can be seen that a higher amount of copper induces a decrease of the photoactivity.

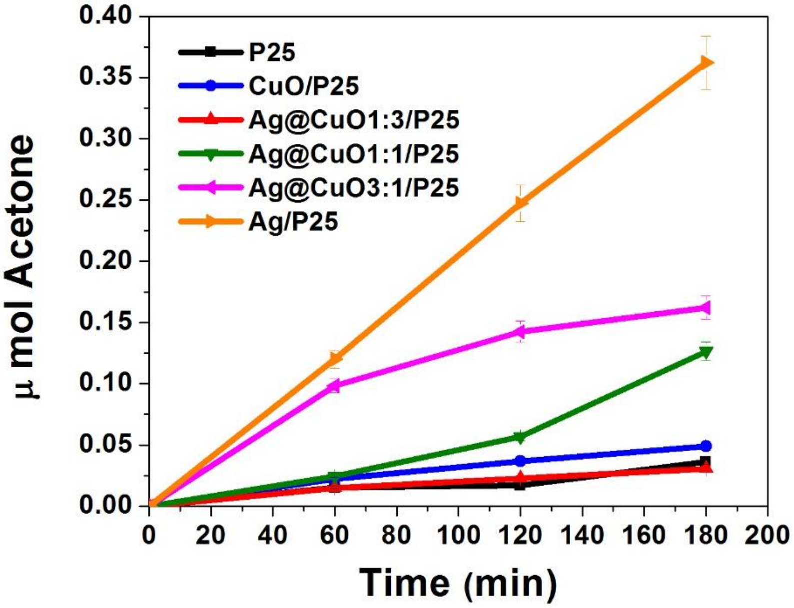

Figure V-15. *Oxidation of 2-propanol (5 v%) under visible light irradiation with pure and modified TiO_2-P25 with silver (Ag) and copper oxide (CuO) in a ratio 10 gL^{-1}.*

5.3.4. Photocatalytic Production of Hydrogen (H_2)

These samples were evaluated in the PWS process for the hydrogen generation, at 470 nm under visible irradiation (**Figure V-16**). In this case, TiO_2-P25 and CuO/P25 do not present activity, but the addition of Ag NPs activates TiO_2-P25 for H_2 production. However, with the increase of amount of CuO and Ag NPs the production of hydrogen increases. The maximum H_2 production was obtained with Ag@CuO ratio of 1:1 (0.25 μmol g^{-1} s^{-1}). Metals with higher work function than that of TiO_2 increase the Schottky barrier effect, which help to decrease the electron–hole recombination. The work functions of Ag is 4.26 eV and for CuO (5.3 eV) are higher than that of TiO_2 (4.2 eV).[9,131] It has to be noted that these values are for bulk materials and vary with the size of the NPs and the support.

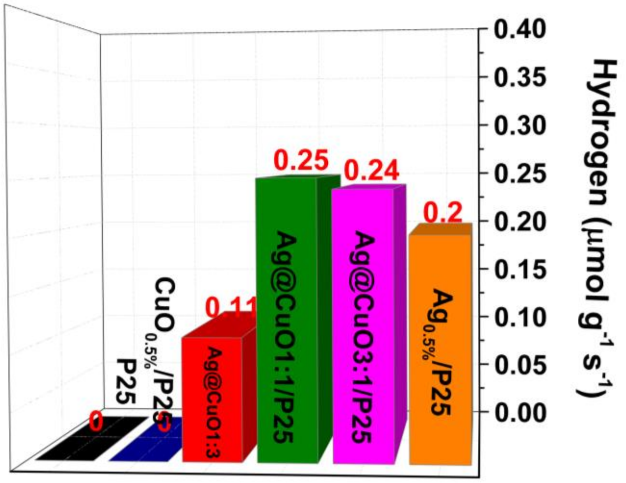

Figure V-16. *Photochemical H_2 generated by methanol dehydrogenation (25 v%) with pure TiO_2-P25 and surface modified TiO_2-P25 with Ag and/or CuO, irradiated with a LED at 470 nm, in a ratio of 1 gL^{-1}.*

In this type of test, TiO_2-P25 is not efficient because its VB position (see **Figure I-26**) is very similar to the reduction level of hydrogen, but the addition of small nanoparticles can induce a much higher change of the Fermi level compared to larger particles, and this change is an indication of a larger charge separation and improved reduction potential for the photocatalyst and the metal/TiO_2 interface.

TRMC signals suggest that electrons are injected in the conduction band of TiO_2-P25 under visible irradiation due to the narrow band gap of CuO and the LSPR of Ag NPs. However, the higher amount of injected electrons from CuO, does not increase the degradation of 2-propanol nor hydrogen production. However, the co-modified TiO_2 and Ag enhance the Hydrogen production, perhaps due to the amount of CuO that was not enough (as we observe in **Ch. 4**), or the addition of Ag NPs serve as sites to catalyze atomic hydrogen ($H^{\bullet}$) in the formation of H_2.

5.3.5. Mechanism of Charge-Carriers Dynamics Under UV and Visible Light

All the above discussed results allow us to propose photoinduced mechanisms for TiO_2-P25 modified with CuO and Ag@CuO nanoparticles under UV and visible light irradiation, and they are shown in **Figure V-17**. Under UV irradiation (**Figure V-17a**), the number of charge-carriers decreases due to the relaxation of CB photogenerated electrons on TiO_2-P25 to the valence band (VB) of CuO, acting in this system as electron traps. The photocatalytic activity is similar to TiO_2-P25 for phenol degradation, but is higher at 350 nm for acetic acid degradation. (**Figure V-11a**, and **Figure V-12a**). Under visible irradiation (**Figure V-17b**), due to the position and the value of the energy band-gap of CuO, visible light photo-generates electrons from CuO, and these electrons are injected into the CB of TiO_2-P25, as it can be observed in TMRC signals in **Figure V-10b**)-**c**) at 450 nm and 470 nm. The photoactivity is always higher than TiO_2-P25 for all the modified samples (**Figure V-11b**, and **Figure V-12b**). For Ag@CuO/P25, in **Figure V-17a**) under UV irradiation, the Ag@CuO-NPs scavenge electrons (as shown by the TRMC signal at 355 nm, **Figure V-10a**), which induces an increase in the photoactivity (see **Figure V-11**, phenol degradation), due to the fact that Ag NPs work as electron traps for both TiO_2-P25 and CuO semiconductors.

When the systems are irradiated under visible light, (**Figure V-17b**), Ag NPs still work as electron traps, trapping the electrons photogenerated by CuO avoiding a part of injection to the CB of TiO_2-P25, decreasing the TRMC signals, and thus decreasing the photoactivity.

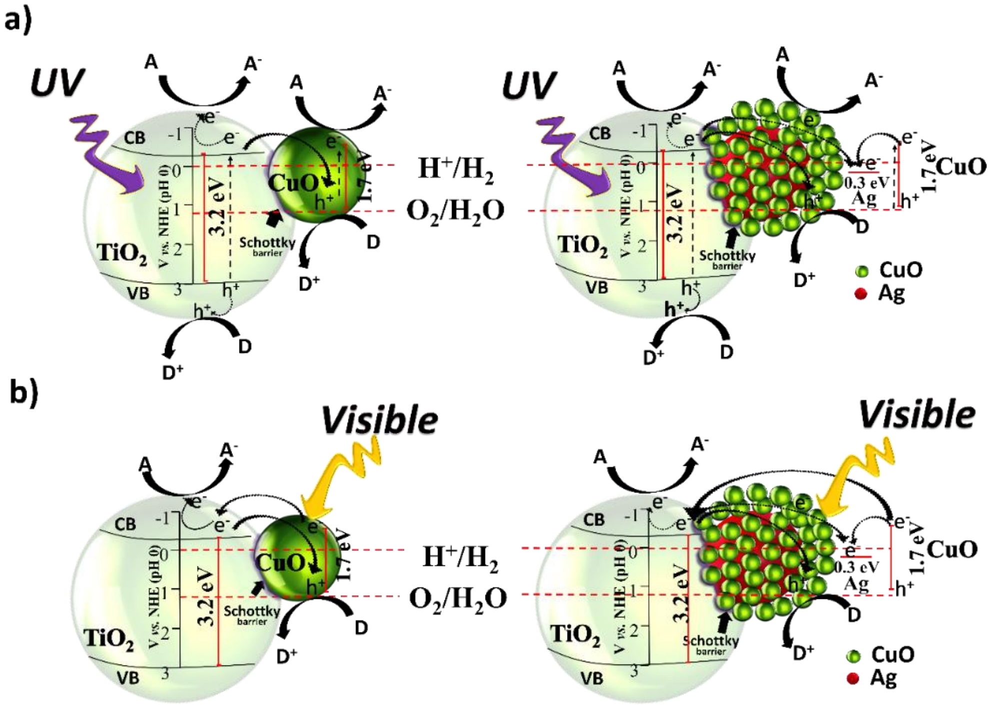

Figure V-17. Proposed photocatalytic mechanisms for TiO_2*-P25 modified with CuO and Ag@CuO,* ***a)*** *under UV and* ***b)*** *under visible irradiation.*

5.3.6. Anti-Fungi Properties

The antifungal properties of pure and modified TiO_2-P25 were investigated by mycelium (vegetative part of a fungus, consisting of a mass of branching, thread-like filamentous structure of a fungus) growth in the dark and under visible light irradiation. Two fungis were used: *Aspergillus Melleus* and *Penecillium Chrysogenum*. The rate of fungal daily growth was evaluated in dark and under visible light, in the media composed of bare and modified (with Ag Ag@CuO and CuO).

Figure V-18 shows the fungal daily growth for *Aspergillus Melleus* and this daily growth is also observed in a control media (no titania or blank). TiO_2-P25 presents an activity only under light irradiation. As we know, TiO_2-P25 is a mixture of two crystalline phases anatase and rutile. Its suggested that rutile of TiO_2-P25 is mainly responsible for titania activity under visible irradiation, due to its narrower band–gap (1.7 eV), and thus ability of visible light absorption. The highest inhibition for this fungi is obtained with Ag@CuO/P25 with the ratio 1:3: A synergystic effect with co-modification with Ag and CuO NPs is obtained. With this sample, the growth inhibition is higher in dark.

It should be pointed that the presence of Ag NPs (Ag@CuO3:1/P25 and Ag/P25) accelerated the growth under dark.

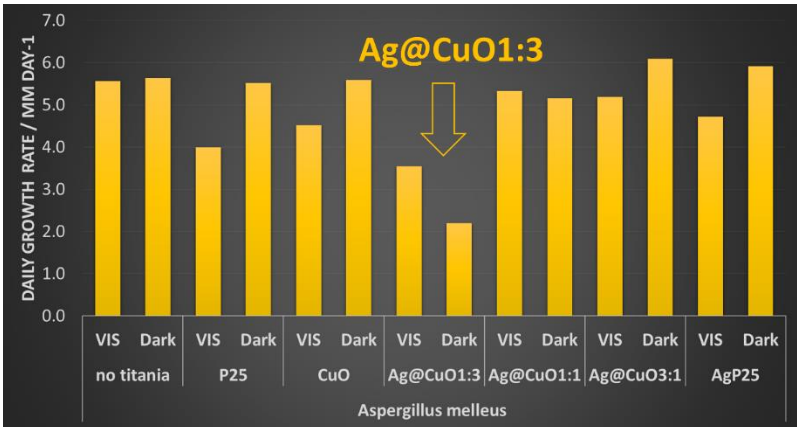

Figure V-18. *Antibacterial daily radius growth under visible (vis) and dark for the fungi Aspergillus Melleus.*

The decrease of the fungus growth diameter and the change of the color of the spores, using TiO_2-P25 and Ag@CuO1:3 is shown in the **Figure V-19**.

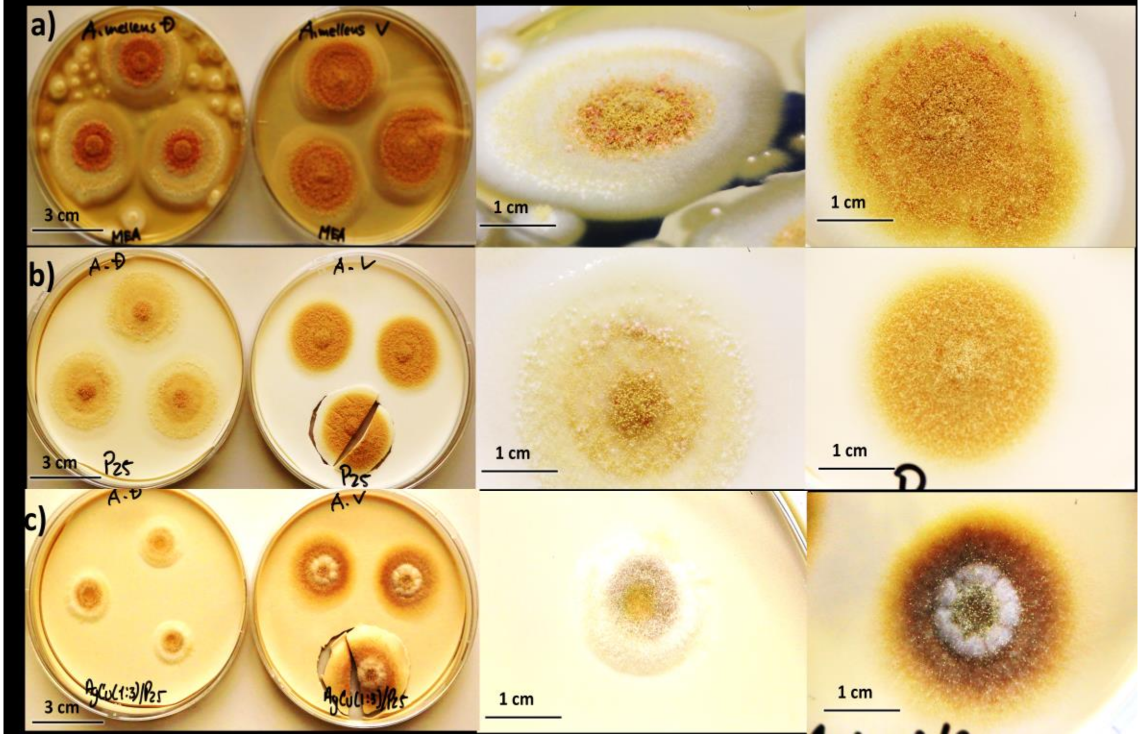

Figure V-19. *Photographs of mycelium growth of Aspergillus Melleus fungi after 8 days incubation of* ***a)*** *blank (no titania),* ***b)*** *P25, and* ***c)*** *AgCu1:3/P25 under visible light and in dark. The left picture: a picture at scale of the fungi growth, and the right picture: the extension of a mycelium.*

We observed that the sporulation and mycotoxin generation (as formed droplets) for the sample Ag@CuO1:3 was highly inhibited in dark and under visible exposition as shown in the **Figure V-20**. One can see clearly the reduction of the number of spores and the decrease of their diameters in air, which is crucial for preventing against the impact of mycotoxins on human health. Mycotoxin production is associated to sporulation, and it has been documented in several articles that mycotoxigenic generate for example *Aspergillus*.[156]

A slight decrease of the sporulation and mycotoxin generation is presented with TiO_2-P25. With titania modified with Ag@CuO1:3, no mycotoxin is detected and highly less sporulation was observed.

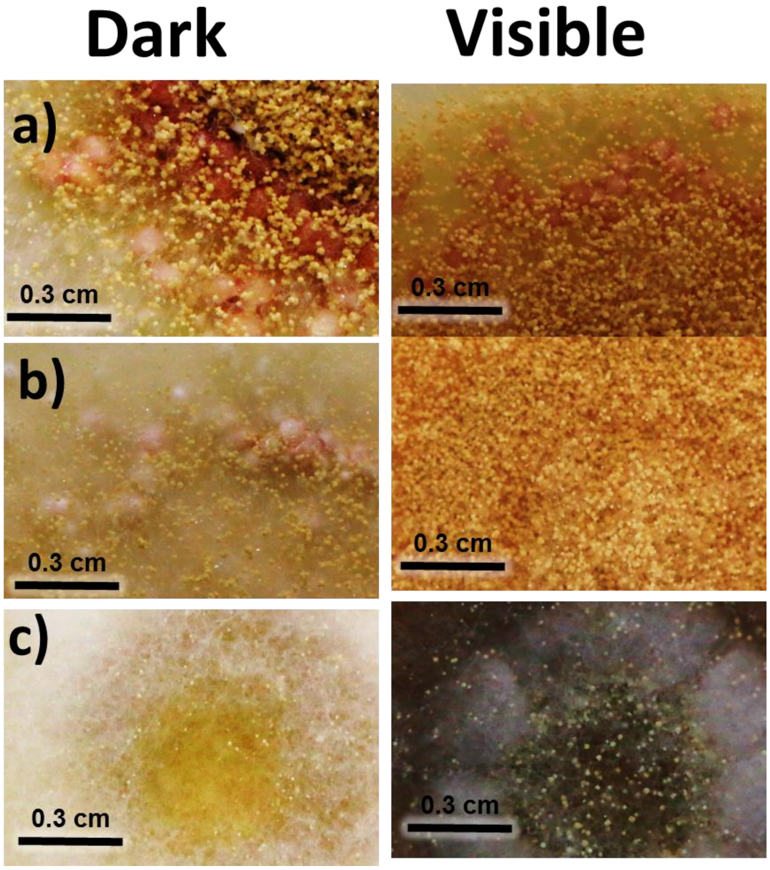

Figure V-20. *Picture of 8-day growth of Aspergillus melleus in the dark and under visible irradiation.* ***a)*** *under media (blank),* ***b)*** *TiO_2-P25, and* ***c)*** *Ag@CuO1:3.*

In **Figure V-21** the fungal daily growth for *Penicillium Chrysogenum* is shown. The growth is higher in dark than under visible light in a control media (without titania), and the pure and the modified samples accelerated the growth of the fungi under visible irradiation. As discussed in **Ch. 4**, the anatase phase can stimulate the fungal growth because of its superhydrophilic properties. Under dark, all the modified samples show an inhibition in the growth, with the exception of CuO-NPs, and a synergystic effect is obtained with co-modification with silver and copper oxide: The Ag@CuO/P25 sample with the ratio1:3 presents the higher inhibition for this fungi growth.

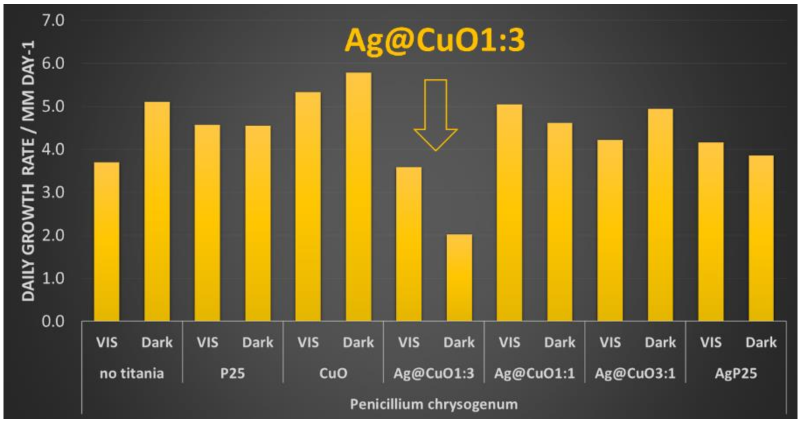

Figure V-21. *Antibacterial daily radius growth under visible (vis) light and in dark for Penicillium Chrysogenum fungi.*

The pictures in **Figure V-22** show the changes of the fungus diameter and of the color of the media, with bare and modified (with Ag@CuO1:3) TiO_2-P25. The inhibition of fungal growth by non-irradiated TiO_2-P25 could be caused by its absorption on the fungal surface, and this could result in inhibition, according to Calvo *et al*.[156]

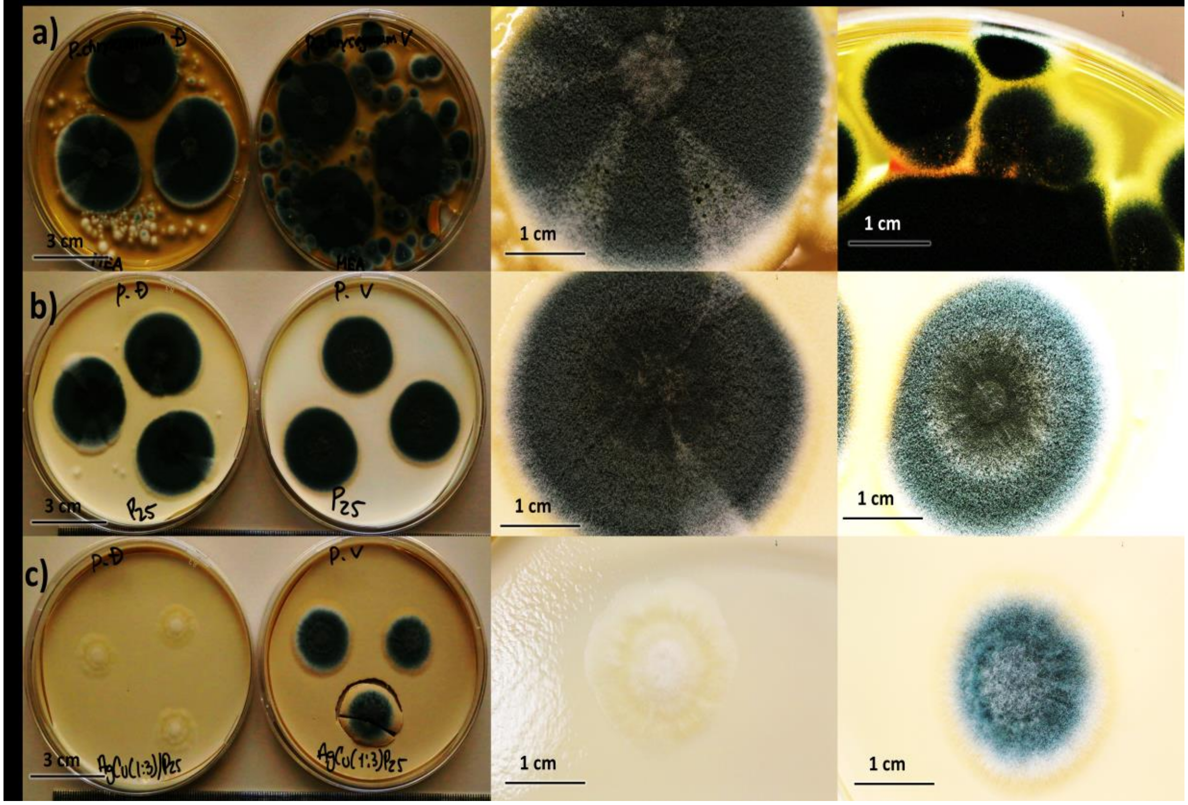

Figure V-22. *Photographs of mycelium growth of Penicillium Chrysogenum fungi after 8 days incubation of a) blank (no titania), b) P25, and c) AgCu1:3/P25 under visible light and in dark. In the left: a picture at scale of the fungi growth, in the right picture the extension of a mycelium.*

In the **Figure V-23**, we can see that the mycotoxin is only present on the media support (blank). The presence of TiO_2-P25 inhibits the formation of droplets of mycotoxin under visible light and dark with Ag@CuO3:1/ P25, inhibition of the sporulation and mycotoxin is observed after 8 days of exposition under visible light but mostly under dark.

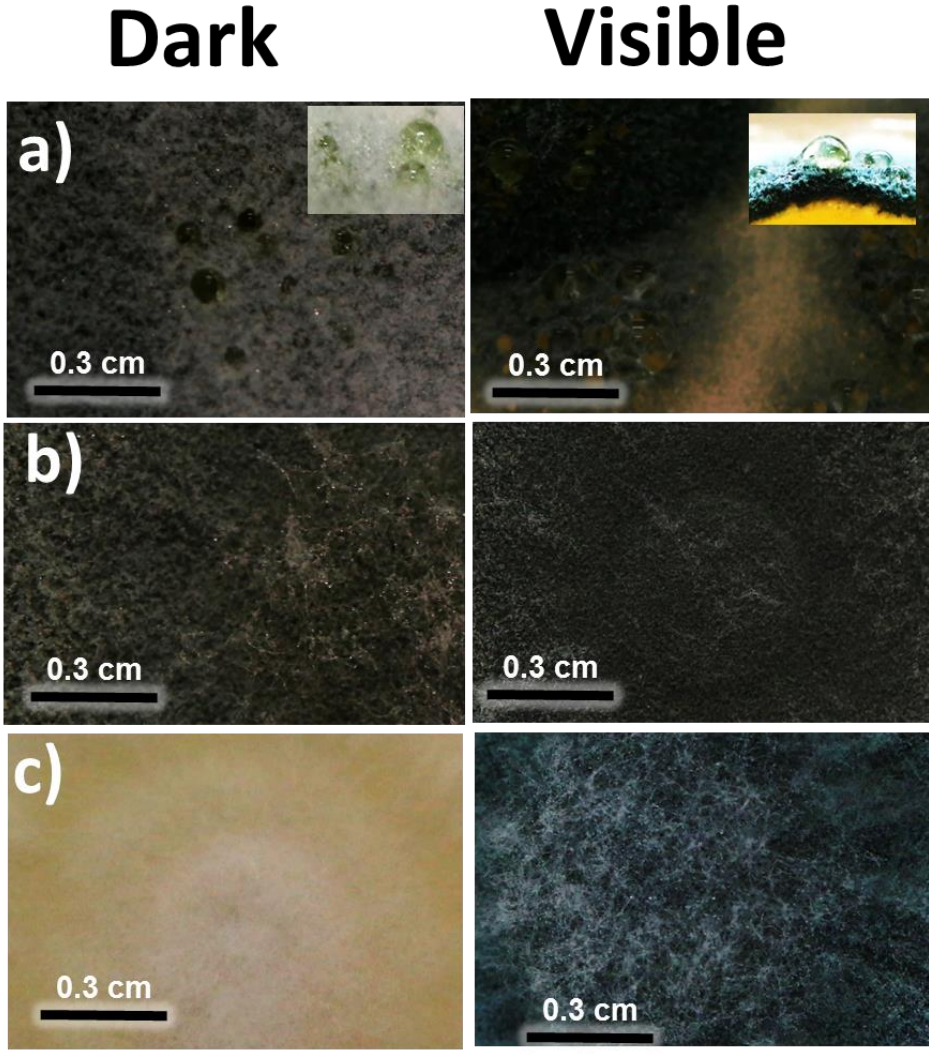

Figure V-23. *Picture of 8-day growth of Penicillium Chrysogenum in dark and under irradiation.* ***a)*** *Under media,* ***b)*** *TiO$_2$-P25, and* ***c)*** *Ag@CuO1:3.*

Different results were obtained with *Aspergillus Melleus* and *Penicillium Chrysogenum*. Indeed, it was reported by Markowska-Szczupak *et al*. that the antifungal properties of titania depend significantly on the nature of the fungi.[155]

The sample Ag@CuO1:3/P25 is the one that presents the best growth inhibition for both fungis in dark and under visible light exposition.

TiO$_2$-P25 and CuO/P25 show inhibition of droplets of mycotoxin for *Penicillium Chrysogenum*, but the system Ag@CuO1:3 is the sample that presents the best inhibition of growth of both fungis in dark and under visible exposition.

5.4 Conclusions

CuO clusters, Ag and Ag@CuO-NPs were synthesized by radiolysis on the surface of TiO_2-P25. HAADF-STEM, XPS and XAS characterizations have shown that, in case of co-modification with silver and copper, core-shell nanoparticles composed of silver cores decorated with small CuO clusters were obtained on TiO_2-P25. Surface modification with Ag, Ag@CuO and CuO nanoparticles induces an enhancement in the photocatalytic activity of TiO_2-P25, under both UV and visible light. Catalytic testing for phenol and acetic acid degradation show that co-modification of TiO_2-P25 with CuO and Ag nanoparticles induces a higher photocatalytic activity under UV light compared to single modification with only Ag or CuO clusters, while the contrary is obtained under visible light. Under visible light, CuO-modified titania exhibits higher activity rather than the plasmonic Ag/P25 and Ag@CuO. TRMC results show that under excitation with UV light, metal Ag NPs, Ag@CuO and CuO clusters act as electron traps decreasing the recombination process, and thus, they present a highly increment in the apparent quantum yield. Under visible excitation, the Ag nanoparticles absorb incident photons due to the LSPR and inject electrons into the CB of TiO_2-P25, as it is shown by TRMC measurements. CuO are excited in the visible range because of their band gap, and the electrons are driven from the CB of CuO to the CB of TiO_2-P25.

In general, the photocatalytic activity of the samples containing CuO is higher, which induces a photocatalytic activity in a wider spectral range compared to that obtained with modification with silver.

Action spectra prove that decomposition of acetic acid is driven by a photocatalytic reaction, and Ag and CuO modification results in a high enhancement of quantum yield under UV and visible light irradiation. However, only a shorter part of visible absorption (< 500 nm) is responsible for photocatalytic activity. For the oxidation reactions tested in this study under visible light irradiation, surface modification of TiO_2-P25 with Ag@CuO clusters leads to samples with lower activity compared to Ag/P25 and CuO/P25.

For the degradation of 2-propanol and for hydrogen production, the photocatalytic activity increases with loading in Ag and CuO.

In the case of co-modification with Ag and CuO, the increase in H_2 production is mainly due to the increasing amount of Ag and CuO, and also that Ag NPs retarding the recombination process and thus increasing the activity.

The antifungal properties of titania modified with copper oxide and silver were studied. The highest antifungal properties were obtained with the sample Ag@CuO1:3/P25 under dark and visible light exposition. A synergy effect for anti-fungal properties was obtained with co-modification of titania with Ag and CuO for both *Aspergillus Melleus* and *Penicillium Chrysogenum* fungis.

Chapter VI

General Conclusions and Perspectives

Chapter 6. General Conclusions and Perspectives

The surface modification of TiO_2 with one or two metal-based nanoparticles, with small sizes (d < 5 nm), has an important effect on the semiconductor properties, changing its photocatalytic activity.

TiO_2 surface modification with noble metal nanoparticles such as Ag and Au (so called plasmonic photocatalysts) has attracted a lot of interest. The most important features of these noble metal and semiconductor composites are the induction by light excitation of electrons into the CB induced by the LSPR, and the metal-semiconductor junction (Schottky barrier), providing different and new properties to TiO_2. Firstly, the modified TiO_2-P25 can be activated under visible light, because of the LSPR of Ag and Au and electrons can be injected in the conduction band of TiO_2-P25, either by electron transfer or by energy transfer. Secondly, the presence of Au or Ag improves the absorption, and the local electric field is enhanced. The third feature, is the formation of the Schottky junction, formed when the noble metal nanoparticles have direct contact with the semiconductor. This Schottky junction enhances the charge transfer and also enhances considerably the separation of the photo-excited electrons and holes, that facilitates the electron transfer or decreases the electron-hole recombination. All these modifications lead to increase of the quantum yield, and therefore the photoactivity will be improved under UV and visible light.

Very small and homogenous nanoparticles were synthesized on titania by radiolysis or by the THPC method.

Time resolved microwave conductivity and action spectra were very useful techniques to understand the charge carrier dynamics and the photocatalytic mechanisms.

The modification with small nanoclusters of CuO provides a less expensive option to enhance the activity of TiO_2 under UV and particularly under visible irradiation. This enhancement of the photoactivity is due to the narrow band gap of

CuO, capable of being activated under the visible region, and electrons can be injected from CuO into the conduction band of TiO_2, or according to the positions of the energy band gaps, the CuO clusters could work as electron traps, though this modification (heterojunction) is less stable with recycling than the modification with noble metal nanoparticles. The modification with the small clusters of CuO shows high TRMC signals under a wide visible range of wavelengths because of injection of electrons from CuO to the CB of TiO_2-P25, and the amount of injected electrons increases with the CuO loading. Under UV irradiation, the TRMC signals decrease proving that electrons can be trapped by CuO nanoclusters. Furthermore, AS show that the modified sample present higher quantum yield than bare TiO_2-P25 under UV and visible region. This evidences that the addition of a semiconductor with a narrow band gap such as CuO (*Type II* assembly), leads to enhancement of the electron transfer and activation of the SC under visible light, and under UV irradiation leads to a decrease of the recombination process.

The coupling with two metal-based NPs with a core-shell structure, such as Ag@CuO/P25, increases the photoactivity under UV irradiation because of the Ag and CuO properties to trap the electrons photogenerated from TiO_2 and CuO. On the other hand, we observed that under visible irradiation in the systems of AgCuO/P25, the photogenerated electrons from CuO are trapped by Ag NPs avoiding a direct transfer of electrons to TiO_2. These electrons probably recombine very fast with the large numbers of holes located on the numerous CuO clusters, decreasing thus the quantum yield.

We can firmly state as general conclusion that the plasmonic photocatalysts (Ag, Au and Ag@CuO) and the herterojuntion with nanoclusters of CuO, activate TiO_2 under visible light, which was one of our objectives, and that these modified photocatalysts can be used in degradation of organic pollutants and in generation of hydrogen as a new energy source. Besides these applications, these photocatalysts display antifungal properties, a synergy effect for anti-fungal properties was obtained with the co-modification Ag@CuO(1:3) on titania for both *Aspergillus Melleus* and *Penicillium Chrysogenum* fungis, under dark and visible light exposition.

These materials could also be used for other applications such as CO_2 reduction, water oxidation etc.

There are still major issues that need to be addressed before photocatalysis can become a viable, efficient and widely accepted process, especially for industrial applications. Still important and practical problems remain such as long term stability and reliable characterization of the photocatalysts performance through standardized reactor geometries and test protocols. Additionally, fundamental properties of photocatalyst materials still need deep understanding and improvement, such as materials design parameters that affect photocatalytic performance, including *i)* Electronic structure; *ii)* Surface structure; and *iii)* Crystal structure.

In our systems there are many things to do to improve their photocatalytic activity, for example we can try to increase the yield in a wide range of the visible light. The main efforts for research groups worldwide working on the subject remain in the general improvement of light absorption, and the extension of light absorption of the semiconductor materials into the visible portion of the solar spectrum.

Modifications with other metals such as: the junction of AgAu (alloy or core-shell structure) or with another semiconductor, such as Bi_2O_3 are interesting options to investigate due to their response and stability under visible light. Preliminary results show that these systems are very promising for degradation of pollutants under visible light.

Appendices

Appendix I: Panoramic Gamma Ray Source

The γ-irradiation source used, is a panoramic cobalt (^{60}Co) source, located in the *Laboratoire de Chimie Physique* (LCP) at *Université Paris-Sud, Orsay*. This is a stores panoramic ^{60}Co source in cylindrical bars in a lead container which withdrawals by is remotely controlled from the control room. When the gamma ray source is working, the cobalt bars will rise from a deep well (vertically placed in the column, (see **Figure A1**). The samples are put on the platform, and the dose rate depends on the distance of the sample to the column. When the irradiation is completed (the irradiation time can be fixed), the cobalt bars sank down to the deep well filled with deionized water.

The radiation chamber is enclosed by thick walls and a radial protective sliding lead door. Samples of different volumes from a few microliters to several liters can be irradiated.

Figure A1. *Panoramic gamma source of the Laboratoire de Chimie Physique, Université Paris-Sud.*

Appendix II: Determination of the Radiolytic Yield

The reduction yield is the number of reduced species (metal atoms multiplied the by the valence of the precursor in our case) formed per absorbed dose, $G_{e_{aq}^{-}} = 0.28\, \mu mol J^{-1}$, $G_{H} = 0.057\, \mu mol J^{-1}$, $G_{HO^{\cdot}} = 0.29\, \mu mol J^{-1}$.

Thus, for a solution containing low metal salt concentrations, the maximum reduction yield for an aqueous containing oxidant radical scavengers like 2-propano l is:

$$G_{red}(max) = G_{e_{aq}^{-}} + G_{H^{\cdot}} + G_{HO^{\cdot}} \approx 0.627\, \mu mol J^{-1} \qquad \textbf{(A. 1)}$$

Therefore, in the case of a metallic salt solution with a concentration (C_0) and oxidation state (Z), the minimum dose (D_{min}) for the complete reduction can be presented as follow:

$$D_{min} = \frac{Z C_0 (mol L^{-1})}{G_{red}(max)(mol L^{-1})} \qquad \textbf{(A. 2)}$$

The absorbance of plasmonic metal nanoparticles increases with the dose of irradiation before reaching a plateau when all the metal ions are reduced. According to Beer-Lambert law: $A = \varepsilon l c$, the concentration (C) of ions reduced by a dose of irradiation (D) can be deduced from the absorbance (A).

The plateau (A_{max}) towards which the curve bends at high dose is due to the total reduction of the metal ions to atoms (**Figure A2.**). Supposing that the final concentration of the metal atoms is equal to the initial concentration (C_0) of the metal ions, the molar extinction coefficient can be deduced from the A_{max}:

$$\varepsilon = \frac{A_{max}}{C_0 l} \qquad \textbf{(A. 3)}$$

Assuming the molar extinction coefficient (ε in L mol^{-1} cm^{-1}) of the metal at a certain wavelength is a constant whatever the aggregation state and the size (what is in fact not really exact), we can deduce the radiolytic reduction yield (linear part of the curve A = f(*D*), **Figure A2.** :

$$G = \frac{Z}{\varepsilon l} x \frac{\Delta(A)}{\Delta(D)} \qquad \textbf{(A. 4)}$$

The curve, C = f(*D*) can be deduced from the absorbance spectra (if ε does not change with the size of the aggregates) recorded at different doses.

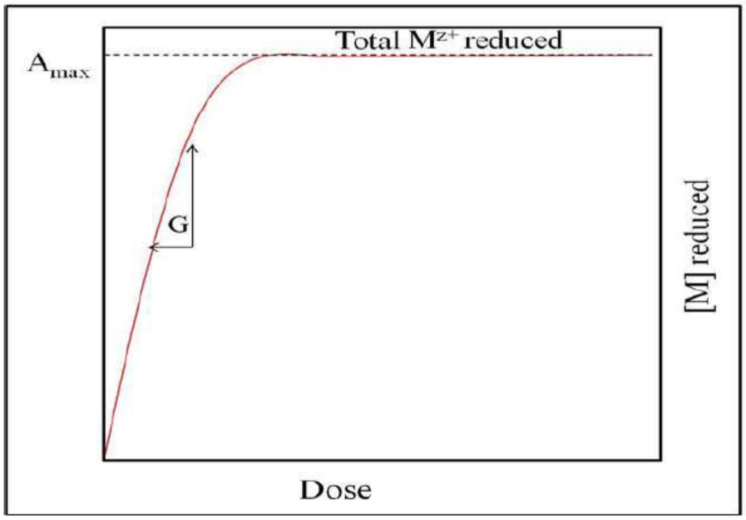

Figure A2. *Evaluation of the advancement of radiolytic reduction as a function of the dose absorbed by the sample.*

Fricke Dosimetry

The dosimetry of Fricke is used to measure the absorbed dose for another low-LET beam quality the accuracy of the absorbed dose measurement is limited by the uncertainty in the value of *G*(Fe^{3+}). The value of *G*(Fe^{3+}) is around 20 and 30 MeV) for ^{60}Co gamma-rays.[180]

$$\mathrm{H_2O} \xrightarrow{\gamma - ray} e^-_{aq}, \mathrm{H_3O^+}, H^\cdot, HO^\cdot, H_2, H_2O_2 \qquad \textbf{(A. 5)}$$

$$Fe^{2+} + H_2O_2 \rightarrow Fe^{3+} + HO^- + HO^\bullet \qquad \textbf{(A. 6)}$$

$$Fe^{2+} + HO^\bullet \rightarrow Fe^{3+} + HO^- \qquad \textbf{(A. 7)}$$

$$H^{\bullet} + O_2 \rightarrow \ HO_2^- \qquad \textbf{(A. 8)}$$

$$Fe^{2+} + \ HO_2^- \rightarrow \ Fe^{3+} + H_2O_2 \qquad \textbf{(A. 9)}$$

Thus, we measure the formed Fe^{3+} concentration by absorption spectrophotometry. The absorbance of Fe^{3+} increases with the dose of irradiation. According to Beer-Lambert law, we measure the absorption or the optical density (*OD*) from the irradiated solutions at 304 nm (maximum Fe^{3+} absorption). The concentration (*C*) of ions reduced by a dose of irradiation (*D*) can be deduced from the absorbance (*A*). In these case: ε= 2204 $L.mol^{-1}.cm^{-1}$, *l* = 1 cm, *C*= molar concentration [mol/l], $G_{Fe}{}^{3+}$[mol/J]. The total formation of Fe^{3+} is observed by a plateau of the absorbance at the value A_{max}.

$$A = \varepsilon x l x C \qquad \textbf{(A. 10)}$$

And the dose rate (d=D/t) as follow

$$\mathrm{d} = \frac{A}{\varepsilon \ l \ G_{Fe}^{3+} \ t} [=] Gy/h \qquad \textbf{(A. 11)}$$

$$G_{red}(Fe^{3+}) = 2G(H_2O_2) + G(OH) + 3G(H) = 1.62x10^{-6} \ mol/J \qquad \textbf{(A. 12)}$$

$$\mathrm{d} = \frac{1}{2204 * 1 * 1.62\mathrm{x}10^{-6}} \frac{A}{t} = \frac{280 * DO}{t} [=] Gy/h \qquad \textbf{(A. 13)}$$

Appendix III: Photocatalytic Reactors

The Xenon lamp of 300 Watts produced by LOT-Orien was used in our experiments in the degradation of Phenol as is shown in **Figure A3**. This arc light source has high UV and VIS output with some lines in the NIR. The lamp can output a collimated beam of a continuous spectrum, ranging from the UV to near-infrared range (250 to 2000 nm). The radiation spectrum is presented in the **Figure A3** the arc light source produce either a highly collimated beam or a small bright focused spot. A water filter (a large cell) was placed between the lamp and the reactor to screen the infrared light and avoid heating of the samples. The cell containing water is made of quartz. Xenon arc lamps have a color temperature of approx. 6000 K which is close to the sun spectrum. The main output is below 900 nm. It is an ideal light source for the visible photocatalysis. Optical filters were used to obtain visible irradiance (wavelength larger than 450 nm) cut-off filter (AM-32603-1, LOT-Oriel).

The Photo-reactor used *in Laboratoire de Chimie Physique in the Université Paris-Sud.*

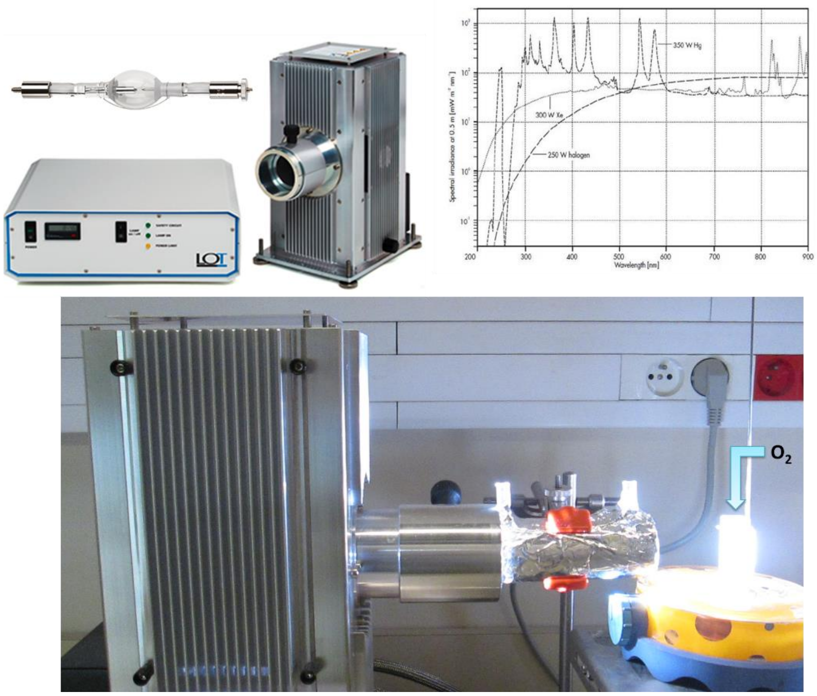

Figure A3. *Photoreactor for phenol degradation.*

In the mechanism of Phenol degradation by photocatalysis using a photocatalyss and light has been studied. It has been found that some intermediates are present, such as: benzoquinone, hydroquinone and the biodegradable molecules like, maleic acid oxalic acid and formic acid.[181] The proposed mechanism is presented in **Figure A4**. However, all the intermediates generated are degradable until the mineralization, which means the complete degradation of the organic molecule to CO_2 and H_2O.

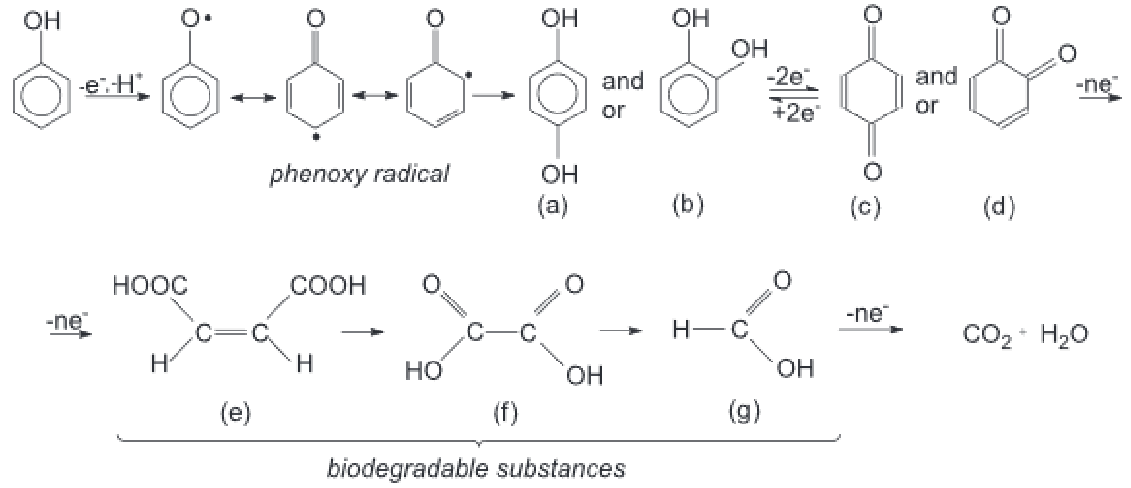

Figure A4. *Phenol degradation process, a) hydroquinone, b) cathecol, c) p-benzoquinone, d) o-benzoquinone, e) maleic acid, f) oxalic acid and formic acid.*[181]

Figure A5 presents the photo-reactor used for the degradation of 2-propanol, a xenon lamp was used with a cut off filter (Y48, Asahi Techno Glass) (λ ≥ 450 nm), The reactor was immersed into a water bath in order to keep the reaction temperature at 25°C. This reactor was used in the *Hokkaido University* in Japan in collaboration with Prof. Bunsho Ohtani and Dr. Ewa Kowalska.

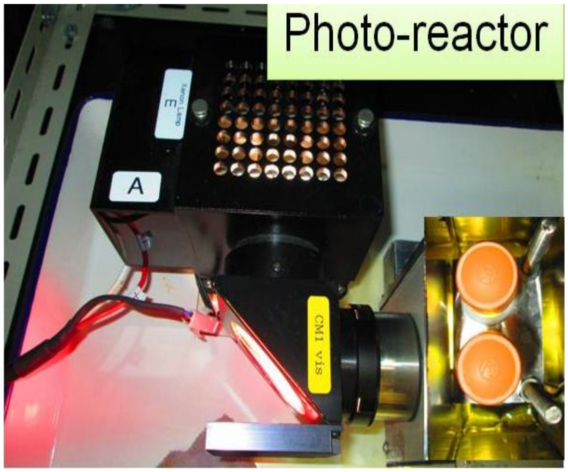

Figure A5. Photoreactor for 2-propanol degradation.

LEDs (Innotas Elektronik) with wavelengths of 400 and 470 nm were used as irradiation sources, with 4 ventilators working to for avoid the heating of the samples.

The photoreactor used in Ulm University in Germany (collaboration with Prof. Sven Rau, in the framework of Concert Japan ERANET project) is shown **Figure A6**.

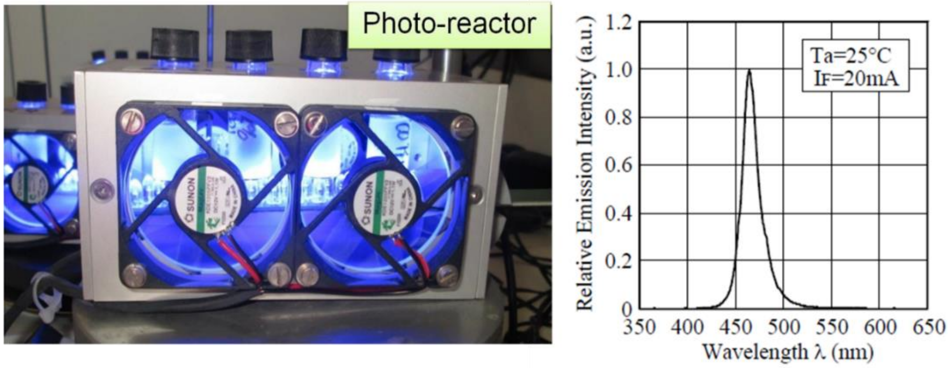

Figure A6. Photoreactor for hydrogen generation by PWS process

Appendix IV: Action Spectra (AS)

The chemical response, depends strongly on the irradiation wavelength, and is most effective at longer wavelength, while at lower wavelengths is ineffective. Thereby at each particular wavelength we have a particular response and the function expressing the relative effectiveness is the action spectra, which is the chemical response at different fixed wavelengths. When a narrow beam of white light is directed at a diffraction grating along its axis, instead of a monochromatic bright fringe (which means light of a single wavelength, λ (or a single frequency, v)), a set of colored spectra are observed on both sides of the central white band as is shown in **Figure A7** .

The term “action spectrum” is used to describe a plot of the intensity of some phenomena (for example, the rate of photosynthesis, or the rate of evolution of a chemicals compounds such as CO_2) produced by a monochromatic light as function of the irradiation wavelength.

Specificifically, we followed the CO_2 production by the degradation of acetic acid.

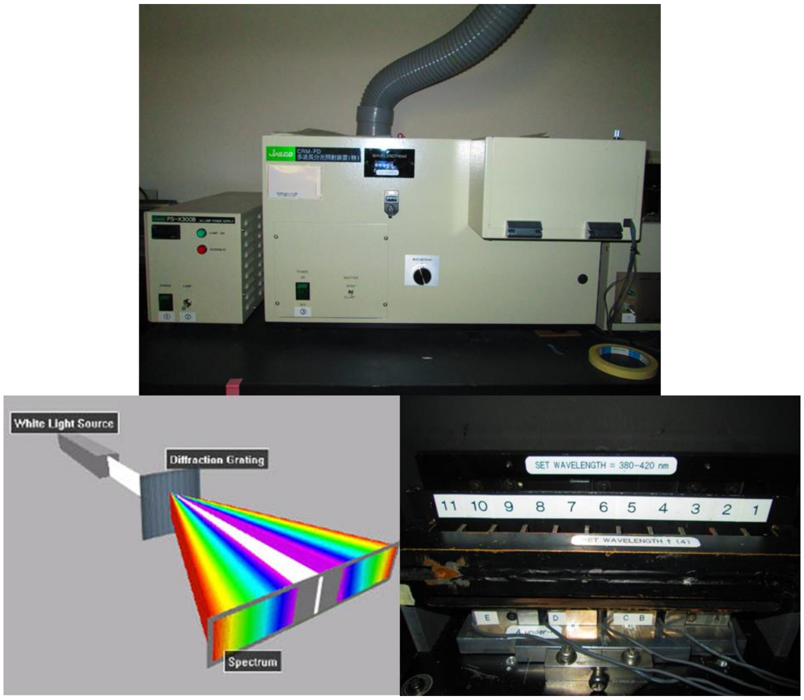

Figure A7. *Photoreactor for acetic acid degradation.*

The analysis of the apparently quantum efficiency was carried out as follows:

$$E_p = \frac{hc}{\lambda}[J] \tag{A. 14}$$

$$E' = E_p x N_A = \left[\frac{J}{mol}\right] \tag{A. 15}$$

$$\Psi = \frac{Intensity\ of\ the\ Light}{E'}\left[\frac{mol}{s}\right] \tag{A. 16}$$

$$\phi_{app} = \frac{Reaction\ rate}{\Psi}[\%] \tag{A. 17}$$

Where E_p is the energy per photon, h is the Planck's constant, c is the light speed N_A is the Avogadro's number, E' is the energy per mol, and the photon flux Ψ. The action spectrum is carried out by following one reaction. The ratio between the reaction rate and Ψ is the quantum efficiency of the sample.

The action spectra analysis was carried out using a diffraction grating type illuminator (Jasco CRM-FD), equipped with a 300 W Xenon lamp (Hamamatsu Photonics C2578-02), allowing the selection of the irradiation wavelength in the range between 350–680 nm, with a step of 30 nm. These experiments were carried out in Hokkaido University in Japan, (collaboration with Prof. Bunsho Ohtani and Dr. Ewa Kowalska, in the framework of Concert Japan ERANET project).

Appendix V: Kinetic in Heterogeneous Photocatalysis

Chemical kinetics addresses important issues in heterogeneous photocatalysis. Generally, it deals with the experimental determination and analysis of the quantity of a substance (usually concentration) as a function of time. In other words, chemical kinetics (concerned with either disappearance or appearance of chemical substances) is concerned with reaction rate and throughput. The rate of reaction is measured based on the property that is easiest to measure such as: colour, concentration or weight.[182]

Consider the photocatalytic transformation of a molecule *A*:

$$A \rightarrow \text{products} \qquad \textbf{\textit{(A. 18)}}$$

The rate of disappearance of A can be given by differential rate equation known as the differential rate law. A general differential rate law is given below.

$$\mathrm{r} = \frac{-d[A]}{dt} = k[reactant]^{n} \qquad \textbf{\textit{(A. 19)}}$$

Where *k* is the rate constant and the power *n* is the order. A reaction is zero, first, second or third order depending on the value of n (0, 1, 2 or 3 respectively) The commonest decay models that are observed in photocatalysis studies are the zero and the first order rate. A reaction can be considered as a zero order reaction when it does not depend on the concentration of any reactant and in the case of first order kinetic when the rate of the reaction is only limited by one reactant.

However, various photocatalytic processes have been described by different kinetic models such as pseudo zero order (when the reactant is in excess, the catalyst surface gets wholly covered all through and the disappearance of the reactant becomes negligibly dependent on concentration) and pseudo first order (in a two reactant, one of the reactants concentration remains more or less unchanged). Indeed, the term “pseudo” is used to prefix the order of reaction.[182]

The decay zero and first order models are show in the **Figure A8**. With a linear fit of the curves [A]=f(t) or ln[A] = f(t) we can get the experimental value of the zero or first order rate constant of a reaction. Rate constant can be utilized in comparing the rate of different reactions.

Zero order reaction

$$\frac{d[A]}{dt} = -k$$

$$d[A] = -kdt$$

Integration at time t=0 and t=t.

$$\int_{[A]_0}^{[A]_t} d[A] = -k\int_0^t dt$$

$$[A]_t - [A]_0 = -k\text{t}$$

$$[A]_t = [A]_0 - kt$$

First order reaction

$$\frac{d[A]}{[A]} = -kdt$$

$$d[A] = -kdt$$

Integration at time t=0 s is $[A]_0$
and t=t s $[A]_t$

$$\int_{[A]_0}^{[A]_t} \frac{d[A]}{[A]} = k\int_0^t dt$$

$$ln[A]_t - ln[A]_0 = -k\text{t}$$

$$ln[A]_t = ln[A]_0 - kt$$

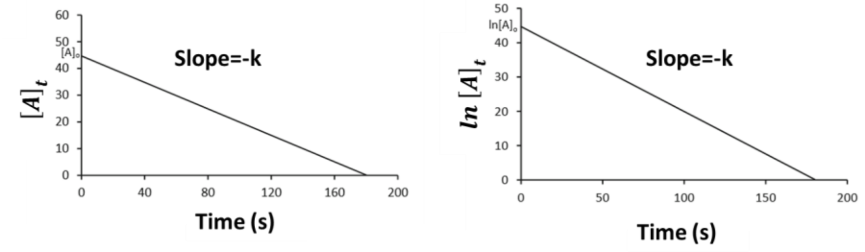

***Figure A8**. Calculation of zero and first order of reaction, for each fit, the zero order show the disappearance of the reactant [A] versus time, and for the first order it shows the decay the Ln [A] versus time.*

For an example in the phenol degradation with the bare and the modified TiO_2-P25 with different loading of Au-NPs, the corresponding kinetics fit is shown in the **Figure A9**.

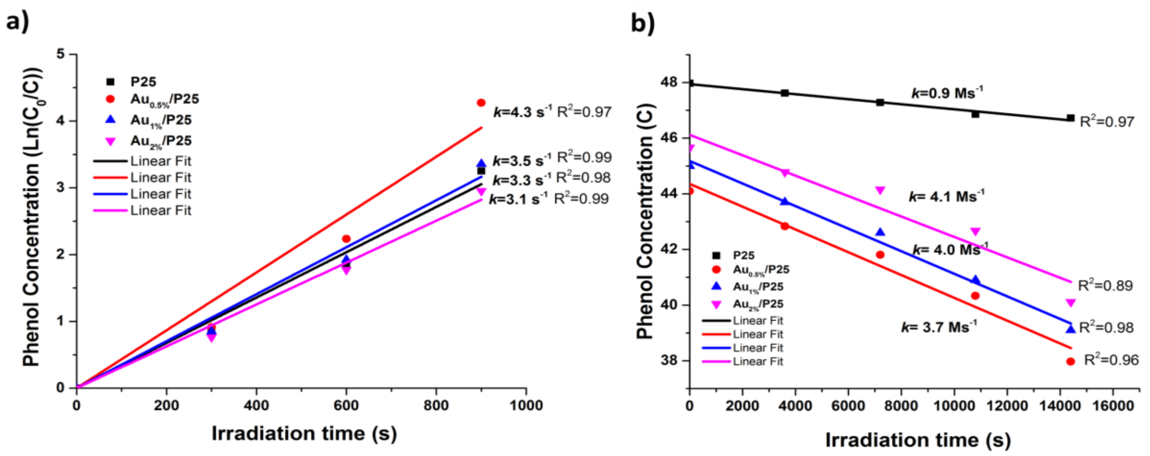

Figure A9. *Kinetic fit for phenol degradation using different Au loading on P25 under UV first order of the reaction and under visible zero order of the reaction.*

It is clear that is not the real order of the reaction, because the fit is not well matched. However, were used zero and first order of the reaction just for have a comparison of the rate of the reaction as a hypothesis.

Appendix VI: Characterization Techniques

Several characterization techniques for modified TiO_2 can be used such as X-ray Diffraction (XRD), Diffuse Reflectance Spectroscopy (DRS), High Resolution Transmission Electron Microscopy (HRTEM), Scanning Transmission Electronic Microscopy (STEM), X-ray Photon Electron Spectroscopy (XPS), X-ray Absorption Spectroscopy (XAS) and Time Resolved Microwaves Conductivity (TRMC).

X-ray Diffraction (XRD)

The XRD is the technique per excellence for studying solid state materials that present crystalline phases. It is a non-destructive technique that allows the qualitative and quantitative analysis of the samples and determining the crystal structure and crystallite size. So, it allows the characterization of crystals, providing information on the crystal symmetry and lattice parameters. The X-ray diffraction occurs when the impinging beam of monochromatic X-rays on a crystalline material, the coherent scattering of the beam occurs, with constructive interference between parallel planes, so that the difference of paths traveled by two rays is *n* times the wavelength of the beam, the so called Bragg's Law (**Figure A10**).

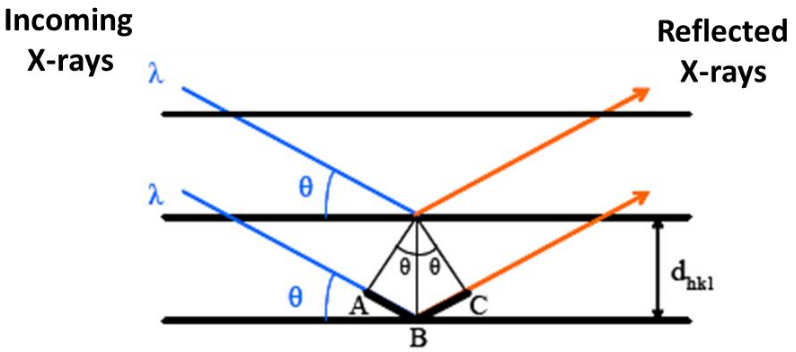

$$\overline{AB} + \overline{BC} = 2d_{hkl}sen\,\theta$$

Figure A10. *Scheme that shows the Braggs Law, representative X-ray diffraction phenomenon*

If $2d_{hkl}sen\ \Theta = n\lambda$, then a maximum of intensity in the diffraction occurs and as we just mentioned, is known the Bragg's law.

$$n\boldsymbol{\lambda} = 2\mathrm{d}_{\mathrm{hkl}}\mathrm{sen}\Theta \qquad \textbf{\textit{(A. 20)}}$$

Where:

λ: Wavelength of the incident beam.

d_{hkl}: Space between planes, depending on the unit cell parameters and the Miller indices.

Ɵ: Angle between the incident beam and the plane on which the diffraction occurs.

Therefore, the diffraction in a polycrystalline material will occur only for certain reflections of the incident beam, called Bragg reflections.

The device consists of an X-ray emitter tube which emits radiation at a particular wavelength. In the same plane there is the X-ray detector, which moves with a constant angular velocity describing a semicircle around the point where the sample to be characterized is placed. It also rotates with half speed the detector, so that the angle between the detector and the sample plane is the same as that the formed by the source and the sample plane. As will be varying the angle between the incident beam and the sample to the value for which the Bragg equation is satisfied, constructive interference phenomena occurs and the maximum intensity detector registers these maxima or constructive interferences.

Thus we obtain a *diffractogram*: a diagram of the intensity of diffracted X-rays ɵ as a function of angle, which is characteristic of each material and from whose analysis we can obtain a wealth of information.[183]

The DRX setups were used in this thesis work using a DX8 Bruker Advance diffractometer at the National Laboratory Nanoscience and Nanotechnology research (LINAN), at *Instituto Potosino de Investigación Científica y Tecnológica IPICYT, A.C.* in collaboration with M.C. Beatríz Labrada.

Appendix VI

Diffuse Reflectance Spectroscopy (DRS)

Solid materials present five reactions to illuminate with a source light, which can be qualified and quantified by spectroscopies: scattering, transmission, reflectance, diffraction and absorption. Transmission spectroscopy is based on the relationship known as the Beer's Law, defined as a quantitative interpretation as to how photons are attenuated in relation to an intervening medium. When used in transmission spectroscopy, Beer's Law is stated as

$$I = I_0 e^{-acl} \tag{A. 21}$$

Where I is the output intensity at a specific wavelength, I_0 is the original intensity at the same wavelength, a is the wavelength and material specific absorptivity, c is the concentration of the analyte, and finally l is the optical path length.

Similarly, the Kubelka-Munk function is a linear relation between the analyte concentration and reflectance from diffuse reflectance spectroscopy.

$$f(R_\infty) = \frac{(1 - R_\infty)^2}{2R_\infty} = \frac{k}{s} \tag{A. 22}$$

Where R_∞ is the reflectance after penetration and scattering throughout a non-absorbing matrix of infinite depth, and $k = \varepsilon C$, being ε, the molar absorptivity, and C, the concentration. This relationship only applies to samples diluted in a non-absorbing matrix.[184]

Since light cannot penetrate opaque (solid) samples, it is reflected on the surface of the samples. As is shown in the **Figure A11**, incident light reflected symmetrically with respect to the normal line is called "specular reflection," while incident light scattered in different directions is called "diffuse reflection".

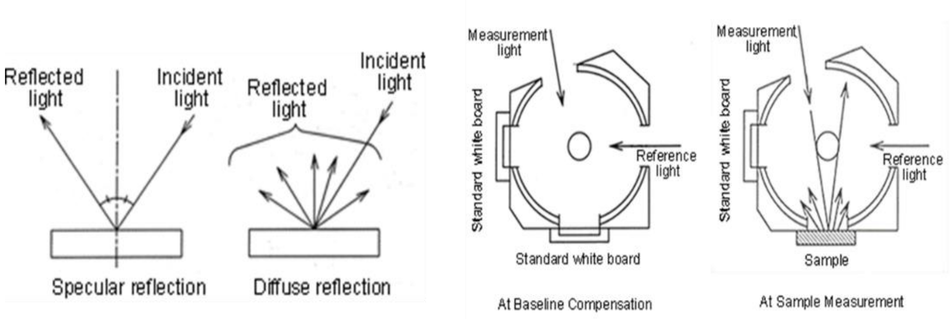

Figure A11. *Measurement of diffuse reflection including specular reflection using an integrating sphere.*[185]

With integrating spheres, measurement is performed by placing the sample in front of the incident light window, and concentrating the light reflected from the sample on the detector using a sphere with a barium sulfate-coated inside. The obtained value becomes the reflectance (relative reflectance) with respect to the reflectance of the reference standard white board, which is taken to be 100%.

When light is directed at the sample at an angle of 0°, specular reflected light exits the integrating sphere and is not detected. As a result, only diffuse reflected light is measured.

The experimental DRS setup used in this thesis work was from the *Laboratoire de Chimie Physique* in the *Université Paris-Sud* in collaboration with Dr. Christophe Humbert.

High Resolution Transmission Electron Microscopy (HRTEM)

TEM has been one of the most used tools for nanomaterials characterization. Electronic microscopies are based on the interaction of an electron beam to the sample. If there is an incident beam of electrons focused on a given material (**Figure A12**), there will be part of these electrons which will be adsorbed or transmitted by the material, but others will result in production of various signals that provide relevant information about the microstructure and composition of the one specific zone of the sample.

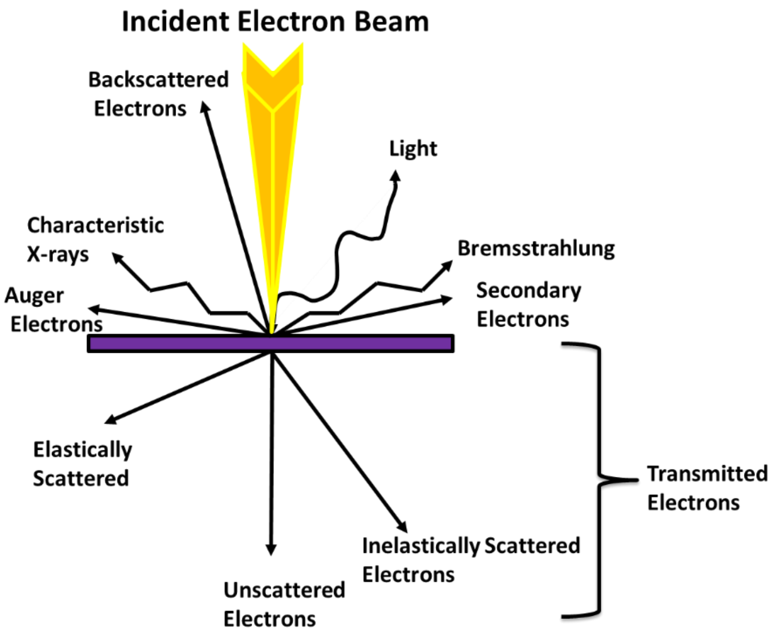

Figure A12. *Electron scattering signals generated by the interaction of a thin sample with a beam of accelerated electrons.*

The use of the transmitted electrons results in the so-called transmission electron microscopy (TEM). TEM consists of an emission source, which may be a tungsten filament, or a lanthanum hexaboride (LaB_6) source. By connecting this gun to a high voltage source (typically ~100–300 kV), and given sufficient current, the gun will begin to emit electrons either by thermionic or field electron emission into the vacuum.

There are several mechanisms of image formation in a TEM. The basic one is related to a projected mass thickness contrast (**Figure A13a**). The image is a map of the projected mass thickness of the sample. This contrast mechanism can be better understood if we recall a simple expression for absorption of radiation (Beer's Law)

$$I = I_0 e^{-\left(\frac{\mu}{\rho}\right)\rho t} \qquad \textit{(A. 23)}$$

I_0 is the original intensity, ρ is the sample density, *t* is the thickness of the sample and μ/ ρ is the mass absorption coefficient. This type of contrast mechanism is dominant in amorphous samples.

Another basic mechanism for image formation is the diffraction contrast. Contrast can be generated between those regions that deflect the beam and those regions that do not (**Figure A13b)**. Which is mainly relevant in crystalline samples. Diffraction contrast image is a map of those regions in the sample that are participating in diffraction processes. The most basic description of the condition for diffraction is Bragg's Law. In this expression λ is the wavelength, d_{hkl} is the distance between the crystal planes (*hkl*) and θ is the Bragg's angle **Eq A.16**.

Diffraction contrast forms the basis for at least two different imaging modes: bright and dark field.

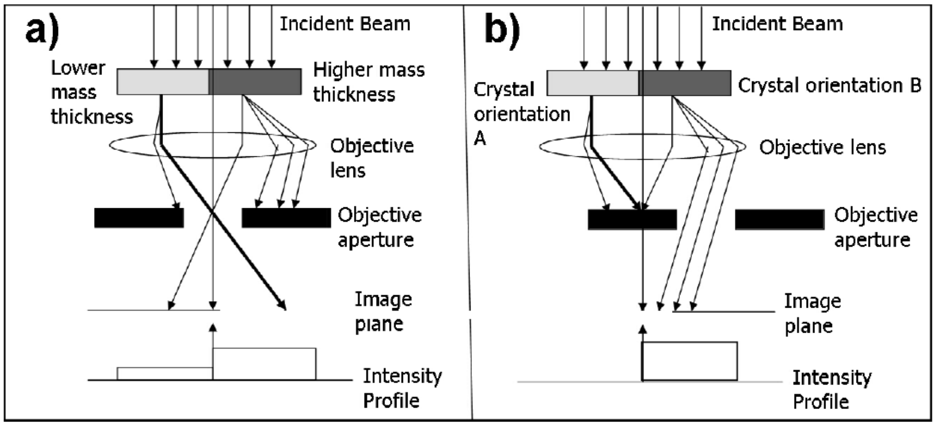

Figure A13. a) *TEM mass contrast imaging mechanism,* ***b)*** *TEM diffraction contrast imaging mechanism.*

The diffraction mode allows us to observe the electron diffraction as a diffraction pattern. The shape of the diffraction pattern can initially determine whether the observed area is amorphous, polycrystalline or crystalline.

Bright Field is, where the TEM image is formed with those regions of the sample that are not being diffracted away from the optical axis; In the bright field mode, the incident electron beam can be deflected by collisions across the sample. The probability of a collision increases with the atomic number Z of the constituents of the sample and the sample thickness, so the areas are darker while areas with lower Z atoms and/or reduced thickness appear bright. This method is widely used to observe metal structures for metal atoms with a high atomic number, and provide excellent contrast against the bright background.

Dark Field is where the TEM image is a map of the those regions of the sample that are diffracting the electron beam away from the optical axis of the microscope such that they pass through an aperture inserted in the back focal plane of the objective lens, called the objective aperture.[186]

The TEM setups were used in this thesis work using a FEI Tecnai F30 microscope equipped with a tungsten field emission gun operated at 300 keV in LINAN laboratory in the Instituto Potosino de Investigación Científica y Tecnológica IPICyT in collaboration with Dr. Nicolás Calletano and Dr. Héctor Silva.

Scanning Transmission Electronic Microscopy (STEM)

In the Scanning Transmission Electron Microscope (STEM) mode (**Figure A14**) the objective lens focuses the electron beam onto an atomic scale probe, and all scattered electrons can then be collected by a variety of detectors placed behind the sample. An image is generated simply by “scanning” the focused beam step by step over the sample. STEM image may be considered as a collection of individual scattering experiments. Different types of signals discriminated in scattering angle and/or energy loss yield different structural and chemical information and may be detected simultaneously in different channels.

The elastically scattered electron signal is used to form images that can be acquired by a variety of different detectors (HAADF, ADF). While the inelastically scattered electrons and related signals can be acquired by several different detectors (EELS, EDS) in order to obtain chemical, electronic and structural information from the sample. This simultaneous and controlled acquisition of information lends itself to quantitative analyses that are difficult to realize with other instruments. This ability of the STEM to provide a reference image makes it a very powerful instrument for microanalysis at high-spatial resolution.

High Angle Annular Dark Field images, also known as Z-contrast, are formed by collecting high-angle (< 50 mrad), incoherent and elastic scattering electron events on an annular detector (**Figure A14**), also known as Howie detector. At increasing angles, the coherent scattering is progressively replaced by thermal diffuse scattering. It is also more chemically sensitive since the scattering factors approach those for nuclear scattering (Rutherford-like scattering).[186]

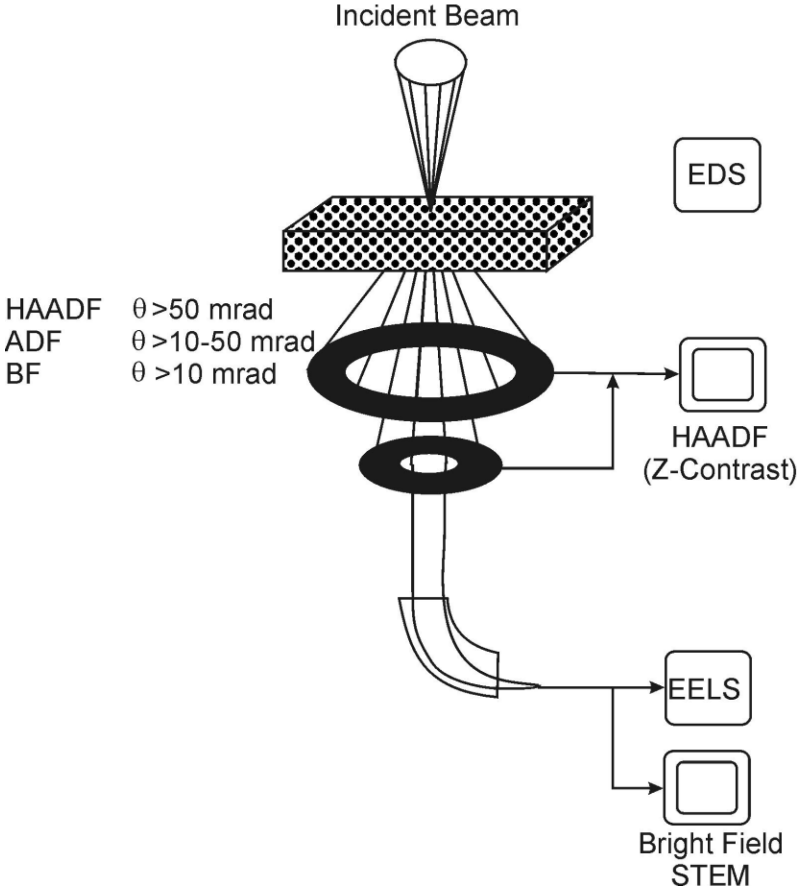

Figure A14. *Schematic illustration of the STEM*

The STEM setups used in this thesis work using a *High Angle Annular Dark Field* (HAADF) with Cs aberration corrected JEOL-ARM-200F electron transmission microscope at 200 kV, with a camera length of 8 cm and the collection angles of 70-280 mrads, *Energy-Dispersive X-ray Spectroscopy* (EDS) were obtained with a solid state detector from Oxford with a 80 mm2 window in Centro de Investigacion y de Estudios Avanzados del Instituto Politecnico Nacional in collaboration with Dr. Daniel Bahena, and the STEM (FEI Tecnai F30 microscope) with Dr. Héctor Gabriel Silva from LINAN at the Advanced Materials Department, IPICYT, San Luis Potosi, SLP, México.

X-ray Photon Electron Spectroscopy (XPS)

XPS is a technique to obtain qualitative or quantitative information of the elemental composition of surfaces. It can determine: chemical state of the elements in the sample, binding energy of electron states, thickness of layers of different materials near the surface, and the density of electronic states. XPS is a technique based on the photoelectric effect, described by A. Einstein in 1905.

The absorption of a photon by an atom, a molecule or surface, has the effect of ejecting an electron, if the incident photon energy is higher than the binding energy of the electron. The principle of photoelectron emission is shown in **Figure A15**.

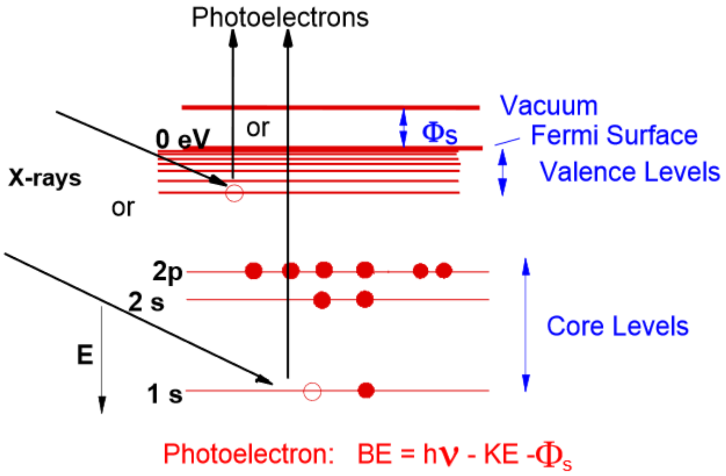

Figure A15. *The principle of photoelectron emission.*

In our experiments, the X-ray photons were generated from the K-line of magnesium (1253.6 eV). The electrons ejected by these photons come regardless of the valence shell or layer of heart and are recorded as a function of their energy by the detector. The results are presented as a spectrum consisting of peaks according to their energy. The integration of the peaks can be traced back to the composition, since the area under the peaks is proportional to the amount of the element in question to the surface of the sample (up to 5 nm, and sometimes more due to the porosity of the material). As the peak shape and binding energies are sensitive to oxidation phenomena and chemical state of the transmitter atom, XPS also provides information on the chemical bonding by applying peaks deconvolution (using a software CasaXPS, among many others).[187,188]

These experiments were conducted on a JEOL JPS-9010MC with a hemispherical electron energy analyzer, using Mg-K_{α} radiation. The samples were mounted on carbon films, each carbon film was fully covered with the sample in order to avoid powder release. In colaboration with Dr. Anais Lehoux, Dr. Ewa Kowalska and Prof. Bunsho Ohtani from Institute for Catalysis, Hokkaido University, Sapporo, Japan. At IPICYT, we used the XPS instrument VersaProbe II 5000 from Physical Electronics, and in colaboración with Dr. Mariela Bravo Sánchez from the the LINAN at the Advanced Materials Department, IPICYT, San Luis Potosi, SLP, México.

X-ray Absorption Spectroscopy (XAS)

X-ray are ionizing radiations and thus, by definition, have sufficient energy to eject a core electron from an atom. Each electronic core shell has a distinct binding energy, and thus absorption is function of energy. The spectrum presents the so-called absorption edge, with each edge represents a different core-electron shell: that is for n=1, L-edge, for n=2, M-edge, etc. An absorption edge by itself value correspond to an elemental identification. X-ray absorption could be used to measure XAS spectra. In addition to X-ray fluorescence, the properties of materials that have been applied the technique include photoconductivity, optical luminescence, and electron yield, although only the latter is widely used. Electron yield detection of XAS is particularly important for studies of surfaces. Since the penetration depth of an electron through matter is quite small, electron yield can be used to make XAS measurements surface sensitive.

A typical XANES spectrum is shown in **Figure A16**. There are several weak transitions below the edge (pre-edge transitions) together with structured absorption on the high energy side of the edge. Some XANES spectra show intense narrow transitions on the rising edge (these can be much more intense than the transition at the edge). These are often referred to as “*white lines”* in reference to the fact that when films are used to record an X-ray absorption spectra, an intense transition would absorb all the incident X-rays, thus preventing the film from being exposed and leaving a white line on the film. Above the edge, there are a variety of structures that show generally oscillatory behavior, ultimately becoming the EXAFS oscillations. The EXAFS region is sensitive to the radial distribution of electron density around the absorbing at om and is used for quantitative determination of bond length and coordination number.[189]

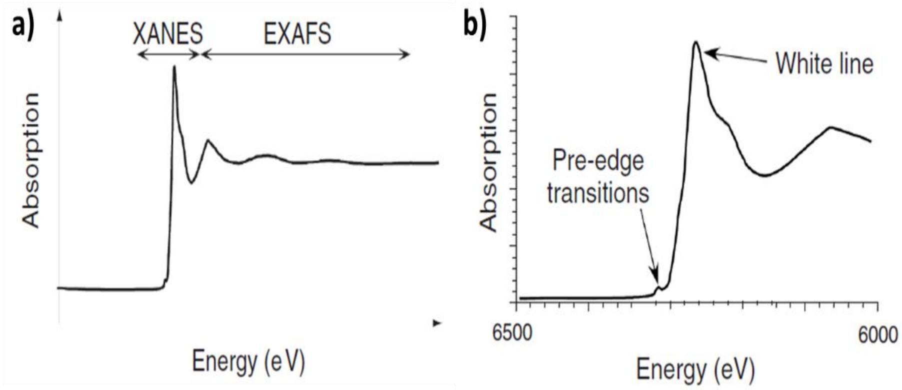

Figure A16. a) *Schematic illustration of an X-ray absorption spectrum, showing the structured absorption eV of the edge XANES and for several hundred to >1,000 eV above the edge EXAFS.* ***b)*** *Expansion of the XANES region showing different features within the XANES region.*

X-ray Absorption Spectroscopy (XAS) includes both Extended X-Ray Absorption Fine Structure (EXAFS) and X-ray Absorption Near Edge Structure (XANES), and is a technique for measuring the linear absorption coefficient μ(E). The terms XANES and EXAFS are used to define the spectral regions. The experiments require a synchrotron radiation facility see **Figure A17**, the energy is selected by a monochromator and the crystals used for X-ray monochromators is Si(220). This characterization was done in collaboration with Dr. Valerie Briois, from *Synchrotron Soleil, France.*

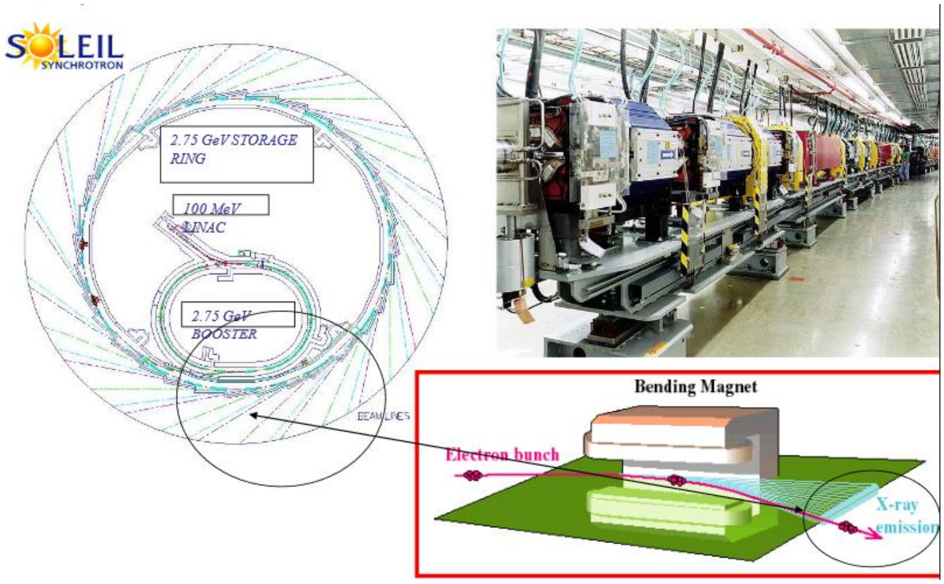

Figure A17. *Soleil Synchrotron radiation used for the XAS experiments.*

Time Resolved Microwaves Conductivity (TRMC)

The principle of this technique was described in previous papers.[8,42,77,190] In brief, TRMC consists in the measurement of the microwave power reflected by a semi-conductor sample during illumination by a nanosecond pulsed laser (*OPO pulsed laser, t*unable from 200-2000nm, 8ns fwhm and10 Hz of repetition). The signal obtained by the diode detector is transformed into voltage for input to the oscilloscope. The difference between the incident and the reflected microwave power gives the absorbed microwave power by the sample, which is directly proportional to the conductivity of the sample, see **Figure A18**.

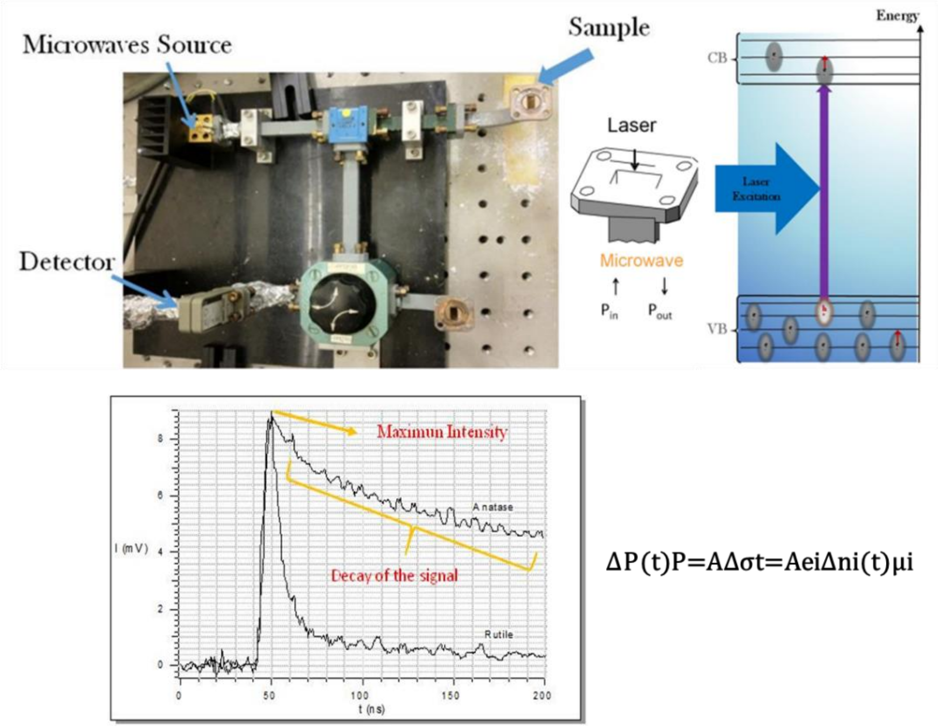

$$\Delta P(t)P = A\Delta\sigma t = Aei\Delta ni(t)\mu i$$

Figure A18. *TRMC setup and sample holder design*

Where Δn_i (t) is the number of excess charge-carriers *i* at time *t* and μ_i is the mobility of charge carrier *i*. The sensitivity factor *A* is independent of time, but depends on the microwave frequency and on the conductivity of the sample.

Considering that the trapped species have a small mobility which can be neglected, Δn_i is reduced to mobile electrons in the conduction band and holes in the valence band. In the specific case of TiO_2, the TRMC signal can be attributed to electrons because their mobility is much larger than that of the holes.

The main data provided by TRMC are given by the maximum value of the signal (I_{max}), which reflects the number of the excess charge-carriers created by the pulse, weighted by the mobility of the charge-carriers and by the influence of charge-carrier decay processes during the excitation, and the decay of the signal *I*(t), which is due to the decrease of the excess electrons controlled by recombination and trapping.[42,191]

The understanding of the whole decay is not obvious because various processes are taking place simultaneously. Detailed explanations and interpretations on the decay in TRMC measurements have been published previously.[77]

TRMC experimental setup used in this thesis work is part of the scientific infrastructure at the *Laboratoire de Chimie Physique* in the *Université Paris-Sud.* The experiments were done in collaboration with Prof. Christophe Colbeau-Justin and Dr. Alexandre Herissan.

Appendix VII: Article Published

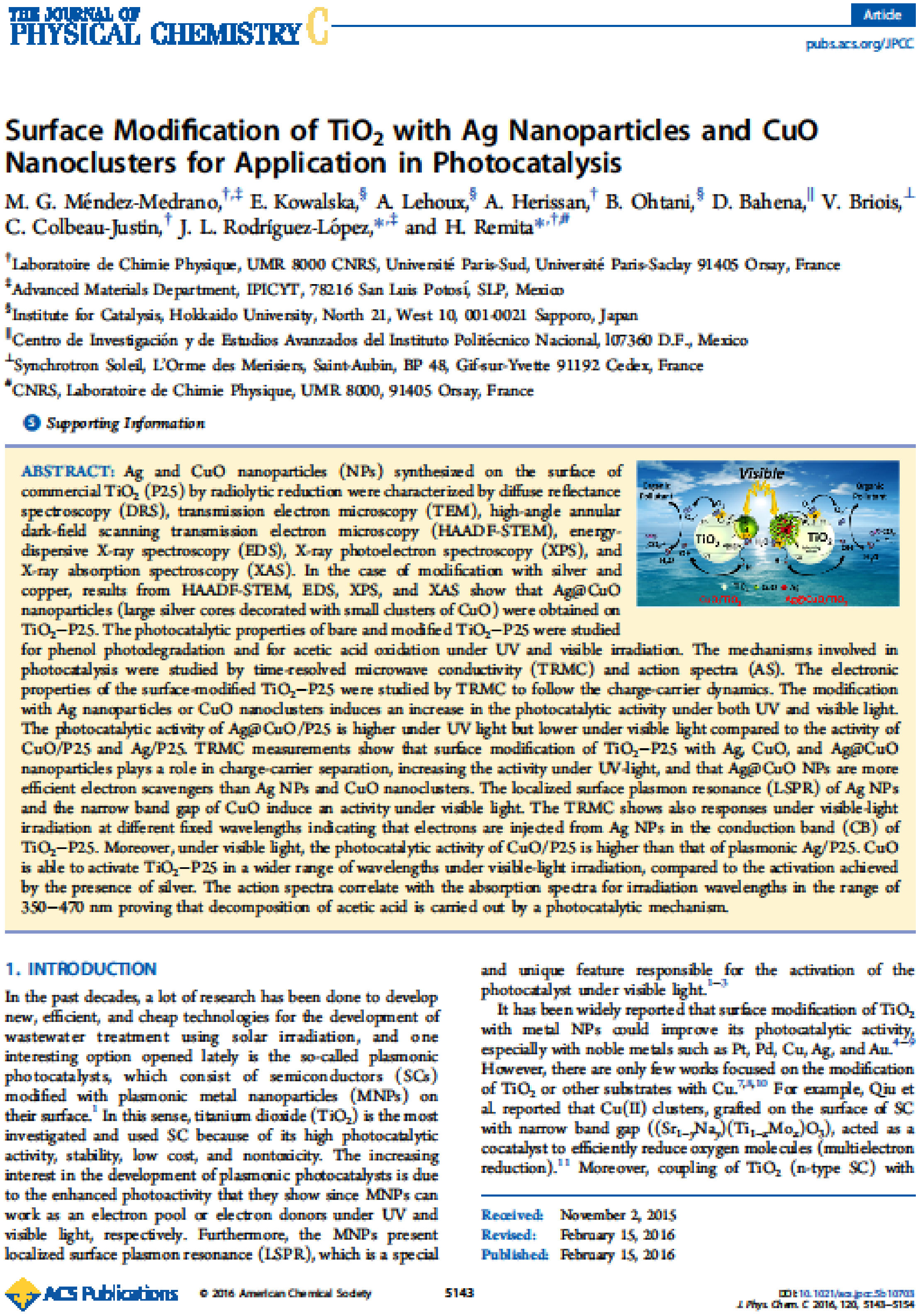

THE JOURNAL OF PHYSICAL CHEMISTRY C
Article
pubs.acs.org/JPCC

Surface Modification of TiO_2 with Ag Nanoparticles and CuO Nanoclusters for Application in Photocatalysis

M. G. Méndez-Medrano,[†,‡] E. Kowalska,[§] A. Lehoux,[§] A. Herissan,[†] B. Ohtani,[§] D. Bahena,[∥] V. Briois,[⊥] C. Colbeau-Justin,[†] J. L. Rodríguez-López,[*,‡] and H. Remita[*,†,#]

[†]Laboratoire de Chimie Physique, UMR 8000 CNRS, Université Paris-Sud, Université Paris-Saclay 91405 Orsay, France
[‡]Advanced Materials Department, IPICYT, 78216 San Luis Potosí, SLP, Mexico
[§]Institute for Catalysis, Hokkaido University, North 21, West 10, 001-0021 Sapporo, Japan
[∥]Centro de Investigación y de Estudios Avanzados del Instituto Politécnico Nacional, 107360 D.F., Mexico
[⊥]Synchrotron Soleil, L'Orme des Merisiers, Saint-Aubin, BP 48, Gif-sur-Yvette 91192 Cedex, France
[#]CNRS, Laboratoire de Chimie Physique, UMR 8000, 91405 Orsay, France

Supporting Information

ABSTRACT: Ag and CuO nanoparticles (NPs) synthesized on the surface of commercial TiO_2 (P25) by radiolytic reduction were characterized by diffuse reflectance spectroscopy (DRS), transmission electron microscopy (TEM), high-angle annular dark-field scanning transmission electron microscopy (HAADF-STEM), energy-dispersive X-ray spectroscopy (EDS), X-ray photoelectron spectroscopy (XPS), and X-ray absorption spectroscopy (XAS). In the case of modification with silver and copper, results from HAADF-STEM, EDS, XPS, and XAS show that Ag@CuO nanoparticles (large silver cores decorated with small clusters of CuO) were obtained on TiO_2−P25. The photocatalytic properties of bare and modified TiO_2−P25 were studied for phenol photodegradation and for acetic acid oxidation under UV and visible irradiation. The mechanisms involved in photocatalysis were studied by time-resolved microwave conductivity (TRMC) and action spectra (AS). The electronic properties of the surface-modified TiO_2−P25 were studied by TRMC to follow the charge-carrier dynamics. The modification with Ag nanoparticles or CuO nanoclusters induces an increase in the photocatalytic activity under both UV and visible light. The photocatalytic activity of Ag@CuO/P25 is higher under UV light but lower under visible light compared to the activity of CuO/P25 and Ag/P25. TRMC measurements show that surface modification of TiO_2−P25 with Ag, CuO, and Ag@CuO nanoparticles plays a role in charge-carrier separation, increasing the activity under UV-light, and that Ag@CuO NPs are more efficient electron scavengers than Ag NPs and CuO nanoclusters. The localized surface plasmon resonance (LSPR) of Ag NPs and the narrow band gap of CuO induce an activity under visible light. The TRMC shows also responses under visible-light irradiation at different fixed wavelengths indicating that electrons are injected from Ag NPs in the conduction band (CB) of TiO_2−P25. Moreover, under visible light, the photocatalytic activity of CuO/P25 is higher than that of plasmonic Ag/P25. CuO is able to activate TiO_2−P25 in a wider range of wavelengths under visible-light irradiation, compared to the activation achieved by the presence of silver. The action spectra correlate with the absorption spectra for irradiation wavelengths in the range of 350−470 nm proving that decomposition of acetic acid is carried out by a photocatalytic mechanism.

1. INTRODUCTION

In the past decades, a lot of research has been done to develop new, efficient, and cheap technologies for the development of wastewater treatment using solar irradiation, and one interesting option opened lately is the so-called plasmonic photocatalysts, which consist of semiconductors (SCs) modified with plasmonic metal nanoparticles (MNPs) on their surface.[1] In this sense, titanium dioxide (TiO_2) is the most investigated and used SC because of its high photocatalytic activity, stability, low cost, and nontoxicity. The increasing interest in the development of plasmonic photocatalysts is due to the enhanced photoactivity that they show since MNPs can work as an electron pool or electron donors under UV and visible light, respectively. Furthermore, the MNPs present localized surface plasmon resonance (LSPR), which is a special and unique feature responsible for the activation of the photocatalyst under visible light.[1−3]

It has been widely reported that surface modification of TiO_2 with metal NPs could improve its photocatalytic activity, especially with noble metals such as Pt, Pd, Cu, Ag, and Au.[4−6] However, there are only few works focused on the modification of TiO_2 or other substrates with Cu.[7,8,10] For example, Qiu et al. reported that Cu(II) clusters, grafted on the surface of SC with narrow band gap $((Sr_{1-y}Na_y)(Ti_{1-x}Mo_x)O_3)$, acted as a cocatalyst to efficiently reduce oxygen molecules (multielectron reduction).[11] Moreover, coupling of TiO_2 (n-type SC) with

Received: November 2, 2015
Revised: February 15, 2016
Published: February 15, 2016

ACS Publications © 2016 American Chemical Society 5143 DOI: 10.1021/acs.jpcc.5b10703
J. Phys. Chem. C 2016, 120, 5143−5154

narrow band gap semiconductors such as CuO (p-type SC) is another strategy to obtain visible-light active photocatalysts.[12,13]

Silver NPs are extremely attractive because of their high catalytic activity, widespread optical properties (size- and shape-dependent), antimicrobial properties, and potential applications in biological and chemical sensing, based on the phenomena of surface-enhanced raman scattering (SERS), LSPR, and metal-enhanced fluorescence (MEF).[6] In addition, modification of TiO_2 with silver NPs results in enhanced photocatalytic activity under both UV and visible-light irradiation and improved antibacterial properties.[6,14,15]

However, the use of Cu, in agreement with Irie et al.,[16] is more desirable due to its low cost and excellent catalytic and antifungal properties. It has recently been reported that surface modification of TiO_2 with bimetallic Ag−Cu nanoparticles leads to enhancement of the photocatalytic activity of TiO_2 for CO_2 reduction compared to its modification with monometallic NPs.[17]

In this work, we present synthesis of Ag nanoparticles and/or CuO nanoclusters by radiolysis on commercial TiO_2−P25. The photocatalytic activity of these photocatalysts has been investigated for photooxidation reactions of phenol and acetic acid. Time-resolved microwave conductivity (TRMC) has been used to study charge-carrier dynamics. The aim of this study was to correlate the photocatalytic activity of modified TiO_2−P25 with Ag nanoparticles and CuO nanoclusters with the AS and TRMC signals obtained at different excitation wavelengths to understand the mechanisms involved in the photocatalytic process under UV and visible light.

2. EXPERIMENTAL SECTION

2.1. Materials. Commercial titanium(IV) oxide P25 (TiO_2−P25, Evonik, surface area of ca. 50 m^2 g^{-1}), composed of a mixture of the crystalline phases, anatase (73−85%), rutile (14−17%), and amorphous titania (0−13%),[18] was used as a support material. Silver sulfate (Ag_2SO_4, Fulka, purity ≥99.4%) and cupric sulfate ($CuSO_4$, Sigma, purity ≈99%) were used as metal precursors. Other used chemicals were deionized water (Milli-Q with 18.6 MΩ), methanol (CH_3OH, ACS reagent, ≥99.8%), phenol (C_6H_5OH, Fulka), 2-propanol ($CH_3CH(OH)CH_3$, Sigma-Aldrich, 99.5%), and acetic acid (CH_3COOH, Wako, 99.7%).

2.2. Photocatalyst Preparation: Modification of P25 by Radiolysis. Ag^+ and/or Cu^{2+} ions were reduced by radiolysis on the TiO_2−P25 surface. Aqueous solutions (with 0.1 M 2-propanol, used as scavenger of $HO^•$ radicals generated by water radiolysis)[19] containing Ag_2SO_4, $CuSO_4$, or a mixture of Ag_2SO_4 and $CuSO_4$ (the total concentration in salt being 1×10^{-3} M) were put in contact with TiO_2−P25 (the loading of Cu or Ag metal was 0.5 wt %). The samples were labeled as P25, Ag/P25, and CuO/P25. For the suspensions containing a mixture of Ag^+ and Cu^{2+}, different molar ratios of Ag:Cu were used, i.e., 1:1, 1:3, and 3:1, keeping the total nominal metal content at 1 wt %. The resulting modified catalysts were, respectively, labeled as Ag@CuO1:1/P25, Ag@CuO1:3/P25, and Ag@CuO3:1/P25.

The suspensions were first sonicated for 3 min, deaerated with nitrogen (under stirring), and then irradiated with a ^{60}Co panoramic gamma source (dose rate = 2.3 kGy h^{-1}) for 3.5 h. The silver and copper ions were reduced by the solvated electrons, and the alcohol radicals were induced by solvent radiolysis. The applied dose is sufficient to reduce all the metal ions into their zero valency. The modified TiO_2−P25 photocatalysts were separated by centrifugation and dried at 60 °C for 18 h. The supernatant was completely transparent after centrifugation, indicating that all the Ag- and Cu-based NPs were deposited on TiO_2−P25.[19,20]

2.3. Materials Characterization. For the transmission electron microscopy (TEM) observations, the samples were dispersed in 2-propanol in an ultrasonic bath for few minutes, and then one drop of the suspension was deposited on gold-coated holey carbon grids (SPI method). The samples were characterized by high-angle annular dark-field scanning transmission electron microscopy (HAADF-STEM). The HAADF-STEM images were recorded using a C_s-corrected JEOL-ARM-200F electron transmission microscope at 200 kV. The HAADF-STEM images were acquired with a camera length of 8 cm and the collection angles of 70−280 mrads.

Energy-dispersive X-ray spectroscopy (EDS) measurements for line-scan profiles and mapping were obtained with a solid-state detector from Oxford with an 80 mm^2 window. X-ray photoelectron spectroscopy (XPS) characterization was conducted on a JEOL JPS-9010MC with a hemispherical electron energy analyzer, using Mg Kα radiation. The samples were mounted on carbon films, and each carbon film was fully covered with the sample in order to avoid powder release. After overnight degassing in the preparation chamber, the samples were inserted in the analysis chamber with a pressure lower than 10^{-7} Torr. High-resolution scans were taken for five elements, and the number of scans differed depending on each element content in the sample, i.e., 50 scans were taken for Ti and O, 100 scans for C, and 300−500 scans for Ag and Cu. Diffuse reflectance spectroscopy (DRS) was recorded with a UV−vis−NIR spectrophotometer, model Cary 5000 Series from Agilent Technologies, equipped with an integrating sphere for diffuse and total reflection measurements and using a KBr reference sample.

Cu K-edge XANES measurements were carried out at the SAMBA beamline (SOLEIL, Saint-Aubin) using a Si(220) fixed-exit double-crystal monochromator. Harmonic rejection was done by two Pd-coated mirrors at 5.5 mrad grazing incidence. Measurements were done on pellets of samples at room temperature in fluorescence mode using a Ge 35 pixel-array detector.

The time-resolved microwave conductivity (TRMC) method was used to study the dynamics of photogenerated charge carriers under UV and visible irradiation. A pulsed laser source with an optical parametric oscillator (OPO) EKSPLA, NT342B, tunable in the range between 220 and 2000 nm was used for TRMC measurements. The full width at half-maximum (fwhm) of one pulse was 8 ns with repetition frequency of the pulses at 10 Hz and microwaves generated by a Gunn diode (30 GHz). Several wavelengths were used, 355, 400, 450, 470, 480, 550, 600, and 650 nm, and the corresponding laser energies were 1.7, 0.9, 6.7, 6.2, 5.8, 4.5, 2.5, and 1.7 mJ cm^{-2}, respectively.

The principle of this technique was described in previous papers.[5,7,21,22] In brief, TRMC consists of the measurement of the microwave power reflected by a semiconductor sample during illumination by a nanosecond pulsed laser. The signal obtained by the diode detector is transformed into voltage for input to the oscilloscope. The difference between the incident and the reflected microwave power gives the absorbed microwave power by the sample, which is directly proportional to the conductivity of the sample.

DOI: 10.1021/acs.jpcc.5b10703
J. Phys. Chem. C 2016, 120, 5143−5154

The main data provided by TRMC are given by (a) the maximum value of the signal (I_{max}), which reflects the number of the excess charge carriers created by the pulse, weighted by the mobility of the charge carriers and by the influence of charge-carrier decay processes during the excitation and (b) the decay of the signal $I(t)$, which is due to the decrease of the excess electrons controlled by recombination and trapping.[21,23]

2.4. Photocatalytic Activity Tests. *2.4.1. Phenol Degradation under UV and Visible Light.* The photocatalytic activity of the modified photocatalysts was tested for photodecomposition of phenol (C_6H_5OH), used as a model pollutant in water (50 ppm), under UV and visible illumination. The photodegradation was carried out in a 10-mm light path quartz cell reactor containing 3.5 mL of phenol solution and 1 g L^{-1} of photocatalyst. Before irradiation, the photocatalyst was dispersed in the solution by sonication for 30 s and then by magnetic stirring for 10 min in the dark to reach the equilibrium between adsorption and desorption. Then, the solution was irradiated using a xenon lamp (Oriel 300 W) with or without cutoff filter (AM-32603-1, LOT-Oriel) for experiments carried out under visible light ($\lambda > 450$ nm) or UV irradiation, respectively. The photocatalytic tests were conducted under oxygen bubbling at a fixed rate flow.

Aliquots of 0.5 mL were sampled from the reactor at different time intervals. The powder was separated by centrifugation, and then the resultant transparent solution was analyzed by high performance liquid chromatography (HPLC, Agilent 1260 infinity quaternary LC) equipped with a UV detector set at 260 nm for phenol analysis. The column was an adsorbosphere C18 in reverse phase (5 μm, $l = 150$ mm, ID = 4.6 mm, Alltech) combined with an All-Guard cartridge system TM (7.5 × 4.6 mm, Alltech) for elution at 1 mL min^{-1} flow rate. An isocratic mobile phase consisted of 80% H_2O and 20% acetonitrile (ACN). Star software was applied for data analysis.

2.4.2. Acetic Acid Degradation–Action Spectrum. The photocatalytic degradation of acetic acid was carried out for 30 mg of photocatalyst suspended in 3 mL of an aqueous solution of acetic acid (5 vol %), inside quartz cells with a volume of ca. 12 mL. The cells were sealed with a septum to avoid the leakage of generated CO_2. The suspensions were stirred in the dark for 10 min (to attain the adsorption equilibrium). The illumination with a 300 W xenon lamp (Hamamatsu Photonics C2578-02) equipped with a diffraction grating type illuminator (Jasco CRM-FD) allowed the selection of the irradiation wavelength in the range between 350 and 680 nm, with a step of 30 nm. The samples were irradiated with a monochromatic light with a full-width at half-maximum (fwhm) of 15 nm irrespective of the selected wavelength and the intensity of irradiation ($1.24–3.9 \times 10^{-8}$ Einstein s^{-1}), measured by a Hioki 3664 optical power meter maintained at ca. 3.5 mW.

The samples were irradiated for 90 min under stirring. Every 30 min, 0.2 mL of gas sample was taken with a syringe from the quartz cell, and generated CO_2 was analyzed with a gas chromatograph (Shimadzu GC-14B) equipped with a flame ionization detector (FID). The sensitivity of a FID detector was enhanced by converting carbon dioxide into methane in an in-line methanizer (Shimadzu MTN-1). The reaction of acetic acid degradation is the following:[9]

$$CH_3COOH + 2O_2 \rightarrow 2CO_2 + 2H_2O$$

The apparent quantum efficiency was calculated as the rate of CO_2 evolution from the decomposition of acetic acid versus the flux of incident photons, assuming that four photons were required.

In this article, we studied the surface-modified TiO_2–P25 with Ag, CuO, and Ag@CuO with different Ag:Cu ratios. The results and figures corresponding to Ag/P25, CuO/P25, and Ag@CuO 1:1/P25 are presented in the main article, while the results for other Ag:Cu ratios (1:3 and 3:1) are mainly shown in the Supporting Information.

3. RESULTS AND DISCUSSION

3.1. Radiolytic Synthesis. Ag^+ and Cu^{2+} were reduced on TiO_2–P25 by solvated electrons and reducing $(CH_3)_2C^{\bullet}OH$ radicals induced by radiolysis. It is well-known that high-energy radiation (γ-rays, X-rays, electrons, or ions beams) of water leads to the formation of free radicals such as solvated electrons (e^-_s) (which are strong reducing species ($E^0(H_2O/e^-_s) = -2.87\ V_{NHE}$)), $H^{\bullet}$ ($E^0(H^+/H^{\bullet}) = -2.3\ V_{NHE}$), and $HO^{\bullet}$ radicals ($E^0(HO^{\bullet}/H_2O) = +2.8\ V_{NHE}$)).[19] The generated hydroxyl radicals $HO^{\bullet}$ (strong oxidant species) are scavenged by addition of 2-propanol (0.1 M), which yields after reactions with $HO^{\bullet}$ and $H^{\bullet}$ to a secondary reducing radical $(CH_3)_2C^{\bullet}OH$ ($E^0((CH_3)_2CO/(CH_3)_2C^{\bullet}OH) = -1.8\ V_{NHE}$).[19] Alcohol radicals and e^-_s are powerful reducing agents, which are able to reduce metal ions to lower valences and finally to metal atoms. The energy deposition throughout the suspension and continuous stirring during radiation ensure homogeneous distribution of the radiolytic radicals and therefore a homogeneous reduction and nucleation leading to the formation of nanoparticles homogeneous in size.[19,20] The radiolytic reduction mechanisms of silver and copper ions have been already described in other publications.[6,24] The modified TiO_2–P25 with Ag and/or Cu presented different colors (see Table 1).

Table 1. Characteristics of the Modified Photocatalysts

photocatalysts	molar ratio of Ag:Cu	color of sample
CuO/P25	0:1	light green
Ag@CuO1:3/P25	1:3	light yellow
Ag@CuO1:1/P25	1:1	light brown
Ag@CuO3:1/P25	3:1	light brown
Ag/P25	0:1	light pink

3.2. Characterization of the Photocatalysts. For all the modified titania samples, TEM observations show metal nanoparticles homogeneously dispersed on the TiO_2–P25 surface (see Figure S1–1). For CuO/P25 and Ag/P25 samples, small nanoparticles of around 1–2 nm were observed on the surface of TiO_2–P25 (Figure S1–2a and S1–2e). For the titania comodified with both elements, larger nanoparticles (5–12 nm) were formed on the TiO_2–P25 surface (see Figure S1–2b–d).

For the titania modified with Cu and/or Ag, the HAADF-STEM images (Figure 1) show metal nanoparticles located on the TiO_2–P25 surface. Since the brightness is approximately proportional to Z^2 (Z being the atomic number), any difference in brightness would reflect the presence of two different elements. Therefore, due to the atomic number difference between Ag (47) and Cu (29), the areas with higher brightness within the NPs are attributed to columns of atoms richer in silver, and the areas with lower brightness are attributed to columns richer in copper. As the brightness is not regular, there is segregation between Ag and Cu. The HAADF-STEM images

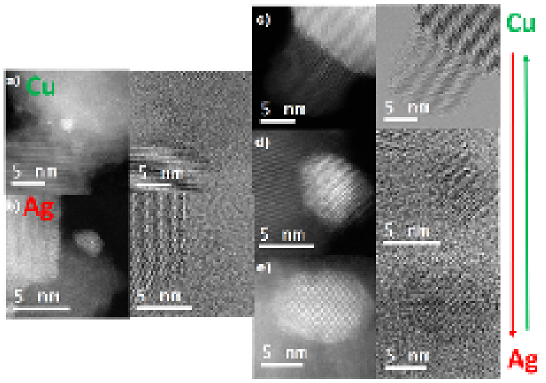

Figure 1. HAADF-STEM (left) and BF-STEM (right) of (a) Cu/P25, (b) Ag/P25 and Ag@CuO systems, (c) Ag@CuO1:3/P25, (d) Ag@CuO1:1/P25, and (e) Ag@CuO3:1/P25.

for the Ag@CuO1:3/P25 sample (Figure 1c) show that Ag–Cu-based nanoparticles have a core–shell structure, where Ag is the core and Cu is the shell part. A similar core–shell structure is obtained for the other Ag:Cu molar ratios, i.e., Ag@CuO1:1 and Ag@CuO3:1, as it can be seen in the Figure 1d and 1e, respectively. In the Ag@CuO3:1/P25 sample, the core composed of Ag covers a larger area of the total particle, compared to that observed in the Ag@CuO1:3/P25 sample. Additionally, an image with the bright-field (BF) observation mode in the STEM technique is shown in the right part of Figure 1a–e where it is possible to observe different arrangements of the crystallographic planes.

The composition of Ag- and Cu-based NPs was investigated by EDS. Different nanoparticles were analyzed, and the profile spectra across the various individual NPs were taken (Figure 2a and Figure S2). Figure 2b shows chemical mappings for Ag- and Cu-based nanoparticles. Ag (L) and Cu (L) maps clearly revealed the formation of the core(Ag)–shell(Cu) (or shell(CuO)) (composite image). Ag nanoparticles seem to be decorated on their surface by small clusters of Cu (Cu^0 or Cu oxides).

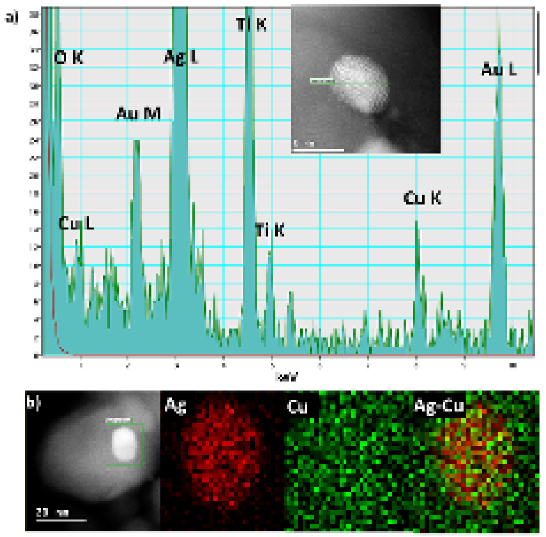

Figure 2. (a) EDS analysis and (b) elemental mapping performed at a nanoparticle of Ag@CuO1:1/P25 on P25 (Cu signal in green and Ag signal in red).

EDS line-scan signals of Ag and Cu are shown in Figure S3. Different intensities along the different regions of the NPs are clearly observed. The HAADF-STEM images of Ag@CuO1:1/P25 show nanoparticles adsorbed on TiO_2–P25 (Figure S3 f, left). Both the Ag-L and Cu-L peaks demonstrate nonhomogeneous dispersion of Ag and Cu atoms where the core is richer in Ag. Therefore, the EDS line scans evidenced the core–shell structure of comodified samples (Figure S3 f, right). The information obtained from high-resolution TEM images, HAADF-STEM, and EDS analyses confirms the formation of core–shell Ag@Cu (or Ag@CuO) NPs on TiO_2–P25. The Cu–Ag system has a strong tendency to phase separate, due to the large difference in the atom size ($r_{Ag}/r_{Cu} = 1.13$, where r_M is the atomic radius of metal M), and the difference in the cohesive energies between the two metals $E^{coh}{}_{Ag} - E^{coh}{}_{Cu} = 0.55$ eV (the biggest atom (Ag) being the less cohesive).[25] This phase segregation has already been reported for the system Ag–Cu.[17,26–28] This surface segregation of silver and copper was also studied by Monte Carlo simulations.[26,28] A recent study has shown that a system at thermodynamic equilibrium possesses silver as a shell around the copper core.[29] Our system is out of equilibrium, and it is suggested that silver is reduced before copper leading to Ag_{core}–Cu_{shell} NPs. It has also been reported that when Cu is oxidized it segregates to the surface of the system.[30]

In order to analyze the chemical composition of the modified TiO_2–P25 and to identify the chemical state of Cu and Ag elements in the samples, XPS measurements were performed. It was found that samples were homogeneous because the XPS signals from different regions of the sample were very reproducible in both chemical composition and energy distribution. XPS analyses attested the metallic nature of Ag nanoparticles, as shown in Figure 3, Figure S4, and Tables 2 and S1. The Ti 2p peaks are characteristic of Ti^{4+} in TiO_2 with two main components at 459.5 and 465.5 eV related to Ti $2p_{3/2}$ and Ti $2p_{1/2}$ orbitals and the O 1s peaks at 530.5 eV attributed to oxygen of TiO_2. The Ag 3d core peaks split into two components, Ag $3d_{5/2}$ and Ag $3d_{3/2}$, due to spin–orbit coupling

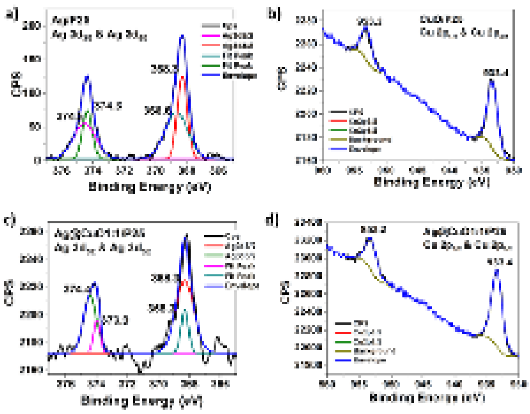

Figure 3. XPS spectra for (a) Ag 3d and (c), (b), and (d) Cu 2p of Ag/P25, Ag@CuO1:1/P25, and CuO/P25 samples.

DOI: 10.1021/acs.jpcc.5b10703
J. Phys. Chem. C 2016, 120, 5143–5154

Table 2. Binding Energies of CuO/P25, Ag/P25, and Ag@CuO1:1/P25 Samples Determined by XPS Showing the Binding Energies of Ag-3d, Cu-2p, Ti-2p, and O-1s

samples	Ag		Cu		Ti		O
	$3d_{3/2}$	$3d_{5/2}$	$2p_{1/2}$	$2p_{3/2}$ [eV]	$2p_{1/2}$	$2p_{3/2}$	1s
CuO/P25	-	-	953.2	933.4	465.5	459.5	530.8
Ag@CuO1:1/P25	374.4	368.3	953.2	933.4	465.8	459.9	531.3
Ag/P25	374.3	368.3	-	-	465.3	459.4	530.6

(Δ_{BE}(Ag $3d_{5/2-3/2}$) = 6 eV), and the binding of the Ag $3d_{5/2}$ core peaks is characteristic of metallic silver.[6,31,32] In Figure 3a–c, the Ag-modified TiO_2−P25 exhibits at the Ag 3d level two reproducible peaks (around 368.3 and 374.3 eV), which are typical for the $3d_{5/2}/3d_{3/2}$ spin−orbit splitting of Ag. The Ag $3d_{5/2}$ binding energy at peak maximum 368.3 eV corresponds to the value reported for metallic Ag.[6,32−34] However, the broadening of the peak width is noticed when compared to that of pure metal for the same recording conditions. This feature is due to additional contributions associated with other chemical Ag environment. The small additional peaks at higher binding energy localized at 368.6 and 374.6 eV cannot be related to silver oxides (which are known to present a positive shift in the binding energy),[6,33−35] and they may correspond to the interaction of Ag NPs with the TiO_2 substrate as has been previously reported.[6]

In the same way, two components Cu $2p_{3/2}$ and Cu $2p_{1/2}$ are observed for the Cu core peaks.[36,37] In Figure 3b–d, the BE positions of Cu $2p_{3/2}$ core levels are in the range of 933.3−933.4 eV. These positions are closer to the positions of CuO (Cu^{II}),[36,38] rather than Cu^0; however the satellite peak characteristic of CuO (or Cu^{II}) is not observed or is very weak, and this behavior is presented in all the samples containing Cu (Figures 3a–d and S4−1). It has to be noted that the positions of the XPS peaks are sensitive to the cluster size, especially for very small clusters (size <3 nm).[39,40] Chusue et al. reported that the XPS shakeup is sensitive to the CuO particle size, and this satellite decreases with the reduction state of Cu but also with the decrease of the particle size.[40]

Therefore, Cu K-edge XANES spectra were measured in order to corroborate the oxidation states of Cu deduced from XPS. It has been found that the energy position of the rising edge of the spectra and shape of the white line for all the TiO_2−P25 modified with copper (Cu alone or associated with Ag) are characteristic of Cu^{II} species,[41] as shown in Figure 4.

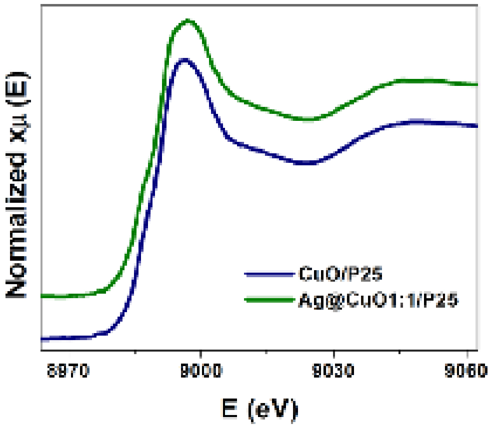

Figure 4. Cu K-edge XAS spectra for CuO/P25 and Ag@CuO1:1/P25 samples.

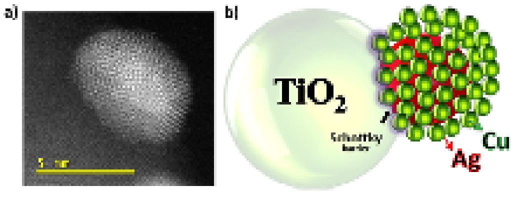

Figure 5. (a) Representative aberration-corrected STEM-HAADF image for a Ag@CuO1:1 particle supported on TiO_2−P25, showing Ag-NPs covered with an ensemble of CuO clusters, and (b) a schematic morphology of the modified TiO_2−P25 with Ag−CuO nanoparticles.

Solvated electrons induced by radiolysis are very strong reducing species able to reduce non-noble metals, which are difficult to reduce by chemical methods.[20,24,42] Silver and copper ions are reduced on TiO_2−P25 by solvated electrons and alcohol radicals.[6,24] However, copper clusters are sensitive to oxygen and are most probably very fast oxidized in air. Thus, the Ag_{core}−Cu_{shell} nanoparticles turn into Ag@CuO in air. Figure 5a shows an aberration-corrected HAADF-STEM image of the Ag@CuO(1:1)/P25 sample allowing us to distinguish two different elements, i.e., Ag and Cu, based on the brightness of the image. Accordingly, as well as from XPS and XAS results, a representative scheme of this core−shell structure on the TiO_2−P25 surface is depicted in Figure 5b.

The optical properties of the modified TiO_2−P25 were studied by DRS. Figure 6 and Figure S5 show the spectra of bare and modified TiO_2−P25. The spectrum of TiO_2−P25 shows an absorption edge at around 400 nm due to the presence of rutile.[43] The DRS spectra of the modified samples exhibit a slight shift in the absorption to longer wavelengths for all surface-modified photocatalysts. This effect has already been reported for TiO_2 modified with Pt, Pd, Ag, and Au−Cu[4−8] and could be attributed to stabilization of the CB of TiO_2−P25 by the interaction with the Ag NPs and CuO nanoclusters. The modified samples absorb in the visible and near-infrared (IR) region, while bare TiO_2−P25 does not. Note that absorption with a maximum at 510 nm was obtained with Ag/P25, while a large absorption band with a maximum at 800 nm was observed for CuO/P25.

These absorptions result in pink and yellow colors of the modified TiO_2−P25 samples. TiO_2−P25 comodified with Ag and CuO absorbs in the visible and near IR. The maximum absorption in the visible region is, respectively, at 480 nm for Ag@CuO1:3/P25 and 470 nm for Ag@CuO1:1/P25 and Ag@CuO3:1/P25 (see Figure 6 and Figure S5). The absorption in the IR is very broad with a maximum at ca. 800 nm for the two samples rich in Cu (Ag@CuO1:3/P25 and Ag@CuO1:1/P25), while the sample Ag@CuO3:1/P25 shows no maximum

DOI: 10.1021/acs.jpcc.5b10703
J. Phys. Chem. C 2016, 120, 5143−5154

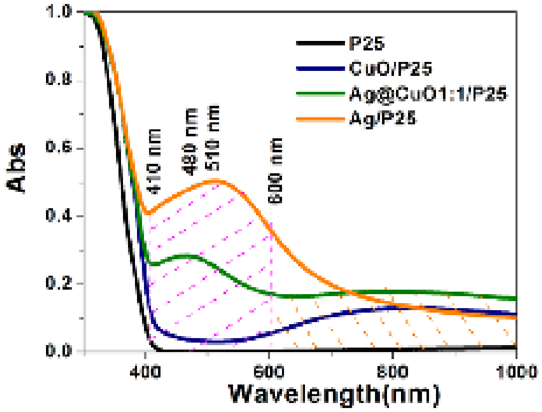

Figure 6. UV−vis diffuse reflectance spectra of the pure TiO_2−P25 and the modified TiO_2−P25 with Ag, CuO, and Ag@CuO1:1 showing the regions of the plasmon band of Ag and the absorption band of CuO.

absorption in this region. Ag NPs are known to exhibit a LSPR with a maximum at around 410 nm in water. It is well known that the position of LSPR depends on the environment and the support.[44] Therefore, a red-shift of LSPR is usually observed as a result of the coupling between the metal nanoparticles and TiO_2 support having a high reflective index (the absorption coefficient and refractive index for anatase at a wavelength of 380 nm are 90 cm^{-1} and 2.19, respectively), as already reported for Au/TiO_2, Ag/TiO_2, and Au−Cu/TiO_2.[1,46,47] The addition of CuO to TiO_2−P25 extends clearly the absorption to visible light. The absorption band in the near IR is observed in the case of Cu loading, and this is attributed to $2E_g \rightarrow 2T_{2g}$ interband transitions in the Cu^{II} clusters deposited on different phases and sites of TiO_2 and with strong interaction with the support.[38]

The electronic properties of the samples were studied by TRMC technique at different wavelengths, considering both UV and visible regions. The excitation wavelengths were 355, 400, 450, 470, 480, 550, 600, and 650 nm, and the corresponding graphs are shown in Figure 7 and Figure S6. The surface modification with Ag and/or CuO NPs shows a strong influence on the charge-carrier dynamics in TiO_2−P25.

TRMC signals show that, under UV excitation at 355 nm (Figure 7a), all the photocatalysts are activated; i.e., free electrons are induced in the CB of TiO_2−P25, as shown by the sharp increase of TRMC signal, reaching I_{max} values. However, the decay of the signals is faster for the modified samples. The TRMC signals are mainly related to the electrons having higher mobility than holes. The decrease of the TRMC signals after modification is probably caused by efficient electron scavenging by Ag deposits on TiO_2−P25, resulting in a decrease in the recombination of charge carriers (e^-/h^+). Silver nanoparticles scavenge electrons, but these electrons can react with oxygen leading to $O_2^{\bullet-}$ radicals. It has to be noted that oxygen presents the trend to adsorb on silver, and this will help the formation of superoxide radicals. At the same time, and because of better separation of charge carriers, more holes and $HO^{\bullet}$ radicals are generated. It should be pointed out that faster decay is observed for TiO_2−P25 comodified with Ag NPs and CuO clusters, and this acceleration increases with the amount of CuO (Figure 7a and Figure S6a). The photogenerated electrons can be trapped by Cu^{II} (due to the unfilled 3d shell, $t_{2g}^6\ e_g^3$ configuration), on the surface of TiO_2−P25, decreasing the recombination process.[45] The TRMC measurements show that Ag@CuO nanoparticles (Ag@CuO(1:3) and Ag@CuO (1:1)) are very efficient in electron scavenging (see Figure 7 and Figure S6a), due to the synergic effect between Ag and CuO. This acceleration of the signal decay, with metal exhibiting capacitive properties, has also been observed for the modification of TiO_2

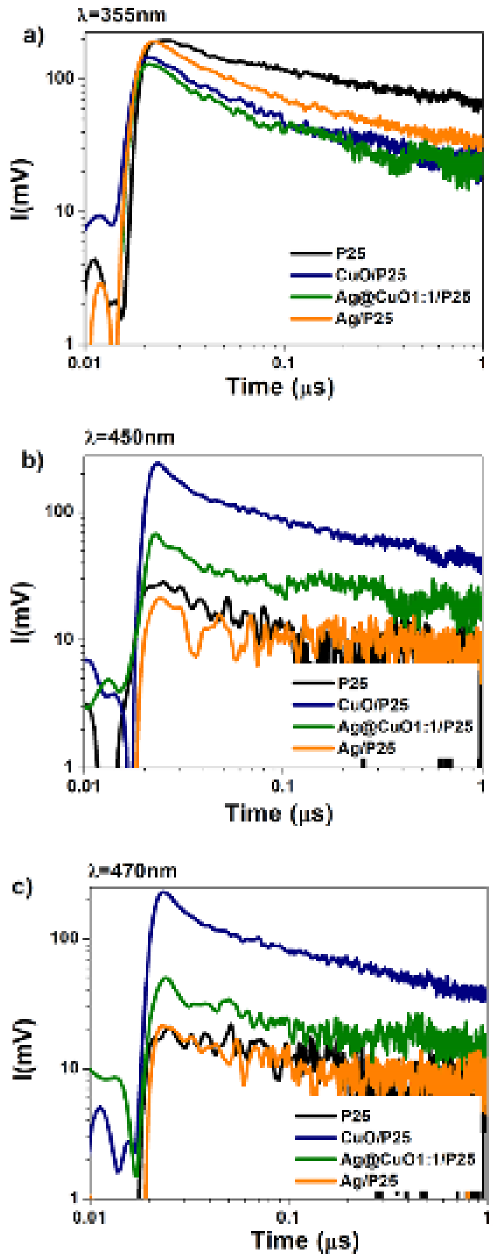

Figure 7. TRMC signals obtained after excitation at 355, 450, and 470 nm of TiO_2−P25, bare and modified with Ag, Ag@CuO1:1, and CuO. The laser energy of these wavelengths were 1.7, 6.7, and 6.2 mJ cm^{-2}, respectively.

DOI: 10.1021/acs.jpcc.5b10703
J. Phys. Chem. C 2016, 120, 5143−5154

with Ag clusters and NPs, Au NPs, and Au−Cu NPs.[6,7,15] This observation is different from our previous results performed with Pt- and Pd-modified TiO_2, where a slowdown of the overall decay was observed.[4,5,46] Indeed, with metals such as Pt and Pd, the experimental data agree with the model of a simple Schottky-type barrier between TiO_2 and metal. An increase in the lifetime of the electrons is observed, due, as expected, to a better separation of charge carriers caused by the barrier.[46]

Nonetheless, an important change is observed in the TRMC signals when the samples were irradiated at 400 nm (Figure S6b), i.e., at the transition between the UV and the visible regions. For P25 and Ag/P25, the I_{max} values are lower than those obtained under 355 nm as expected since the irradiation energy is lower than the band gap of anatase, and thus only the rutile phase, being in the minority, can be activated. However, the samples containing copper reach a higher I_{max} value, which represents a higher amount of free electrons in the CB of TiO_2−P25. This is consistent with the shift of the band gap toward the visible region observed by DRS for these samples compared to bare TiO_2−P25.

Under excitation in the visible region, there is no light absorption by pure TiO_2−P25 because of its large band gap. Under excitation with wavelengths of 450 and 470 (see Figure 7), TRMC signals are obtained with the samples modified with CuO due to its narrow band gap, attesting the generation of free electrons in the conduction bands of TiO_2−P25 (see also Figures S6 e−h). The highest I_{max} for all irradiation ranges, is obtained for TiO_2−P25 modified with CuO (CuO/P25). This suggests that a large amount of excess electrons are injected in the CB of TiO_2−P25 after excitation of the metal oxide clusters. Thus, under visible light, copper oxide is excited, and then electrons from its CB are transferred to the CB of the TiO_2−P25. This excitation of CuO induces also the same large amount of holes located on these clusters. However, the decay of the TRMC signals is very fast in the case of CuO/TiO_2 (Figure 7b,c). This fast decay is probably due to fast recombination of the electrons injected from CuO in the conduction band of TiO_2 with excess holes located on the numerous CuO clusters. However, for the Ag@CuO comodified samples, it should be reminded that silver-based NPs are still working as electron traps, decreasing the TRMC signal with the Ag loading. In this case, the electrons coming from excited CuO are not injected in the conduction band of TiO_2, but they are trapped by Ag NPs. These electrons probably recombine very fast with the holes located on CuO because of the large concentration of CuO clusters on AgNPs. It must be pointed out that electron transfer from silver NPs could not be excluded since TRMC operates at longer times (ns) than plasmonic excitation; e.g., 240 fs was reported for electron transfer from 10 nm size gold to titania.[47] At longer wavelengths (600 and 650 nm) (see Supporting Information Figure S6) only small signals for the samples with larger amount of copper, i.e., Ag@CuO1:3/P25 and CuO/P25, were detected.

These results show that under visible-light excitation electrons are promoted from CuO NPs to the CB of TiO_2−P25. Also, it is worth noting that copper oxide clusters are able to activate the TiO_2−P25 photocatalyst in a wider range of wavelengths under visible-light irradiation, compared to the activation with the presence of silver.

3.3. Photocatalytic Tests. The photocatalytic activity of the modified TiO_2−P25 samples was evaluated for the degradation of phenol and acetic acid under UV and visible light.

The curves for phenol degradation are shown in Figure 8. Surface modification of TiO_2−P25 with Ag NPs and CuO clusters does not influence markedly the photocatalytic activity of TiO_2−P25 under UV light. However, an enhancement of the photocatalytic activity is observed for samples modified with Ag@CuO clusters. Under UV irradiation, (Figure 8a) the Ag−CuO-modified titania and Ag@CuO1:1/P25 (see also the systems Ag@CuO3:1/P25 and Ag@CuO1:3/P25 in Figure S7−1a) achieve the complete degradation of phenol after 15 min. The kinetic data can be fitted with a pseudo-first-order reaction, and the estimated reaction rates are shown in Tables 3 and S2. Under UV excitation, the oxidation is due to $HO^{\bullet}$ and $O_2^{\bullet-}$ radicals, but under visible light the oxidation is mainly due to $O_2^{\bullet-}$ radicals. We considered zero order for visible light and pseudo-first-order for UV light excitation which fits better the curves, but it does not have a physical meaning as the mechanism is much more complex.

The highest photocatalytic activity is obtained with the sample Ag@CuO1:1/P25 with a reaction rate of around 3.4 × 10^{-3} s^{-1}, which is approximately 1.2 times higher than that of bare TiO_2−P25 (2.5 × 10^{-3} s^{-1}). This increase in the photocatalytic activity is attributable to the reduction of the recombination process of the charge carriers due to the electron

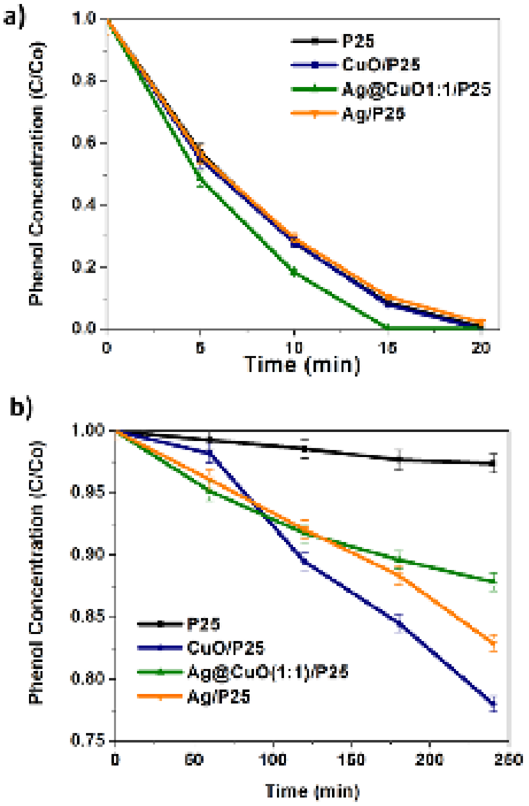

Figure 8. Degradation curves of phenol under (a) UV and (b) visible light (λ > 450 nm) for bare and modified (with, Ag, Ag@CuO1:1, and CuO) TiO_2−P25.

DOI: 10.1021/acs.jpcc.5b10703
J. Phys. Chem. C 2016, 120, 5143−5154

Table 3. Photocatalytic Reaction Rates for Phenol Degradation with Ag/P25, CuO/P25, and Ag@CuO1:1/P25 under UV Irradiation (Pseudo-First-Order Reaction) and Visible Light (Zero-Order Reaction)[a]

sample	UV light ($\times 10^{-3}$ s^{-1})	visible light ($\times 10^{-4}$ M s^{-1})
P25	2.5	0.9
CuO/P25	2.6	7.5
Ag@CuO1:1/P25	3.4	3.6
Ag/P25	2.3	5.3

[a] The relative uncertainty for UV light is 5% and for visible light is 3%.

scavenging by Ag NPs and to the reduction of Cu^{II} into Cu^{I}.[45] Foster et al. found that the oxidation of Cu^{I} into Cu^{II} by O_2 decreased the electron–hole recombination.[48] These photocatalytic results can be related to the TRMC signals: TRMC data (λ_{ex} = 355 nm) indicate electron sinking by comodification with Ag and CuO clusters (lower I_{max} and faster decay, Figure 7a) beneficial for the photocatalytic activity.

However, surface modification with Ag and/or CuO NPs significantly increases the photoactivity of TiO_2–P25 under visible irradiation.

Under visible light, the photoactivity of the pure TiO_2–P25 is usually very low because the illumination energy is lower than the band gap energy. Modification of titania results in visible photocatalytic activity, as shown in Figure 8b and Figure S7–1b for phenol degradation. The modification with CuO leads to a slightly higher enhancement in the photocatalytic properties compared to the modification with Ag or Ag@CuO. 25% and 17% phenol degradation are reached after 4 h irradiation of CuO/P25 and Ag/P25, respectively. Surface modification with silver and copper oxide nanoparticles changes the absorption properties of the photocatalysts, particularly as an enhancement of the absorption in the visible range creating an activity under visible light.

The CuO/P25 sample exhibits the highest photocatalytic activity for phenol degradation under visible light. This photocatalytic activity can be related to the TRMC signals as previously discussed: The CuO/P25 sample showed the highest I_{max} value in a wide range of excitation wavelengths within the visible range (Figures 7b and 7c), which represents more electrons in the CB of the semiconductor TiO_2–P25. The corresponding kinetics data following a zero order for the degradation of phenol under visible light are shown in Tables 3 and S2. The highest values of the reaction rates are obtained with Ag/P25 and CuO/P25. It has to be noted that the CuO/P25 sample shows a reaction rate seven times higher than bare TiO_2–P25, thus demonstrating the enhancement of the photoactivity of TiO_2–P25 with its surface modification with CuO.

The modified TiO_2–P25 samples were also evaluated for the photocatalytic evolution of CO_2 as a result of the decomposition of acetic acid under monochromatic irradiation. Exemplary data for two different irradiation regions, i.e., UV at λ = 350 nm and visible light at λ = 470 nm, are shown in Figure 9, Figure S7–2a, and Figure S7–2b.

Figure 9 shows that the modified TiO_2–P25 samples are in general more active in the generation of CO_2 compared to bare TiO_2–P25, especially under visible light.

Under UV irradiation, at 350 nm (Figure 9a), the modified titania are more active than bare TiO_2–P25. TRMC signals at 355 nm show that CuO-based nanoparticles on TiO_2–P25 are efficient in electron scavenging (Figure 7a). This higher photocatalytic activity (higher generation of CO_2) at 350 nm for TiO_2–P25 modified with CuO-based nanoparticles (Ag, Ag@CuO1:3, Ag@CuO1:1, and CuO) can be caused by better charge-carrier separation, with the exception of the Ag@CuO3:1/P25 sample (see Figure S7–2a).

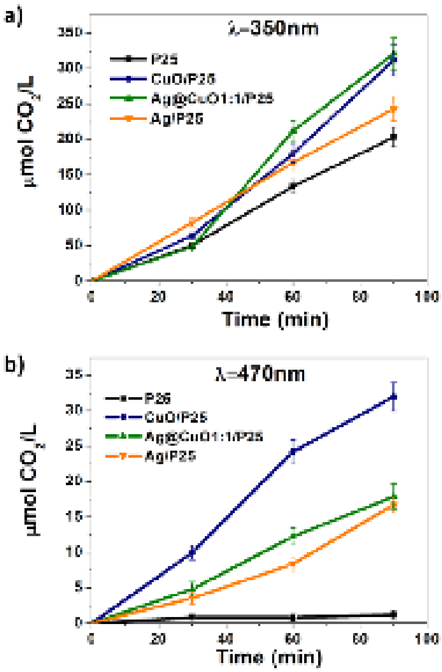

Figure 9. Photocatalytic evolution of CO_2 resulting from the decomposition of acetic acid under irradiation with (a) 350 nm and (b) 470 nm for the pure system TiO_2–P25 and modified systems with Ag, Ag@CuO1:1, and CuO.

Under visible light at 470 nm irradiation (Figure 9b and Figure S7–2b), surface-modified TiO_2–P25 with Ag and CuO clusters is more active in the production of CO_2 compared to bare TiO_2–P25. Surface modification with CuO nanoclusters induces a higher increase in the photocatalytic activity under visible light compared to the modification with plasmonic Ag and Ag@CuO nanoparticles. The highest production of CO_2 is again obtained with CuO/P25. Indeed, it has to be noted that CuO/P25 presents a higher TRMC signal at 470 nm compared to Ag@CuO/P25, and this indicates that more electrons are generated in the CB of CuO-modified TiO_2–P25.

On the basis of acetic acid decomposition at various monochromatic irradiations, the AS of the synthesized samples were obtained, and the results are shown in Figures 10 and S8g. The samples containing mainly CuO/P25 exhibit higher activity than bare TiO_2–P25 under UV irradiation. In the visible range, the modified TiO_2–P25 with Ag and CuO shows higher apparent quantum efficiency in the range between 410 and 500 nm, which can be related to the LSPR of silver and to the injection of electrons from CuO in the CB of TiO_2–P25.

It has to be noted that, under visible light, for both phenol degradation and CO_2 generation the modification with CuO induces the highest photocatalytic activity. These results are shown in Figure 8b and Figure 9b. In the case of CuO/P25, CuO is in direct contact with TiO_2, and a high amount of

DOI: 10.1021/acs.jpcc.5b10703
J. Phys. Chem. C 2016, 120, 5143–5154

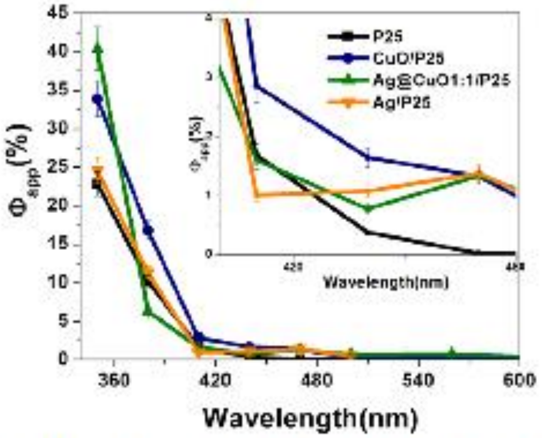

Figure 10. Action spectra for the acetic acid decomposition on bare and modified TiO_2−P25 (with Ag, CuO, and Ag@CuO1:1).

electrons are directly injected from CuO into the CB of TiO_2−P25 as is shown by the TRMC signals under excitation with the visible light. However, in the case of TiO_2−P25 modified with Ag@CuO, the CuO shell is deposited on Ag nanoparticles. Under visible-light excitation, the electrons cannot be directly injected from CuO into the CB of TiO_2−P25, due to the interaction of the Ag_{core}@CuO_{shell} structure. This is consistent with the TRMC signals under visible excitation, which are lower for Ag@CuO/P25 than for CuO/P25 (Figure 7b,c), affecting the photoactivity as is shown in most of the tested reactions, where the activity of Ag@CuO/P25 samples is lower than that of Ag/P25 and CuO/P25.

The AS were compared to the absorption spectra obtained by DRS (Figure S8), and they indicate that the photoreaction is carried out by a photocatalytic mechanism.[49] The action spectrum correlates well with the absorption spectrum for bare titania, reaching a quantum yield of 22.8%, 10.2%, and 1.7% for irradiation with 350, 380, and 410 nm, respectively. However, for the modified samples, only a part of the absorption spectra (below 480 nm) correlates with their photocatalytic activity, reaching a maximum at 470 nm, which confirms that the LSPR of Ag NPs and the narrow band gap of CuO are responsible for the photocatalytic activity under visible-light irradiation.

CuO/P25 and Ag@CuO/P25 exhibit no photocatalytic activity at $\lambda > 500$ nm (negligible quantum efficiency) but present small TRMC signals: We hypothesized that these generated electrons with lower energy are mobile but inactive for degradation of organic compounds or these electrons are reactive but with lower quantum yield.

It is important to mention that the DRS of dried Ag-modified samples differ from suspended ones,[15,50] showing a red-shift due to enhanced scattering, which is highly dependent on particle size and shape,[42] contrasting with Au/TiO_2 systems, that shows almost the same DRS.[9]

These combined results by TRMC and AS shed light on the photocatalytic mechanism: Under UV light, the Ag nanoparticles and CuO clusters work as electron pools, retarding the recombination process as it is supported by the TRMC results. This scavenging phenomenon helps to increase the photoreactions due to the formation of the Schottky junction when Ag and CuO are in contact with the semiconductor TiO_2−P25. It is known that coupling of TiO_2 with other semiconductors of different redox energy levels can lead to a more efficient charge-carrier separation process, i.e., an increase in the lifetime of the charge carriers and an enhancement of the interfacial charge-

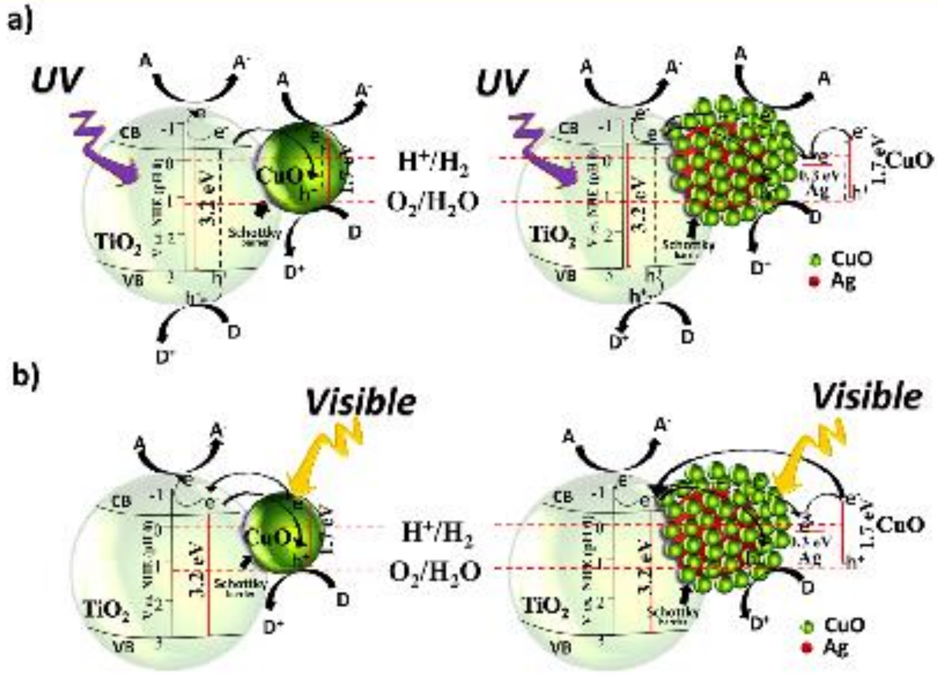

Figure 11. Proposed photocatalytic mechanisms of TiO_2−P25 modified with CuO and Ag@CuO (a) under UV and (b) under visible irradiation.

DOI: 10.1021/acs.jpcc.5b10703
J. Phys. Chem. C 2016, 120, 5143−5154

transfer efficiency to adsorbed substrate.[51,52] It is proposed that electrons trapped by CuO would react with adsorbed oxygen or air retarding (or inhibiting) the electron−hole recombination.[45] TRMC signals show that Ag@CuO nanoparticles are more efficient in electron scavenging compared to Ag NPs and CuO clusters, and this leads to higher photocatalytic activity under UV light. Under visible-light excitation, TRMC signals and AS show that Ag NPs, due to their surface plasmon resonance, and CuO, due to its narrow band gap (1.7 eV),[52] induce an activity in the visible. It has to be noted that this energy band gap value increases with the size of CuO; e.g., Ge et al. reported that for CuO nanoclusters the band gap decreases from 2.6 to 1.4 eV when the size increases from 1.1 to 2 nm.[53] The CuO clusters are excited under visible-light injecting electrons in the CB of TiO_2−P25. In the case of CuO/P25, more electrons are injected compared to the other modified samples, and this corresponds to higher photocatalytic activity under visible light. However, the photocatalytic activity under visible light of TiO_2−P25 comodified Ag@CuO clusters is lower than that of CuO/P25 and Ag/P25. This behavior is probably due to the electron scavenging by Ag, instead of transferring the electrons to the CB of titania.

All the above-discussed results allow us to propose photoinduced mechanisms for TiO_2−P25 modified with CuO and Ag@CuO nanoparticles under UV and visible-light irradiation, and they are shown in Figure 11: under UV irradiation (Figure 11a), the number of charge carriers decreases due to the relaxation of CB photogenerated electrons on TiO_2−P25 to the valence band (VB) of CuO, acting in this system as electron traps. The photocatalytic activity is similar to TiO_2−P25 for phenol degradation but is higher at 350 nm for acetic acid degradation (Figure 8a and Figure 9a,b). Under visible irradiation (Figure 11b), due to the position and the value of the energy band gap of CuO, visible light photogenerates electrons from CuO, and these electrons are injected into the CB of TiO_2−P25, as can be observed in TRMC signals in Figure 7b,c at 450 and 470 nm. The photoactivity is always higher than TiO_2−P25 for all the modified samples (Figure 8b and Figure 9b). For Ag@CuO/P25, in Figure 11a, under UV irradiation, the Ag@CuO NPs scavenge electrons (as shown by the TRMC signal at 355 nm, Figure 7a), which induces an increase in the photoactivity (see Figure 8, phenol degradation), due to the fact that Ag NPs work as electron traps of both TiO_2−P25 and CuO semiconductors. When the systems are irradiated under visible light (Figure 11b) Ag NPs still work as electron traps, trapping the electrons photogenerated by CuO avoiding a part of injection to the CB of TiO_2−P25, decreasing the TRMC signals, and thus decreasing the photoactivity.

■ CONCLUSIONS

CuO clusters, Ag, and Ag@CuO NPs were synthesized by radiolysis on the surface of TiO_2−P25. HAADF-STEM, XPS, and XAS characterization have shown that, in the case of comodification with silver and copper, core−shell nanoparticles composed of silver cores decorated with small CuO clusters were obtained on TiO_2−P25. Surface modification with Ag, Ag@CuO, and CuO nanoparticles induces an enhancement in the photocatalytic activity of TiO_2−P25, under both UV and visible light. Catalytic tests for phenol and acetic acid degradation show that comodification of TiO_2−P25 with CuO and Ag nanoparticles induces a higher photocatalytic activity under UV light compared to single modification with only Ag or CuO clusters, while the contrary is obtained under visible light. Under visible light, CuO-modified titania exhibits higher activity than plasmonic Ag/P25 and Ag@CuO/P25. TRMC results show that under excitation with UV light metal Ag NPs, Ag@CuO, and CuO clusters act as electron traps decreasing the recombination process, and thus they present a high increment in the apparent quantum yield. Under visible excitation, the Ag nanoparticles absorb incident photons due to the LSPR and inject electrons into the CB of TiO_2−P25, as is shown by TRMC measurements. CuO are excited in the visible range because of their band gap, and the electrons are driven from the CB of CuO to the CB of TiO_2−P25.

In general, the photocatalytic activity of the samples containing CuO is higher, which induces a photocatalytic activity in a wider spectral range compared to that obtained with modification with silver. AS prove that decomposition of acetic acid is driven by photocatalytic reaction, and Ag and CuO modification results in high enhancement of quantum yield under UV and visible-light irradiation. However, only a shorter part of the visible absorption (<500 nm) is responsible for photocatalytic activity. For the oxidation reactions tested in this study under visible-light irradiation, surface comodification of TiO_2−P25 with Ag@CuO clusters leads to samples with lower activity compared to Ag/P25 and CuO/P25.

The antibacterial and antifungal properties of titania modified with copper and silver are under investigation.

■ ASSOCIATED CONTENT

Supporting Information

The Supporting Information is available free of charge on the ACS Publications website at DOI: 10.1021/acs.jpcc.5b10703.

> Additional energy-dispersive X-ray spectroscopy line scans and STEM-HAADF images of Ag- and Cu-modified TiO_2, additional TRMC signals, XPS analysis, and the photocatalytic tests for the samples with different ratios of Ag/CuO (PDF).

■ AUTHOR INFORMATION

Corresponding Authors

*E-mail: hynd.remita@u-psud.fr. Fax: +33 (0)1 69 15 30 55. Tel.: +33 (0)1 69 15 72 58.
*E-mail: jlrdz@ipicyt.edu.mx. Tel.: +52 44 48 34 20 00, Ext. 7217.

Notes

The authors declare no competing financial interest.

■ ACKNOWLEDGMENTS

The authors thank Arnaud Etcheberry (ILV, Université Versailles Saint-Quentin en Yvelines) for helpful discussions and Emiliano Fonda (SOLEIL, Saint-Aubin) for providing the beamtime at the SAMBA beamline. Financial support from the CNRS, ECOS-Nord M11-P02 project (CNRS-CONACYT bilateral project), the CONCERT-Japan Joint Call on Efficient Energy Storage (CNRS France, JST Japan), and the COST Nanoalloys and CONACYT (Mexico grant numbers 106437, 216315 and 356872) are highly acknowledged. M.G.M.M. acknowledges Campus France for the *Eiffel Excellence* Scholarship. The authors acknowledge also C'Nano *Ile de France for* the financial support for *the gamma source and* for TRMC setup. The RTRA Triangle de la Physique and the ANR project PhotoNorm are also acknowledged for the TRMC setup.

REFERENCES

(1) Linic, S.; Christopher, P.; Ingram, D. B. Plasmonic-Metal Nanostructures for Efficient Conversion of Solar to Chemical Energy. *Nat. Mater.* 2011, *10*, 911−921.

(2) Zhang, X.; Chen, Y. L.; Liu, R.-S.; Tsai, D. P. Plasmonic Photocatalysis. *Rep. Prog. Phys.* 2013, *76*, 046401.

(3) Banerjee, S.; Pillai, S. C.; Falaras, P.; O'Shea, K. E.; Byrne, J. A.; Dionysiou, D. D. New Insights into the Mechanism of Visible Light Photocatalysis. *J. Phys. Chem. Lett.* 2014, *5*, 2543−2554.

(4) Kowalska, E.; Remita, H.; Colbeau-Justin, C.; Hupka, J.; Belloni, J. Modification of Titanium Dioxide with Platinum Ions and Clusters: Application in Photocatalysis. *J. Phys. Chem. C* 2008, *112*, 1124−1131.

(5) Tahiri Alaoui, O.; Herissan, A.; Le Quoc, C.; Zekri, M.; el, M.; Sorgues, S.; Remita, H.; Colbeau-Justin, C. Elaboration, Charge-Carrier Lifetimes and Activity of Pd-TiO_2 Photocatalysts Obtained by Gamma Radiolysis. *J. Photochem. Photobiol., A* 2012, *242*, 34−43.

(6) Grabowska, E.; Zaleska, A.; Sorgues, S.; Kunst, M.; Etcheberry, A.; Colbeau-Justin, C.; Remita, H. Modification of Titanium(IV) Dioxide with Small Silver Nanoparticles: Application in Photocatalysis. *J. Phys. Chem. C* 2013, *117*, 1955−1962.

(7) Hai, Z.; Kolli, N. E.; Uribe, D. B.; Beaunier, P.; José-Yacaman, M.; Vigneron, J.; Etcheberry, A.; Sorgues, S.; Colbeau-Justin, C.; Chen, J.; et al. Modification of TiO_2 by Bimetallic Au−Cu Nanoparticles for Wastewater Treatment. *J. Mater. Chem. A* 2013, *1*, 10829−10835.

(8) Hai, Z.; Kolli, N. E.; Chen, J.; Remita, H. Radiolytic Synthesis of Au−Cu Bimetallic Nanoparticles Supported on TiO_2: Application in Photocatalysis. *New J. Chem.* 2014, *38*, 5279−5286.

(9) Kowalska, E.; Mahaney, O. O. P.; Abe, R.; Ohtani, B. Visible-Light-Induced Photocatalysis through Surface Plasmon Excitation of Gold on Titania Surfaces. *Phys. Chem. Chem. Phys.* 2010, *12*, 2344−2355.

(10) Shiraishi, Y.; Sakamoto, H.; Sugano, Y.; Ichikawa, S.; Hirai, T. Pt−Cu Bimetallic Alloy Nanoparticles Supported on Anatase TiO_2: Highly Active Catalysts for Aerobic Oxidation Driven by Visible Light. *ACS Nano* 2013, *7*, 9287−9297.

(11) Qiu, X.; Miyauchi, M.; Yu, H.; Irie, H.; Hashimoto, K. Visible-Light-Driven Cu(II)-(Sr(1-y)Na(y)) (Ti(1-x)Mo(x))O_3 Photocatalysts Based on Conduction Band Control and Surface Ion Modification. *J. Am. Chem. Soc.* 2010, *132*, 15259−15267.

(12) Luna, A. L.; Valenzuela, M. A.; Colbeau-Justin, C.; Vázquez, P.; Rodriguez, J. L.; Avendaño, J. R.; Alfaro, S.; Tirado, S.; Garduño, A.; De la Rosa, J. M. Photocatalytic Degradation of Gallic Acid over CuO−TiO_2 Composites under UV/Vis LEDs Irradiation. *Appl. Catal., A* 2015, DOI: 10.1016/j.apcata.2015.10.044.

(13) Zhao, L.; Cui, T.; Li, Y.; Wang, B.; Han, J.; Han, L.; Liu, Z. Efficient Visible Light Photocatalytic Activity of P−n Junction CuO/TiO_2 Loaded on Natural Zeolite. *RSC Adv.* 2015, *5*, 64495−64502.

(14) Zielińska-Jurek, A.; Kowalska, E.; Sobczak, J. W.; Lisowski, W.; Ohtani, B.; Zaleska, A. Preparation and Characterization of Monometallic (Au) and Bimetallic (Ag/Au) Modified-Titania Photocatalysts Activated by Visible Light. *Appl. Catal., B* 2011, *101*, 504−514.

(15) Kowalska, E.; Wei, Z.; Karabiyik, B.; Herissan, A.; Janczarek, M.; Endo, M.; Markowska-Szczupak, A.; Remita, H.; Ohtani, B. Silver-Modified Titania with Enhanced Photocatalytic and Antimicrobial Properties under UV and Visible Light Irradiation. *Catal. Today* 2015, *252*, 136−142.

(16) Irie, H.; Miura, S.; Kamiya, K.; Hashimoto, K. Efficient Visible Light-Sensitive Photocatalysts: Grafting Cu(II) Ions onto TiO_2 and WO_3 Photocatalysts. *Chem. Phys. Lett.* 2008, *457*, 202−205.

(17) Ovcharov, M. L.; Shvalagin, V. V.; Granchak, V. M. Photocatalytic Reduction of CO_2 on Mesoporous TiO_2 Modified with Ag/Cu Bimetallic Nanostructures. *Theor. Exp. Chem.* 2014, *50*, 175−180.

(18) Ohtani, B.; Prieto-Mahaney, O. O.; Li, D.; Abe, R. What Is Degussa (Evonik) P25? Crystalline Composition Analysis, Reconstruction from Isolated Pure Particles and Photocatalytic Activity Test. *J. Photochem. Photobiol., A* 2010, *216*, 179−182.

(19) Remita, H.; Remita, S. Metal Clusters and Nanomaterials: Contribution of Radiation Chemistry. In *Recent Trends in Radiation Chemistry*; World Scientific, 2010; pp 347−383.

(20) Belloni, J.; Mostafavi, M.; Remita, H.; Marignier, J. L.; Delcourt, M.-O. Radiation-Induced Synthesis of Mono- and Multi-Metallic Clusters and Nanocolloids. *New J. Chem.* 1998, *22*, 1239−1255.

(21) Colbeau-Justin, C.; Kunst, M.; Huguenin, D. Structural Influence on Charge-Carrier Lifetimes in TiO_2 Powders Studied by Microwave Absorption. *J. Mater. Sci.* 2003, *38*, 2429−2437.

(22) Kouamé, N. A.; Alaoui, O. T.; Herissan, A.; Larios, E.; José-Yacaman, M.; Etcheberry, A.; Colbeau-Justin, C.; Remita, H. Visible Light-Induced Photocatalytic Activity of Modified titanium(IV) Oxide with Zero-Valent Bismuth Clusters. *New J. Chem.* 2015, *39*, 2316−2322.

(23) Martin, S. T.; Herrmann, H.; Choi, W.; Hoffmann, M. R. Time-Resolved Microwave Conductivity. Part 1. TiO_2 Photoreactivity and Size Quantization. *J. Chem. Soc., Faraday Trans.* 1994, *90*, 3315.

(24) Khatouri, J.; Mostafavi, M.; Amblard, J.; Belloni, J. Radiation-Induced Copper Aggregates and Oligomers. *Chem. Phys. Lett.* 1992, *191*, 351−356.

(25) Hansen, M.; Elliott, R. P.; Shunk, F. A. *Constitution of binary alloys*, 15th ed.; McGraw-Hill: New York, 1958.

(26) Lequien, F.; Creuze, J.; Berthier, F.; Braems, I.; Legrand, B. Superficial Segregation, Wetting, and Dynamical Equilibrium in Bimetallic Clusters: A Monte Carlo Study. *Phys. Rev. B: Condens. Matter Mater. Phys.* 2008, *78*, 075414.

(27) Moreno, V.; Creuze, J.; Berthier, F.; Mottet, C.; Tréglia, G.; Legrand, B. Site Segregation in Size-Mismatched Nanoalloys: Application to Cu−Ag. *Surf. Sci.* 2006, *600*, 5011−5020.

(28) Lequien, F.; Creuze, J.; Berthier, F.; Legrand, B. Dynamical Equilibrium in Nanoalloys. *Faraday Discuss.* 2008, *138*, 105−117.

(29) Guisbiers, G.; Mendoza-Cruz, R.; Bazán-Díaz, L.; Velázquez-Salazar, J. J.; Mendoza-Perez, R.; Robledo-Torres, J. A.; Rodriguez-Lopez, J. L.; Montejano-Carrizales, J. M.; Whetten, R. L.; José-Yacamán, M. Electrum, the Gold−Silver Alloy, from the Bulk Scale to the Nanoscale: Synthesis, Properties, and Segregation Rules. *ACS Nano* 2016, *10*, 188.

(30) Pellarin, M.; Issa, I.; Langlois, C.; Lebeault, M.-A.; Ramade, J.; Lermé, J.; Broyer, M.; Cottancin, E. Plasmon Spectroscopy and Chemical Structure of Small Bimetallic Cu(1−x)Agx Clusters. *J. Phys. Chem. C* 2015, *119*, 5002−5012.

(31) Verbruggen, S. W.; Keulemans, M.; Filippousi, M.; Flahaut, D.; Van Tendeloo, G.; Lacombe, S.; Martens, J. A.; Lenaerts, S. Plasmonic Gold−silver Alloy on TiO_2 Photocatalysts with Tunable Visible Light Activity. *Appl. Catal., B* 2014, *156*, 116−121.

(32) Stathatos, E.; Lianos, P.; Falaras, P.; Siokou, A. Photocatalytically Deposited Silver Nanoparticles on Mesoporous TiO_2 Films. *Langmuir* 2000, *16*, 2398−2400.

(33) Waterhouse, G. I. N.; Bowmaker, G. A.; Metson, J. B. Oxidation of a Polycrystalline Silver Foil by Reaction with Ozone. *Appl. Surf. Sci.* 2001, *183*, 191−204.

(34) Bielmann, M.; Schwaller, P.; Ruffieux, P.; Gröning, O.; Schlapbach, L.; Gröning, P. AgO Investigated by Photoelectron Spectroscopy: Evidence for Mixed Valence. *Phys. Rev. B: Condens. Matter Mater. Phys.* 2002, *65*, 235431.

(35) Han, Y.; Lupitskyy, R.; Chou, T.-M.; Stafford, C. M.; Du, H.; Sukhishvili, S. Effect of Oxidation on Surface-Enhanced Raman Scattering Activity of Silver Nanoparticles: A Quantitative Correlation. *Anal. Chem.* 2011, *83*, 5873−5880.

(36) Espinós, J. P.; Morales, J.; Barranco, A.; Caballero, A.; Holgado, J. P.; González-Elipe, A. R. Interface Effects for Cu, CuO, and Cu_2O Deposited on SiO_2 and ZrO_2. XPS Determination of the Valence State of Copper in Cu/SiO_2 and Cu/ZrO_2 Catalysts. *J. Phys. Chem. B* 2002, *106*, 6921−6929.

(37) Pauly, N.; Tougaard, S.; Yubero, F. Determination of the Cu 2p Primary Excitation Spectra for Cu, Cu_2O and CuO. *Surf. Sci.* 2014, *620*, 17−22.

DOI: 10.1021/acs.jpcc.5b10703
J. Phys. Chem. C 2016, 120, 5143−5154

(38) Colón, G.; Maicu, M.; Hidalgo, M. C.; Navío, J. A. Cu-Doped TiO_2 Systems with Improved Photocatalytic Activity. *Appl. Catal., B* **2006**, *67*, 41–51.

(39) Peters, S.; Peredkov, S.; Neeb, M.; Eberhardt, W.; Al-Hada, M. Size-Dependent XPS Spectra of Small Supported Au-Clusters. *Surf. Sci.* **2013**, *608*, 129–134.

(40) Chusuei, C. C.; Brookshier, M. A.; Goodman, D. W. Correlation of Relative X-Ray Photoelectron Spectroscopy Shake-up Intensity with CuO Particle Size. *Langmuir* **1999**, *15*, 2806–2808.

(41) Klepka, M. T.; Drzewiecka, A.; Wolska, A.; Ferenc, W. XAS Studies on Cu(II) Complexes with Derivatives of Phenoxyacetic and Benzoic Acids. *Chem. Phys. Lett.* **2012**, *553*, 59–63.

(42) Chettibi, S.; Keghouche, N.; Benguedouar, Y.; Bettahar, M. M.; Belloni, J. Structural and Catalytic Characterization of Radiation-Induced Ni/TiO_2 Nanoparticles. *Catal. Lett.* **2013**, *143*, 1166–1174.

(43) Chiarello, G. L.; Selli, E.; Forni, L. Photocatalytic Hydrogen Production over Flame Spray Pyrolysis-Synthesised TiO_2 and Au/TiO_2. *Appl. Catal., B* **2008**, *84*, 332–339.

(44) Mizeikis, V.; Kowalska, E.; Juodkazis, S. Resonant Localization, Enhancement, and Polarization of Optical Fields in Nano-Scale Interface Regions for Photo-Catalytic Applications. *J. Nanosci. Nanotechnol.* **2011**, *11*, 2814–2822.

(45) Chiang, K.; Amal, R.; Tran, T. Photocatalytic Degradation of Cyanide Using Titanium Dioxide Modified with Copper Oxide. *Adv. Environ. Res.* **2002**, *6*, 471–485.

(46) Emilio, C. A.; Litter, M. I.; Kunst, M.; Bouchard, M.; Colbeau-Justin, C. Phenol Photodegradation on Platinized-TiO_2 Photocatalysts Related to Charge-Carrier Dynamics. *Langmuir* **2006**, *22*, 3606–3613.

(47) Furube, A.; Du, L.; Hara, K.; Katoh, R.; Tachiya, M. Ultrafast Plasmon-Induced Electron Transfer from Gold Nanodots into TiO_2 Nanoparticles. *J. Am. Chem. Soc.* **2007**, *129*, 14852–14853.

(48) Foster, N. S.; Noble, R. D.; Koval, C. A. Reversible Photoreductive Deposition and Oxidative Dissolution of Copper Ions in Titanium Dioxide Aqueous Suspensions. *Environ. Sci. Technol.* **1993**, *27*, 350–356.

(49) Nishijima, K.; Ohtani, B.; Yan, X.; Kamai, T.; Chiyoya, T.; Tsubota, T.; Murakami, N.; Ohno, T. Incident Light Dependence for Photocatalytic Degradation of Acetaldehyde and Acetic Acid on S-Doped and N-Doped TiO_2 Photocatalysts. *Chem. Phys.* **2007**, *339*, 64–72.

(50) Kowalska, E.; Janczarek, M.; Rosa, L.; Juodkazis, S.; Ohtani, B. Mono- and Bi-Metallic Plasmonic Photocatalysts for Degradation of Organic Compounds under UV and Visible Light Irradiation. *Catal. Today* **2014**, *230*, 131–137.

(51) Orendorff, C. J.; Sau, T. K.; Murphy, C. J. Shape-Dependent Plasmon-Resonant Gold Nanoparticles. *Small* **2006**, *2*, 636–639.

(52) Marschall, R. Semiconductor Composites: Strategies for Enhancing Charge Carrier Separation to Improve Photocatalytic Activity. *Adv. Funct. Mater.* **2014**, *24*, 2421–2440.

(53) Ge, Y.; Shah, Z. H.; Wang, C.; Wang, J.; Mao, W.; Zhang, S.; Lu, R. In Situ Encapsulation of Ultrasmall CuO Quantum Dots with Controlled Band-Gap and Reversible Thermochromism. *ACS Appl. Mater. Interfaces* **2015**, *7*, 26437–26444.

DOI: 10.1021/acs.jpcc.5b10703
J. Phys. Chem. C 2016, 120, 5143–5154

Publications

"***Surface Modification of TiO_2 with Ag Nanoparticles and CuO Nanoclusters for Application in Photocatalysis***", M.G. Méndez-Medrano, E. Kowalska, A. Lehoux, A. Herissan, B. Ohtani, D. Bahena, V. Briois, C. Colbeau-Justin, J. L. Rodríguez-López, and H. Remita, in the Journal of Physical Chemistry C, **2016**, 120, 5143–5154, DOI: 10.1021/acs.jpcc.5b10703, 2016.

Article in process: "***Surface Modification of TiO_2 with Au Nanoclusters: Applications in Water Treatment and Hydrogen Generation*",** M.G. Méndez-Medrano, A. Lehoux, A. Herissan, E. Kowalska, B. Ohtani, S. Rau, C. Colbeau-Justin, J. L. Rodríguez-López, and H. Remita, to be submitted

Article in process: "***Visible Light Photo-Oxidation of Organic Pollutants and Hydrogen Production in Water with Copper Oxide Nanoclusters Supported on TiO_2***", M.G. Méndez-Medrano, E. Kowalska, D. Bahena, B. Ohtani, C. Colbeau-Justin, J. L. Rodríguez-López, and H. Remita, to be submitted.

Article in process: "**Synergic Effect of AgCuO on TiO_2 for the growth inhibition of Aspergillus Melleus and Penecillium Chrysogenum**", M.G. Méndez-Medrano, M. Endo, E. Kowalska, B. Ohtani, C. Colbeau-Justin, J. L. Rodríguez-López, and H. Remita, to be submitted.

Conferences

Oral Presentations:

- *"**Enhanced Photoactivity of TiO_2 under Visible Light using Mono and Bimetallic Nanoparticles of Ag and Cu**"*, Méndez-Medrano, M. G.; Herissan, A; Kowalska, E; Lehoux A; Ohtani, B; Bahena, D; Colbeau-Justin, C; Rodríguez-López, J. L.; Remita, H. XXIV International Materials Research Congress 2015, August 17th 2015, Cancun, Mexico.

- *"**Au/TiO_2 Plasmonic Photocatalyst: Applications in Water Treatment and Hydrogen Generation**"*, M.G. Méndez-Medrano, A. Herissan, E. Kowalska, A. Lehoux, B. Ohtani, S. Rau, C. Colbeau-Justin, J. L. Rodríguez-López, and H. Remita. Or-Nano, 23 March 2015, Paris, France.

- "***Mono and Bimetallic Nanoparticles Supported on TiO_2: Applications in Photocatalysis***", M. G. Méndez-Medrano, A. Herissan, J. L. Rodríguez-López, C. Colbeau-Justin. The final Conference of COST Action MP0903, 5-9 April 2014, Santa Margherita Ligure, Italy.

- *"**Modification of Titanium Dioxide with Metallic Nanoparticles: Application to Wastewater treatment**"*, M. G. Méndez-Medrano, A. Herissan, J. L. Rodríguez-López, C. Colbeau-Justin, III Simposio Becarios Conacyt, 6-8 November 2013, Strasbourg, France.

- *"**Plasmonic Photocatalysts with Mono and Bimetallic Nanoparticles Supported on TiO_2**",* M. G. Méndez-Medrano, J. L. Rodríguez-López, and H. Remita, XXII International Materials Research Congress, XXII International Materials Research Congress, 11 -15 August, 2013, Cancun, Mexico.

Poster Presentaions:

- *"**Enhanced Photoactivity of Ag-Cu/TiO_2 under UV and Visible Light**"*, M. G. Méndez-Medrano A. Herissan, E. Kowalska, A. Lehoux, B. Ohtani, D. Bahena, C. Colbeau-Justin, J. L. Rodríguez-López, and H. Remita, GDR Nanoalliages, 17 May 2015, Porquerolles, France.

- *"**Synthesis by Radiolysis Method of AgCu Clusters Supported on TiO_2**"*, M. G. Méndez, A. Herissan, C. Colbeau-Justin, Sven Rau, J. L. Rodríguez-López, H. Remita, CRC International Symposium, 14 October 2014, Sapporo, Japan.

- *"**Gold Nanoparticles Supported on TiO_2: Application in Photocatalysis**"*, M. G. Méndez, A. Herissan, C. Colbeau-Justin, H. Remita, Annual Meeting on Photochemistry, 11-13 October 2014, Sapporo, Japan.

- *“**Mono and Bimetallic Nanoparticles Supported on TiO$_2$: Applications in Photocatalysis and Water Splitting**”*, M. G. Méndez-Medrano, J. L. Rodríguez-López, A. Herissan, C. Colbeau-Justin, H. Remita. 8th European Meeting on solar Chemistry and Photocatalysis SPEA8, 25-28 June 2014, Thessalonik, Greece.

- Attendance to NanoTech 2012, 9th Topical Meeting on Nanostructured Materials and Nanotechnology, 6th Annual Meeting of DINANO, SMF, in the University of San Luis Potosi and IPICYT, 20 -22 Mai, 2012, San Luis Potosi, Mexico.

- 13° Research Seminar, in the presentation modality of the work "***Synthesis of reduced graphene oxide and graphene for its addition within a polymer matrix to enhance its conductive properties***". University of Aguascalientes 16 -18 Mai, 2012, San Luis Potosi, Mexico.

References

(1) Schaming, D.; Remita, H. Nanotechnology: From the Ancient Time to Nowadays. *Found. Chem.* **2015**, *17*, 187–205.

(2) Linic, S.; Christopher, P.; Ingram, D. B. Plasmonic-Metal Nanostructures for Efficient Conversion of Solar to Chemical Energy. *Nat. Mater.* **2011**, *10*, 911–921.

(3) Bian, Z.; Tachikawa, T.; Zhang, P.; Fujitsuka, M.; Majima, T. Au/TiO_2 Superstructure-Based Plasmonic Photocatalysts Exhibiting Efficient Charge Separation and Unprecedented Activity. *J. Am. Chem. Soc.* **2014**, *136*, 458–465.

(4) Zhang, X.; Chen, Y. L.; Liu, R.-S.; Tsai, D. P. Plasmonic Photocatalysis. *Rep. Prog. Phys.* **2013**, *76*, 046401.

(5) Linsebigler, A.; Lu, G.; Yates, J. Photocatalysis on TiOn Surfaces: Principles, Mechanisms, and Selected Results. *Chem Rev* **1995**, *95*, 735–758.

(6) Grabowska, E.; Zaleska, A.; Sorgues, S.; Kunst, M.; Etcheberry, A.; Colbeau-Justin, C.; Remita, H. Modification of Titanium(IV) Dioxide with Small Silver Nanoparticles: Application in Photocatalysis. *J. Phys. Chem. C* **2013**, *117*, 1955–1962.

(7) Ingram, D. B.; Christopher, P.; Bauer, J. L.; Linic, S. Predictive Model for the Design of Plasmonic Metal/Semiconductor Composite Photocatalysts. *ACS Catal.* **2011**, *10*, 1441–1447.

(8) Hai, Z.; Kolli, N. E.; Uribe, D. B.; Beaunier, P.; José-Yacaman, M.; Vigneron, J.; Etcheberry, A.; Sorgues, S.; Colbeau-Justin, C.; Chen, J.; et al. Modification of TiO_2 by Bimetallic Au–Cu Nanoparticles for Wastewater Treatment. *J. Mater. Chem. A* **2013**, *1*, 10829–10835.

(9) Ortega Méndez, J. A.; López, C. R.; Pulido Melián, E.; González Díaz, O.; Doña Rodríguez, J. M.; Fernández Hevia, D.; Macías, M. Production of Hydrogen by Water Photo-Splitting over Commercial and Synthesised Au/TiO2 Catalysts. *Appl. Catal. B Environ.* **2014**, *147*, 439–452.

(10) Wang, C.; Astruc, D. Nanogold Plasmonic Photocatalysis for Organic Synthesis and Clean Energy Conversion. *Chem. Soc. Rev.* **2014**, *43*, 7188–7216.

(11) Singer, S. F. Global Effects of Environmental Pollution. *Eos Trans. Am. Geophys. Union* **1970**, *51*, 476–478.

(12) Bernier, J.-C. L'eau, Un Nouvel « or Bleu » -. *l'actualité chimique*. **2014**, pp 5–6.

(13) Total Renewable Water Resources per capita by Country http://chartsbin.com/view/1470 (accessed Oct 1, **2015**).

(14) Agnès Jacquesy, R. L'eau, Une Ressource Vitale - Le Rôle de La Chimie. *L'Actualité Chimique*. **2014**, 3–6.

(15) Tiwari, D. K.; Behari, J.; Sen, P. *Application of Nanoparticles in Waste Water Treatment 1*.

(16) Bhatnagar, A.; Sillanpää, M. Applications of Chitin- and Chitosan-Derivatives for the Detoxification of Water and Wastewater — A Short Review. *Adv. Colloid Interface Sci.* **2009**, *152*, 26–38.

(17) Ayati, A.; Ahmadpour, A.; Bamoharram, F. F.; Tanhaei, B.; Mänttäri, M.; Sillanpää, M. A Review on Catalytic Applications of Au/TiO2 Nanoparticles in the Removal of Water Pollutant. *Chemosphere* **2014**, *107*, 163–174.

(18) CO2 emissions (metric tons per capita) | Data | Graph http://data.worldbank.org/indicator/EN.ATM.CO2E.PC/countries/1W-MX-FR?display=graph (accessed Oct 2, **2015**).

(19) Hydrogen Energy and Fuel Cell Technology http://www.renewableenergyworld.com/hydrogen/tech.html (accessed Oct 4, **2015**).

(20) Hydrogen Energy - The Perfect Energy Source for the Future http://www.azocleantech.com/article.aspx?ArticleID=29 (accessed Oct 4, **2015**).

(21) Chueh, W. C.; Falter, C.; Abbott, M.; Scipio, D.; Furler, P.; Haile, S. M.; Steinfeld, A. High-Flux Solar-Driven Thermochemical Dissociation of CO_2 and H_2O Using Nonstoichiometric Ceria. *Science* **2010**, *330*, 1797–1801.

(22) Ogden, J. M.; Williams, R. H. Electrolytic Hydrogen from Thin-Film Solar Cells. *Int. J. Hydrog. Energy* **1990**, *15*, 155–169.

(23) Sartorel, A.; Carraro, M.; Toma, F. M.; Prato, M.; Bonchio, M. Shaping the Beating Heart of Artificial Photosynthesis: Oxygenic Metal Oxide Nano-Clusters. *Energy Environ. Sci.* **2012**, *5*, 5592–5603.

(24) Murdoch, M.; Waterhouse, G. I. N.; Nadeem, M. A.; Metson, J. B.; Keane, M. A.; Howe, R. F.; Llorca, J.; Idriss, H. The Effect of Gold Loading and Particle Size on Photocatalytic Hydrogen Production from Ethanol over Au/TiO_2 Nanoparticles. *Nat. Chem.* **2011**, *3*, 489–492.

(25) *Technoeconomic Analysis of Photoelectrochemical (PEC) Hydrogen Production, Direct*.

(26) Ohtani, B. Preparing Articles on Photocatalysis-Beyond the Illusions, Misconceptions, and Speculation. *Chem. Lett.* **2008**, *37*, 216–229.

(27) Glaze, W. H.; Kang, J.-W.; Chapin, D. H. The Chemistry of Water Treatment Processes Involving Ozone, Hydrogen Peroxide and Ultraviolet Radiation. *Ozone Sci. Eng.* **1987**, *9*, 335–352.

(28) Rao, P. S.; Hayon, E. Redox Potentials of Free Radicals. IV. Superoxide and Hydroperoxy Radicals . O_2- and. HO_2. *J. Phys. Chem.* **1975**, *79*, 397–402.

(29) Andreozzi, R.; Caprio, V.; Insola, A.; Marotta, R. Advanced Oxidation Processes (AOP) for Water Purification and Recovery. *Catal. Today* **1999**, *53*, 51–59.

(30) Haag, W. R.; Yao, C. C. D. Rate Constants for Reaction of Hydroxyl Radicals with Several Drinking Water Contaminants. *Environ. Sci. Technol.* **1992**, *26*, 1005–1013.

(31) Herrmann, J.-M. Heterogeneous Photocatalysis: Fundamentals and Applications to the Removal of Various Types of Aqueous Pollutants. *Catal. Today* **1999**, *53*, 115–129.

(32) Hashimoto, K.; Irie, H.; Fujishima, A. TiO_2 Photocatalysis: A Historical Overview and Future Prospects. *Jpn. J. Appl. Phys.* **2005**, *44*, 8269.

(33) Hoffmann, M. R.; Martin, S. T.; Choi, W.; Bahnemann, D. W. Environmental Applications of Semiconductor Photocatalysis. *Chem. Rev.* **1995**, *95*, 69–96.

(34) Chen, H. M.; Chen, C. K.; Liu, R.-S.; Wu, C.-C.; Chang, W.-S.; Chen, K.-H.; Chan, T.-S.; Lee, J.-F.; Tsai, D. P. A New Approach to Solar Hydrogen Production: A ZnO–ZnS Solid Solution Nanowire Array Photoanode. *Adv. Energy Mater.* **2011**, *1*, 742–747.

(35) Chen, H. M.; Chen, C. K.; Lin, C. C.; Liu, R.-S.; Yang, H.; Chang, W.-S.; Chen, K.-H.; Chan, T.-S.; Lee, J.-F.; Tsai, D. P. Multi-Bandgap-Sensitized ZnO Nanorod Photoelectrode Arrays for Water Splitting: An X-Ray Absorption Spectroscopy Approach for the Electronic Evolution under Solar Illumination. *J. Phys. Chem. C* **2011**, *115*, 21971–21980.

(36) Wu, J. C. S.; Wu, T.-H.; Chu, T.; Huang, H.; Tsai, D. Application of Optical-Fiber Photoreactor for CO_2 Photocatalytic Reduction. *Top. Catal.* **2008**, *47*, 131–136.

(37) Fujishima, A.; Rao, T. N.; Tryk, D. A. Titanium Dioxide Photocatalysis. *J. Photochem. Photobiol. C Photochem. Rev.* **2000**, *1*, 1–21.

(38) Nakata, K.; Fujishima, A. TiO2 Photocatalysis: Design and Applications. *J. Photochem. Photobiol. C Photochem. Rev.* **2012**, *13*, 169–189.

(39) Ohtani, B. Revisiting the Fundamental Physical Chemistry in Heterogeneous Photocatalysis: Its Thermodynamics and Kinetics. *Phys Chem Chem Phys* **2014**, *16*, 1788–1797.

(40) Pichat, P. A Brief Survey of the Potential Health Risks of TiO2 Particles and TiO_2-Containing Photocatalytic or Non-Photocatalytic Materials. *J. Adv. Oxid. Technol.* **2010**, *13*, 238–246.

(41) Pottier, A.; Chanéac, C.; Tronc, E.; Mazerolles, L.; Jolivet, J.-P. Synthesis of Brookite TiO_2 Nanoparticles by Thermolysis of TiCl4 in Strongly Acidic Aqueous Media. *J. Mater. Chem.* **2001**, *11*, 1116–1121.

(42) Colbeau-Justin, C.; Kunst, M.; Huguenin, D. Structural Influence on Charge-Carrier Lifetimes in TiO_2 Powders Studied by Microwave Absorption. *J. Mater. Sci.* **2003**, *38*, 2429–2437.

(43) Schindler, K. M.; Kunst, M. Charge-Carrier Dynamics in Titania Powders. *J. Phys. Chem.* **1990**, *94*, 8222–8226.

(44) Zhang, Z.; Yates, J. T. Band Bending in Semiconductors: Chemical and Physical Consequences at Surfaces and Interfaces. *Chem. Rev.* **2012**, *112*, 5520–5551.

(45) Kamat, P. V. Manipulation of Charge Transfer Across Semiconductor Interface. A Criterion That Cannot Be Ignored in Photocatalyst Design. *J. Phys. Chem. Lett.* **2012**, *3*, 663–672.

(46) Serpone, N.; Emeline, A. V. Semiconductor Photocatalysis — Past, Present, and Future Outlook. *J. Phys. Chem. Lett.* **2012**, *3*, 673–677.

(47) Marschall, R. Semiconductor Composites: Strategies for Enhancing Charge Carrier Separation to Improve Photocatalytic Activity. *Adv. Funct. Mater.* **2014**, *24*, 2421–2440.

(48) Zaleska, A. Doped-TiO_2: A Review. *Recent Pat. Eng.* **2008**, *2*, 157–164.

(49) Zheng, S.; Wei, Z.; Yoshiiri, K.; Braumüller, M.; Ohtani, B.; Rau, S.; Kowalska, E. Titania Modification with a ruthenium(II) Complex and Gold Nanoparticles for Photocatalytic Degradation of Organic Compounds. *Photochem. Photobiol. Sci.* **2016**, *15*, 69–79.

(50) Asahi, R.; Morikawa, T.; Irie, H.; Ohwaki, T. Nitrogen-Doped Titanium Dioxide as Visible-Light-Sensitive Photocatalyst: Designs, Developments, and Prospects. *Chem. Rev.* **2014**, *114*, 9824–9852.

(51) Irie, H.; Watanabe, Y.; Hashimoto, K. Nitrogen-Concentration Dependence on Photocatalytic Activity of TiO_2-xNx Powders. *J. Phys. Chem. B* **2003**, *107*, 5483–5486.

(52) Ihara, T.; Miyoshi, M.; Iriyama, Y.; Matsumoto, O.; Sugihara, S. Visible-Light-Active Titanium Oxide Photocatalyst Realized by an Oxygen-Deficient Structure and by Nitrogen Doping. *Appl. Catal. B Environ.* **2003**, *42*, 403–409.

(53) Tachibana, Y.; Moser, J. E.; Grätzel, M.; Klug, D. R.; Durrant, J. R. Subpicosecond Interfacial Charge Separation in Dye-Sensitized Nanocrystalline Titanium Dioxide Films. *J. Phys. Chem.* **1996**, *100*, 20056–20062.

(54) Dai, Q.; Rabani, J. Photosensitization of Nanocrystalline TiO_2 Films by Anthocyanin Dyes. *J. Photochem. Photobiol. Chem.* **2002**, *148*, 17–24.

(55) Sato, S.; White, J. M. Photodecomposition of Water over Pt/TiO_2 Catalysts. *Chem. Phys. Lett.* **1980**, *72*, 83–86.

(56) Awazu, K.; Fujimaki, M.; Rockstuhl, C.; Tominaga, J.; Murakami, H.; Ohki, Y.; Yoshida, N.; Watanabe, T. A Plasmonic Photocatalyst Consisting of

Silver Nanoparticles Embedded in Titanium Dioxide. *J. Am. Chem. Soc.* **2008**, *130*, 1676–1680.

(57) Wang, P.; Huang, B.; Dai, Y.; Whangbo, M.-H. Plasmonic Photocatalysts: Harvesting Visible Light with Noble Metal Nanoparticles. *Phys. Chem. Chem. Phys.* **2012**, *14*, 9813–9825.

(58) Wang, Z.; Liu, J.; Chen, W. Plasmonic Ag/AgBr Nanohybrid: Synergistic Effect of SPR with Photographic Sensitivity for Enhanced Photocatalytic Activity and Stability. *Dalton Trans.* **2012**, *41*, 4866.

(59) Lombardi, J. R.; Birke, R. L. A Unified Approach to Surface-Enhanced Raman Spectroscopy. *J. Phys. Chem. C* **2008**, *112*, 5605–5617.

(60) Stefan Alexander, M. *Plasmonics: Fundamentals and Applications*; Springer US: Boston, MA, 2007.

(61) Zielińska-Jurek, A. Progress, Challenge, and Perspective of Bimetallic TiO_2-Based Photocatalysts. *J. Nanomater.* **2014**, *2014*, 1–17.

(62) Kelly, K. L.; Coronado, E.; Zhao, L. L.; Schatz, G. C. The Optical Properties of Metal Nanoparticles: The Influence of Size, Shape, and Dielectric Environment. *J. Phys. Chem. B* **2003**, *107*, 668–677.

(63) Thomann, I.; Pinaud, B. A.; Chen, Z.; Clemens, B. M.; Jaramillo, T. F.; Brongersma, M. L. Plasmon Enhanced Solar-to-Fuel Energy Conversion. *Nano Lett.* **2011**, *11*, 3440–3446.

(64) Mubeen, S.; Hernandez-Sosa, G.; Moses, D.; Lee, J.; Moskovits, M. Plasmonic Photosensitization of a Wide Band Gap Semiconductor: Converting Plasmons to Charge Carriers. *Nano Lett.* **2011**, *11*, 5548–5552.

(65) Zhdanov, V. P.; Hägglund, C.; Kasemo, B. Relaxation of Plasmons in Nm-Sized Metal Particles Located on or Embedded in an Amorphous Semiconductor. *Surf. Sci.* **2005**, *599*, L372–L375.

(66) Langhammer, C.; Yuan, Z.; Zorić, I.; Kasemo, B. Plasmonic Properties of Supported Pt and Pd Nanostructures. *Nano Lett.* **2006**, *6*, 833–838.

(67) Wu, Z.-C.; Zhang, Y.; Tao, T.-X.; Zhang, L.; Fong, H. Silver Nanoparticles on Amidoxime Fibers for Photo-Catalytic Degradation of Organic Dyes in Waste Water. *Appl. Surf. Sci.* **2010**, *257*, 1092–1097.

(68) Sun, S.; Wang, W.; Zhang, L.; Shang, M.; Wang, L. Ag@C Core/shell Nanocomposite as a Highly Efficient Plasmonic Photocatalyst. *Catal. Commun.* **2009**, *11*, 290–293.

(69) Kreibig, U.; Vollmer, M. *Optical Properties of Metal Clusters*; Toennies, J. P., Gonser, U., Osgood, R. M., Panish, M. B., Sakaki, H., Lotsch, H. K. V., Series Eds.; Springer Series in Materials Science; Springer Berlin Heidelberg: Berlin, Heidelberg, **1995**; 25.

(70) Bohren, C. F.; Huffman, D. R. Absorption and Scattering by a Sphere. In *Absorption and Scattering of Light by Small Particles*; Wiley-VCH Verlag GmbH, **1998**; 82–129.

(71) Huang, X.; El-Sayed, I. H.; Qian, W.; El-Sayed, M. A. Cancer Cell Imaging and Photothermal Therapy in the Near-Infrared Region by Using Gold Nanorods. *J. Am. Chem. Soc.* **2006**, *128*, 2115–2120.

(72) Orendorff, C. J.; Sau, T. K.; Murphy, C. J. Shape-Dependent Plasmon-Resonant Gold Nanoparticles. *Small Weinh. Bergstr. Ger.* **2006**, *2*, 636–639.

(73) Mock, J. J.; Barbic, M.; Smith, D. R.; Schultz, D. A.; Schultz, S. Shape Effects in Plasmon Resonance of Individual Colloidal Silver Nanoparticles. *J. Chem. Phys.* **2002**, *116*, 6755–6759.

(74) Kowalska, E.; Mahaney, O. O. P.; Abe, R.; Ohtani, B. Visible-Light-Induced Photocatalysis through Surface Plasmon Excitation of Gold on Titania Surfaces. *Phys. Chem. Chem. Phys.* **2010**, *12*, 2344–2355.

(75) Hai, Z.; Kolli, N. E.; Chen, J.; Remita, H. Radiolytic Synthesis of Au–Cu Bimetallic Nanoparticles Supported on TiO_2: Application in Photocatalysis. *New J. Chem.* **2014**, *38*, 5279–5286.

(76) Kowalska, E.; Remita, H.; Colbeau-Justin, C.; Hupka, J.; Belloni, J. Modification of Titanium Dioxide with Platinum Ions and Clusters: Application in Photocatalysis. *J. Phys. Chem. C* **2008**, *112*, 1124–1131.

(77) Tahiri Alaoui, O.; Herissan, A.; Le Quoc, C.; Zekri, M. el M.; Sorgues, S.; Remita, H.; Colbeau-Justin, C. Elaboration, Charge-Carrier Lifetimes and Activity of Pd-TiO_2 Photocatalysts Obtained by Gamma Radiolysis. *J. Photochem. Photobiol. Chem.* **2012**, *242*, 34–43.

(78) Zieliska-Jurek, A.; Reszczyska, J.; Grabowska, E.; Zalesk, A. Nanoparticles Preparation Using Microemulsion Systems. In *Microemulsions - An Introduction to Properties and Applications*; Najjar, R., Ed.; InTech, **2012**.

(79) Shiraishi, Y.; Sakamoto, H.; Sugano, Y.; Ichikawa, S.; Hirai, T. Pt–Cu Bimetallic Alloy Nanoparticles Supported on Anatase TiO_2: Highly Active Catalysts for Aerobic Oxidation Driven by Visible Light. *ACS Nano* **2013**, *7*, 9287–9297.

(80) Nwosu, C. An Electronegativity Approach to Catalytic Performance. *J. Tech. Sci. Technol.* **2012**, *1*, 25–28.

(81) Kowalska, E.; Janczarek, M.; Rosa, L.; Juodkazis, S.; Ohtani, B. Mono- and Bi-Metallic Plasmonic Photocatalysts for Degradation of Organic Compounds under UV and Visible Light Irradiation. *Catal. Today* **2014**, *230*, 131–137.

(82) McGilvray, K. L.; Decan, M. R.; Wang, D.; Scaiano, J. C. Facile Photochemical Synthesis of Unprotected Aqueous Gold Nanoparticles. *J. Am. Chem. Soc.* **2006**, *128*, 15980–15981.

(83) Haruta, M. Size- and Support-Dependency in the Catalysis of Gold. *Catal. Today* **1997**, *36*, 153–166.

(84) Hidalgo, M. C.; Murcia, J. J.; Navío, J. A.; Colón, G. Photodeposition of Gold on Titanium Dioxide for Photocatalytic Phenol Oxidation. *Appl. Catal. Gen.* **2011**, *397*, 112–120.

(85) Kimling, J.; Maier, M.; Okenve, B.; Kotaidis, V.; Ballot, H.; Plech, A. Turkevich Method for Gold Nanoparticle Synthesis Revisited. *J. Phys. Chem. B* **2006**, *110*, 15700–15707.

(86) Xu, Z.-C.; Shen, C.-M.; Yang, T.-Z.; Zhang, H.-R.; Li, H.-L.; Li, J.-Q.; Gao, H.-J. From Aqueous to Organic: A Step-by-Step Strategy for Shape Evolution of Gold Nanoparticles. *Chem. Phys. Lett.* **2005**, *415*, 342–345.

(87) Duff, D. G.; Baiker, A.; Edwards, P. P. A New Hydrosol of Gold Clusters. *J. Chem. Soc. Chem. Commun.* **1993**, 96–98.

(88) Primo, A.; Corma, A.; García, H. Titania Supported Gold Nanoparticles as Photocatalyst. *Phys. Chem. Chem. Phys. PCCP* **2011**, *13*, 886–910.

(89) Duff, D. G.; Baiker, A.; Edwards, P. P. A New Hydrosol of Gold Clusters. 1. Formation and Particle Size Variation. *Langmuir* **1993**, *9*, 2301–2309.

(90) Duff, D. G.; Baiker, A.; Gameson, I.; Edwards, P. P. A New Hydrosol of Gold Clusters. 2. A Comparison of Some Different Measurement Techniques. *Langmuir* **1993**, *9*, 2310–2317.

(91) Wishart, J. F.; Rao, B. *Recent Trends in Radiation Chemistry*; WORLD SCIENTIFIC, 2010.

(92) Belloni, J. Nucleation, Growth and Properties of Nanoclusters Studied by Radiation Chemistry: Application to Catalysis. *Catal. Today* **2006**, *113*, 141–156.

(93) Remita, H.; Remita, S. Metal Clusters and Nanomaterials: Contribution of Radiation Chemistry. In *Recent Trends in Radiation Chemistry*; World Scientific, **2010**; 347–383.

(94) Abidi, W.; Remita, H. Gold Based Nanoparticles Generated by Radiolytic and Photolytic Methods. *Recent Pat. Eng.* **2010**, *4*, 170–188.

(95) Buxton, G. V.; Greenstock, C. L.; Helman, W. P.; Ross, A. B. Critical Review of Rate Constants for Reactions of Hydrated Electrons, Hydrogen Atoms and Hydroxyl Radicals (·OH/·O− in Aqueous Solution. *J. Phys. Chem. Ref. Data* **1988**, *17*, 513–886.

(96) Delcourt, M.-O.; Belloni, J.; Marigner, J.-L.; Mory, C.; Colliex, C. Metal Microaggregates Prepared by Radiolytic Reduction in Liquids. *Radiat. Phys. Chem.* **1984**, *23*, 485–487.

(97) Dey, G. R.; El Omar, A. K.; Jacob, J. A.; Mostafavi, M.; Belloni, J. Mechanism of Trivalent Gold Reduction and Reactivity of Transient Divalent and Monovalent Gold Ions Studied by Gamma and Pulse Radiolysis. *J. Phys. Chem. A* **2011**, *115*, 383–391.

(98) Henglein, A. The Reactivity of Silver Atoms in Aqueous Solutions (A γ-Radiolysis Study). *Berichte Bunsenges. Für Phys. Chem.* **1977**, *81*, 556–561.

(99) Henglein, A.; Meisel, D. Radiolytic Control of the Size of Colloidal Gold Nanoparticles. *Langmuir* **1998**, *14*, 7392–7396.

(100) Belloni, J.; Mostafavi, M.; Remita, H.; Marignier, J.-L.; Delcourt, and M.-O. Radiation-Induced Synthesis of Mono- and Multi-Metallic Clusters and Nanocolloids. *New J. Chem.* **1998**, *22*, 1239–1255.

(101) Luna, A. L.; Novoseltceva, E.; Louarn, E.; Beaunier, P.; Kowalska, E.; Ohtani, B.; Valenzuela, M. A.; Remita, H.; Colbeau-Justin, C. Synergetic Effect of Ni and Au Nanoparticles Synthesized on Titania Particles for Efficient Photocatalytic Hydrogen Production. *Appl. Catal. B Environ.*

(102) Ni, M.; Leung, M. K. H.; Leung, D. Y. C.; Sumathy, K. A Review and Recent Developments in Photocatalytic Water-Splitting Using for Hydrogen Production. *Renew. Sustain. Energy Rev.* **2007**, *11*, 401–425.

(103) Ohtani, B.; Prieto-Mahaney, O. O.; Li, D.; Abe, R. What Is Degussa (Evonik) P25? Crystalline Composition Analysis, Reconstruction from Isolated Pure Particles and Photocatalytic Activity Test. *J. Photochem. Photobiol. Chem.* **2010**, *216*, 179–182.

(104) Duff,Daniel G., Alfons,Baiker,Edwards,Peter P.Bunsho Ohtani,and Hiroshi Kominami. A New Hydrosol of Gold Clusters. 1. Formation and Particle Size Variation. *Langmuir* **1993**, *9*, 2301–2309.

(105) Takei, T.; Akita, T.; Nakamura, I.; Fujitani, T.; Okumura, M.; Okazaki, K.; Huang, J.; Ishida, T.; Haruta, M. Chapter One - Heterogeneous Catalysis by Gold. In *Advances in Catalysis*; Bruce C. Gates and Friederike C. Jentoft, Ed.; Academic Press, **2012**; 55, 1–126.

(106) Orlov, A.; Jefferson, D.; Macleod, N.; Lambert, R. Photocatalytic Properties of TiO_2 Modified with Gold Nanoparticles in the Degradation of 4-Chlorophenol in Aqueous Solution. *Catal. Lett.* **2004**, *92*, 41–47.

(107) Aguilar-Tapia, A.; Zanella, R.; Calers, C.; Louis, C.; Delannoy, L. Synergistic Effects of Ir-Au/TiO2 Catalysts in the Total Oxidation of Propene: Influence of the Activation Conditions. *Phys. Chem. Chem. Phys. PCCP* **2015**, *17*, 28022–28032.

(108) Hashmi, A. S. K.; Hutchings, G. J. Gold Catalysis. *Angew. Chem. Int. Ed.* **2006**, *45*, 7896–7936.

(109) Yamakata, A.; Ishibashi, T.; Onishi, H. Time-Resolved Infrared Absorption Study of Nine TiO_2 Photocatalysts. *Chem. Phys.* **2007**, *339*, 133–137.

(110) Murdoch, M.; Waterhouse, G. I. N.; Nadeem, M. A.; Metson, J. B.; Keane, M. A.; Howe, R. F.; Llorca, J.; Idriss, H. The Effect of Gold Loading and Particle Size on Photocatalytic Hydrogen Production from Ethanol over Au/TiO_2 Nanoparticles. *Nat. Chem.* **2011**, *3*, 489–492.

(111) Wang, G.; Xu, L.; Zhang, J.; Yin, T.; Han, D.; Wang, G.; Xu, L.; Zhang, J.; Yin, T.; Han, D. Enhanced Photocatalytic Activity of Powders (P25) via Calcination Treatment, Enhanced Photocatalytic Activity of Powders (P25) via Calcination Treatment. *Int. J. Photoenergy Int. J. Photoenergy* **2012**, *2012*, 265760.

(112) Chiarello, G. L.; Selli, E.; Forni, L. Photocatalytic Hydrogen Production over Flame Spray Pyrolysis-Synthesised TiO_2 and Au/TiO_2. *Appl. Catal. B Environ.* **2008**, *84*, 332–339.

(113) Nishimura, S.; Abrams, N.; Lewis, B. A.; Halaoui, L. I.; Mallouk, T. E.; Benkstein, K. D.; van de Lagemaat, J.; Frank, A. J. Standing Wave Enhancement of Red Absorbance and Photocurrent in Dye-Sensitized Titanium Dioxide Photoelectrodes Coupled to Photonic Crystals. *J. Am. Chem. Soc.* **2003**, *125*, 6306–6310.

(114) Tsukamoto, D.; Shiraishi, Y.; Sugano, Y.; Ichikawa, S.; Tanaka, S.; Hirai, T. Gold Nanoparticles Located at the Interface of Anatase/Rutile TiO_2 Particles as Active Plasmonic Photocatalysts for Aerobic Oxidation. *J. Am. Chem. Soc.* **2012**, *134*, 6309–6315.

(115) Wen, Y.; Liu, B.; Zeng, W.; Wang, Y. Plasmonic Photocatalysis Properties of Au Nanoparticles Precipitated Anatase/rutile Mixed TiO_2 Nanotubes. *Nanoscale* **2013**, *20*, 9739–9746.

(116) Wang, X.; Dornom, T.; Blackford, M.; Caruso, R. A. Solvothermal Synthesis and Photocatalytic Application of Porous Au/TiO_2 Nanocomposites. *J. Mater. Chem.* **2012**, *22*, 11701–11710.

(117) Cárdenas-Lizana, F.; Gómez-Quero, S.; Idriss, H.; Keane, M. A. Gold Particle Size Effects in the Gas-Phase Hydrogenation of M-Dinitrobenzene over Au/TiO_2. *J. Catal.* **2009**, *268*, 223–234.

(118) Amaniampong, P. N.; Li, K.; Jia, X.; Wang, B.; Borgna, A.; Yang, Y. Titania-Supported Gold Nanoparticles as Efficient Catalysts for the Oxidation of Cellobiose to Organic Acids in Aqueous Medium. *ChemCatChem* **2014**, *6*, 2105–2114.

(119) Zielińska-Jurek, A.; Kowalska, E.; Sobczak, J. W.; Lisowski, W.; Ohtani, B.; Zaleska, A. Preparation and Characterization of Monometallic (Au) and Bimetallic (Ag/Au) Modified-Titania Photocatalysts Activated by Visible Light. *Appl. Catal. B Environ.* **2011**, *101*, 504–514.

(120) Bian, Z.; Tachikawa, T.; Zhang, P.; Fujitsuka, M.; Majima, T. Au/TiO_2 Superstructure-Based Plasmonic Photocatalysts Exhibiting Efficient Charge Separation and Unprecedented Activity. *J. Am. Chem. Soc.* **2014**, *136*, 458–465.

(121) Esumi, K.; Sarashina, S.; Yoshimura, T. Synthesis of Gold Nanoparticles from an Organometallic Compound in Supercritical Carbon Dioxide. *Langmuir* **2004**, *20*, 5189–5191.

(122) Kowalska, E.; Abe, R.; Ohtani, B. Visible Light-Induced Photocatalytic Reaction of Gold-Modified titanium(IV) Oxide Particles: Action Spectrum Analysis. *Chem. Commun.* **2009**, 241–243.

(123) Takai, A.; Kamat, P. V. Capture, Store, and Discharge. Shuttling Photogenerated Electrons across TiO_2–Silver Interface. *ACS Nano* **2011**, *5*, 7369–7376.

(124) Méndez-Medrano, M. G.; Kowalska, E.; Lehoux, A.; Herissan, A.; Ohtani, B.; Bahena, D.; Briois, V.; Colbeau-Justin, C.; Rodríguez-López, J. L.; Remita, H. Surface Modification of TiO_2 with Ag Nanoparticles and CuO Nanoclusters for Application in Photocatalysis. *J. Phys. Chem. C* **2016**.

(125) Orlov, A.; Jefferson, D. A.; Tikhov, M.; Lambert, R. M. Enhancement of MTBE Photocatalytic Degradation by Modification of TiO_2 with Gold Nanoparticles. *Catal. Commun.* **2007**, *8*, 821–824.

(126) Sonawane, R. S.; Dongare, M. K. Sol–gel Synthesis of Au/TiO_2 Thin Films for Photocatalytic Degradation of Phenol in Sunlight. *J. Mol. Catal. Chem.* **2006**, *243*, 68–76.

(127) Chavadej, S.; Phuaphromyod, P.; Gulari, E.; Rangsunvigit, P.; Sreethawong, T. Photocatalytic Degradation of 2-Propanol by Using Pt/TiO_2 Prepared by Microemulsion Technique. *Chem. Eng. J.* **2008**, *137*, 489–495.

(128) Tanaka, A.; Nakanishi, K.; Hamada, R.; Hashimoto, K.; Kominami, H. Simultaneous and Stoichiometric Water Oxidation and Cr(VI) Reduction in Aqueous Suspensions of Functionalized Plasmonic Photocatalyst Au/TiO_2–Pt under Irradiation of Green Light. *ACS Catal.* **2013**, *3*, 1886–1891.

(129) Waterhouse, G. I. N.; Wahab, A. K.; Al-Oufi, M.; Jovic, V.; Anjum, D. H.; Sun-Waterhouse, D.; Llorca, J.; Idriss, H. Hydrogen Production by Tuning the Photonic Band Gap with the Electronic Band Gap of TiO_2. *Sci Rep* **2013**, *3*.

(130) Joo, J. B.; Dillon, R.; Lee, I.; Yin, Y.; Bardeen, C. J.; Zaera, F. Promotion of Atomic Hydrogen Recombination as an Alternative to Electron Trapping for the Role of Metals in the Photocatalytic Production of H_2. *Proc. Natl. Acad. Sci. U. S. A.* **2014**, *111*, 7942–7947.

(131) Zhang, Y.; Pluchery, O.; Caillard, L.; Lamic-Humblot, A.-F.; Casale, S.; Chabal, Y. J.; Salmeron, M. Sensing the Charge State of Single Gold Nanoparticles via Work Function Measurements. *Nano Lett.* **2015**, *15*, 51–55.

(132) Caretti, I.; Keulemans, M.; Verbruggen, S. W.; Lenaerts, S.; Doorslaer, S. V. Light-Induced Processes in Plasmonic Gold/TiO_2 Photocatalysts Studied by Electron Paramagnetic Resonance. *Top. Catal.* **2015**, *58*, 776–782.

(133) Priebe, J. B.; Karnahl, M.; Junge, H.; Beller, M.; Hollmann, D.; Brückner, A. Water Reduction with Visible Light: Synergy between Optical Transitions and Electron Transfer in Au-TiO_2 Catalysts Visualized by In Situ EPR Spectroscopy. *Angew. Chem. Int. Ed.* **2013**, *52*, 11420–11424.

(134) Haruta, M.; Kobayashi, T.; Sano, H.; Yamada, N. Novel Gold Catalysts for the Oxidation of Carbon Monoxide at a Temperature Far Below 0 °C. *Chem. Lett.* **1987**, *16*, 405–408.

(135) Helaïli, N.; Bessekhouad, Y.; Bouguelia, A.; Trari, M. Visible Light Degradation of Orange II Using xCuyOz/TiO_2 Heterojunctions. *J. Hazard. Mater.* **2009**, *168*, 484–492.

(136) Xu, S.; Sun, D. D. Significant Improvement of Photocatalytic Hydrogen Generation Rate over TiO_2 with Deposited CuO. *Int. J. Hydrog. Energy* **2009**, *34*, 6096–6104.

(137) Luna, A. L.; Valenzuela, M. A.; Colbeau-Justin, C.; Vázquez, P.; Rodriguez, J. L.; Avendaño, J. R.; Alfaro, S.; Tirado, S.; Garduño, A.; De la Rosa, J. M. Photocatalytic Degradation of Gallic Acid over CuO–TiO_2 Composites under UV/Vis LEDs Irradiation. *Appl. Catal. Gen.*

(138) Zhao, L.; Cui, T.; Li, Y.; Wang, B.; Han, J.; Han, L.; Liu, Z. Efficient Visible Light Photocatalytic Activity of P–n Junction CuO/TiO_2 Loaded on Natural Zeolite. *RSC Adv.* **2015**, *5*, 64495–64502.

(139) Qiu, X.; Miyauchi, M.; Yu, H.; Irie, H.; Hashimoto, K. Visible-Light-Driven Cu(II)-(Sr(1-y)Na(y))(Ti(1-x)Mo(x))O3 Photocatalysts Based on Conduction Band Control and Surface Ion Modification. *J. Am. Chem. Soc.* **2010**, *132*, 15259–15267.

(140) Irie, H.; Miura, S.; Kamiya, K.; Hashimoto, K. Efficient Visible Light-Sensitive Photocatalysts: Grafting Cu(II) Ions onto TiO_2 and WO_3 Photocatalysts. *Chem. Phys. Lett.* **2008**, *457*, 202–205.

(141) Seo, S.-D.; Jin, Y.-H.; Lee, S.-H.; Shim, H.-W.; Kim, D.-W. Low-Temperature Synthesis of CuO-Interlaced Nanodiscs for Lithium Ion Battery Electrodes. *Nanoscale Res. Lett.* **2011**, *6*, 397.

(142) Espinós, J. P.; Morales, J.; Barranco, A.; Caballero, A.; Holgado, J. P.; González-Elipe, A. R. Interface Effects for Cu, CuO, and Cu_2O Deposited on SiO_2 and ZrO_2. XPS Determination of the Valence State of Copper in Cu/SiO_2 and Cu/ZrO_2 Catalysts. *J. Phys. Chem. B* **2002**, *106*, 6921–6929.

(143) Moretti, G.; Fierro, G.; Lo Jacono, M.; Porta, P. Characterization of CuO–ZnO Catalysts by X-Ray Photoelectron Spectroscopy: Precursors, Calcined and Reduced Samples. *Surf. Interface Anal.* **1989**, *14*, 325–336.

(144) Chusuei, C. C.; Brookshier, M. A.; Goodman, D. W. Correlation of Relative X-Ray Photoelectron Spectroscopy Shake-up Intensity with CuO Particle Size. *Langmuir* **1999**, *15*, 2806–2808.

(145) Klepka, M. T.; Drzewiecka, A.; Wolska, A.; Ferenc, W. XAS Studies on Cu(II) Complexes with Derivatives of Phenoxyacetic and Benzoic Acids. *Chem. Phys. Lett.* **2012**, *553*, 59–63.

(146) Khatouri, J.; Mostafavi, M.; Amblard, J.; Belloni, J. Radiation-Induced Copper Aggregates and Oligomers. *Chem. Phys. Lett.* **1992**, *191*, 351–356.

(147) Chettibi, S.; Keghouche, N.; Benguedouar, Y.; Bettahar, M. M.; Belloni, J. Structural and Catalytic Characterization of Radiation-Induced Ni/TiO_2 Nanoparticles. *Catal. Lett.* **2013**, *143*, 1166–1174.

(148) Colón, G.; Maicu, M.; Hidalgo, M. C.; Navío, J. A. Cu-Doped TiO_2 Systems with Improved Photocatalytic Activity. *Appl. Catal. B Environ.* **2006**, *67*, 41–51.

(149) Chiang, K.; Amal, R.; Tran, T. Photocatalytic Degradation of Cyanide Using Titanium Dioxide Modified with Copper Oxide. *Adv. Environ. Res.* **2002**, *6*, 471–485.

(150) Foster, N. S.; Noble, R. D.; Koval, C. A. Reversible Photoreductive Deposition and Oxidative Dissolution of Copper Ions in Titanium Dioxide Aqueous Suspensions. *Environ. Sci. Technol.* **1993**, *27*, 350–356.

(151) Sreethawong, T.; Yoshikawa, S. Comparative Investigation on Photocatalytic Hydrogen Evolution over Cu-, Pd-, and Au-Loaded Mesoporous TiO_2 Photocatalysts. *Catal. Commun.* **2005**, *6*, 661–668.

(152) Chavadej, S.; Phuaphromyod, P.; Gulari, E.; Rangsunvigit, P.; Sreethawong, T. Photocatalytic Degradation of 2-Propanol by Using Pt/TiO_2 Prepared by Microemulsion Technique. *Chem. Eng. J.* **2008**, *137*, 489–495.

(153) Nishijima, K.; Ohtani, B.; Yan, X.; Kamai, T.; Chiyoya, T.; Tsubota, T.; Murakami, N.; Ohno, T. Incident Light Dependence for Photocatalytic Degradation of Acetaldehyde and Acetic Acid on S-Doped and N-Doped TiO_2 Photocatalysts. *Chem. Phys.* **2007**, *339*, 64–72.

(154) Ge, Y.; Shah, Z. H.; Wang, C.; Wang, J.; Mao, W.; Zhang, S.; Lu, R. In Situ Encapsulation of Ultrasmall CuO Quantum Dots with Controlled Band-Gap and Reversible Thermochromism. *ACS Appl. Mater. Interfaces* **2015**, *7*, 26437–26444.

(155) Markowska-Szczupak, A.; Wang, K.; Rokicka, P.; Endo, M.; Wei, Z.; Ohtani, B.; Morawski, A. W.; Kowalska, E. The Effect of Anatase and Rutile Crystallites Isolated from Titania P25 Photocatalyst on Growth of Selected Mould Fungi. *J. Photochem. Photobiol. B* **2015**, *151*, 54–62.

(156) Calvo, A. M.; Wilson, R. A.; Bok, J. W.; Keller, N. P. Relationship between Secondary Metabolism and Fungal Development. *Microbiol. Mol. Biol. Rev. MMBR* **2002**, *66*, 447–459, table of contents.

(157) Kowalska, E.; Wei, Z.; Karabiyik, B.; Herissan, A.; Janczarek, M.; Endo, M.; Markowska-Szczupak, A.; Remita, H.; Ohtani, B. Silver-Modified Titania with Enhanced Photocatalytic and Antimicrobial Properties under UV and Visible Light Irradiation. *Catal. Today* **2015**, *252*, 136–142.

(158) Ovcharov, M. L.; Shvalagin, V. V.; Granchak, V. M. Photocatalytic Reduction of CO2 on Mesoporous TiO_2 Modified with Ag/Cu Bimetallic Nanostructures. *Theor. Exp. Chem.* **2014**, *50*, 175–180.

(159) Yao, X.; Zhang, X.; Wu, H.; Tian, L.; Ma, Y.; Tang, B. Microstructure and Antibacterial Properties of Cu-Doped TiO_2 Coating on Titanium by Micro-Arc Oxidation. *Appl. Surf. Sci.* **2014**, *292*, 944–947.

(160) Matsunaga, T.; Tomoda, R.; Nakajima, T.; Wake, H. Photoelectrochemical Sterilization of Microbial Cells by Semiconductor Powders. *FEMS Microbiol. Lett.* **1985**, *29*, 211–214.

(161) Guillard, C.; Bui, T.-H.; Felix, C.; Moules, V.; Lina, B.; Lejeune, P. Microbiological Disinfection of Water and Air by Photocatalysis. *Comptes Rendus Chim.* **2008**, *11*, 107–113.

(162) Zhao, J.; Yang, X. Photocatalytic Oxidation for Indoor Air Purification: A Literature Review. *Build. Environ.* **2003**, *38*, 645–654.

(163) Hansen, M.; Elliott, R. P.; Shunk, F. A. *Constitution of binary alloys.*, 15a ed.; McGraw-Hill: New York, 1958.

(164) Lequien, F.; Creuze, J.; Berthier, F.; Braems, I.; Legrand, B. Superficial Segregation, Wetting, and Dynamical Equilibrium in Bimetallic Clusters: A Monte Carlo Study. *Phys. Rev. B* **2008**, *78*, 075414.

(165) Moreno, V.; Creuze, J.; Berthier, F.; Mottet, C.; Tréglia, G.; Legrand, B. Site Segregation in Size-Mismatched Nanoalloys: Application to Cu–Ag. *Surf. Sci.* **2006**, *600*, 5011–5020.

(166) Lequien, F.; Creuze, J.; Berthier, F.; Legrand, B. Dynamical Equilibrium in Nanoalloys. *Faraday Discuss.* **2008**, *138*, 105–117;

(167) Guisbiers, G.; Mendoza-Cruz, R.; Bazán-Díaz, L.; Velázquez-Salazar, J. J.; Mendoza-Perez, R.; Robledo-Torres, J. A.; Rodriguez-Lopez, J.-L.; Montejano-Carrizales, J. M.; Whetten, R. L.; José-Yacamán, M. Electrum, the Gold–Silver Alloy, from the Bulk Scale to the Nanoscale: Synthesis, Properties, and Segregation Rules. *ACS Nano* **2015**.

(168) Pellarin, M.; Issa, I.; Langlois, C.; Lebeault, M.-A.; Ramade, J.; Lermé, J.; Broyer, M.; Cottancin, E. Plasmon Spectroscopy and Chemical Structure of Small Bimetallic Cu(1–x)Agx Clusters. *J. Phys. Chem. C* **2015**, *119*, 5002–5012.

(169) Verbruggen, S. W.; Keulemans, M.; Filippousi, M.; Flahaut, D.; Van Tendeloo, G.; Lacombe, S.; Martens, J. A.; Lenaerts, S. Plasmonic Gold–silver Alloy on TiO_2 Photocatalysts with Tunable Visible Light Activity. *Appl. Catal. B Environ.* **2014**, *156*, 116–121.

(170) Stathatos, E.; Lianos, P.; Falaras, P.; Siokou, A. Photocatalytically Deposited Silver Nanoparticles on Mesoporous TiO_2 Films. *Langmuir* **2000**, *16*, 2398–2400.

(171) Waterhouse, G. I. N.; Bowmaker, G. A.; Metson, J. B. Oxidation of a Polycrystalline Silver Foil by Reaction with Ozone. *Appl. Surf. Sci.* **2001**, *183*, 191–204.

(172) Bielmann, M.; Schwaller, P.; Ruffieux, P.; Gröning, O.; Schlapbach, L.; Gröning, P. AgO Investigated by Photoelectron Spectroscopy: Evidence for Mixed Valence. *Phys. Rev. B* **2002**, *65*, 235431.

(173) Han, Y.; Lupitskyy, R.; Chou, T.-M.; Stafford, C. M.; Du, H.; Sukhishvili, S. Effect of Oxidation on Surface-Enhanced Raman Scattering Activity of Silver Nanoparticles: A Quantitative Correlation. *Anal. Chem.* **2011**, *83*, 5873–5880.

(174) Pauly, N.; Tougaard, S.; Yubero, F. Determination of the Cu 2p Primary Excitation Spectra for Cu, Cu_2O and CuO. *Surf. Sci.* **2014**, *620*, 17–22.

(175) Peters, S.; Peredkov, S.; Neeb, M.; Eberhardt, W.; Al-Hada, M. Size-Dependent XPS Spectra of Small Supported Au-Clusters. *Surf. Sci.* **2013**, *608*, 129–134.

(176) Kowalska, E.; Remita, H.; Colbeau-Justin, C.; Hupka, J.; Belloni, J. Modification of Titanium Dioxide with Platinum Ions and Clusters: Application in Photocatalysis. *J. Phys. Chem. C* **2008**, *112*, 1124–1131.

(177) Mizeikis, V.; Kowalska, E.; Juodkazis, S. Resonant Localization, Enhancement, and Polarization of Optical Fields in Nano-Scale Interface Regions for Photo-Catalytic Applications. *J. Nanosci. Nanotechnol.* **2011**, *11*, 2814–2822.

(178) Emilio, C. A.; Litter, M. I.; Kunst, M.; Bouchard, M.; Colbeau-Justin, C. Phenol Photodegradation on Platinized-TiO_2 Photocatalysts Related to Charge-Carrier Dynamics. *Langmuir* **2006**, *22*, 3606–3613.

(179) Furube, A.; Du, L.; Hara, K.; Katoh, R.; Tachiya, M. Ultrafast Plasmon-Induced Electron Transfer from Gold Nanodots into TiO_2 Nanoparticles. *J. Am. Chem. Soc.* **2007**, *129*, 14852–14853.

(180) Klassen, N. V.; Shortt, K. R.; Seuntjens, J.; Ross, C. K. Fricke Dosimetry: The Difference between G(Fe^{3+}) for ^{60}Co Gamma-Rays and High-Energy X-Rays. *Phys. Med. Biol.* **1999**, *44*, 1609–1624.

(181) Andrade, L. S.; Laurindo, E. A.; Oliveira, R. V. de; Rocha-Filho, R. C.; Cass, Q. B. Development of a HPLC Method to Follow the Degradation of Phenol by Electrochemical or Photoelectrochemical Treatment. *J. Braz. Chem. Soc.* **2006**, *17*, 369–373.

(182) Gaya, U. I. Kinetic Concepts of Heterogeneous Photocatalysis. In *Heterogeneous Photocatalysis Using Inorganic Semiconductor Solids*; Springer Netherlands, **2014**; 43–71.

(183) Powder X-ray Diffraction and its Application to Biotherapeutic Formulation Development http://www.americanpharmaceuticalreview.com/Featured-Articles/38371-Powder-X-ray-Diffraction-and-its-Application-to-Biotherapeutic-Formulation-Development/ (accessed Oct 14, **2015**).

(184) Genevieve Christine, S. Diffuse reflectance spectroscopy for the characterization of calcareous gracial till soils from north central montana

http://scholarworks.montana.edu/xmlui/bitstream/handle/1/2352/StewardG1206.pdf?sequence=1 (accessed Oct 20, **2015**).

(185) UV-Vis Spectrophotometers - Diffuse Reflectance Measurement: Shimadzu ScientificInstrumentshttp://www.ssi.shimadzu.com/products/product.cfm?product=uv_accy_solid_guide1 (accessed Oct 20, **2015**).

(186) Gutiérrez, G.; Ixcóatl, D. Transmission Electron Microscopy Characterization of Composite Nanostructures. Transmission electron microscopy characterization of composite nanostructures, **2008**.

(187) Zibin, H. Modification of Titania with Gold-Copper Bimetallic Nanoparticles and Preparation of Copper-Based Photocatalysts : Application in Water Treatment. Modification of Titania with Gold-Copper Bimetallic Nanoparticles and Preparation of Copper-Based Photocatalysts : Application in Water Treatment, Université Paris Sud - Paris XI, **2013**.

(188) Scudiero, L. X-Ray Photoelectron Spectroscopy (XPS) http://public.wsu.edu/~scudiero/documents/571-XPS-Lecture1.pdf (accessed Oct 16, **2015**).

(189) J.E. Penner-Hahn. X-Ray Absorption Spectroscopy, The University of Michigan: Ann Arbor, MI, USA.

(190) Kouamé, N. A.; Alaoui, O. T.; Herissan, A.; Larios, E.; José-Yacaman, M.; Etcheberry, A.; Colbeau-Justin, C.; Remita, H. Visible Light-Induced Photocatalytic Activity of Modified titanium(IV) Oxide with Zero-Valent Bismuth Clusters. *New J. Chem.* **2015**, *39*, 2316–2322.

(191) Martin, S. T.; Herrmann, H.; Choi, W.; Hoffmann, M. R. Time-Resolved Microwave Conductivity. Part 1. TiO_2 Photoreactivity and Size Quantization. *J. Chem. Soc. Faraday Trans.* **1994**, *90*, 3315.